Precise tune determination and split beam emittance reconstruction at the CERN PS synchrotron

Dissertation
zur Erlangung des Doktorgrades
der Naturwissenschaften

vorgelegt beim Fachbereich Physik
der Johann Wolfgang Goethe -Universität
in Frankfurt am Main

von
Giulia Russo
aus Reggio Emilia
Frankfurt 2022

(D 30)

Accepted by the Faculty of Physics of the Johann Wolfgang Goethe University as a dissertation.

Dean: Prof. Dr. Roger Erb

Reviewer: Prof. Dr. Giuliano Franchetti
Prof. Dr. Ulrich Ratzinger

Date of the oral defence: 31.01.2023

A mia mamma,
grazie.

Abstract

In accelerator physics, the need to improve the performance and better control the operating point of an accelerator has become, year after year, an increasingly important need in order to achieve higher energies and brightness, as well as point-like particle beams. If this involves increasingly advanced technological developments (in terms, for example, of materials for more intense superconducting magnets), it can not take place in the absence of targeted studies of linear and non-linear beam dynamics.

In the context of this Ph.D. thesis in physics, linear and non-linear dynamics of charged particles in circular accelerators is the topic that will be discussed and treated in detail. In particular, the presentation and discussion of the results will be divided in two main topics: the need to know the physical properties of a proton beam; and the development of innovative methods to determine and study the accelerator's working point.

With regard to the first topic, an innovative procedure will be presented to determine the transverse size of the PS beam in the beam extraction phase. Among the different ways the extraction occurs at the PS, the analysed one is based on the transverse splitting of the beam by means of non-linear fields. Thus, the knowledge of the transverse beam size is not trivial since resonant linear and non-linear beam structures (namely, core and islands) arise and, for each of them, the beam size has to be quantified. This parameter is crucial for two main reasons: the accelerator that will receive the beam exiting the upstream accelerator may have restrictions (physical or magnetic) that involve a partial or total loss of the incoming beam; and any experiments located downstream of the considered accelerator may need a beam with a transversal size as constant as possible; consequently, its monitoring and control are essential.

The second topic concerns the accurate determination of the working point of an accelerator, defined as the number of transverse oscillations the particle beam travels per unit of accelerator circumference, both horizontally and vertically. This quantity is called horizontal and vertical tune, respectively. Their knowledge is also crucial to understand whether the beam will be stable or unstable. In fact, not all tune values are acceptable, as there are particular values that bring the beam into resonance. In this configuration, the amplitude of the transverse oscillations of the particles increases in an uncontrolled manner and leads to the loss of all or part of the beam. Note that, in particular operating conditions, the resonant conditions are sought and desired to model, in a suitable way, the transversal shape of the beam, such as the above mentioned PS extraction scheme. It is even clearer how much the determination of the machine working point is essential to determine the operating conditions of an accelerator. In this context, several methods (also taken from the field of applied mathematics) to calculate the tune will be demonstrated and tested numerically on different types of synthetic signals. At the end of this description, the use of experimental data will allow to obtain the benchmark of a new method for the direct calculation of some characteristic quantities of non-linear beam dynamics (namely, the amplitude detuning, i.e. the variation of tune as a function of intensity of the perturbation provided to the beam).

ZUSAMMENFASSUNG

In der Beschleunigerphysik wird die Notwendigkeit, die Beschleunigerleistung zu verbessern und den Arbeitspunkt besser zu steuern, Jahr für Jahr immer wichtiger, um höhere Energien und Luminositäten, sowie punktförmige Teilchenstrahlen zu erreichen. Dies ist einerseits mit einer immer weiter fortgeschrittenen technologischen Entwicklung (in Bezug auf Materialien und Werkzeuge) verbunden, andererseits kann dies ohne gezielte Untersuchungen zur linearen und nichtlinearen Strahldynamik nicht erfolgen. Daher ist es notwendig, das Wissen und die Werkzeuge, die in diesem Bereich verwendet werden, zu vertiefen und zu verbessern.

Im Rahmen dieser Doktorarbeit in Physik wird die lineare und nichtlineare Strahldynamik von Teilchenbeschleunigern das Thema sein, das ausführlich diskutiert und behandelt wird. Es ist jedoch wichtig zu betonen, dass, obwohl der Doktorandenkurs am CERN (Conseil Européen pour la Recherche Nucléaire) in Genf (Schweiz) durchgeführt wird, die behandelten und diskutierten Themen auf jeden Teilchenbeschleuniger anwendbar sind, insbesondere auf Synchrotrone. Die Präsentation und Diskussion der Ergebnisse gliedert sich in zwei Hauptthemen: einerseits die Notwendigkeit, die physikalischen Eigenschaften eines Teilchenstrahls zu kennen, andererseits die Entwicklung innovativer Methoden zur Bestimmung und Untersuchung des Arbeitspunktes des Beschleunigers. Die Dissertation wurde so strukturiert, dass dem Leser ein Manuskript zur Verfügung steht, das nützliche Informationen zum Verständnis der in den letzten Kapiteln beschriebenen Ergebnisse enthält. Insbesondere sind die Hauptprobleme und die gefundenen Lösungen wie folgt strukturiert.

Rekonstruktion der transversalen Große für einen geteilten transversalen Strahl

Unter den verschiedenen Möglichkeiten, wie der PS-Ring den Strahl extrahieren kann, konzentriert sich die vorliegende Diskussion auf die Multi-Turn Extraction (MTE) Methode, eine neuartige Technik, die den Strahl quer in n gleich besetzte Beamlets aufteilt, die dann nacheinander extrahiert werden. Insbesondere wird am PS die MTE Methode mittels einer stabilen Resonanz der Ordnung 4 ausgeführt, was es ermöglicht, fünf Beamlets zu erhalten, die über fünf aufeinanderfolgende Umläufe extrahiert werden.

Mit nichtlinearen Magneten (z. B. Sextupolen, Oktupolen und anderen Magneten mit einer größeren Polzahl) wird ein quergeteilter Teilchenstrahl erzeugt und geformt. Der Strahl ist dadurch gekennzeichnet, dass er einen linearen zentralen Bereich hat, der auch "Kern" genannt wird, sowie eine stark nichtlineare periphere Struktur. Diese Struktur kann je nach dem Verhalten der Teilchen weiter klassifiziert werden: Wenn die Amplitude der Oscilationen dazu neigt, unkontrolliert zuzunehmen, ist der Randbereich durch instabile Fixpunkte gekennzeichnet. Wenn die Teilchen dagegen dazu neigen, stabil um einen Punkt zu kreisen, handelt es sich um einen stabilen Fixpunkt, und die Teilchen können auf unbestimmte Zeit in diesem Bereich bleiben (solange es keine störenden Phänomene gibt) und es bilden sich sogenannte "Inseln".

In dem in der vorliegenden Konfiguration analysierten Fall ist der transversale Phasenraum dadurch gekennzeichnet, dass er einen Kern und vier Inseln hat. Diese Bedingung wird durch eine Resonanz vierter Ordnung erzielt. Welche Querabmessung hat ein so quer geteilter Balken? Die Antwort hängt von mehreren Faktoren ab. Einerseits hängt viel vom verwendeten Messgerät ab, andererseits davon, wie die Querabmessung des Strahls in diesem Resonanzzustand definiert ist. Da diese Analyse am CERN PS-Beschleuniger durchgeführt wurde, dessen Strahl eine Umlaufzeit von etwa 2.1 μs hat, war das gewählte Instrument ein Diamantdetektor mit einer Zeitauflösung von 2 ns. Zwischen 2012 und 2017 wurden mehrere Versuchskampagnen durchgeführt, um die Querabmessung des Strahls zu bestimmen, aber der verwendete Ansatz erlaubte es nie, die Größe jedes Beamlets (des Kerns und der einzeln vier Inseln) genau zu bestimmen. Im Jahr 2019 wurde eine neue Methode vorgeschlagen, die die Bestimmung der Größe der fünf Beamlets mit dem oben erwähnten Diamantdetektor ermöglicht. Diese Technik besteht darin, die Strahlverluste während der Extraktionsphase zu messen. Diese Kurven werden dann mit einer Gaußschen Kurve angepasst und es wird gezeigt, dass die Amplitude der Gaußschen Kurve in direktem Zusammenhang mit der Querabmessung des Strahls steht.

Im Rahmen dieser Forschung wurde einerseits der experimentelle Benchmark der Kernemittanz anhand der experimentellen Daten der Kampagne 2017 erstellt, andererseits wurde erstmals und eindeutig definiert, wie das Quermaß für die Inseln zu berechnen ist. Da sie eine extrem nichtlineare Dynamik haben, können sie tatsächlich nicht als Kern behandelt werden [...] sondern es ist eine genanere Betrachtung notwendig. An dieser Stelle wurde die Sensitivitätsanalyse einiger Maschinenparameter durchgeführt, um zu verstehen, wie sich die Querabmessung der Inseln verändert. Es wurde festgestellt, dass kleine Abweichungen von den Nennbedingungen äußerst signifikante Änderungen in der Dynamik der Inseln hervorrufen, so stark, dass von etwa 1000 synthetischen Modellen nur etwas mehr als 200 analysiert werden können. Der Rest wurde verworfen, da die Variation einiger physikalischer Größen nicht akzeptabel war und es in der praxis zu einem erheblichen, wenn nicht vollständigen Strahlverlust geführt hätte. Die durchgeführte Sensitivitätsanalyse beschränkte sich auf die Berücksichtigung der Variation einiger nichtlinearer magnetischer Komponenten, jedoch können andere ebenso wichtige Variablen signifikante Auswirkungen auf die Größe und Position der Inseln im Phasenraum haben.

Die Wichtigkeit hochpräziser Frequenzbestimmung

In diesem Kapitel werden zwei weitere Parameter analysiert, die sich im Laufe der Jahre als deterministisch für die korrekte Verteilung der Partikel zwischen Kernen und Inseln sowie in ihrer Stabilität und Größe herausgestellt haben.

Zunächst wurde die Effizienz der Aufspaltung betrachtet, definiert als das Verhältnis zwischen der Anzahl der Partikel in den Inseln dividiert durch die Gesamtzahl aller Partikel. Dieser Parameter hat sich in den letzten 10 Jahren als besonders problematisch erwiesen, da zunächst unerklärbare Schwingungen observiert wurden. Nach zahlreichen Studien wurden die Ursachen verstanden und gelöst, was zu einer gleichmäßigen Verteilung der Partikel zwischen Kernen und Inseln führte. Dieser Erfolg ist absolut bemerkenswert, da er garantiert, fünf in der Querebene getrennte Beamlets zu haben, die, wenn sie nacheinander extrahiert werden, die notwendige und erforderliche Gleichmäßigkeit zum Beschleuniger oder zum nachgeschalteten Experiment gewährleisten. Die Analyse der Spaltungs-Effizienz wurde auch an den Daten durchgeführt, die in der vorherigen Analyse verwendet wurden, um zu verifizieren, dass es keine unentdeckten Anomalien gab.

Zweitens wurde untersucht, ob eine Änderung des Arbeitspunktes des Beschleunigers (der

Proton Synchrotron, PS, da die experimentellen Daten aus Messungen stammen, die an dieser Maschine durchgeführt wurden) zu Änderungen in der Form und/oder Größe der Inseln im Phasenraum führen würde. Aus der Analyse der numerischen Ergebnisse ging klar hervor, dass eine Erhöhung oder Verringerung des Tunes einen unterschiedlichen Effekt im transversalen Phasenraum erzeugt. Insbesondere ist eine Erhöhung des Tunes in der Ebene, in der der Strahl geteilt wird, kritischer als ihre Verringerung. Tatsächlich wird festgestellt, dass die Inseln nach einer Erhöhung des Tunes dazu neigen, sich voneinander wegzubewegen, was zu einer Annäherung an die durch den Beschleuniger auferlegten physikalischen und magnetischen Grenzen und daher zu möglichen unerwünschten Verlusten führt. Zusätzlich zu dieser Verschiebung gibt es auch eine weitere Verringerung des stabilen Raums um den Fixpunkt herum, mit einer daraus resultierenden Verringerung der Anzahl der enthaltenen Teilchen und daher einer größeren Ungleichmäßigkeit zwischen den in den Inseln und im Kern enthaltenen Teilchen.

Aus dieser Analyse wird geschlossen, dass es wichtig ist,die Frequenz, also den Arbeitspunkt eines Beschleunigers, mit äußerster Präzision zu bestimmen.

Methoden zur hochpräzisen Frequenzbestimmung

Dieses Kapitel beschreibt die in den späten 1990er Jahren entwickelten Methoden, die die Grundlagen und den Stand der Technik für die präzise Berechnung des Tunes bildeten. Die Beschreibung dieser Methoden und ihrer numerischen Simulation ermöglicht es, den Ausgangspunkt dieser Forschung vollständig zu beschreiben und somit zu definieren. Diese Verfahren sind alle dadurch gekennzeichnet, dass sie auf der Fast Fourier-Transformation (FFT) basieren. Die FFT ist einerseits ein bekanntes und etabliertes Werkzeug in der Analyse von Signalen und diskreten Zeitreihen, sie hat andererseits aber auch ihre intrinsischen Grenzen. Für eine korrekte Verwendung der FFT muss das analysierte Signal (oder die Zeitreihe) über die gesamte Zeit sowohl eine konstante Amplitude als auch eine konstante Frequenz haben.

Auf dem Gebiet der Beschleunigerphysik werden die analysierten zeitlichen Signale durch die durchschnittliche Position des Schwerpunkts des Strahls bestimmt, der an einem bestimmten Punkt des Beschleunigers (d.h. dort, wo die Beam Position Monitors, BPMs, installiert sind) für eine bestimmte Anzahl von Umläufen beobachtet wird. Unter diesen Bedingungen ist die Messfrequenz konstant sowie auch, die Frequenz des Signals (wenn die Messung bei konstanter Energie erfolgt). Jedoch ist die Amplitude dieses Signals nicht immer konstant: sie hängt davon ab, wie die experimentelle Messung durchgeführt wird. Daher ist es von grundlegendem Interesse, die Leistungsfähigkeit der Verfahren, die den Stand der Technik darstellen, in Gegenwart eines amplitudenmodulierten Signals zu untersuchen. Diese Analyse und die damit verbundenen Ergebnisse werden in diesem Kapitel vorgestellt.

Die zweite in diesem Kapitel behandelte Frage betrifft die Möglichkeit, neue analytische Formeln zur Berechnung des Tunes für ein Signal mit konstanter Amplitude zu bestimmen. Daher wird eine neue Gleichung vorgestellt und analysiert, die aus der Verwendung der Zero-Padding-Technik abgeleitet wird. Die Ergebnisse dieser Methode werden mit denen der Methoden nach dem Stand der Technik verglichen.

Der gewichtete Birkhoff-Mittelwert ist die letzte Methode, die vorgestellt und diskutiert wird, um die Analyse von Signalen mit konstanter Amplitude abzuschließen. Diese Methode ist im Bereich der angewandten Mathematik bekannt, wo die Langzeitstabilität von Abbbildungen und die Identifizierung chaotischer, resonanter und stabiler Bereiche von grundlegender Bedeutung und Interesse sind. Es wird erstmals auf dem Gebiet der Beschleunigerphysik und insbesondere

der Bestimmung des Tunes angewendet. Das Skalengesetz, das das Verhältnis zwischen der Zahl der Umläufe und der Unschärfe des Tunes definiert, wird durch numerische Simulationen bestimmt, da ein rein analytischer Ansatz nicht möglich ist. Es wird darauf hingewiesen, dass dieses Skalierungsgesetz besser ist als das von allen anderen Verfahren. Folglich wird die Verwendung des Birkhoff-Mittelwerts bei synthetischen Signalen dringend empfohlen, um die Frequenz des Signals selbst zu analysieren.

Eine zusätzliche Studie wurde unter Berücksichtigung der Auswirkungen von Rauscken durchgeführt. Unter diesen Bedingungen wurden die bisher beschriebenen und entwickelten Verfahren getestet und ihre Leistungsfähigkeit verglichen. Präzisere Methoden wie Birkhoff und Hanning liefern eine schlechtere Bestimmung der Tunegenauigkeit, als die interpolierte FFT. Daher sollte bei Vorhandensein von Rauschen diese letztere Methode bevorzugt werden.

Bevor mit der Analyse der amplitudenmodulierten Signale fortgefahren wurde, wurde die Henon-Abbildung untersucht. Diese 4D-Abbildung beschreibt einen Beschleuniger, der nur aus Dipolen und Quadrupolen besteht, denen ein sextupolarer Kick hinzugefügt wurde. Folglich erweist es sich als die einfachste mögliche Beschreibung eines Ringbeschleunigers mit einem nichtlinearen Beitrag. Nachdem die horizontalen und vertikalen Tune-Werte definiert wurden, werden 10^5 Anfangsbedingungen für 10^6 Umdrehungen ausgewertet, um ihre Stabilität zu untersuchen. Nachdem die Grenzen des stabilen Bereichs definiert und verstanden wurden, wird die Tuneanalyse für diejenigen Fälle durchgeführt, die die Stabilitätsbedingung erfüllen. Zwei Methoden (Hanning, die beste Methode zur Berechnung der Tonhöhe unter den im Stand der Technik beschriebenen, sowie der gewichtete Birkhoff-Durchschnitt) werden verwendet, um den Tune für stabile Bedingungen für N und $2N$ Umdrehungen zu bestimmen. Unter den stabilen Bedingungen ist insbesondere die Identifizierung der Anfangsbedingungen von Interesse, die die Resonanzbedingung in der Beschleunigerphysik erfüllen (definiert als $\ell Q_x + mQ_y = N_{res}$), also ℓ mal der horizontale Tune (Q_x) addiert zu m mal dem vertikalen Tune (Q_y) sind gleich der Ordnung der Resonanz (N_{res}), definiert als die Summe aus ℓ und m. Aus dem Vergleich der Ergebnisse lässt sich erkennen, dass Birkhoff durch die höhere Präzision derTunebestimmung „unsichtbare“ Resonanzverhältnisse für Hanning ermitteln kann. Dieselbe Analyse wird auch bei Frequenzmodulation durchgeführt, wobei ähnliche Ergebnisse präsentiert und diskutiert werden.

Die Untersuchung amplitudenmodulierter Signale beginnt mit der einfachsten Modulationsanalyse: einer gedämpften Exponentialfunktion. Für diesen Fall wurde 2015 eine Gleichung zur Berechnung des Tunes und des Dämpfungskoeffizienten ermittelt. Daher wurde in Analogie zu dieser Studie eine neue Gleichung für die Berechnung des Tunes und des Dämpfungskoeffizienten für ein mit einer abnehmenden Exponentialfunktion moduliertes Signal ermittelt, deren Genauigkeit besser ist als die des abgeleiteten Verfahrens aus dem Jahr 2015. Jedoch ist der Fall des gedämpften Exponentials ist nur eine von vielen möglichen Modulationen. Um die Frequenz eines Signals unabhängig von seiner Amplitudenmodulation zu bestimmen, werden die Hilbert-Transformation und einige grundlegende Konzepte eingeführt, die in der anschließenden Analyse verwendet werden. Die Hilbert-Transformation ermöglicht es, die Einhüllende des Signals zu bestimmen und somit die zeitliche Entwicklung der Amplitude des Signals selbst zu rekonstruieren. Es ist daher möglich, die Signalamplitude zu normieren und ein Signal mit konstanter Amplitude zu erhalten, das daher mit den in den vorherigen Abschnitten beschriebenen und entwickelten Verfahren analysiert werden kann.

Die Hilbert-Transformation zur Normierung amplitudenmodulierter Signale und der gewichtete Birkhoff-Mittelwert werden auf ein Signal angewendet, dessen Amplitudenmodulation durch chromatische Phänomene definiert und beschrieben wird, d.h. bezogen auf die Energieverteilung

eines Teilchenstrahls. In diesem Zusammenhang wurde die Leistungsfähigkeit der entwickelten Verfahren für Signale mit konstanter Amplitude sowohl am ursprünglichen chromatischen Signal als auch an dem mit der Hilbert-Transformation normierten evaluiert. Die erhaltenen Ergebnisse scheinen zunächst kontraintuitiv. Die Ergebnisse des gewichteten Birkhoff-Mittelwerts haben das gleiche Skalierungsgesetz für die Berechnung des Tunes, ungeachtet der An-oder Abwescnheit einer Amplitudenmodulation. Durch eine tiefergehende Analyse dieses Ergebnisses konnte gezeigt werden, dass dieser Effekt daraus resultiert, den Tune aus dem Phasenvorlauf zwischen zwei aufeinanderfolgenden Iterationen berechnet. Diese Größe ist unabhängig vom Betrag der beiden Vektoren, die sie definieren, folglich ist sie unabhängig von einer möglichen Amplitudenmodulation.

Eine zweite und innovative Verwendung der Hilbert-Transformation wurde beschrieben und getestet. Die Hilbert-Transformation erlaubt es, die Amplitudenmodulation eines generischen Signals zu berechnen, aber die im Rahmen dieser Forschungsarbeit betrachteten Signale haben immer ein physikalisches Prinzip, das ihr Verhalten beschreibt und bestimmt. Beispielsweise basiert die Amplitudenmodulation eines chromatischen Signals auf einem bewährten und bekannten physikalischen Modell. Folglich ist es neben der Normalisierung des Signals zur Bestimmung seines Tunes möglich, das physikalische Modell, das die Entwicklung des Signals beschreibt, an die mit Hilbert berechnete Einhüllende anzupassen. Auf diese Weise ist es möglich, die physikalischen Eigenschaften des Strahls direkt zu bestimmen. Dieser Ansatz wurde zunächst auf synthetische chromatische Signale angewendet, was die Machbarkeit des Ansatzes demonstrierte. Tatsächlich war es möglich, die bei der Erzeugung des synthetischen Signals verwendeten physikalischen Größen zu rekonstruieren. In einem zweiten Schritt wurde dieses Verfahren auf reale Beschleunigerdaten angewendet, namentlich solche, die im LHC während einer der Experimentkampagnen 2012 gewonnen wurden. Ziel dieser Kampagne war es, die Amplitudenabweichungen aus Tuning-Messungen abzuschätzen und die erhaltenen Werte mit denen des numerischen Modells zu vergleichen. Der gerade beschriebene innovative Ansatz wurde daher verwendet, um die Einhüllende der vom LHC kommenden Signale zu rekonstruieren und lieferte erstmals eine direkte Bewertung der Amplitudenabweichun. Die erhaltenen Werte stimmen mit den im Jahr 2012 ermittelten überein. Im Allgemeinen werden Größen wie Chromatizität und Amplitudenabweichung indirekt aus anderen Messgrößen z.B. dern Tunes erhalten. Daher ist es wichtig zu betonen, wie das gerade beschriebene Verfahren direkte Messungen von linearen und nichtlinearen Maschinenparametern liefern kann, vorausgesetzt, dass das physikalische Modell, das seine Entwicklung erklärt und bestimmt, bekannt ist.

Zusammenfassung und Ausblick

Im Rahmen dieser Forschungsarbeit wurden verschiedene theoretische, experimentelle und numerische Aspekte abgedeckt und behandelt.

Zunächst wurde der experimentelle Benchmark des Modells zur Rekonstruktion der Querabmessung des Teilchenstrahls erreicht. Seine Kenntnis ist aus zwei Hauptgründen von grundlegender Bedeutung: Der Beschleuniger, der den aus dem vorgelagerten Beschleuniger austretenden Strahl empfängt, kann Beschränkungen (physisch oder magnetisch) aufweisen, die einen teilweisen oder vollständigen Verlust des einfallenden Strahls beinhalten; und alle Experimente, die nachgelagert angeordnet sind, benötigen möglicherweise einen Strahl mit einer möglichst konstanten transversalen Größe. Folglich ist seine Überwachung und Steuerung unerlässlich. Obwohl dieses Verfahren beschrieben und auf den PS-Ring am CERN angewendet wurde, ist seine Anwendung auf jeden Ringbeschleuniger, der eine stabile Resonanz n-ter Ordnung ausnutzt, um

den Strahl in Querrichtung zu teilen, viel breiter.

Bei der Bestimmung des Tunes können mehrere Aspekte berücksichtigt werden. Für spezifische Bedingungen wurden innovative Methoden zur Berechnung des Tunes entwickelt (z.B. für ein mit Nullen aufgefülltes Signal mit konstanter Amplitude und die Hanning-FFT-Gleichung für Tune und Dämpfungsfaktor für das exponentiell gedämpfte Signal). Darüber hinaus wurden innovative Anwendungen von Methoden (der gewichtete Birkhoff-Durchschnitt) und Tools (Hilbert-Transformation) eingeführt und auf verschiedene Arten von Signalen angewendet, sowohl synthetische als auch reale. Insbesondere der gewichtete Birkhoff-Mittelwert zeigte die gleiche Präzision in der Tuneauswertung sowohl für amplitudenmodulierte als auch für konstante Amplitudensignale. Die Hilbert-Transformation ermöglichte die Normierung der Amplitude in amplitudenmodulierten Signalen und damit deren Tunebestimmung unter Verwendung der für konstante Amplitudensignale entwickelten Verfahren. Darüber hinaus wurde seine Eigenschaft, die Einhüllende eines Signals zu bestimmen, ausgenutzt, um physikalische Eigenschaften des Rings aus der Anpassung des physikalischen Modells, das die Entwicklung des Signals beschreibt, an die Hilbert-Einhüllende zu bestimmen. Die Bestimmung neuer analytischer Formeln zur Bestimmung des Tunes, sowie die innovative Nutzung der Hilbert-Transformation zur Berechnung von Ringeigenschaften, eröffnen die Möglichkeit, Tune-stabilitäts-Karten zu untersuchen und Maschinenparameter zu bestimmen, die zuvor nur indirekt für jeden Kreisbeschleuniger bestimmt wurden.

Abschließend ist hervorzuheben, dass die Anwendung der oben genannten Tune-Gleichungen nicht nur auf die Analyse und Optimierung gegenwärtiger und zukünftiger Ringbeschleuniger beschränkt ist, sondern auch in der Analyse von Tracking-Daten sinnvoll genutzt werden kann. Insbesondere die sehr schnelle Konvergenz des Birkhoff-Verfahrens zur Maschinenpräzision innerhalb weniger tausend Umdrehungen könnte die Anzahl der Umdrehungen im Trackingvertfahren erheblich reduzieren und somit die Zeit reduzieren, die zum Simulieren bestimmter Bedingungen benötigt wird. Darüber hinaus findet das beschriebene innovative Verfahren zur Bestimmung von Maschineneigenschaften (wie Chromatizität und Amplitudenabweichung) basierend auf der Verwendung der Hilbert-Transformation zusätzliche Anwendung als Benchmark-Werkzeug in jedem Ringbeschleuniger. Beispielsweise können für Elektronenringe der Tune und die Dämpfung mit den in dieser Arbeit bewiesenen Gleichungen bestimmt werden, und die Hilbert-Transformation kann verwendet werden, um den Wert der Dämpfung zu bewerten. In ähnlicher Weise könnten FCC und Myon Collider Vorteile bei der Verwendung der oben genannten Gleichungen und Methoden erhalten.

Table of Contents

List of Tables

Table **Page**

List of Figures

CHAPTER 1

INTRODUCTION AND MOTIVATION

The intergovernmental meeting of UNESCO was held in Paris in December 1951. In this context, the first resolution concerning the establishment of an European Council for Nuclear Research (in French, Conseil Européen pour la Recherche Nucléaire) was adopted. One year and a half later, on June 1953, the final draft of the CERN Convention was agreed upon and signed by twelve Member States. It laid out the ways in which Member States would contribute to CERN's budget, as well as early indications of CERN's ethos and organisation. Signing the convention led to a very quick staff recruitment, architects were brought in, and plans were drawn up. Since 1954, many significant breakthroughs have been made, both in particle physics and in technologies that have helped to improve our daily lives. Among the numerous discoveries in the particle physics field, it is worth mentioning the Z and W bosons. In 1993, Enrico Fermi was the first one to develop a theory for the weak force, and only during 1960s, Glashow, Salam, and Weinberg were able to fully develop the theory that considered the W and the Z bosons as the carriers of the weak force. For their theory, they received the Nobel Prize in Physics in 1979 [1]. However, it was necessary to wait until 1983 [2] to discover the predicted weak force carriers. Their discovery was performed at CERN, where in 1979 the SPS ring was converted into a proton-antiproton collider. Carlo Rubbia was the spokeperson for the UA1 experiment that detected the W and Z bosons. Simon van der Meer was the inventor of the stochastic cooling technique, fundamental for the performance optimisation of the collider. For this reason, both were awarded with the Nobel Prize in Physics in 1984 [3]. The escalation of promising results culminated with the discovery of the last fundamental piece of the Standard Model: the Higgs boson, discovered at the Large Hadron Collider (LHC) at CERN, the biggest particle accelerator in the world. In fact, even if the Higgs boson was theorised in 1964 [4], several decades passed before it was actually possible to detect it. It was only in 2012 that two

independent CERN experiments were able to detect it, the results of their independent analysis are reported in [5, 6]. Apart from being a research centre for particle physics, at CERN engineers, technicians and scientists work on several technological domains. Among the major technological breakthroughs, it is worth mentioning the Timepix detector, widely used in space applications. It can detect several types of ionising radiation, such as heavy ions, and, for each of them, the energy can be determined. At the moment, it is on board the International Space Station and will soon be used in the Artemis programme for the NASA lunar exploration mission [7].

1.1 The CERN accelerator complex

CERN is a research centre where several accelerators are installed and operated on a daily basis to provide beams of particles to other accelerators (for particle physics, where one beam collides with one against the other) or to experimental areas (for fixed-target experiments, where a beam is brought into collision with a stationary target).

The accelerators can produce either continuous particle beams or a sequence of bunches of particles. For colliding beam physics the latter type of beams is adopted; while for fixed-target experiments both can be used, depending on the aim of the experiment. For both particle physics research and fixed-target experiments, the particles have to have enough energy to actually observe new phenomena or discover new particles. As far as fixed-target experiments are concerned, the beam energy together with its spatial distribution and size are the most relevant features. However, for colliders, additional considerations are necessary. When two relativistic beams made of the same particles are considered, the energy of the centre of mass of the colliding beams is twice the energy of each beam during the collision. The energy at the collision point is not only the relevant parameter. To enhance the probability of observing the desired phenomenon, additional features have to be considered and possibly optimised. For this purpose, the luminosity has been introduced and defined as

$$\boldsymbol{L} = \frac{f_c N_1 N_2}{4\pi\sigma_1\sigma_2}, \tag{1.1}$$

where, f_c represents the collision frequency between the two counter-rotating beams, N_1 and N_2 indicates the number of particles for each beam, σ_1 and σ_2 quantify the transverse dimension of each beam at the collision point. The aim is to make the luminosity always bigger in order to increase the production rate. There are several ways to obtain it: the number of particles per beam can be increased as well as the frequency rate of collision; another way is to reduce the beam dimensions at the interaction point, with the mathematical limit case of having point-like beams that would lead to infinite luminosity. The increase of the first two parameters is strongly limited by two physical phenomenon: the increase of the interaction strength between particles in each bunch; and the increase in the interaction strength between adjacent bunches. The reduction of the transverse beam dimension requires lot of efforts in the focusing systems [8].

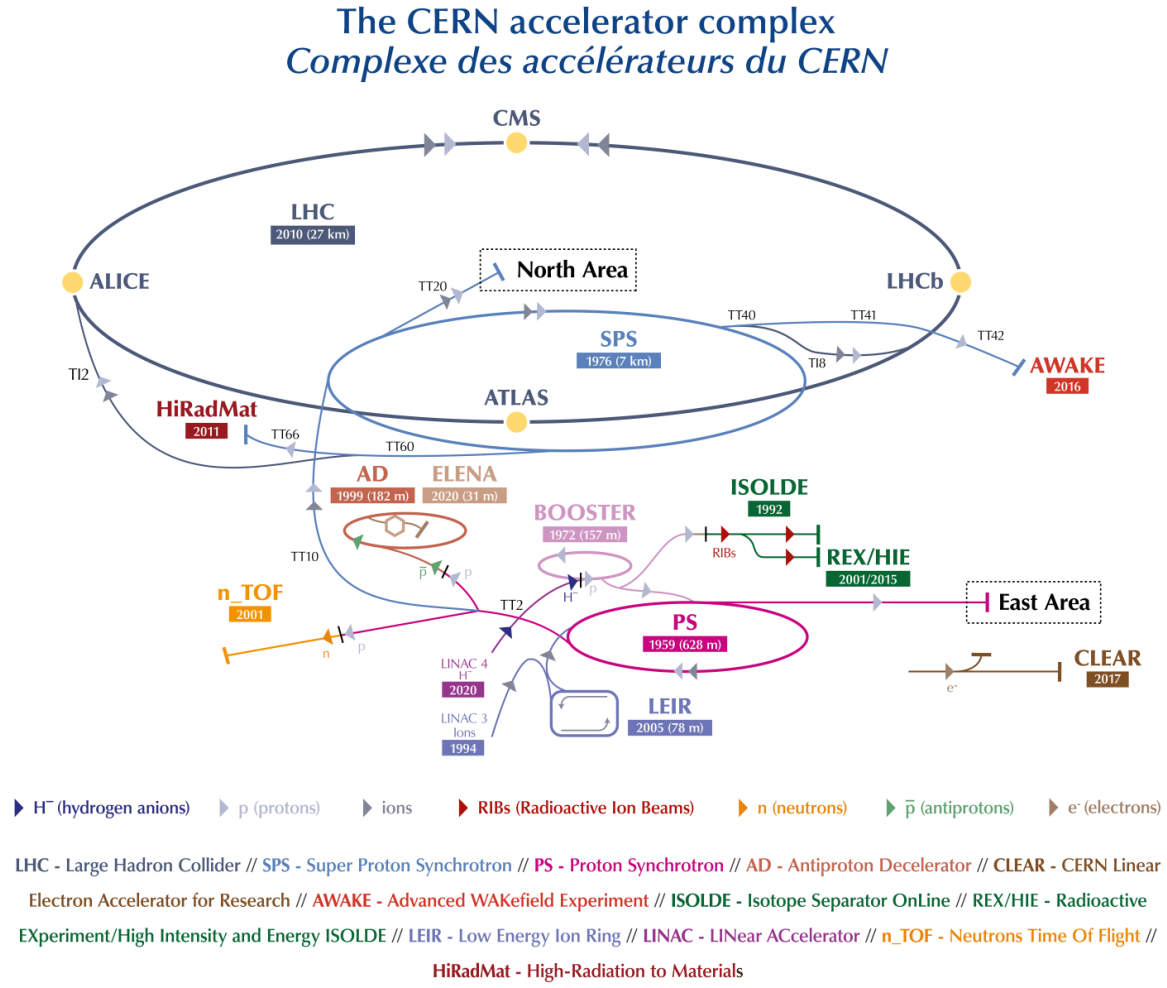

Figure 1.1: The CERN accelerator complex.

CERN hosts the largest accelerator in the word: the Large Hadron Collider (LHC). It has been built over ten years (1998-2008), the first beam in the machine was achieved on the 10th of September 2008 and the first collision was obtained one year later, on the 23rd of November 2009. At its beginnings, the LHC had a centre of mass energy of 7 TeV, which means that two counter-rotating beams each at 3.5 TeV. During the years, the energy at the collision point has increased to current 13.6 TeV (thus, 6.8 TeV per beam). This has been possible because of the progressive optimisation and upgrade of all the accelerators that bring the beam from the source to the LHC. The complex of accelerators and experiments installed at CERN is shown in Figure 1.1 [9]. CERN does not accelerate and enables only proton-proton collisions, but also ion-ion collisions are carried out at LHC, even though it is worth to highlight that the first ion collision with a fixed-target was obtained in 1986 at the SPS. One of the key reasons in performing head-on collisions with heavy ions is the separation of the protons and neutrons in their nuclei into their

elementary components: quarks and gluons. For the first time in 2000, CERN scientists proved the evidence that a new state of matter was observed: the quark-gluon plasma [10]. It is of great interest to study this state of the matter because it was the one existing at the moment the universe was created, just after the Big Bang. The study of its properties, the theoretical understanding of the measurements and its time evolution are at the base of the problems in quantum chromodynamics nowadays.

At CERN two major species are generated and accelerated: protons and heavy ions. They undergo to multiple acceleration from their generation to their collision, being injected and extracted from different accelerators, shown in Figure 1.1, but the two species follow a different acceleration path. The proton beam can be considered as such only after injection into the Proton Synchrotron Booster (PSB). Before the PSB the proton beam actually consists in a beam of hydrogen atoms with an additional electron. This beam is accelerated up to the kinetic energy of 160 MeV into the Linear Accelerator 4 (LINAC 4), then the additional electrons are stripped with a thin foil at the injection into the PSB, leaving only protons. In the PSB protons are accelerated up to a kinetic energy of 2 GeV. Successively, after they are injected in the Proton Synchrotron (PS), they are accelerated up to 26 GeV kinetic energy. The beam of protons is then injected into the Super Proton Synchrotron (SPS), where it is accelerated up to 450 GeV kinetic energy. Finally, protons are injected into the two LHC beam pipes where they reach the maximum energy of 6.8 TeV. The two beams circulate in opposite directions, and they can circulate for many hours inside the LHC beam pipes under normal operating conditions. The two beams are brought into collision inside each one of the four detectors – ALICE [11], ATLAS [12], CMS [13] and LHCb [14] – where the total energy at the collision point is 13.6 TeV.

The acceleration path followed by heavy ions is slightly different. They are produced with the GTS-LHC 14.5 GHz Electron Cyclotron Resonance (ECR) ion source, then they are accelerated in the LINAC 3 and injected into the Low Energy Ion Ring (LEIR). LEIR is an accelerator that started working in 2003 after the decommission and conversion of a previous particle decelerator (Low Energy Anti-proton Ring - LEAR). The work needed to convert LEAR into LEIR lasted for almost 2 years (2003-2005) and the commissioning of LEIR lasted a few months. From 2006 to 2010 it was used to commission the PS and the SPS to accelerate ion beams and, finally, in November 2010 the first ion beam reached LHC for collisions. Although the increase in kinetic energy in the LEIR ring is rather small (68 MeV/nucleon) one of its main functions is to strongly reduce the size of the ion beam thanks to the electron cooling system to match the LHC luminosity target for ion collisions [15, 16].

All the beams (ions and protons) that are generated and accelerated do not always reach the LHC for collisions. There are other experiments, that use the CERN beams for their purposes. For example, the Antimatter Decelerator (AD) and Extra Low Energy Antiproton ring (ELENA) is a complex of two decelerators and several experiments. The beam extracted from the PS is sent against a target for the production of antiprotons that are then decelerated to a minimum kinetic

energy of 5 keV. Thus, the anti-proton beam is sent towards one of the several experiments in the area. One of the major results was obtained in 2011 when for the first time the anti-proton was isolated and confined thanks to magnetic traps [17].

1.2 Research goals

In this framework, the machine performance optimisation is fundamental to achieve always larger luminosity. On the one hand, optimisation can be achieved by improving, updating, and consolidating the electronic systems used for operating the CERN accelerator complex. However, significant and relevant improvements can also be obtained from the study of beam dynamics. The focus of this research is on the latter aspect, with a special attention for linear and non-linear effects.

The performance of a circular accelerator is determined by the proper choice of the working point as well as the shape of and the space occupied by the beam in the accelerator itself. As far as the first topic is concerned, the determination of the working point is fully determined by the choice of the horizontal and vertical tunes (namely, the number of transverse oscillations performed per unit of longitudinal turn). As far as the second topic is concerned, the transverse beam dimensions have to be controlled and, generally, minimised in order to reach high-intensity and point-like beams. Both these topics have been addressed in the context of this research topic.

At first, the analysis of the transverse size is analysed. In fact, when a beam of particle is transferred (namely, extracted) from one ring to another, it is necessary to assess whether the extracted beam has the correct shape and orientation before it is injected into the downstream accelerator, otherwise an increased in the beam transverse size is usually detected together with possible losses. The same holds true also for fixed-target experiments, with the only difference that the increased constraints on the beam characteristics are imposed by the aim of the experiments. It has been decided to focus the attention on the CERN PS ring since it is has a key role in the production of proton beams for LHC, thus, the optimisation of its performance for High-Luminosity LHC is strongly desired. Moreover, as it will described in detail in the next chapters, the characterisation of its horizontal size is of great interest. The PS extraction technique has been developed, implemented and made operational over more than 15 years of studies and exploits a non-linear phenomenon (namely, the crossing of a stable resonance of order four) to transversely divide the beam without losses into beamlets of smaller intensity but with the same transverse size. In this configuration, the characterization of the transverse beam size becomes fundamental to assess whether this beamlets can be inject into the downstream accelerator (the SPS). During the past decades, several studies and attempts have been made in the determination of the transverse size of the beamlets. However, they were all limited by the use of a linear approach in the determination of the transverse beam dimension. In the context of the thesis, the experimental benchmark of a model developed in 2019 has been obtained for

the first time and a comparison of the results that would have been obtained in the case the linear approach would have been used will be performed and conclusions will be drawn. This result showed the feasibility of determining the transverse beam size of a beam that has been transversely split by means of non-linear fields.

As a second topic, the determination of the tune has been considered. In particular, its precise determination is important to define precisely the working point of an accelerator. Moreover, the tune defines the long-term stability of the beam. The determination of the tune is performed by analysing the frequency of a synthetic or real beam signal. During the 1990s several methods for the precise tune determination based on the use of the Fast Fourier Transform (FFT) have been developed and tested. Today, they are the state of the art. New analytical formulae have been developed for both constant- and varying-amplitude signals. Their mathematical proof and their performance on test signals will be described and discussed in detail. In this framework, a new innovative approach coming from the field of applied mathematics has been used to compute the tune. Thus the comparison of different methods on different signals will highlight which method performs better for a specific case study. As a final step, some of the methods and formulae used to determine the tune of a test signal will be applied to a real-case study. In this case, given a specific model that describes the time evolution of the beam centroid in the ring, a new approach to determine some ring features will be described. The results obtained have been benchmarked against 2012 results and, at the end, a possible additional application of this approach will be provided and justified.

In conclusion, it is worth highlighting that even though experimental data analysis has been performed at the PS and LHC ring at CERN, no specific assumption has been made. Thus, the results obtained for the determination of the transverse size of a split beams could possibly be obtained (with some adjustments and modifications) in any circular accelerator that exploits a similar extraction technique. On the contrary, the tune equation and the methods described to either compute the tune or to normalise the signal amplitude are valid for any beam signal. As a consequence, they might be used in future colliders such as FCC as well as in the unique FAIR accelerator.

CHAPTER 2

INTRODUCTION TO ACCELERATOR PHYSICS

A particle accelerator increases particle energy by means of an electric field and keeps particles confined by means of a magnetic field. One of the simplest and most intuitive way to classify particle accelerators is according to their geometrical shape. Accelerators can be either linear (LINAC) or circular. The design of linear accelerators (named also LinAcs) strongly depends on the type of particle to be accelerated, electrons or heavy ions and their application (injection in synchrotrons, medical applications, nuclear energy production, nuclear waste treatment, spallation source, etc.). Circular accelerators can be further classified according to the way particles are accelerated. Betatrons are circular accelerators that increase the beam energy using the magnetic induction principle. Cyclotrons exploits the physical principle of Faraday cages to create two regions in which only the magnetic field and only electric field exists separately. And finally, synchrotrons where the increase of particles energy is achieved by means of an electric field, generated by a radio-frequency (RF) cavity. In the following discussion, the focus will be on the latter type of accelerators, being the PS a synchrotron. The particle dynamics in a synchrotron is defined according to the motion of a very specific particle: the reference particle. The sequence of magnetic elements that enables particles to follow a circular path is defined to allow the reference particle to move on a circular orbit that closes on itself after one single turn in the accelerator. The motion of all the other particles in the ring is defined with respect to the reference particle. Therefore, a reference system centred on the reference particle and co-moving with it along the accelerator ring is defined. The bending of the particles along the longitudinal direction is achieved by dipole magnets while their transverse focusing is mainly controlled by quadrupole magnets. Beam physics may be studied from two different points of view: when the beam is considered as a single particle and thus its properties are referred to the gravitational centroid of the beam itself or when every particle in the beam is studied separately

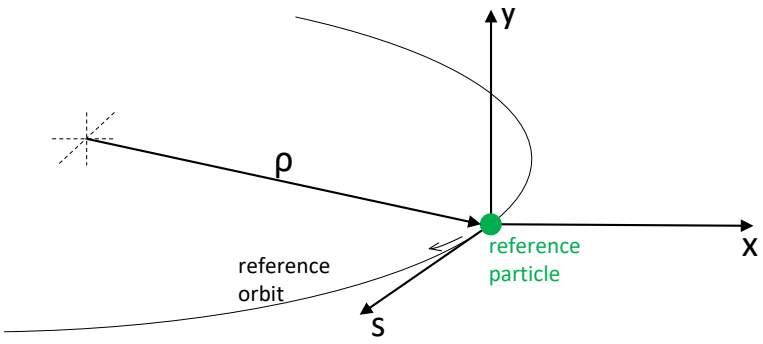

Figure 2.1: Reference particle (in green) and reference orbit. It is possible to observe the reference system usually adopted in the description of beam dynamics in synchrotrons. The labels x and y refers to the horizontal and vertical transverse plane, respectively; while s indicates the longitudinal direction. The radius of the accelerator is usually indicated by ρ that, if multiplied times the magnetic field of the dipoles, quantifies the magnetic rigidity[1].

and thus intra-particle (such as the internal field between particles, namely space charge, and scattering between particles, namely intra-beam scattering) effects have to be considered above the interactions with external and internal electric and magnetic fields. The first approach will be used in the following discussions. The ordered sequence of magnetic elements and free-field regions is called the accelerator lattice. The motion of a particle, with charge e moving with velocity $\vec{v}$ in a region where both the electric $\vec{\mathbf{E}}$ and magnetic fields $\vec{\mathbf{B}}$ exist, is governed by the Lorentz force:

$$\frac{d\vec{\mathbf{p}}}{dt} = \frac{d}{dt}\left(\vec{\mathbf{p}_\mathbf{x}} + \vec{\mathbf{p}_\mathbf{y}} + \vec{\mathbf{p}_\mathbf{s}}\right) = e(\vec{\mathbf{E}} + \vec{v} \times \vec{\mathbf{B}}). \tag{2.1}$$

It is possible to write the particle's momentum expression along the three directions x, y and s, shown in Figure 2.1, as:

$$\begin{aligned} p_\mathrm{x} &= e(E_x + v_\mathrm{y}B_\mathrm{z} - v_\mathrm{s}B_\mathrm{y}) \\ p_\mathrm{y} &= e(E_y + v_\mathrm{s}B_\mathrm{x} - v_\mathrm{x}B_\mathrm{x}) \\ p_\mathrm{s} &= e(E_s + v_\mathrm{x}B_\mathrm{y} - v_\mathrm{y}B_\mathrm{x}). \end{aligned} \tag{2.2}$$

The last equation in Eq. 2.2 describes the particle motion along the s direction. As it is possible to observe in Figure 2.1, the s direction corresponds to the direction where bending occurs, thus along the plane where particles perform circular paths. This direction is known as longitudinal direction. The first two equations in Eq. 2.2 describe the particle motion in the (x, y) plane. These two directions, as shown in Figure 2.1, are orthogonal to the longitudinal direction and describe the particle motion in the transverse plane. In particular, x is known as horizontal transverse direction while y is the vertical transverse direction. Any other particle in the accelerator can be described relative to the reference particle by means of six coordinates $(x, x', y, y', s, \delta)$ in the

[1]The magnetic rigidity ($B\rho = \frac{p}{e}$) quantifies the stiffness of a particle. It gives a measure of the angular deflection the particle undergoes when it experiences a given magnetic field. Thus, for a given magnetic field, the greater the particle momentum, the less it will be bent. On the contrary, the larger the particle's charge is, the more it will be bent.

six-dimensional phase space. The horizontal (x), vertical (y) and longitudinal (s) direction are well represented in Figure 2.1; $x' = dx/ds$ ($y' = dy/ds$) represents the horizontal (vertical) slope, it quantifies how much the horizontal (vertical) position changes per unit of longitudinal path; and, $\delta = \Delta p/p$ is the relative momentum deviation of the particle from the reference one.

2.1 Longitudinal dynamics

Along the longitudinal direction s (see Figure 2.1), the beam is accelerated by one (or more) radio-frequency (RF) cavities. A RF cavity is a closed structure in which electromagnetic waves propagate, being reflected (with a certain efficiency) by the walls of the chamber. The way electromagnetic waves are generated is out of the context of this thesis, but, as an example, they could be generated by a klystron (a particular linear beam vacuum chamber for RF amplification) and then transported by wave guides till the RF cavity. Once the wave reaches the cavity, it is amplified until it reaches a steady state condition at the resonance frequency of the chamber: in this case, the wave is called a standing wave. The amplitude and profile of the wave does not change in space, but it oscillates in time and the frequency at which the wave oscillates is called frequency of the RF cavity (ω_{RF}). The interaction between particles and the electromagnetic wave in the cavity could lead possibly to their acceleration. In a very simplified form, a synchrotron can be considered as a closed sequence of a RF cavity and an acceleration free region, which is composed by all components that do not accelerate the beam such as dipoles, quadrupoles, sextupoles, octupoles, free drift, kickers, correction magnets, etc. During the beam acceleration, particles cross the RF cavity multiple times, increasing their energy turn after turn. Therefore, the magnetic field has to ramp up to keep bending and confining the beam along the desired trajectory. The common practice suggests to impose a time-dependent law for the magnetic field, and so for the energy gain of the particles, and then adjust the RF cavity parameters so that they satisfy the energy condition in Eq. 2.3. Every time a charged particle crosses the RF cavity, it gains an amount of energy equal to ΔE_0. Assuming that the RF generator imposes a sinusoidal potential difference, then it is possible to relate the energy gain to the voltage amplitude (V_{RF}) of the RF and to its phase (Φ_{RF}), using:

$$\Delta E_0 = eV_{RF}\sin(\Phi_{RF}). \tag{2.3}$$

The phase of the RF cavity can be also expressed in terms of the RF frequency (ω_{RF}) as: $\Phi_{RF} = t \cdot \omega_{\mathrm{RF}}$. As the energy of the particles increases, their momentum increases too, therefore, the magnetic field has to ramp-up to keep confining and bending the beam inside the accelerator. It is possible to express this relation as:

$$B(t)\rho = \frac{p(t)}{e}, \tag{2.4}$$

being the bending radius ρ (see Figure 2.1) constant as well as the charge number e (if the particle momentum is expressed in terms of eV/c) , then the energy gain, i.e., the kinetic energy

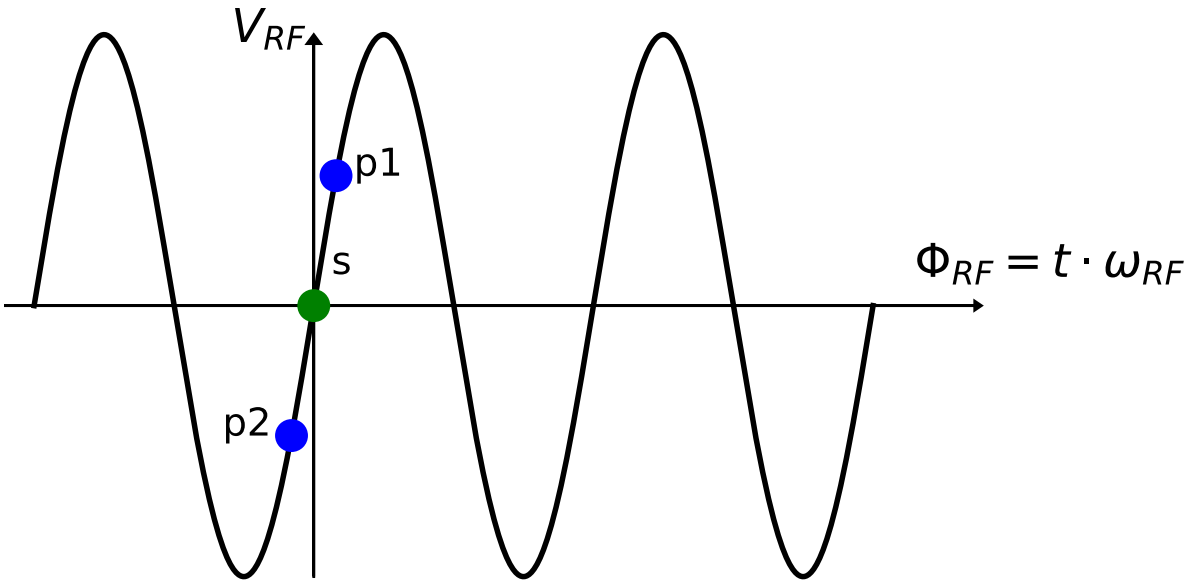

Figure 2.2: Evolution of the RF voltage as a function of the RF phase. The synchronous particles is shown in green and it will be referred to as s and two more particles are shown in light blue and they will referred to as $p1$ and $p2$.

relative increase, is proportional to the time-dependent law of the magnetic field. The increase of particle energy has to be guaranteed by the RF generator, so the potential difference V_{RF} and the phase Φ_{RF} have to change in time and, at the same time, they always have to satisfy Eq. 2.3. The description performed until now implicitly refers to a specific particle that is called the synchronous particle, i.e., the one that is exactly synchronized with the RF cavity and so the only one that will increase its energy by ΔE_0 every time it crosses the RF cavity, during acceleration. The synchronous particle is centred on the zero phase of the RF voltage so that the dynamics of any other particle in the beam can be directly referred with respect to the synchronous one, as shown in Figure 2.2. If now particles $p1$ and $p2$ are considered, it is possible to notice that, for a fix value of the RF frequency (ω_{RF}), the particle $p1$ arrives in advance in time with respect to the synchronous one and the particle $p2$ arrives later than it [18]. This means that the two particles will see a different accelerating voltage. Particle $p1$ will receive less energy than the synchronous one (s) while particle $p2$ will receive more energy than particle s. Therefore, after the energy gain that each particle got in the RF cavity, at the next turn the particle $p1$ will reduce its advance with respect to the synchronous one, being "more in time"; while particle $p2$ will reduce its delay. For both particles ($p1$ and $p2$) a reduction of their delay or advance (with respect to the synchronous particle) is obtained. It is possible to conclude that turn after turn these particles will approach the synchronous one up to the point that they will exchange "roles" (thus particle $p1$ will arrive later than the the synchronous one and particle $p2$ will arrive in advance). Therefore, they oscillate around the synchronous particles, these oscillations are called

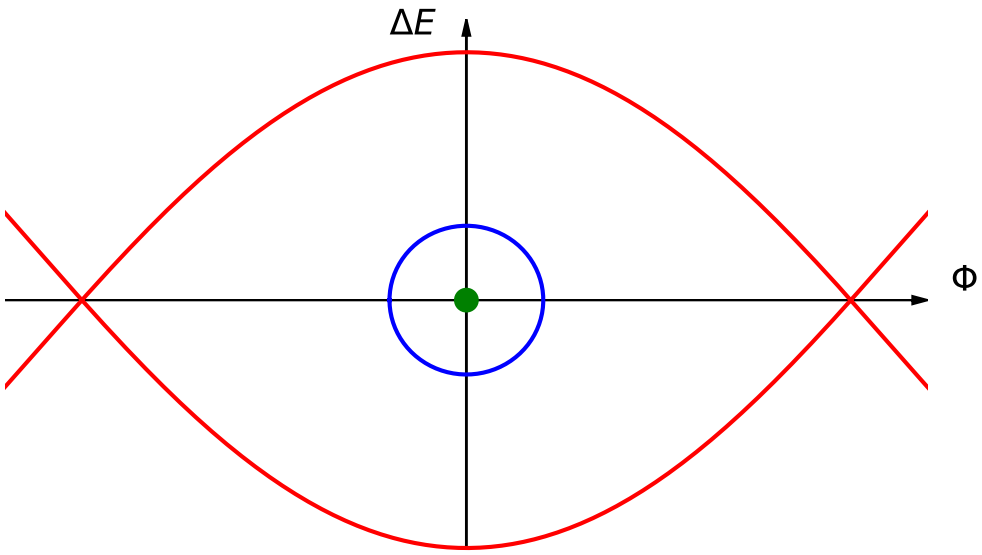

Figure 2.3: Longitudinal phase space portrait. In red, the shape of the separatrix is reported while in blue the orbit of a particle with a slight energy deviation with respect to the synchronous one is shown. The synchronous particle is reported in green.

synchrotron oscillations. On the contrary, if the synchronous particle phase is shifted by π (thus it still has zero voltage but rather than laying on the increasing edge of the voltage, it lays on the decreasing one) then also particles $p1$ and $p2$ would lay on the opposite edge, thus the decreasing one, of the voltage in Figure 2.2. In this case, they would experience an increase of their advance and delay, respectively, leading to possible losses. An exhaustive and detailed explanation of the longitudinal beam dynamics can be found in [8, 18]. The longitudinal phase space can be divided into two regions: a stable region where the particles have a closed and stable orbit (inside the red line in Figure 2.3) and an unstable region (outside the red line in Figure 2.3). The phase space trajectory that separates the stable from the unstable region is called the separatrix and the area within this region is called the RF bucket (red line in Figure 2.3). Since the dynamics of any other particle is referred to the one of the synchronous one, the synchronous particle is centred in the longitudinal phase-space (green dot in Figure 2.3). Particles that have a slight energy difference with respect to the synchronous one will perform almost circular orbits around it, as shown with the blue curve if Figure 2.3. But the larger is the energy deviation the more deformed is the trajectory. The mathematical proof of the longitudinal equation of motion can be found in Appendix A [18], moreover, in the same section, the characteristic shape of the longitudinal phase space is explained. Within the RF bucket, the particle motion is stable and each particle will perform synchrotron oscillations around the synchronous particle at different amplitudes. Particles that share the same bucket form a bunch (of particles). When the RF cavity is turned off, the particles are not anymore confined within the separatrix and therefore the beam is said to

be coasting. The debunching-rebunching process is a very well-known technique commonly used also to change the number of bunches in the accelerator or to increase the space between them.

2.2 Transverse dynamics

As already discussed in the introductory part of this chapter, the reference particle moves on the reference orbit that closes on itself after one turn. Until 1952, particles accelerator exploited the physical principle of the weak focusing. It arises from the equilibrium condition between the Lorentz force and the centrifugal force. In a magnetic field with no dependence on the azimuthal direction, the particle motion is stable if restoring forces (i.e., centrifugal force since the motion occurs on a circular path) spontaneously arise when the particle moves away from the design path. Particles that move on an arc with radii of curvature slightly larger than the reference one (therefore, they are horizontally displaced) will experience a Lorentz force bigger than the centrifugal one. This ensures that particles move back on the nominal path. On the contrary, those particles that move at radii smaller than the reference one will experience a bigger centrifugal force than the Lorentz one, that will make them move back towards the nominal trajectory. A similar rationale can be adopted for all those particles that are vertically displaced with respect to the plane where the design orbit lays. This effect is known as weak focusing and enables particles to get confined in the transverse planes. In 1952 a research carried on by E. Courant, M. Livingston and H. Snyder proved that it was possible to obtain a net transverse focusing effect of particles beam when strong focusing and defocusing magnetic fields gradients were alternated [19]. The application of this working principle to particle accelerators brought to the alternating-gradient synchrotron. Nowadays, strong focusing is widely used in all synchrotrons, such as the PS ring at CERN [20]. Weak focusing always provides its contribution in transverse beam dynamics but the additional focusing to better control the transverse beam dimension is achieved with the strong focusing (namely, using quadrupole magnets). Particles that are horizontally or vertically displaced with respect to the reference particle will perform oscillations around its orbit (the reference orbit). These oscillations are known as betatron oscillations.
The number of oscillations that particles perform in one turn in the horizontal (vertical) plane is known as the horizontal (vertical) tune (generally referred to as ν_x and ν_y). The particle motion is described in the coordinate system co-moving with the reference particle along the reference orbit, as shown in Figure 2.4, where the unit direction vectors are shown in red. The equation of motion for a particle in an accelerator can be derived using the reference system centred on the reference particle or by referring this system of coordinates with respect to the stationary reference system of the laboratory. In the latter case, to determine the equation of motion, the particle position has to be expressed in terms of the design radius of the reference orbit ρ, as a function of the radial position r (to account for a possible horizontal displacement) and the

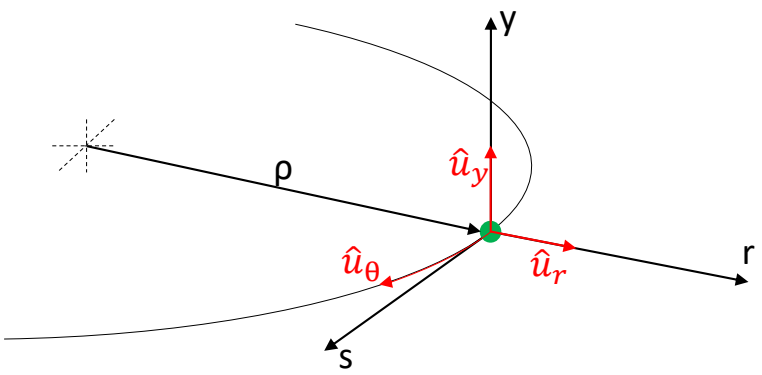

Figure 2.4: The direction vectors that define the main axis of the reference systems are shown in red. The reference particle is shown in green, and it moves on the reference orbit.

vertical one y (to consider also vertical displacements):

$$\mathbf{R} = \hat{\rho} + r\hat{\mathbf{u}}_\mathbf{r} + y\hat{\mathbf{u}}_\mathbf{y}. \tag{2.5}$$

By making twice the derivative of Eq. 2.5 with respect to time, it is possible to obtain the acceleration:

$$\ddot{\mathbf{R}} = (\ddot{r} - r\dot{\theta}^2)\hat{\mathbf{u}}_\mathbf{r} + (2\dot{r}\dot{\theta} + r\ddot{\theta})\hat{\mathbf{u}}_\theta + \ddot{y}\hat{\mathbf{u}}_\mathbf{y}, \tag{2.6}$$

where the unit direction vector $\hat{\mathbf{u}}_\theta$ comes from the time derivative of the radial unit direction vector. In the determination of Eq. 2.6 the following rules for the time derivative of the unit direction vectors have been applied:

$$\frac{d\hat{\rho}}{dt} = 0, \qquad \frac{d\hat{\mathbf{u}}_\mathbf{r}}{dt} = \dot{\theta}\hat{\mathbf{u}}_\theta, \qquad \frac{d\hat{\mathbf{u}}_\theta}{dt} = -\dot{\theta}\hat{\mathbf{u}}_\mathbf{r}, \qquad \frac{d\hat{\mathbf{u}}_\mathbf{y}}{dt} = 0.$$

It is important to highlight that the equation above can be applied only when the particle passes in a dipolar magnetic field, and thus when a radius of curvature can be identified. In this situation, the time derivative of the azimuthal angle is related to the curvature radii with $\dot{\theta} = 1/\rho^2$. From the discussion performed at the beginning of the chapter, it was possible to describe the particle motion with three equations (Eq. 2.2), after the discussion on the longitudinal beam dynamics it is possible to simplify those equation removing the electric field. Acceleration occurs only in the longitudinal direction; this leads to the removal of the electric field component from the two transverse equations and, when the particle has a fixed energy (absence of acceleration) then the electric field component can be removed also from the longitudinal equation of motion. Therefore, it is possible to describe the particle motion simplifying Eq. 2.2 with the considerations discussed above and writing the explicit form of the particle momenta (p_x, p_y and p_z) as the product of the particle mass ($\gamma_\mathrm{rel} m$, where γ_rel is the relativistic Lorentz factor to account for possible particle motion in relativistic conditions) and the acceleration, expressed using Eq. 2.6. The equations of motion read as follows:

$$r: \qquad \gamma_\mathrm{rel} m(\ddot{r} - r\dot{\theta}^2) = e(v_\theta B_y - v_y B_\theta); \tag{2.7}$$

$$\theta: \qquad \gamma_{\text{rel}} m(2\dot{r}\dot{\theta} + r\ddot{\theta}) = e(v_y B_r - v_r B_y); \tag{2.8}$$

$$y: \qquad \gamma_{\text{rel}} m\ddot{y} = e(v_r B_\theta - v_\theta B_r). \tag{2.9}$$

Eq. 2.7, Eq. 2.8 and Eq. 2.9 are the equation of motion in the radial, azimuthal (longitudinal) and vertical directions, respectively. The solutions of Eq. 2.8 describe the motion along the longitudinal direction, a brief description has been provided in Appendix A. To find the solutions of Eq. 2.7 and Eq. 2.9 some simplifications are applied. First, it is possible to assume that the magnetic field does not depend on the azimuthal direction ($B_\theta = 0$) and that the component of the particle velocity along the azimuthal direction is the dominant one with respect to the other two ($v_\theta >> v_r$ and $v_\theta >> v_y$), therefore, it can be referred to as v. Under these assumptions, known as the paraxial approximation, Eq. 2.7 and Eq. 2.9 read as:

$$\gamma_{\text{rel}} m\left(\ddot{r} - r\frac{1}{\rho^2}\right) = evB_y, \qquad \gamma_{\text{rel}} m\ddot{y} = -evB_r. \tag{2.10}$$

Although the discussion carried out so far concerned the vertical (y) and radial (r) direction, it is possible to observe from the comparison of Figure 2.1 and Figure 2.4, that the horizontal (x) direction coincides with the radial one. Therefore, a change of notation can be applied without loss of meaning. Moreover, from a physical point of view, it is more interesting to observe how variables change along the longitudinal axes of the machine (s) rather than their time variation. It is possible to find the solutions of Eq. 2.10 by performing a linear approximation of the transverse magnetic field:

$$B_y = B_0 + \frac{\partial B_y}{\partial x}x = B_0 + B_1 x, \qquad B_x = \frac{\partial B_x}{\partial y}y = -B_1 y, \tag{2.11}$$

where B_0 and B_1 are the dipolar and quadrupolar components of the field, respectively and $B_1 = \frac{\partial B_y}{\partial x} = \frac{\partial B_x}{\partial y}$ comes from the solution of Maxwell's equations ($\nabla \cdot \mathbf{B} = 0$ and $\nabla \times \mathbf{B} = 0$) for the linearized magnetic field in Eq. 2.11, a detailed derivation can be found in [21]. Therefore, Eq. 2.10 read as:

$$\begin{cases} \frac{d^2x}{ds^2} + \left(k_x(s) + \frac{1}{\rho^2}\right)x = \frac{1}{\rho(s)}\frac{\Delta p}{p_0} \\ \frac{d^2y}{ds^2} - k_y(s)y = 0, \end{cases} \tag{2.12}$$

with,

$$k(s) = g\frac{1}{B_0\rho} = g\frac{e}{p}, \tag{2.13}$$

where g is the magnetic field gradient, defined as the ratio between the magnetic field of the poles and the radial aperture. The quantity $k(s)$ defined in Eq. 2.13 in known as normalised focusing strength. The solution of the motion equation along the x direction is given by the sum of the homogeneous solution and the particular solution of the inhomogeneous equation. The first one describes the betatron motion along the x transverse direction, the latter describes the momentum-dependent component of the motion. Assuming, at first, that there is no momentum

spread ($\delta = \Delta p/p = 0$) and thus all particles have the same momentum as the reference particle, the equation of motion in Eq. 2.12 read as:

$$\begin{cases} \frac{d^2x}{ds^2} + K_x(s)x = 0, & K_x(s) = k(s) + \frac{1}{\rho(s)^2} \\ \frac{d^2y}{ds^2} + K_y(s)y = 0, & K_y(s) = -k(s), \end{cases} \tag{2.14}$$

where $K_x(s)$ and $K_y(s)$ functions describe the focusing properties of the lattice, they are periodic with period C, being C the accelerator circumference ($K_x(s+C) = K_x(s)$ and $K_y(s+C) = K_y(s)$). The Eq. 2.14 is known as Hill's equation. The solutions of Hill's equation describe the motion of mono-energetic particles, i.e., all the particles share the same value of energy ($\delta = \Delta p/p = 0$). This motion is called betatronic motion. The solution of Eq.2.14 reads as:

$$u(s) = \sqrt{2J_u\beta_u(s)}\cos(\Phi(s) + \Phi_0), \tag{2.15}$$

where J_u is the particle action (defined as the area of the particle orbit divided by 2π), β_u is called the betatron function and it contains the amplitude dependence on the longitudinal position, the initial value of the phase Φ_0 is determined by initial conditions of the particle while the phase $\Phi(s)$ is related to the betatronic function by:

$$\Phi(s) = \int_0^s \frac{1}{\beta(s)}\, ds. \tag{2.16}$$

The mathematical definition of the tune is:

$$Q = \frac{1}{2\pi}\Delta\Phi = \Phi(C) - \Phi(0), \tag{2.17}$$

and, as will be shown later on, it is an important parameter that determines whether the particle motion is stable or unstable. It is a fractional number and usually its decimal part is of more interest. For this reason, it is usually identified as ν:

$$Q = \lfloor Q \rfloor + \nu \tag{2.18}$$

From the substitution of the horizontal (x) and vertical (y) coordinates to u in Eq.2.15, it is possible to obtain the equation of motion of a particle in the transverse planes:

$$\begin{cases} x(s) = \sqrt{2J_x\beta_x(s)}\cos(\Phi_x(s) + \Phi_{x,0}) \\ y(s) = \sqrt{2J_y\beta_y(s)}\cos(\Phi_y(s) + \Phi_{y,0}) \end{cases} \tag{2.19}$$

To fully determine the motion along the horizontal direction, it is necessary to compute the particular solution of Eq. 2.12. Thus, removing the assumption made before that all the particles share the same momentum as the reference one (no momentum spread, $\delta = 0$). As particles with different momenta pass through a dipole they will be bent less effectively than the reference particle. It is possible to determine the motion equation of off-momentum particles starting from the one describing the motion of on-momentum particles. The complete demonstration can be

found in [8, 22]. The major result is that the off-momentum particles closed orbit can be described as:

$$x_p(s) = x_\beta + D_x(s)\frac{\Delta p}{p}, \tag{2.20}$$

The dispersion $D_x(s)$ is created by the momentum dependency of the bending radius of a particle in dipole magnets (see Eq. 2.13) and therefore, it appears only in the plane of bending; for circular accelerators it occurs on the horizontal plane. Off-momentum particles will be bent in a less effective way with respect to on-momentum particles. Therefore, both on-momentum and off-momentum particles perform betatronic oscillations, the former oscillate around the equilibrium orbit (defined by x_β in Eq. 2.20) while the latter is around an orbit that is horizontally displaced by a quantity equal to the second term on the right-hand-side (RHS) of Eq. 2.20. It is useful to consider the particle motion in phase space (x, x') (or equivalently (y, y')) rather than the physical space (x, y). Using Eq. 2.15, Eq. 2.16, and by making the derivative of the horizontal (x) and vertical (y) directions with respect to the longitudinal position, it is possible to find the analytical expression for x' and y'. The particle equation of motion in the horizontal plane (x, x') reads as:

$$\begin{cases} x(s) = \sqrt{2J_x\beta_x(s)}\cos(\Phi_x(s) + \Phi_{x,0}) \\ x'(s) = -\sqrt{\frac{2J_x}{\beta_x(s)}}\Big(\alpha_x(s)\cos\Big(\Phi_x(s) + \Phi_{x,0}\Big) + \sin\Big(\Phi_x(s) + \Phi_{x,0}\Big)\Big), \end{cases} \tag{2.21}$$

where,

$$\alpha_x(s) = -\frac{1}{2}\frac{d\beta_x(s)}{ds}. \tag{2.22}$$

In the same way, the equation of motion along the vertical direction reads as:

$$\begin{cases} y(s) = \sqrt{2J_y\beta_y(s)}\cos(\Phi_y(s) + \Phi_{y,0}) \\ y'(s) = -\sqrt{\frac{2J_y}{\beta_y(s)}}\Big(\alpha_y(s)\cos\Big(\Phi_y(s) + \Phi_{y,0}\Big) + \sin\Big(\Phi_y(s) + \Phi_{y,0}\Big)\Big). \end{cases} \tag{2.23}$$

The trace space is a coordinate system where particle motion is described using (x, x', y, y') but it is also possible to describe the transverse motion in the phase space defined by the coordinates (x, p_x, y, p_y), this system of coordinates is called physical phase space. The angles with respect to the longitudinal position x' and y' (in radiant units) are related to the transverse momenta p_x and p_y (in units GeV/c) with:

$$p_x = mc\beta_{\text{rel}}\gamma_{\text{rel}}x', \tag{2.24}$$

where β_{rel} and γ_{rel} are the relativistic Lorentz factors, m is the rest mass of the particle and c is the speed of light ($c = 1$, being the transverse momenta defined with respect to the speed of light). The particle motion in the physical phase space, at two different longitudinal locations (s_1 and s_2) is shown in Figure 2.5 where, it is possible to observe that turn after turn, the evolution of the particle coordinates describe an ellipse. According to the value of the tune, the particle will perform a certain number of complete betatronic oscillations per turn that is quantified by the integer part of the tune. If the non-integer (or fractional) part of the tune (see Eq. 2.18

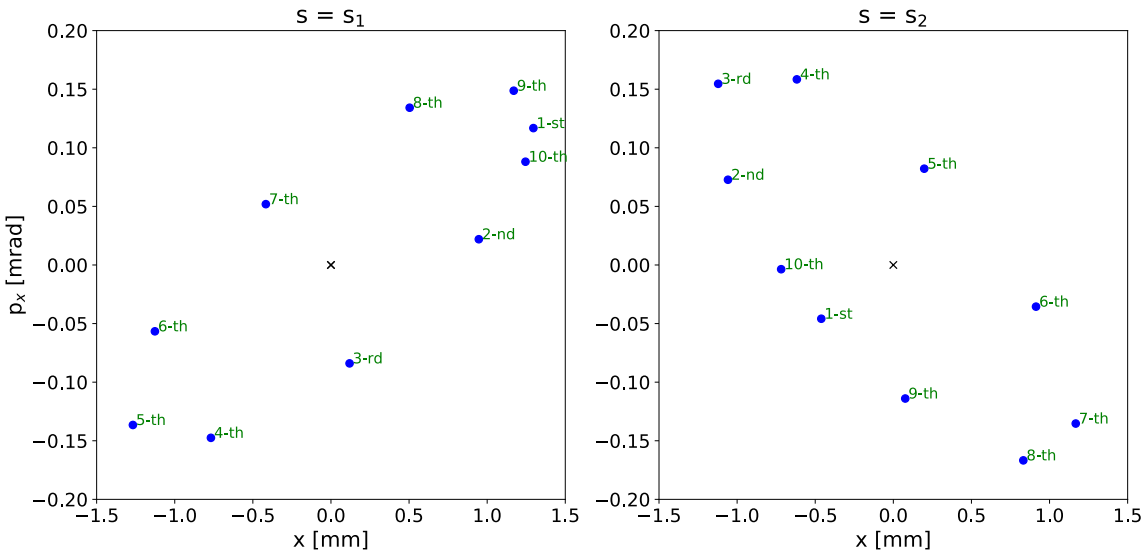

Figure 2.5: Evolution of the particle orbit in the horizontal physical phase space. The particle orbit is displayed at two different longitudinal locations $s1$ and $s2$ for ten successive turns.

for definition) is zero, and if the particles coordinates were observed in a specific longitudinal location along the ring, they will be same they were at the turn before, meaning that the particle orbit will close on itself. If the fractional part is non-zero then after one turn, the particle orbit will not have the same coordinates it had at the turn before because its trajectory will not close on itself. It is possible to observe this latter case in Figure 2.5 where the particle trajectory (namely, particle orbit) is tracked for 10 turns and it is displayed at two different longitudinal positions. Moreover, from Figure 2.5, it is also possible to observe that as the particle moves in the accelerator, the ellipse rotates, shrinks, or enlarges. This evolution of the ellipse is governed by optical parameters, also known as Twiss parameters: α_x, defined in Eq. 2.22, the betatron function β_x and γ_x defined as:

$$\gamma(s)_x = \frac{1+\alpha_x^2(s)}{\beta_x(s)}. \tag{2.25}$$

It is possible to show that even if the particle ellipse changes, the area enclosed by the ellipse itself is constant. It is easier to prove and visually observe this property in the normalised phase space. The change of coordinates between the trace space (x,x') and the normalised phase space (X,X') reads as:

$$\begin{cases} X(s) = \frac{1}{\sqrt{\beta_x(s)}}x(s) \\ X'(s) = \sqrt{\beta_x(s)}x'(s) + \frac{\alpha_x(s)}{\sqrt{\beta_x(s)}}x(s). \end{cases} \tag{2.26}$$

The same particle, whose motion in the physical phase space is shown in Figure 2.5, it is also shown in Figure 2.6, where its motion is represented using the normalised phase space coordinates (X,X'). When moving from the physical to normalised phase space, the ellipsis turns to circles, under the assumption that non-linear effects are neglected or absent. Otherwise, in

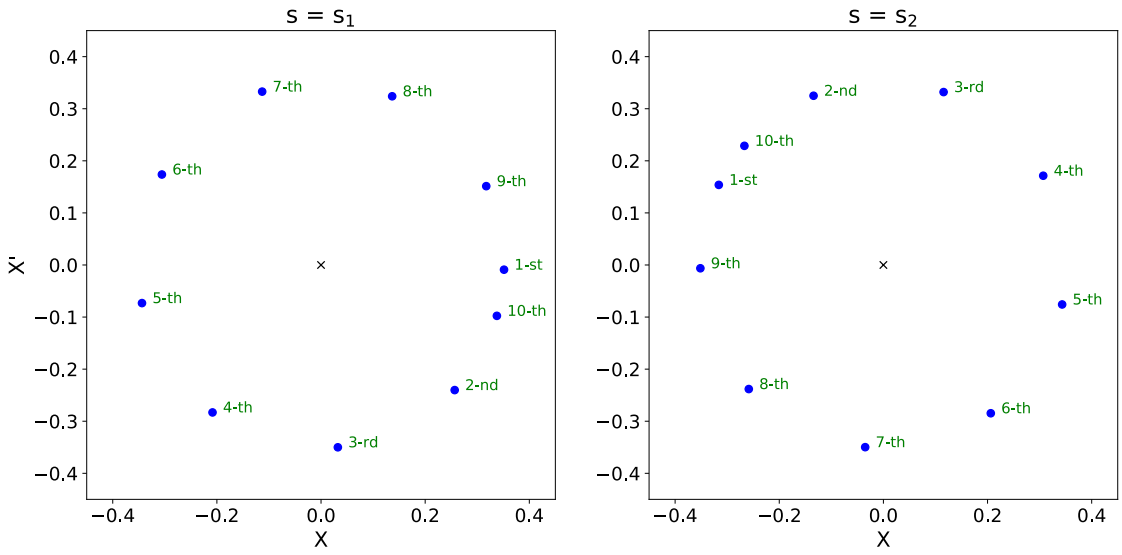

Figure 2.6: The evolution of the particle coordinates is shown in the normalised phase space coordinate system for two different longitudinal positions s_1 on the left and s_2 on the right.

case non-linearities are considered, the particle orbit in the normalised phase space might not have a circular shape. Figure 2.6 shows clearly that the area enclosed by the circle and thus by the ellipse, is constant. In fact, it is possible to observe that even though the sequence of points between s_1 and s_2 is not the same, the x and p_x limits at the two longitudinal positions are the same. But this is only an observation, and it is necessary to provide the mathematical proof that is performed by substituting Eq. 2.21 into Eq. 2.26. Then, by making the square of each term, it is straightforward to prove that:

$$X(s)^2 + X'(s)^2 = 2J_x \longrightarrow J_x = \frac{A}{2\pi}, \tag{2.27}$$

where A represents the area enclosed by the circle in the normalised phase space. The area of the circle (ellipse) is an invariant of motion because the particle action (J_x) is determined by the particle initial conditions. It is preferred to refer to the particle's action J_x as the invariant of motion rather than to the area itself because the action has the same units as the beam emittance, as it will be explained in the next section. There is an analogous way to determine the particle invariant of motion. In fact, the Twiss parameters are enough to fully describe the linear dynamics in an accelerator. In particular, using these parameters, it is possible to rewrite the equation of motion (Eq. 2.21) as:

$$\begin{cases} x(s) = \epsilon_{CS}\sqrt{\beta_x(s)}\cos\left(\Phi_x(s) + \Phi_{x,0}\right) \\ x'(s) = -\epsilon_{CS}\sqrt{\frac{1}{\beta_x(s)}}\left(\alpha_x(s)\cos\left(\Phi_x(s) + \Phi_{x,0}\right) + \sin\left(\Phi_x(s) + \Phi_{x,0}\right)\right) \end{cases} \tag{2.28}$$

Then, by squaring each term, the constant ϵ_{CS}, called the Courant-Snyder invariant, can be expressed as:

$$\epsilon_{CS}^2 = \gamma(s)x(s)^2 + 2\alpha(s)x(s)x'(s) + \beta(s)x'(s)^2 \tag{2.29}$$

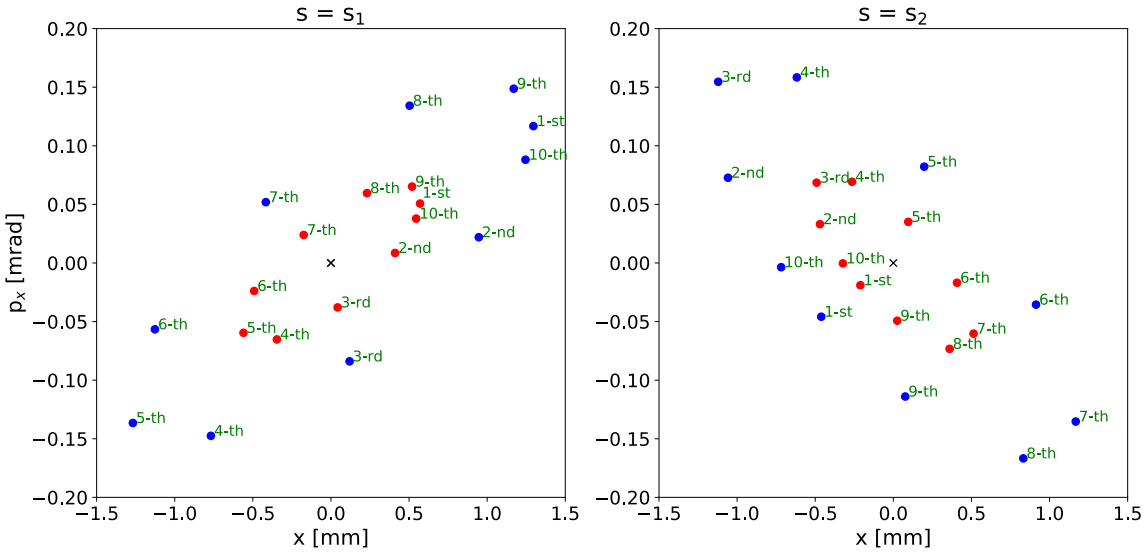

Figure 2.7: Physical phase space for two particles at two different betatron amplitudes.

In conclusion, thanks to the proper definition of the Twiss parameters, it was possible to prove that the evolution of the particle coordinates can be described using characteristic parameters of the transverse beam dynamics, namely the Twiss parameters, as reported in Eq. 2.29. This equation represents an ellipse in the (x, x') trace space that evolves and changes as the particle moves in the accelerator. Its shape is determined at any point along the ring by the Twiss parameters and its area is constant. Therefore, the area of the ellipse is invariant and it is called Courant-Snyder invariant. In the next section (Section 2.2.1) the relation between the different definitions of beam emittance and invariant of motion will be discussed. The discussion presented so far has considered only on momentum particles, thus the dispersion term in Eq. 2.20 has been neglected. On the one hand, this has been done because all the considerations performed on the horizontal plane are true also on the vertical one. Thus, by replacing in the appropriate way the subscript x with the subscript y it is possible to obtain the same conclusions for the vertical transverse plane. On the other hand, the dispersion term is present only in the horizontal direction and, as explained before, it leads the particles to perform betatron oscillations around a new closed orbit that is horizontally displaced with respect to the equilibrium orbit by a quantity equal to Eq. 2.20.

2.2.1 Beam transverse emittance

Every particle performs betatron oscillations at a specific amplitude, therefore each of them has an emittance, as reported in Figure 2.7 where a second particle (in red) oscillating at a smaller betatron amplitude has been added to the one previously shown in Figure 2.5. A beam of particles will have a particle emittance between zero (when a particle moves exactly on the reference orbit) and a maximum value. This maximum value is usually known as admittance and it corresponds

to the emittance value of the particle with the largest betatron oscillation amplitude. In order to provide an estimation of the space occupied by the beam in the horizontal (or vertical) direction the admittance is used. The emittance of a single particle is not a practical quantity to use to estimate the space occupied by the beam in phase space. Therefore, additional quantities are defined:

- If the position and momentum distributions of particles in the beam are known, then the Root Mean Square (RMS) emittance ϵ_{RMS}, in Eq. 2.30, gives a statistical information on the area occupied by the beam. The first term of Eq. 2.30 is the product of the variances of the particle's position and momentum, while the second one represents the position-momentum correlation of the particles in the beam. The RMS emittance is defined as:

$$\epsilon_{\text{RMS}} = \sqrt{\langle x^2 \rangle \langle p_x^2 \rangle - \langle x \cdot p_x \rangle^2}, \tag{2.30}$$

  where,

$$\begin{gathered} \sigma_x^2 = \langle x^2 \rangle = \frac{1}{N}\sum_i^N (x_i - \bar{x})^2; \qquad \sigma_{p_x}^2 = \langle p_x^2 \rangle = \frac{1}{N}\sum_i^N (p_{x,i} - \bar{p_x})^2; \\ \sigma_x \sigma_{p_x} = \langle x \cdot p_x \rangle = \frac{1}{N}\sum_i^N (x_i - \bar{x})(p_{x,i} - \bar{p_x}). \end{gathered} \tag{2.31}$$

- The emittance of a beam made by both on-momentum and off-momentum particles is determined by the linear combination of betatron oscillations and momentum spread. The emittance of such a beam is generally called physical emittance ϵ_{ph}. From the knowledge of the particle horizontal displacement with respect to the equilibrium orbit:

$$x = x_\beta + D(s)\frac{\Delta p}{p}. \tag{2.32}$$

  It is possible to determine the physical emittance by averaging the squares of the two terms on the RHS of Eq. 2.32:

$$\langle x^2 \rangle = \langle x_\beta^2 \rangle + 2\langle x_\beta D \frac{\Delta p}{p} \rangle + \langle D^2 \frac{\Delta p}{p} \rangle.$$

  Using Eq. 2.31 and simplifying the term in the middle that averages to zero, the physical emittance reads as:

$$\epsilon_{\text{ph}} = \frac{\sigma_x^2 - D_x^2(s)\left(\frac{\Delta p}{p}\right)^2}{\beta_x(s)}. \tag{2.33}$$

- The Courant-Snyder invariant is an alternative way to define the beam emittance. Even if it has been defined as the invariant of motion for a single particle, it is easy to generalise its definition to a beam of particles, whose position and momentum distributions are known. Starting from Eq. 2.29 and averaging each term:

$$\langle \epsilon_{CS}^2 \rangle = \langle \gamma(s) x(s)^2 + 2\alpha(s) x(s) x'(s) + \beta(s) x'(s)^2 \rangle.$$

By fixing the longitudinal position, and thus, evaluating the emittance at a specific point along the machine ring, the average Courant-Snyder emittance reads as:

$$\epsilon_{CS}^2 = \gamma(s_1)\langle x(s)^2\rangle + 2\alpha(s_1)\langle x(s)x'(s)\rangle + \beta(s_1)\langle x'(s)^2\rangle. \tag{2.34}$$

Of course, it is possible to evaluate the Courant-Snyder invariant at any point, provided that the position and momentum distributions are known. The Twiss parameters are known at any point along the ring.

- The action J_x is another particle invariant of motion. It has been defined as the area enclosed by the particle orbit divided by 2π. By averaging Eq. 2.27 for any particle of the beam, it is possible to find the generalised definition:

$$\langle J\rangle = \langle\frac{A}{2\pi}\rangle \equiv \epsilon_{\langle J\rangle}. \tag{2.35}$$

Thus, for a particle beam, the emittance can be also evaluated as the average of the action of every particle in the beam itself.

The emittance as average of actions $\epsilon_{<J>}$ as well as the emittance in the Courant-Snyder approach ϵ_{CS}, are both invariants of motion. Therefore, their value is always the same in any point along the ring. This is not true for the RMS emittance and the physical one. During acceleration, the amplitude of betatron oscillations is damped, the phenomenon is known as adiabatic damping. Therefore, it is necessary to define a quantity that does not change during acceleration, thus, that is independent of kinematic factors. The definition of the normalised emittance is:

$$\epsilon^* = \epsilon_{\mathrm{RMS}}\beta_{\mathrm{rel}}\gamma_{\mathrm{rel}} = \epsilon_{\mathrm{ph}}\beta_{\mathrm{rel}}\gamma_{\mathrm{rel}}, \tag{2.36}$$

where β_{rel} and γ_{rel} are the relativistic Lorentz factors. From the comparison of Eq. 2.21 and Eq. 2.28 it is possible to find a relation between the Courant-Snyder invariant and the action. Thus, the generalisation of Eq. 2.36 for all the definitions of emittance given so far, it is straightforward:

$$\epsilon^* = \epsilon_{\mathrm{RMS}}\beta_{\mathrm{rel}}\gamma_{\mathrm{rel}} = \epsilon_{\mathrm{ph}}\beta_{\mathrm{rel}}\gamma_{\mathrm{rel}} = \epsilon_{<J>} = \epsilon_{\mathrm{CS}}. \tag{2.37}$$

Even though the normalised emittance should be an invariant of motion, there are particular phenomena that may lead to emittance grow (or blow-up). Intra-beam scattering (collisions between particles within the beam or with residual gasses in the vacuum chamber), random noise from the RF cavities or from the magnets power supply as well as errors in the transfer lines between accelerators can cause emittance blow-up. Only the latter topic will be discussed since it will be useful for future discussions. When a beam is transferred from one accelerator to another through a transfer line, it is of fundamental importance to match the beam ellipse of the extracted beam with the lattice ellipse of the receiving accelerator. This gymnastic is usually performed in transfer lines. If the beam ellipse does not have the same orientation and aspect ratio as the

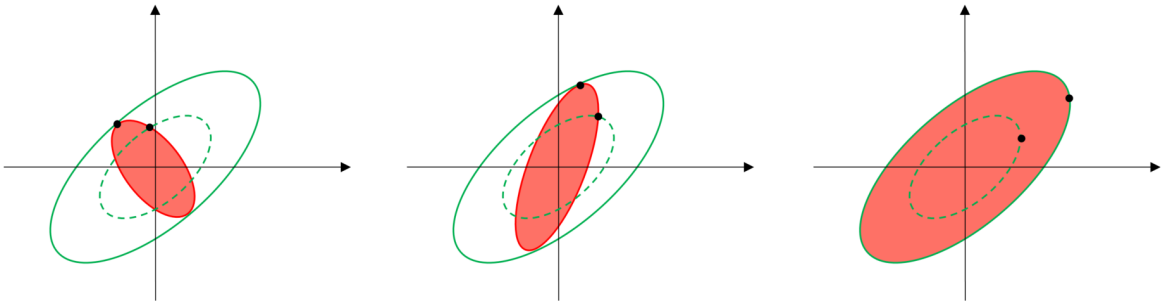

Figure 2.8: Emittance mismatch and filamentation in phase space. Comparison of particle orbit in the matched (green dashed) configuration and in the unmached one (green continuous). At the end of the filamentation process the emittance of the beam is larger compared to the one right after injection (last and first diagram, respectively).

one of the accelerator downstream, then the beam is said unmatched. In these conditions, the beam will filament and the resulting emittance will be larger than the original one. In Figure 2.8 is reported a schematic representation of emittance blow-up caused by emittance mismatch at injection. If the lattice emittance and the beam emittance were matched, then the particle (represented as a black dot) would have moved on the green dashed ellipse. In case of mismatch, the same particle will move on an ellipse of larger area (green continuous ellipse). A beam of particles would behave in the same way: the particles will move on ellipses of larger amplitude than those they would have been moving on in the case of a matched beam. The beam ellipse would remain unchanged in case the beam dynamics in the accelerator would be fully linear. In real cases, non-linear field components as well as non-linear effects play an important role. Therefore, turn after turn the beam ellipse will deform and after some turns it will occupy the entire lattice ellipse. The beam emittance has increased and the phenomenon is called dilution of phase space by filamentation.

2.3 Resonances

The above considerations are valid in an ideal machine with no errors. In reality, problems during the fabrication of magnets as well as errors during their alignment in the ring might occur. However, the possible sources of error might depend also on the field at the edge of the magnet, on the parasitic current in the coils, on the variation of steel properties as well as on the eddy currents in the vacuum chamber that may perturb the linear field. Even if during the design process all these aspects are taken into account and they are minimised as much as possible, it is not possible to completely remove them. Therefore, it is necessary to consider the effects of non-linear fields when the beam dynamics is studied. The simplest synchrotron to study would be composed by dipole and quadrupoles only, in this configuration and in absence of errors, the beam dynamics would be linear. If in this configuration, a dipole has either been tilted during

installation or it has undergone problems during fabrication, the resulting beam dynamics will not be linear anymore. In both cases (tilted or fabrication errors), the resulting magnetic field can be considered as the linear composition of the nominal (i.e., in the absence of errors) magnetic field and a dipolar error. In the first case, the dipolar error will kick the beam vertically by a quantity θ, in the latter one, it will kick the beam horizontally by the same quantity. It is possible to solve the equation of motion and find the analytical expression for the closed orbit (the complete demonstration can be found in Refs. [8, 20, 22]), here below the horizontal position evolution is reported:

$$x(s) = \frac{\theta\sqrt{\beta_x(s)\beta_{x,0}}}{2\sin(\pi Q_x)}\cos\Big(\big|\Phi_x(s) - \Phi_{x,0}\big| - \pi Q_x\Big). \tag{2.38}$$

From Eq. 2.38, it is clear that the horizontal tune plays an important role. For integer values of the tune, Eq. 2.38 is not anymore well defined, in particular, the amplitude of the oscillation increases rapidly up to the point where it is not stable anymore. In this condition, the integer resonance is excited. A way to overcome this issue consists in imposing a non-integer value of the tune. In particular, the half value of the tune (namely 0.5) is quite interesting since the dipolar kick would be cancelled in two consecutive turns. It is possible to observe similar phenomena when a quadrupole is tilted or misaligned. In the first case, the quadrupolar field is composed by the linear combination of a normal quadrupole and a tilted (skew) quadrupole inducing coupling between the horizontal and vertical plane. In the latter case, when a horizontal (vertical) misalignment occurs, the resulting quadrupolar field is the linear combination of the nominal quadrupolar field (i.e., in the absence of errors) and a horizontal (vertical) dipolar field. It is possible to demonstrate that quadrupole errors mainly induce modifications in the amplitude of betatron oscillations, as reported below (the mathematical proof can be found in Ref. [23]):

$$\Delta\beta_x(s_0) = -\frac{\beta_x(s_0)}{2\sin(2\pi Q_x)}\int_s^{s+C}\beta_x(s)\Delta K(s)\cos\Big(2\big|\Phi_x(s_0) - \Phi_x(s)\big| - 2\pi Q_x\Big)ds'. \tag{2.39}$$

From Eq. 2.39 it is possible to observe that an horizontal tune of half-integer would cause a periodic uncontrolled increase of betatron oscillations. However, this happens also when the horizontal tune has an integer value. Therefore, it is clear that the value of the tune has to be chosen with extreme care. The integer and half-integer values have to be avoided, because they induce first- and second-order resonances. Being these resonances caused by linear field errors, they are known as linear resonances. Therefore, it is expected to have higher order resonances induced by non-linear error in higher order multipoles (namely, non-linear resonance). It is possible to generalise what has been briefly discussed above concerning the excitation of resonances: multipoles of order n can excite resonances of the same order as well as lower order resonances with lower strength as the order of the resonance reduces. However, for stronger excitation, multipoles of order n can excite higher order resonances. Even though Eq. 2.38 and Eq. 2.39 have been reported for the horizontal plane, the same holds true also for the vertical one. Thus, it is important to avoid resonant phenomena in both planes at the same time. It is crucial

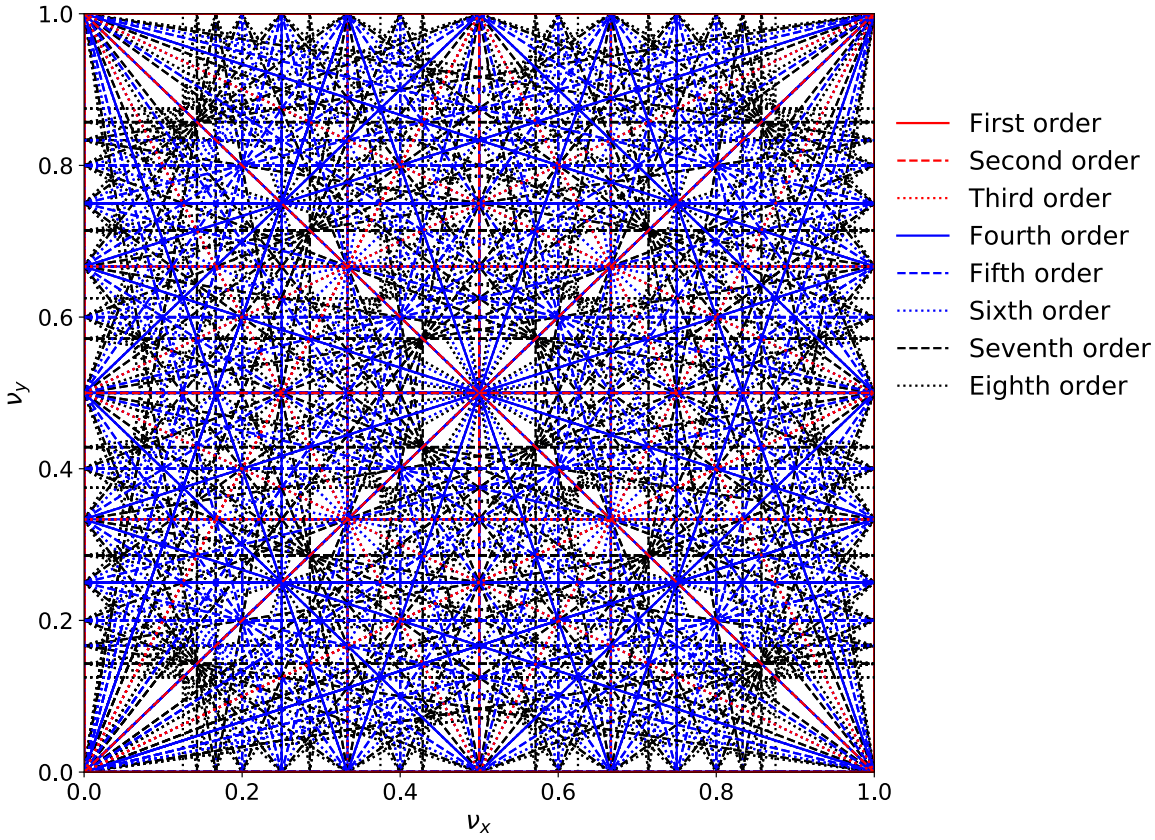

Figure 2.9: The horizontal (ν_x) and vertical (ν_y) fractional part of the tune are shown in the interval between 0 and 1. Several resonance lines (from the first to the eights order) are reported.

to properly evaluate the horizontal and vertical tunes so that the resonant condition

$$kQ_x + \ell Q_y = m \tag{2.40}$$

is not satisfied for $\forall k, \ell, m \in N$. The choice of the tunes defines the working point of the accelerator in the tune diagram space, shown in Figure 2.9. The resonant conditions defined as in Eq. 2.40 are shown with different colours and different styles up to the 8^{th} order. It is possible to observe in Figure 2.9 that there are regions between two adjacent resonances that are wider than others. These areas should be preferred since the unavoidable tune spread (that might be caused by transverse non-linearities as well as energy spread) in the beam leads the working point to be defined by an area itself rather than a point in the tune diagram. At first sight, it might be clear that according to the type of multipoles present in the accelerator, certain resonances have to be avoided; in reality, resonances are also widely exploited in accelerator physics. There are many interesting applications, but, the next discussion is focused on using resonances in beam extraction.

2.3.1 Fourth-order resonance

A general and exact closed analytical solution of the non-linear equation that describes particles motion in the presence of non-linear fields, cannot be found. Therefore, computational tracking is used to determine the particle position and momentum turn after turn along the six dimensions. These analysis are carried out by particle tracking codes that, given the accelerator lattice, are able to estimate the optics parameters (Twiss functions and dispersion) and to track the distribution of particles throughout the lattice, on a turn-by-turn basis. The most common codes are the Methodical Accelerator Design (MAD-X) [24] and the Polymorphic Tracking Code (PTC) [25] both developed at CERN and used in the context of this thesis. In MAD-X, it is possible to describe an accelerator (circular or linear) and transfer lines by defining every magnetic element, RF cavity and drift. It is nowadays widely used to compute the optics parameters, closed orbit and, more in general, to study and optimise the performance of accelerators and transfer lines. It also allows for particle tracking by propagating particle coordinates (in phase space along the transverse and longitudinal directions), given the lattice and for the number of turns over which the analysis has to be performed. In MAD-X, it is common practice to redefine the magnets as a sequence of thin slices with zero length. However, MAD-X is a non-symplectic integrator. Therefore, when thick magnetic elements are analysed, the phase space is not conserved. To overcome this issue, PTC has been embedded in MAD-X as a library. Whenever a symplectic integration is needed, it is possible to call the PTC library within the MAD-X script. This approach has been used for tracking particles in the PS ring. As it will be described in Chapter 3, the complex structure of the Main magnetic Unit (MU) of the PS needs the magnetic element to be defined as thick elements. Thus, the use of PTC is mandatory.

Non-linear fields can generate either unstable or stable resonances and their stability is determined by their behaviour when approaching the resonant tune. Unstable resonances of order n split the beam in n beamlets. When the $n-$th order resonance is crossed, particles are repelled from the centre of phase space and rotate around n stable fixed points. When the beam crosses a stable resonance of order n, it is split into $n+1$ beamlets: one of them is the centre of the phase space (around which particles rotated before the resonance crossing) and n new beamlets around the stable fixed points originate. Moreover, a stable resonance shows a periodic behaviour: the beamlet at the centre of phase space closes on itself after one turn and the n beamlets close on themselves after n turns. Thus, a stable resonance of order n shows two structures: a SFP at the centre whose beam dynamics is linear and whose orbits are known as core; and n SFP with their orbits with periodicity n, whose dynamics is strongly non-linear and they are known as islands [22]. The resonant tune has to be approached slowly (adiabatic with respect to the time scale introduced by the betatron oscillations) to allow particles to be trapped around the fixed points. It is interesting to analyse in detail the fourth-order resonance because it is the one used to extract the beam with MTE technique, additional clarifications and explanation on this technique will be provided in Section 3.3.2. In principle, the fourth-order resonance can be

achieved by using only octupoles. However, precise control over several parameters, such as the size of the islands, the horizontal tune, linear and non-linear chromaticity, and detuning with amplitude, is desired. This can be achieved by properly tuning octupoles and sextupoles. From the knowledge of the lattice, it is possible to build the transport matrix that describes the particle position and angle (defined as the longitudinal derivative of the position) evolution as it moves in the ring. Given some initial conditions for each particle, it is possible to compute their positions and momentum at any desired longitudinal position in the accelerator. Therefore, following the description in [26], it is possible to write the one-turn matrix as:

$$\begin{pmatrix} x \\ x' \end{pmatrix}_{n+1} = \begin{pmatrix} \cos(2\pi\nu_0) & \sin(2\pi\nu_0) \\ -\sin(2\pi\nu_0) & \cos(2\pi\nu_0) \end{pmatrix}, \begin{pmatrix} x \\ x' + x^2 + \kappa x^3 \end{pmatrix}_n \tag{2.41}$$

where ν_0 is the fractional part of the tune, and (x, x') are derived from the normalised phase space coordinate (X, X') using:

$$\mathbf{x} = \frac{K_2 \beta_x^{3/2}}{2} \mathbf{X}$$

where,

$$K_2 = \frac{L}{B_0 \rho} \frac{\partial^2 B}{\partial x^2}; \qquad \kappa = \frac{2}{3} \frac{K_3}{\beta_x K_2}; \qquad K_3 = \frac{L}{B_0 \rho} \frac{\partial^3 B}{\partial x^3}.$$

Equation 2.41 describes the time evolution of the fourth-order resonance if we let ν_0 be the slowly changing tune that allows the resonance crossing, island formation and particles trapping in the islands, thus, $\nu_0 = \nu_0(n)$. Assuming that the sextupolar and octupolar fields that generate the resonance are represented in the single-kick approximation [26], in the resonance rotating frame, the Hamiltonian of the system can be described as [27]:

$$H(J, \psi) = E \longrightarrow H \approx \delta J + \frac{1}{2} \mu J^2 + g J^{\frac{m}{2}} \cos m\psi. \tag{2.42}$$

Where, J and ψ are the action-angle conjugate variables; $\delta = \nu_0 - \frac{\ell}{m}$ where ℓ and m satisfy the fourth order resonant condition $m\nu_0 = \ell$; μ is the nonlinear detuning parameter arising from higher-order multipoles and g is the integrated resonance strength of the fourth-order resonance. The Hamiltonian motion equation reads as:

$$\begin{cases} \dfrac{dJ}{d\theta} = m g J^{\frac{m}{2}} \sin m\psi \\ \dfrac{d\psi}{d\theta} = \delta + \mu J + \dfrac{m}{2} g J^{\frac{m}{2}-1} \cos m\psi \end{cases} \tag{2.43}$$

where θ is the orbital angle. A point in phase space is a fixed point of order n if it represents a trajectory that repeats after n periods. This trajectory yields n fixed points of order n. The centre of phase space is itself a stable fixed point for the way it has been defined. Moreover, it is possible to compute the additional stable fixed points of the system by looking at the points that satisfy

$$\left. \frac{\partial E}{\partial J} \right|_{\sin m\psi = 0} = 0. \tag{2.44}$$

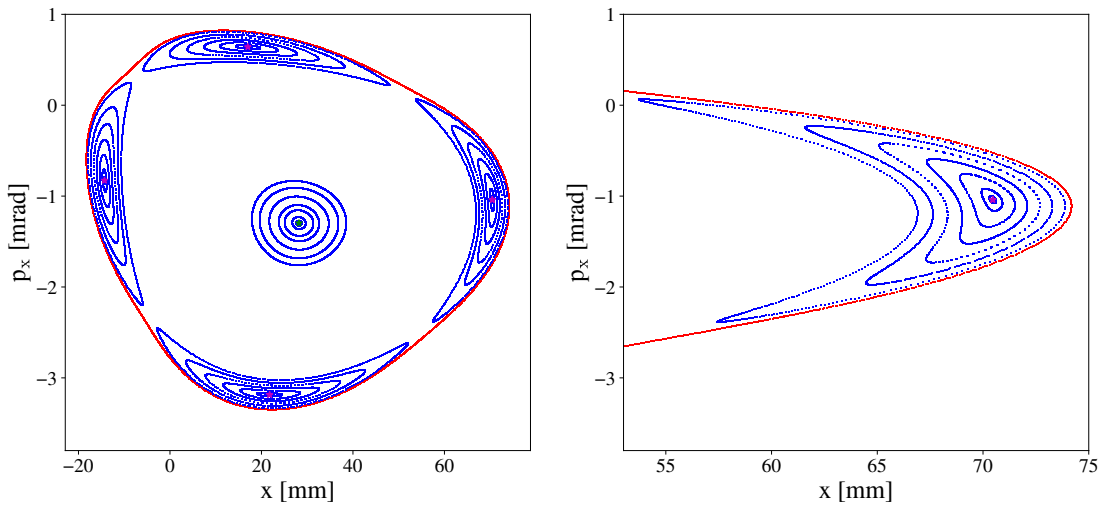

Figure 2.10: Left: phase space representing beam split in a central core and four 4-turns periodic islands. The orbit of a particle not trapped in the islands is shown with the red line. Moreover, the stable fixed points are in cyan and magenta for the core and islands respectively. Right: Zoom on the outermost island that aims at highlighting the particles orbit at different amplitudes.

The stable fixed point coordinates $(J_{\mathrm{SFP}}, \psi_{\mathrm{SFP}})$ are determined by solving:

$$\sin m\psi_{\mathrm{SFP}} = 0 \qquad \text{and} \qquad \delta + \mu J_{\mathrm{SFP}} \pm \frac{m}{2} g J_{\mathrm{SFP}}^{\frac{m}{2}-1} = 0 \tag{2.45}$$

The stable fixed points (SFPs) are stable if they correspond to a local maximum (or minimum) of Eq. 2.44, unstable fixed points correspond to saddle points on the energy surface. Being Eq. 2.42 quadratic, the separatrix will be given by the intersection of two "ellipses". The separatrix divides the phase space into regions inaccessible from one another and it is the surface that passes through the unstable fixed points. As a first approximation, the particles' motion in the close vicinity of the stable fixed point is linear [28]. As particles with larger betatron oscillation amplitude are considered, the effect of non-linearities can be observed: the deformation of particles' orbits is evident and the motion is strongly non-linear. This is evident for the islands on the right hand side of Figure 2.10. In the close vicinity of the Stable Fixed Point (SFP) the motion is almost linear, it is possible to observe the characteristic particle orbit (ellipse). As the amplitude of oscillations increases, the effect of non-linear field increases and the orbit is distorted into a half-moon shape (for this specific case). Particle motion is not limited by the separatrix. Those that are not trapped inside the island during the tune modulation may still rotate in a trapezoidal-like closed orbit outside the separatrix. All these features are shown in Figure 2.10, where also the SFPs are represented with a cyan dot for the core and magenta ones for the islands.

CHAPTER 3

THE CERN PROTON SYNCHROTRON

Right after the Council has held its first meeting on May 1952, four working groups were established, among these the Proton Synchrotron (PS) one. The PS project aimed at reproducing on a larger scale (five times bigger), the synchrotron built in Brookhaven, since it had just accelerated protons up to the kinetic energy of 1 GeV in May of that same year. During those intense years, the new alternating-gradient accelerator had been thought and developed. The PS group decided to invest on this new idea rather than the classical one (weak-focusing). The great idea behind alternating gradient synchrotrons is to let the field gradient index vary rapidly between large and small values. In this way, the horizontal and vertical oscillation stability is increased strongly. At the same time, during the development of the project, new limitations and problems were found. Among these, the stronger focusing effect needed a higher precision of the magnetic field and a precise alignment of the magnets themselves. Moreover, when the relative change of the beam velocity goes from being greater to being smaller than the relative change of orbit length (namely, crossing of the transition energy), then beam loss occurs. The entire PS project followed the suggestion of Werner Heisenberg who strongly suggested to "build a machine that could be operated up without difficulty in the region above 20 GeV but which could, in the limit, be extended in energy to 30 GeV" [20]. The PS started operations on 1959 and it was the very first synchrotron based on the alternating-gradient principle. It is still part of the accelerator chain that brings the proton and ion beams to the LHC or to other experiments. Nowadays, it receives the beam from the PSB at 2 GeV (kinetic energy) and it accelerates it up to the maximum energy of 26 GeV. In the following sections the main features of the PS ring will be collected and explained, but the focus will be on components and techniques related to beam extraction.

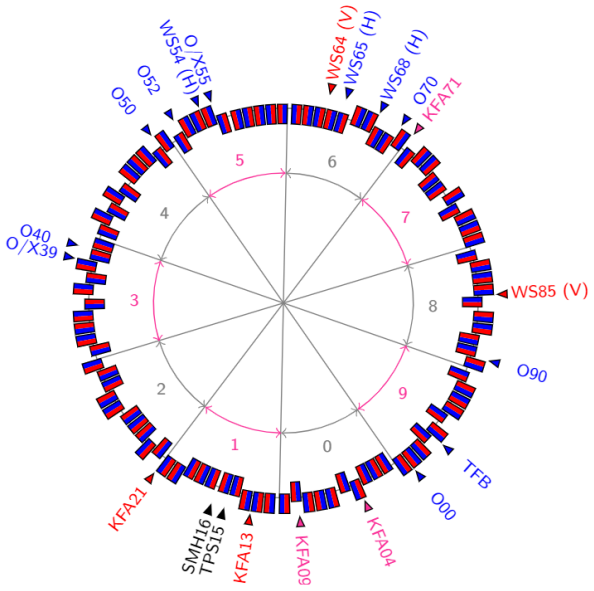

Figure 3.1: PS layout. Special highlight on its super-periodicity and on the key MTE elements.

3.1 Overview of general parameters

The PS is the second last accelerator before the beam reaches the LHC. It has been built in three years from 1955 and 1957, and the first beam inside the PS has been registered in 1959 [20]. It has a radius of 100 m and it can accelerate both protons and ions.

The longitudinal bending and the transverse focusing is achieved within the Main magnetic Units (MU) that are combined-function magnets where these functions are carried out simultaneously. Their structure is very peculiar, since a magnetic unit is composed by a sequence of ten blocks and each block weights around 30 tonnes and it is 417mm long. There are one hundred main magnets, and they are electrically powered in series while the cooling is performed on a parallel-type circuit. In particular, the cooling system is based on the very well known technique of forced-conduction of water in cooling pipes, since the magnets are composed of conductive materials at room temperature. Additional details on the PS MUs will be provided in Section 3.2. The PS structure, as shown in Figure 3.1, has a periodicity of ten. The accelerator lattice is of the FOFDOD type, meaning that an half-focusing section is followed by an half-defocusing section, the detailed explanation will be provided in Section 3.2. The control of optics parameters and the beam stability is achieved by multipoles [20]:

- there are 20 quadrupoles with a gradient of dB/dr = 7000 G/cm divided in two sets of identical magnets from the electrical point of view.

- There are 20 sextupoles with a gradient of d^2B/dr^2 = 72 G/cm^2 and an effective length of 33 cm.

- There are also 20 octupoles with a gradient of $d^3B/dr^3 = 41$ G/cm^3 and an effective length of 43 cm.

Sextupoles and octupoles are divided in two identical groups (each of 10 magnets per type), where each group is powered by the same power supply in series.

During acceleration, the beam crosses the transition energy at 5.72 GeV. The acceleration is performed by 11 adjustable frequency RF cavities (ferrite-loaded coaxial resonators), each of them has a frequency between 2.6 MHz and 9.5 MHz and has a maximum voltage of 20 kV. There are four auxiliary RF systems at 13 MHz (installed in 2002), 40 MHz (installed in 1996), 80 MHz (installed in 1998) and 200 MHz (installed between 1977 and 1979). Their installation was necessary to allow the PS to adapt to the continuous needs of particle beams for physics.

Once the beam has reached the desired energy, it can be sent to the experimental areas distributed around the ring or to the SPS and the downstream experiments (see Figure 1.1 for reference). In the PS ring, the beam can be extracted with different techniques: fast (i.e. one turn) extraction, slow extraction or multi-turn extraction. As far as this latter method is concerned, from the 1970s to 2015, the beam was extracted using the Continuous Transfer (CT), but from that year on-wards, the beam is extracted with the Multi-Turn Extraction (MTE). It is a novel process that required around 10 years of study, measurements, electronic upgrade, and installation of new magnetic elements to be operational. The most important and relevant parameters described above are summarised in Table 3.1 [20].

3.2 The Main magnetic Units

The PS Main magnetic Units are the main magnetic component of the PS ring and are composed of normal conducting and combined-function magnets that focus the beam while bending it. The magnets are placed in a ring-shaped structure of 200π m circumference. Each one of the 100 combined-function magnets is composed of a focusing half-section and a defocusing half-section. Between two subsequent magnets there is a region where no bending occurs, namely a straight section (SS). In this region, it is possible to place instrumentation, injection, extraction, and accelerating sections. The focusing and defocusing half-units are composed of ten (five for each half-unit) adjacent C-shaped steel blocks, schematically represented in Figure 3.2 [29]. This component acts as a physical support for the magnets that are installed on it [29]. The main normal conducting magnets are installed around the two open sides of the C-shaped blocks. In particular, the profile's shape of the block facing the beam, namely the pole profile, can be either closed or open, as show in Figure 3.2 [29]. This feature ensures the alternation of the gradient, and thus the focusing (or defocusing) action while the beam is bent in the longitudinal plane. It has been designed in such a way that both the dipolar field and the focusing (or defocusing) strength are kept constant all over its length. However, due to the finite length of the magnet

Construction years	1955-1957 (3 years)
First beam	1959
Accelerator circumference [m]	200π
Accelerator circumference w.r.t. SPS [-]	$\frac{10}{11}$
Injection energy [GeV]	1.4
Maximum extraction energy [GeV]	26
Magnetic lattice	Alternating gradient
Focusing	Combined-function
Lattice sequence	FOFDOD
Number of MU	100
Number of quadrupoles	20
Number of sextupoles	20
Number of octupoles	20
Transition energy [GeV]	5.72
Number of RF cavity	11
Cavity type	Ferrite-loaded coaxial
Frequency range of each cavity [MHz]	2.6 – 9.5
Voltage per cavity [kV]	20
Auxiliary RF systems [MHz]	13, 40 80, 200
Beam extraction	Fast, Slow, Multi-turn (CT, MTE)

Table 3.1: Principal PS parameters (geometry of the ring, magnetic properties, longitudinal characteristics and extraction schemes).

Type name	Number of magnets	Yoke position	Sequence half-sections
R	35	Outside	defocusing-focusing
S	15	Outside	focusing-defocusing
T	35	Inside	defocusing-focusing
U	15	Inside	focusing-defocusing

Table 3.2: In the PS four different MUs are installed. For each of them the number of installed magnets, the return yoke position and the ordered sequence of focusing and defocusing half sections is reported.

element itself and the finite magnetic properties of the materials there are non-linear effects at the edge of the magnetic field (additional information can be found in Ref. [29]).

It is possible to classify the main magnets according to the order of installation among the focusing and the defocusing half-sections as well as to the position of the return yoke of the C-shaped blocks. There are four configurations whose features are reported in Table 3.2 [20] and whose schematic representation can observed in Figure 3.3 [20]. These main units provide the main dipolar and quadrupolar fields. To further control and correct the magnetic field of the main magnet, auxiliary coils have been installed:

- The Pole-Face Winding (PFW) are mounted on the pole surface of focusing and defocusing

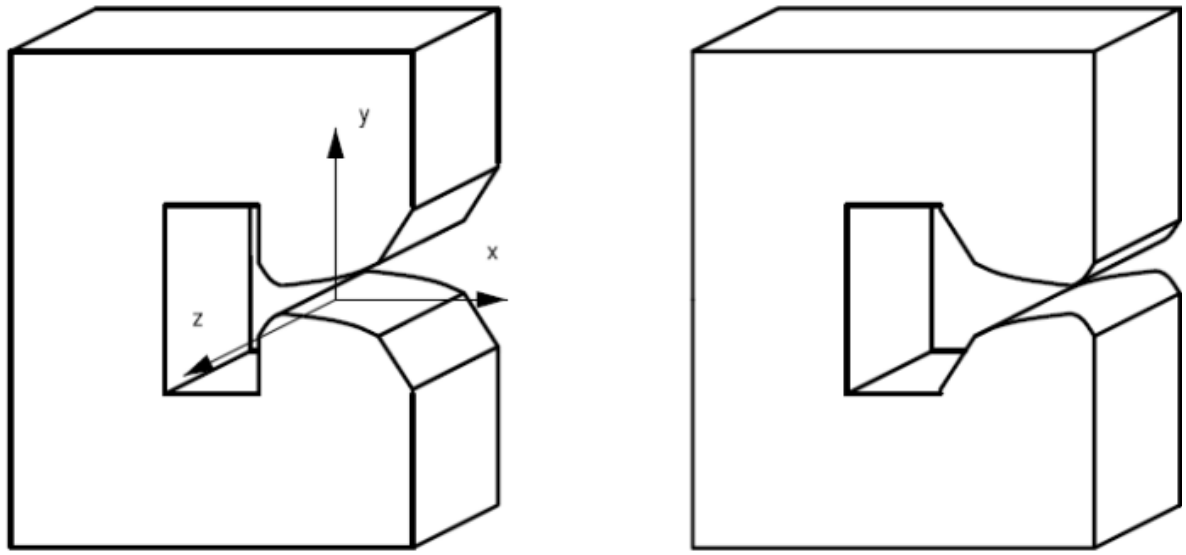

Figure 3.2: Right (left): C-shape steel block with an open (close) pole profile facing the beam. The reference system used to describe the particle motion within the magnet is also reported where the longitudinal direction is described by z.

half-unit. They are constituted of two separate circuits (in Figure 3.4 right) called narrow and wide focusing (defocusing) PFW for the focusing (defocusing) half-unit on which they are installed.

- The figure-of-eight loop (F8) is mounted around the top and bottom of the magnet face poles, thus in the vicinity of the main normal conducting magnet. The F8 is a eight-shaped normal conductor, as the name suggested, and it goes around the pole faces of focusing and defocusing half-units and crosses between them. The crossing allows for having opposite currents, and thus opposite magnetic fields, in the two half-units.

They provide a means to control the horizontal and vertical tune and chromaticity since the main quadrupolar field is generated by the configuration of the C-shaped blocks. From the schematic representation in Figure 3.4 [20] it is possible to observe that the PFW plate is installed on the face of the pole. Each main magnet has four PFW plates installed on the focusing and defocusing half-units. Additional quadrupoles, sextupoles and octupoles are installed in the straight sections to have a full control on the beam optic parameters all over the ring, as shown in Figure 3.1, where octupoles are identified by the capital O, and sextupoles by the capital X. Moreover, it is possible to find in black and pink the relevant components used in the beam extraction, that will be described in detail in Section 3.3; while the instrumentation used to determine the beam position in the vacuum chamber is identified as WS (Wire Scanner), its technology and usage will be described in Chapter 4.

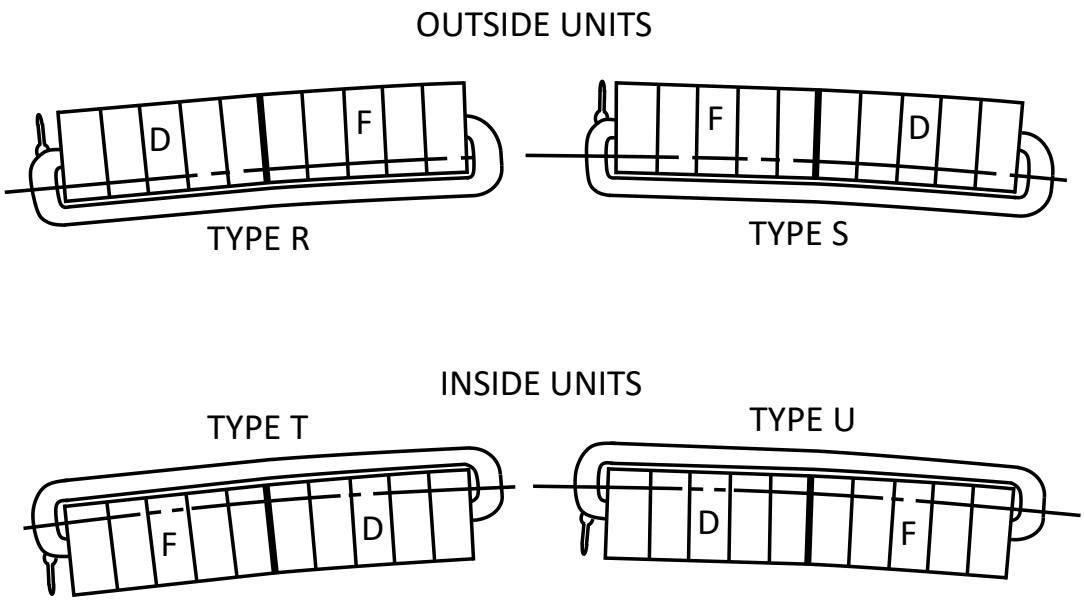

Figure 3.3: PS main magnet unit types. The internal or external position of the return yoke is defined with respect to the beam orbit, shown with the long dashed line. The letters *F* and *D* refers to the half-focusing and half-defocusing sections, respectively. Different types of magnets have different the return yoke in different position as well as a different sequence of focusing and defocusing half sections.

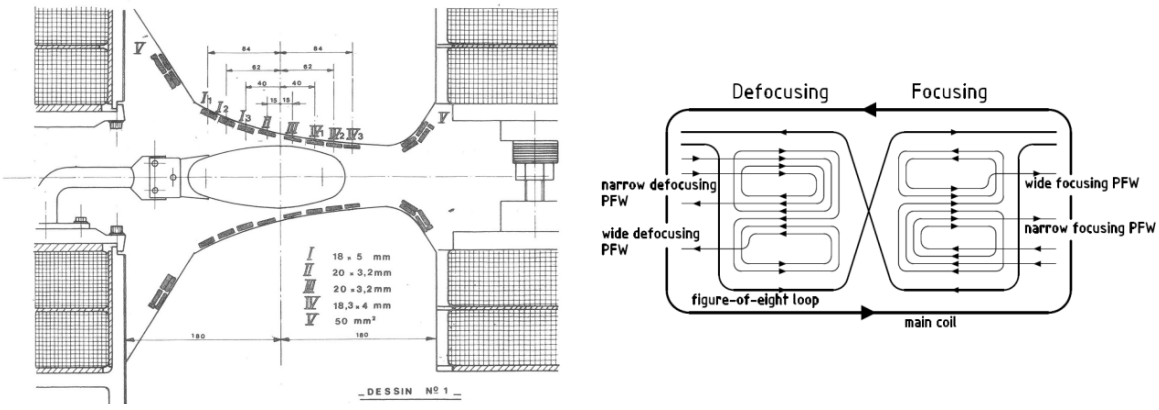

Figure 3.4: Left: transverse section of a main magnet. The pole profile is open-type. On its surface it is possible to observe the presence of the PFW wires as well as the F8 loop and the main coil (on the four corners). Right: a schematic representation of the PFW, F8 and main coil is reported.

3.3 Beam extraction techniques from the PS

Two different approaches could be used to extract particles from an accelerator: fast extraction or slow extraction. The two approaches strongly differ in the time (or, equivalently in the number of turns) needed to extract the beam (or part of it) from an accelerator. The latter technique is adopted for several applications such as medical accelerator for cancer treatment [30] or at the PS for the East Area experiments (see Figure 1.1, the reason is that it is of fundamental importance to obtain a beam that lasts some seconds (between 1s and 10s) and which intensity, i.e. the number of particles reaching the patient or the experiment, is kept constant in time. The present discussion focuses on the first type of extraction, namely, the fast extraction. It is possible to further classify it as single-turn or multiturn extraction. The single-turn fast extraction allows the transfer of the entire beam to another accelerator, or towards experimental areas in a single turn. The multiturn extraction is usually performed when an accelerator with a larger circumference has to be filled. The beam extracted from the PS can be sent to the East Area by means of a resonant slow extraction, to the n-TOF (neutron Time of Flight facility) exploiting a single-turn fast extraction of PS proton beams at 20 GeV/c, to the Antiproton Decelerator (AD) where the antimatter is generated by 26 GeV/c PS proton beams impinging over a target or towards the Super Proton Synchrotron (SPS) which is filled with two consecutive multi-turn extractions from the PS (see Figure 1.1 for reference). The PS can extract the beam in both ways (multi-turn and resonant), but for the purposes of future discussions, the focus will be only on the multiturn extraction, the aim being to uniformly fill the SPS for the fixed target physics programme (SFTPRO) in the North Area. Before going into the details of beam extraction it is worth mentioning that the longitudinal structure of the beam has no impact on the extraction process. The beam can be either bunched or debunched. A continuous longitudinal structure will cause unavoidable losses when the beam is extracted because, due to the finite rise time of the kickers, there is no space to accommodate their pulse.

3.3.1 Continuous Transfer (CT)

Until 2015, one of the extraction techniques adopted at the PS to extract the beam over few turns was the Continuous Transfer (CT) technique. The beam from the PS was supposed to completely fill the SPS, but being the SPS circumference eleven-tenth times bigger than that of the PS, a multi-turn extraction was needed. The first theoretical idea was to fill the SPS with eleven continuous extractions from the PS. This approach would have caused unavoidable losses in the SPS since there was no place to accommodate the injector kickers pulse without causing beam losses. Therefore, a ten-turn version became operational. In this way, the rise up of the injector kickers could have been done without any beam loss. In particular, with one extraction from the PS it was possible to fill ten-elevenths of the SPS. This extraction technique aims at lengthening the spill from the PS by continuously "shaving" the circulating beam with the

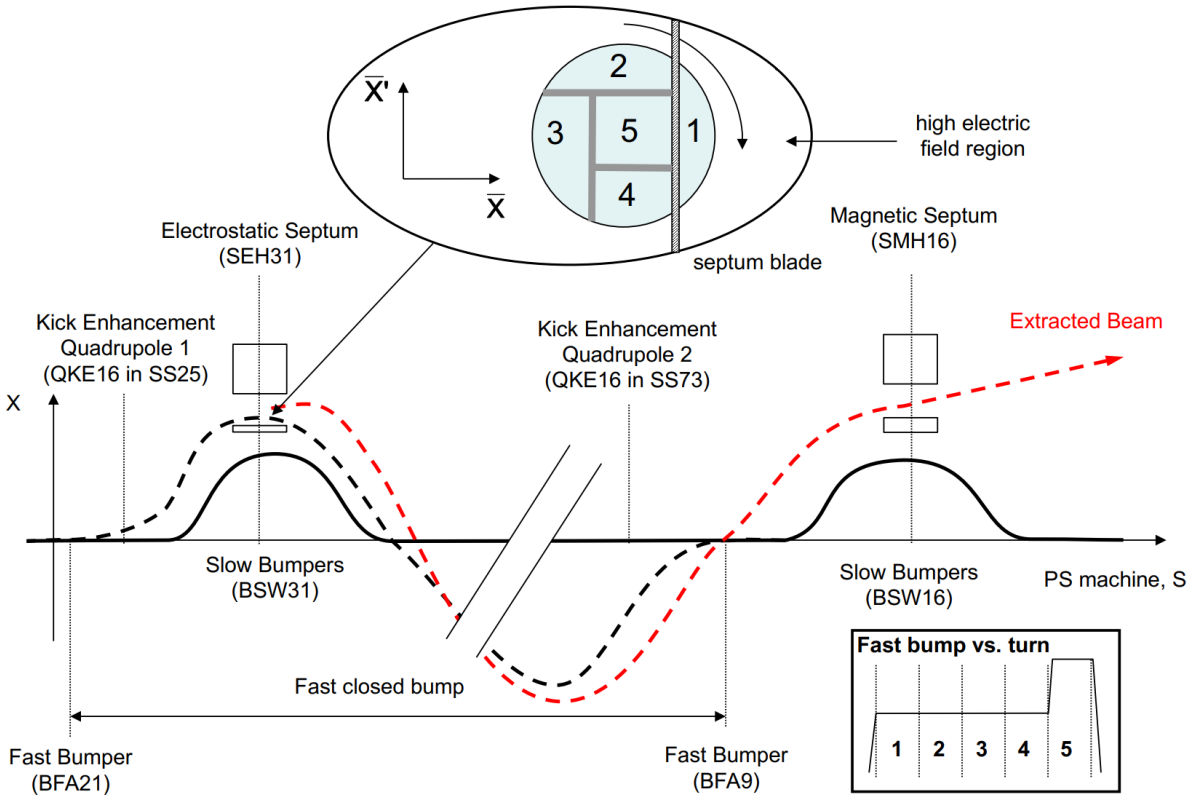

Figure 3.5: Schematic representation of a multiturn beam extraction.

electrostatic septum. The fractional part of the horizontal tune plays a fundamental role since it has to be properly chosen to allow the correct rotation of the beam in phase space. For the particular case shown in Figure 3.5 [31], a horizontal tune of 6.25 was chosen. This value of the horizontal tune allows for a rotation of $\frac{\pi}{2}$ in the horizontal phase space at every turn. Therefore, at every turn, a different part of the circulating beam will be extracted and over five turns the entire beam is extracted.

After the beam has reached the desired extraction energy, its closed orbit is modified to progressively bring the beam closer to the electrostatic septum (located in SS 31 and named SEH31 in Figure 3.5). The orbit perturbation is performed by slow bumpers (located in proper sections) that allow one to obtain the desired bump in SS 31, where the electrostatic septum is located, and 16, where the magnetic one is installed (named SMH16 in Figure 3.5). The continuous black line in Figure 3.5 shows the orbit deformation in correspondence to the electrostatic and magnetic septa.

The beam extraction occurs when the fast[1] kicker magnets are turned on. At first, the kickers located in SS21 (namely BFA21 in Figure 3.5) and the one located in SS09 (namely BFA9 in Figure 3.5), are turned on and their amplitude is kept constant for four turns. At every turn, the

[1]The difference between slow and fast kickers refers to the time needed to rise up to the nominal value and thus to perform the required orbit deformation.

electrostatic septum SEH31 shaves a specific portion of the beam. During the first turn, slice number 1 of the beam receives a deflection from SEH31 (red dashed line), while the remaining part of the beam (from 2 to 5), called circulating beam, keeps rotating in the accelerator. Both the deflected and the circulating beam will continue to oscillate in the PS until the magnetic septum SMH16 is reached. As they circulate in the ring, the deflected beam and the circulating beam will spatially separate. The combination of the electrostatic septum's deflection and the non-zero phase advance between the electrostatic and magnetic septum defines the spatial separation between the circulating beam and the deflected beam at the magnetic septum. Once the deflected beam reaches the magnetic septum SMH16, it will fall into the non-zero magnetic field region and it will be deflected towards the transfer line to the SPS. Therefore, the extraction of the first slice has been achieved. During four turns, the beam slices from 1 to 4 will be extracted and only the central part of the beam, number 5, will remain in the ring. It is necessary to increase the strength of the extraction kickers to allow for the extraction of the central part of the beam. In conclusion, it is worth mentioning that the presence of defocusing quadrupoles (component QKE16 in Figure 3.5) between the fast kickers and the electrostatic and magnetic septa further enhance the effect of the kicker. From here the name "kick enhancement quadrupole".

The need to replace the CT with a new and innovative extraction technique is justified by three main problems.

- The CT extraction is based on the interaction between the electrostatic septum and the particles in the beam. Therefore, there are unavoidable losses that may amount to about 10% – 15% of the total beam intensity.
- As a consequence of the reduction of the beam intensity due to the interaction between particles and septa, the interaction point, thus the electrostatic septum SEH31, becomes a very radioactive area. As a result of the high radiation doses, exceptionally high radiation damage can be detected in the surrounding structures and components. Therefore, long cool-down periods are needed before technical personnel can have access to the area to perform maintenance.
- The extracted slices do not have the typically matched circular (elliptical) form in normalised (physical) phase space. This generates a betatronic mismatch and thus emittance blow-up in the SPS. Furthermore, different slices have different emittance.

The first two issues are not actually solvable within this extraction scheme, since its the interaction between the beam and the electrostatic septum blade that split the beam into beamlets that are then extracted. As far as the last problem is concerned, it is not actually possible to produce beams with equal emittance since the shape of the extracted beam from the PS will always have a non-matched ellipse, as shown in Figure 3.6 left. The only possible option is to equalise the intensity of the five beamlets, as shown in Figure 3.6 right. Moreover, it turns out that the two approaches are not compatible, and trying to equalise the beam intensity leads to very different

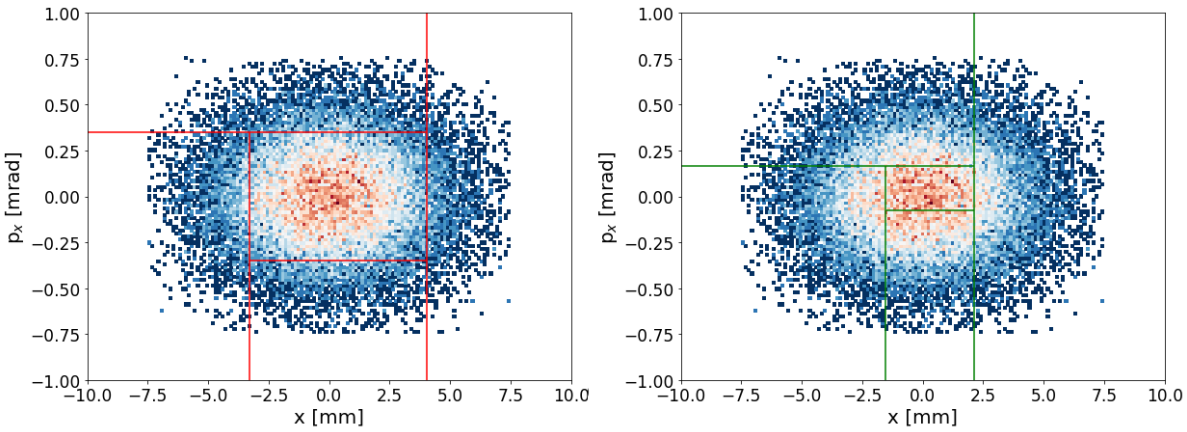

Figure 3.6: Representation in the physical phase space of the five slices when the emittance has been equalised (left, red lines) and when the intensity has been equalised (right, green lines).

beam emittances [20]. This is also shown in Figure 3.6, where emittance equalisation (left) is compared with intensity equalisation (right). It is clearly visible that both approaches provide slices of different forms, the shape of which is very different from that of the conventional lattice ellipse. Therefore, an emittance blow-up is expected at the SPS injection.

3.3.2 Multi-Turn Extraction (MTE)

The MTE has been developed to replace CT extraction and overcome its limitations. The first and most important drawback of the CT was the highly radioactive area around the electrostatic septum SEH31 due to physical interaction between the particles and the septum blade and therefore the reduction of beam intensity. MTE is a beam extraction technique that exploits non-linear fields and a stable resonance to transversely split the beam. Therefore, the shavings and its drawbacks (namely, high beam loss and highly radioactive area) are overcome. The transverse beam splitting is achieved by crossing a specific resonance. In particular, following the description of Section 2.3.1 and considering that the SPS has to be filled with two consecutive extractions from the PS (in order to fill 10/11 of the SPS circumference), the resonance of order four is the one that respects these criteria. In fact, it is a stable resonance thus part of the beam will be trapped in four islands rotating with a periodicity of four PS turns around the central part of the remaining beam, namely the core, that has a periodicity of one PS turn. In order to try to achieve five equally populated beamlets, particles are adiabaticaly trapped in the islands by means of an appropriate tune variation by crossing the fourth-order resonance, generated by sextupolar and octupolar non-linear fields. Although there were already non-linear elements (sextupoles and octupoles) installed in the PS, their position and their design had to be changed in order to find the optimal configuration for the MTE extraction [32]. In particular, both multipoles were necessary, and the pair sextupole-octupole position and strengths were optimised to match the following constraints:

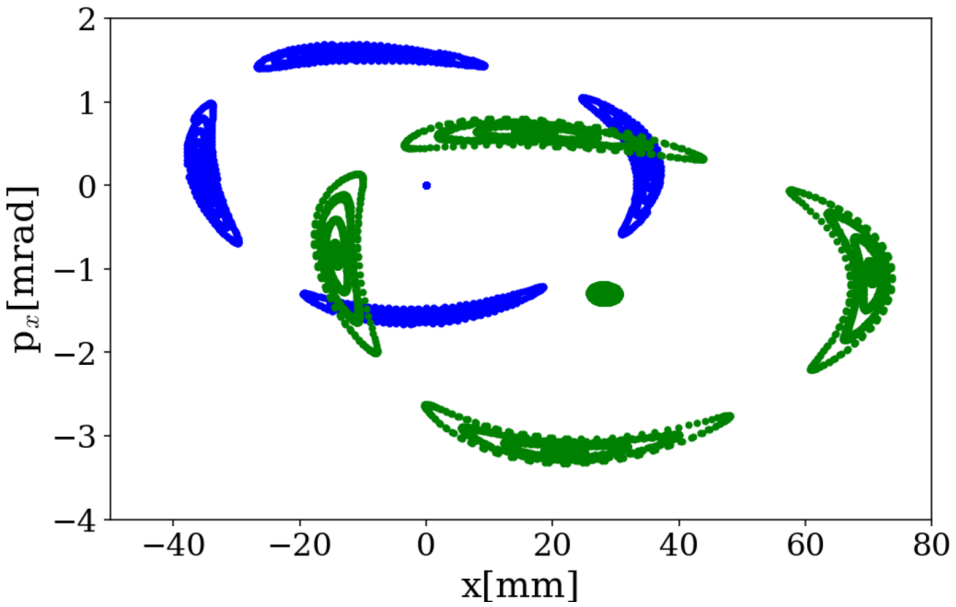

Figure 3.7: Split beam before (blue) and after (green) the rise of the slow bumpers to their nominal value. It is possible to notice that without the effect of the slow bumpers (blue configuration) the beam core is centred at the centre of the phase-space while in green the distribution is reported at the end of the ramp up of the slow bumpers.

- Two pairs are needed for the proper tuning of the extraction parameters;
- The pair has to be located in the same straight section;
- The pair has to be outside the fast and slow extraction bumps;

These conditions were satisfied only if the two pairs were located in Sections 39 and 55, as shown in Figure 3.1.

Once the beam has been split, the core and islands rotate in the PS around the closed orbit located at the centre of the phase space, as reported by the blue points in Figure 3.7. The extraction is achieved in three main steps:

- At first, the beam is brought closer to the extraction magnetic septum SS16 with slow bumpers, as it can be observed in Figure 3.7 where the comparison between the horizontal beam distribution before (blue) and after (green) the bumpers have been switched on can be noticed. As well as on the left-hand side of Figure 3.8 [33], where the longitudinal evolution of the beamlets in the island and in the core can be observed. In contrast with the CT scheme, there is no longer the need to create two slow bumps in correspondence of the electrostatic and magnetic septum. It is sufficient that the beam approaches only the magnetic septum SMH16. Therefore, the same magnets (kickers in SS09 and SS21) that were used in the CT scheme can be used. Their strengths were changed in order to match the requirements of MTE.

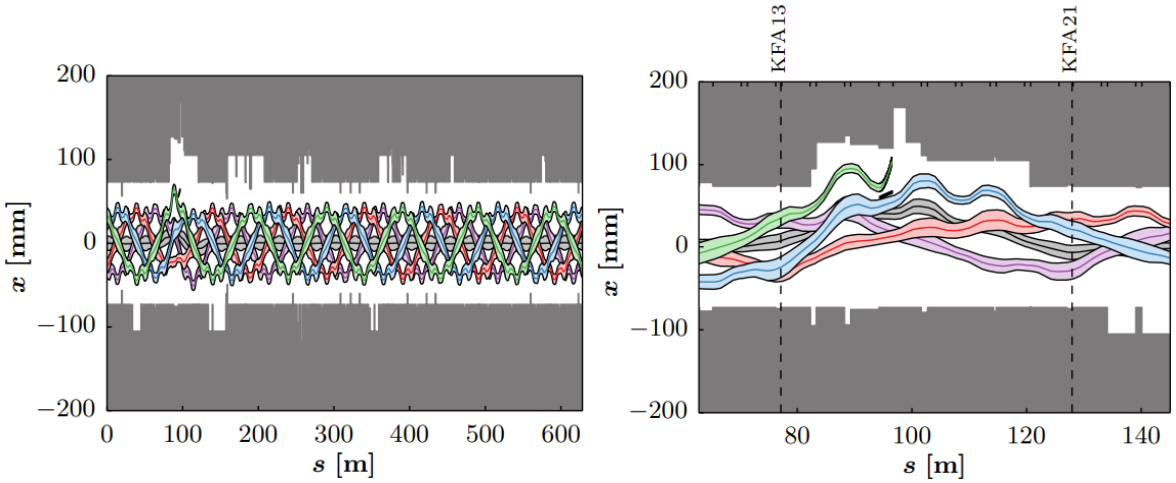

Figure 3.8: Left: horizontal evolution of the islands (green, red, purple, and blue) and core (grey) as a function of the PS longitudinal length after the slow bumpers have reached their nominal value. Right: zoom around the extraction region. It is possible to observe that green-coloured island is on the other side of the magnetic septum thus the extraction process is happening, while the other island and the core oscillate in the ring.

- Then, three pulsed magnets (also called fast kickers) create a fast bump that enables a portion of the beam to be properly deflected and jump beyond the magnetic septum blade, as it can be observe on the right-hand side of Figure 3.8. In particular, in this plot it is possible to observe the extraction of the outermost island, thus the one that is located at larger x values in Figure 3.7. As far as the fast kickers are concerned, two of these three kickers have been installed in SS13 and SS21, while the third one was already installed in the PS, it is located in SS09 and it enables the closure of the bump. The combination of these three elements enables the creation of a closed bump around the magnetic septum. This process lasts for four turn, over which the four islands are extracted one after the other.

- Finally, to extract the core, two additional fast kickers have to be turned on. One of the two kickers was already installed, and it is located in SS71-79 a new one is needed, and it has been located in SS04.

The characteristics of the fast kickers are reported in Table 3.3 [34], these values will be important in the analysis performed in Chapter 4, and it is possible to observe their position in the ring in Figure 3.1. The whole extraction lasts five turns, the first fours are needed to extract the islands, and the last one to extract the core.

[2]Evaluated at 14 GeV/c
[3]From 10% up to 90% of the kick angle
[4]The two variables refer per unit module.

Location	Identifier	Pulse length	Strength	Angle[2] [mrad]	Time[3][ns]
SS 04	KFA04	1 PS turn	26.7mT·m @ 80kV	0.57	86
SS 09	KFA09	5 PS turn	23.3mT·m @ 30kV	0.50	350
SS 13	KFA13	5 PS turns	94mT · m @ 75kV	2.0	350
SS 21	KFA21	5 PS turns	94mT · m @ 75kV	2.0	350
SS 71-79	KFA71-79	1 PS turn	13.9mT · m @ 80kV[4]	0.3[4]	56

Table 3.3: Fast kickers parameters for MTE extraction. For each kicker, the location where it is installed, its identifier and the pulse length are displayed. Additional information on the kicker strength, the kicker angle and the rise-time are given in the last three columns.

The beam is kept longitudinally bunched during the whole manipulation to achieve the beam splitting and the approach to the septum in order to keep under control the radial position. The beam is debunched right after the splitting and just prior the extraction. This choice was based on the experimental observation that a bunched beam led to higher losses in the SPS [35]. During the operational experience achieved during 2010 two main problems were observed [36]:

- There were significant fluctuations in the efficiency of the splitting process, as well as fluctuations in the trajectories along the transfer line;
- there were unacceptable high losses and thus high activation levels in the vicinity of the magnetic septum is SS16.

The unacceptable high losses of the extraction process are cause by the longitudinal structure of the beam. Being it continuous, there is no space where to allocate the rise up of the extraction kickers, leading to unavoidable losses during the beam extraction. A solution that had been considered but that was discarded consisted in changing (thus, reducing) the rising time of the kickers. The main reason for discarding this solution was due to the high implementation costs and the higher complexity level of the system. Therefore, it was decided to install a "dummy" septum that if properly located and oriented could shield the magnetic septum located downstream. In this way, losses could have been well localised at a precise point and a proper shield could have been installed. It was decided to install the dummy septum in SS15 due to its proximity to the magnetic septum. It is a passive component (from here the name "dummy") that consists of a copper blade 800 mm long and 4.4 mm thick. During the rise up of the kickers, particles sweep through the dummy septum, which intercepted them without interfering with the circulating beam. Of course, due to the physical interaction between particles and blade, secondaries as well as scattered particles may be found in the vicinity of the magnetic septum. Although the dummy septum has numerous advantages, one of the main limitations is caused by the reduced aperture available in the extraction region. Thus, after its installation and during the measurement campaigns that aimed at optimising its position and orientation, additional studies have been performed in order to re-design the extraction trajectories of all the users that

were affected by its installation. In principle, it is possible to make the MTE a loss-free extraction technique. In recent years, the idea of having a longitudinal empty structure (called barrier bucket) has been successfully implemented at the PS [37]. It consists of creating a longitudinal empty structure by means of an RF cavity that depletes a well-defined longitudinal portion of the beam. Although its feasibility has been demonstrated, additional studies are needed to synchronise the barrier bucket with the circulating beam in the SPS.

CHAPTER 4

TRANSVERSE EMITTANCE RECONSTRUCTION

Emittance measurement is essential for circular accelerators to know and control its performance. As far as colliders, such as LHC, are concerned, the emittance is strongly related to luminosity and thus with the probability of having head-on collisions. As far as other circular accelerators are concerned, emittance measurement and control is fundamental to ensure the required beam size at the fixed target experiments located downstream to their extraction line. There are a large number of devices that can be used for emittance measurements. Most of the time, the choice in the type of instrument is conditioned by some features of the beam, such as particles, current, and energy. Thus, among the different instruments available to measure the beam transverse emittance, only a subclass of devices will be analysed in this context. In particular, only those techniques that could be used to perform emittance measurements for a proton beam with energy between 14 GeV and 26 GeV and with intensity $\approx 1 \times 10^{13}$ protons will be considered. These beam features are given by the fact that the reconstruction of the beam transverse emittance was performed at the PS ring during beam extraction for the SPS fixed-target experiment. For the first time, the emittance reconstruction was achieved for split beams, thus for beams in a highly non-linear regime, using beam losses data. The results will be presented and discussed in the following sections. First, a brief description of the methods available for emittance measurements will be provided. This section will make clear the advantages of exploiting beam losses for emittance reconstruction. Later on the mathematical description of the model used to derive the beam emittance will be discussed in detail. The description of the results from numerical simulations as well as the analysis of the experimental data will be presented. In conclusion, the sensitivity analysis will show which parameters most affects the reconstruction of the beam transverse emittance.

4.1 Transverse emittance measurements: overview of the different techniques

Even if colliders and standard circular accelerators need emittance measurement for different purposes, the techniques generally adopted for both accelerators are the same. The main difference can be identified when linear or circular accelerator are considered. In fact, in circular machine, the beam passes multiple times at the measurement point, while in LINACs or in transfer lines the beam passes only once. Therefore, the techniques used for the two types of accelerators are different. In most cases, especially for a circular accelerator, the least destructive method is chosen to leave the beam properties almost unchanged turn after turn. For this reason, methods such as scintillation screens and Secondary Electron emission (SEM) grids are less preferred compared to Wire Scanners (WS) and Ionisation Profile Monitors (IPM) [38].

SEM monitors are made up of a grid of wires or ribbons with which the beam interacts. As a consequence of the interaction, secondary electrons, arising from the ionization of the material's atoms that composes the wires (ribbons), are emitted. Therefore, a certain current flows through the wire, and it is possible to reconstruct the local beam intensity knowing that the current is proportional to the number of particles that collide with the wire. Thus, the beam profile is obtained by collecting the beam intensity from each wire. The beam emittance can be reconstructed from the beam profile measurement performed with three properly spaced SEM grids. Among the major advantages of this technology, the simplicity of the device as well as the robust construction is worth highlighting. On the contrary, it is worth noticing that one of the major drawbacks is caused by the limited spatial resolution that is determined by the wire spacing (it is difficult to allow a spacing below 0.25mm [38]) as well as the high costs for the electronics.

WS are another widely used technique to measure beam emission through the measurement of beam profiles. The working principle is similar to SEM but rather than having a fixed grid, WS are composed by a single string that can be mounted either on a rotating system or on a linear one. In the first case, the wire is swept through the beam, in the latter it is pushed (or pulled) inside (outside) [38]. Depending on the place where the rotation (or the linear motion) occurs, the horizontal or vertical emittance is retrieved. In analogy to SEM, the beam profile can be measured from either the current in the wire itself or the flux of secondary particles emitted after the interaction beam-wire. The latter approach is preferred for high-intensity beams, where the energy deposited on the wire during the interaction causes the emission of γ rays that interfere with the secondary emission current. Reconstruction of the beam position is enabled by the presence of radiation detectors in the vicinity of the WS. Detectors are placed on both sides of the vacuum chamber to account for possible beam asymmetry with respect to the centre of the vacuum chamber. Thus, the signal coming from both detectors is analyzed to determine the beam position. Fast WS (which usually have a speed between 10 m/s and 20 m/s) are almost

non-destructive and can provide information on the beam size with a spatial resolution of some micrometers. However, this quantity is affected by the uncertainty related to the knowledge of the position of the wire during the measurement, to possible vibration induced by the mechanical system moving the wire inside the beam and the actual dimension of the wire itself [39].

IPM working principle is the ionization of the residual gas left in the vacuum chamber [40]. Secondary particles, generated by the ionization process, are collected and sent towards a dedicated detector (a Micro Channel Plate - MCP) with an electric field, orthogonal to the beam direction, generated by high voltage electrodes (maximum voltage of 50 kV [41]). The electric field is mandatory to guide the secondary particle towards the MCP on a straight line, in this way the image of the beam is not distorted. The MCP aims to multiply the number of secondary particles, thus amplifying the signal read by the electronics. An MCP with an area of 100×50 mm^2 enables a multiplication of 10^3 in the number of electrons and it has a spatial resolution of 20μm (see [41] for more details). A possible way to improve the performances and thus the accuracy consists in installing an assembly of two MCP detectors [41].

Among the different available technologies used to control beam emittance, it is worth mentioning that additional instrumentation is installed in circular accelerators to control, e.g., beam position or beam losses. Beam losses occur at many different locations around the ring, and the reasons might be quite different: beam-gas interactions, intrabeam scattering, collective effects, equipment failures, transition crossing, and interactions with instrumentation inside the vacuum chamber. Therefore, it is common practice to install Beam Loss Monitors (BLM)[42] around the ring. In fact, BLMs can be used as diagnostic components (to keep track of beam loss intensity); as damage prevention components (when properly integrated with the protection system, they can enable the beam dump to protect the machine and its components from damage) [38]. Generally, BLMs are installed outside the vacuum chamber; therefore, they detect the shower of secondary particles generated by the interaction of the fraction of the beam lost with the vacuum chamber. The outcome is a signal that is proportional to the number of detected particles and thus to the loss of particles. The ratio between the signal and the number of lost particles defines the detector efficiency and is determined with particle-matter simulation codes (for example, FLUKA [43]). Among the different types of BLMs, only two will be analysed since these have been installed in the PS ring: the ionization chambers (IC) and the diamond detectors [44].

IC [42] consists of two parallel metallic electrodes connected to a high voltage source (usually in the range of several kV). The gap between the electrodes is filled with a noble gas, such as Xenon, Argon, Neon, or simply air. The cascade of secondary particles ionises the gas in the IC when they cross it, producing electron-ion pairs. Thus, electrons are deviated towards the anode, provided that the electric field is larger than the Coulomb field close to the ion, otherwise recombination between electron and ion occurs; while ions are deviated towards the cathode. Details on optimisation of IC performances, such as length and voltage, can be found in [42].

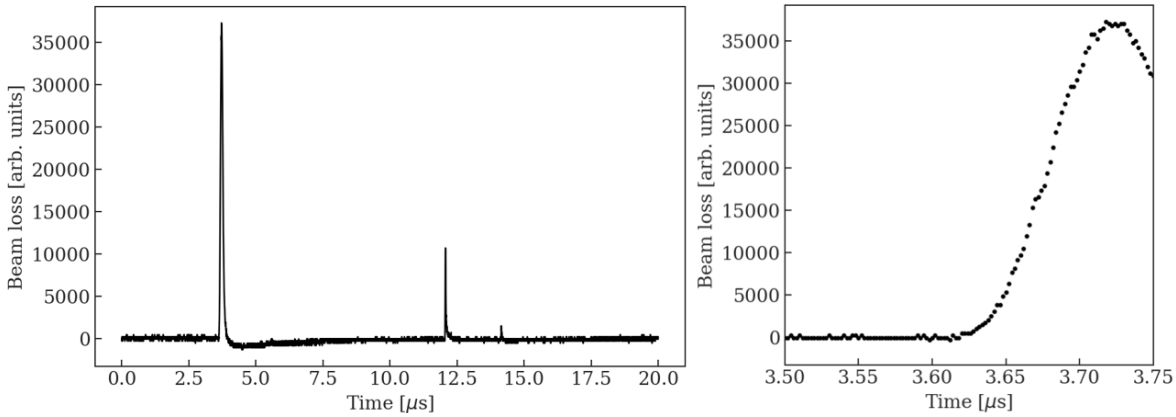

Figure 4.1: An example of the signal recorded from the diamond detector is reported. The amplitude of the signal is in arbitrary units while the time is in μs. On the right hand side a zoom of the highest peak is reported, highlighting the capability of the instrument to have a time resolution of nano-seconds.

Diamond detectors are widely used in the field of High Energy Physics (HEP) instrumentation because they can generate a faster signal in response to the passage of a particle than silicon detectors [45]. Diamond detectors can use two different types of synthetic diamonds: the single crystal Chemical Vapour Deposition (scCVD or sCVD) and the poly-crystalline CVD (pCVD or pcCVD) [45]. The latter has been installed at the PS [46]. An electron-hole (e-h) pair is generated by the energy deposited by a charged particle (that is, the avalanche of secondary particles) when it passes through the material. Due to a biased voltage, the pairs drift towards the electrodes installed near the material, inducing a current. This current is then amplified and, if necessary, analysed due to downstream electronics; a detailed description of the front-end electronics and its optimisation can be found in [45]. One of the most attractive features of diamond detectors is their precise time resolution; for this reason, they are also called "fast timing detectors" [45]. Particle counting for particle physics experiments is among the different applications where precise time resolution is needed. An example of the signal detected by the diamond detector installed in the PS ring can be observed in Figure 4.1.

4.2 Mathematical model

As described in Section 3.3.2, during the MTE scheme beam losses occur when the extraction kickers are turned on. At first, the islands are extracted and, when the outermost island sweeps through the dummy septum, a fraction of the beam is lost because of its continuous debunched structure. Then, the core is extracted and, also in this case, a fraction of the beam is lost when it crosses the dummy septum. Two diamond detectors have been installed in the extraction region of the PS ring to record losses during beam extraction. In particular, these devices have been installed on the main magnetic unit downstream the straight section 15 (SS15) and 16 (SS16) where the dummy septum and the magnetic septum, respectively, are installed. The choice of the type of the detector has been driven by their precise time resolution. In fact, they ensure a sub-turn[1] sampling rate, being able to detect particles loss with a sampling rate of $\approx$ 2ns. The expected signal has the shape reported in Figure 4.1, where the first peak refers to the first extracted structure (the islands) and the second peak refers to the other structure (the core). The difference in height is due to the different speeds with which islands and the core are extracted. From the knowledge of beam losses during extraction it is possible to reconstruct the transverse beam emittance for split beams. This idea was described for the first time by Huschauer et al. in Ref. [47]. The horizontal beam distribution can be considered a Gaussian distribution

$$\rho(\hat{x},t) = \frac{N_p}{\sqrt{2\pi}\,\sigma_x}\exp\Big[-\frac{1}{2}\frac{(\hat{x}-\mu_x(t))^2}{\sigma_x^2}\Big], \tag{4.1}$$

where N_p is the number of particles that make up the distribution (namely the beam intensity), σ_x is the width of the distribution (the beam size) and $\mu_x(t)$ is the instantaneous displacement induced by the kickers during their rise to the nominal value. During this time interval, the beam displacement is described as

$$\mu_x(t) = \frac{A}{2}\sin\Big[2\Big(t-\frac{\pi}{4}\zeta\Big)\frac{1}{\zeta}+1\Big]; \quad 0 \le t \le \frac{\pi}{2}\zeta, \tag{4.2}$$

where A is the maximum horizontal displacement of the beam at the location where losses are detected and ζ is a kicker parameter. That is defined as:

$$\zeta = \frac{\tau_\alpha}{\arcsin\Big(2\alpha-1\Big)}, \tag{4.3}$$

where τ_α, with α equal to 90%, is the time it takes for the kicker to rise from the 10% to the 90% of the nominal kick angle (the numerical values are summarised in Table 3.3). The time evolution of the kick angles for the kickers used in the MTE scheme is shown in Figure 4.2. In order to be able to compute the instantaneous position $\mu_x(t)$, the maximum horizontal displacement A has to be evaluated. A complete and detailed description of the PS lattice was implemented during previous years in MAD-X [24], therefore, it is possible to study the evolution of the islands'

[1] The time needed to complete one revolution in the PS is $\approx 2.1\mu$s

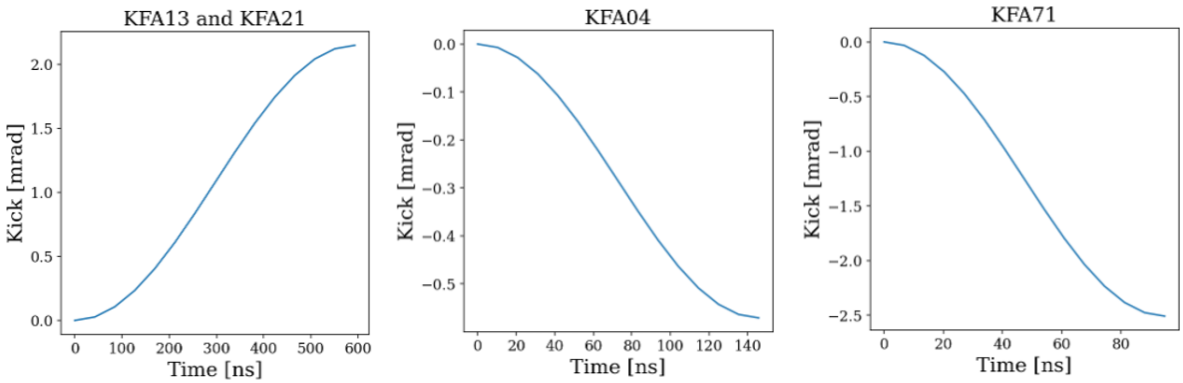

Figure 4.2: Kick angle as a function of time for the extraction kickers used for the MTE scheme. From left to right: the kickers KFA13 and KFA21, used to extract the islands, have the same parameters; therefore, their rise curve is the same. The other two kickers (KFA04 and KFA71) are used to extract the core.

and core's stable fixed point evolution during the kickers' rise up performing a Twiss analysis. The Twiss module in MAD-X enables the computation of linear lattice functions such as tune, positions, divergences, Twiss parameters, etc., providing to the module the lattice sequence of the accelerator, initial conditions, etc. For this specific case, the evolution of the SFP is evaluated, providing position and divergence as initial conditions. In particular, to evaluate their evolution during the rise time of the kickers a step-by-step procedure has been implemented. The rise of the kickers, reported in Figure 4.2, is divided into $N = 15$ steps[2] and at each step a specific value of the kick is set, thus determining the position and divergence of the SFPs. The result of this analysis, thus the time evolution of the SFP of the core and island is shown in Figure 4.3. It is important to note that the time evolution of the SFP has been determined simulating the physics of the phenomenon. Therefore, the extraction kickers responsible for the island extraction have been first turned on and increased up to their nominal value (namely, the kicker in SS13, KFA13, and the kicker in SS21, KFA21). At the first step, the initial condition is set to be equal to the SFP position when the kickers are turned off. Further steps consider as the initial condition the position and divergence of the SFP computed at the previous step. During this time also the core is moved towards the dummy septum (TPS15) and its position has been recorded. After ≈ 600 ns, thus at the end of the time needed for the kickers responsible for the island extraction to rise up to the nominal value, the position of the core SFP is ≈ 61mm (as can be observed from Figure 4.3 left). From 4.3 left it is also possible to notice that the core has not been extracted yet, being its horizontal location smaller compared to dummy septum one (represented as the continuous black line in Figure 4.3). Therefore, the kickers responsible for the core extraction have to be turned on. The strength of KFA04 and KFA71-79 had to be properly tuned to allow for

[2]The number of steps had been chosen so that an average difference of 0.4 mm was obtained between two subsequent steps. More refined data were not needed because the aim was the determination of the position excursion between final and initial steps.

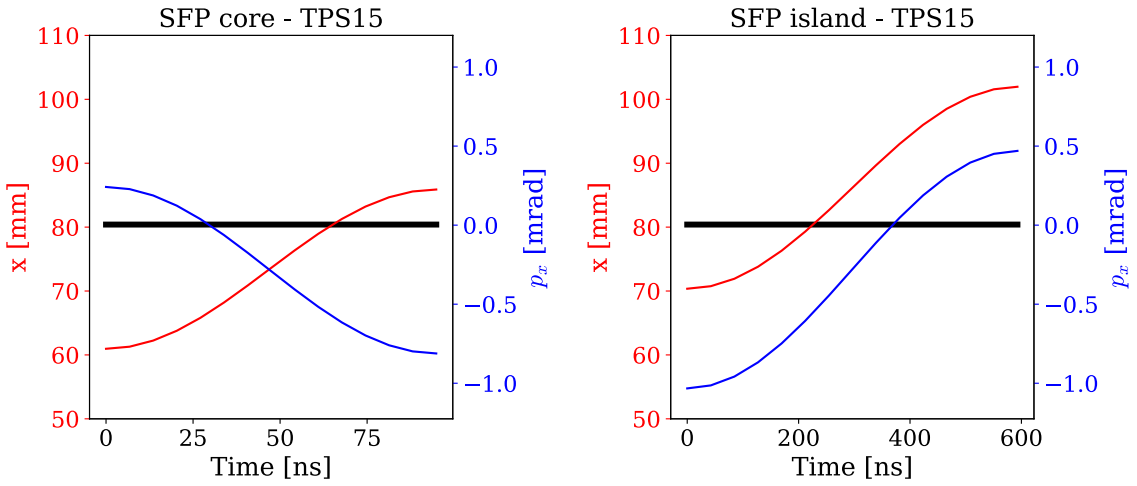

Figure 4.3: SFP time evolution of the islands (right) and core (left) in terms of position and divergence. The black line represents the horizontal position of the dummy septum.

the core extraction. Based on machine operations, all modules of KFA71-79 have been used and raised to their nominal value, while the kicker KFA04 only reached 70% of its nominal power. The time evolution of the stable fixed points is reported in Figure 4.3, where in black the horizontal position of the dummy septum is reported. The difference between the final and initial value of the SFP position gives the maximum horizontal displacement: for the core $A = 24.95$ mm, while for the islands $A = 31.61$ mm. In Figure 4.3 it is also possible to notice that during the rise-up of the kickers, both structures (islands and core) cross the horizontal position of the dummy septum, highlighting the moment when losses occur. Beam losses occur over five revolution turns, meaning the five turns over which the four islands, first, and core, later, are extracted. It is possible to determine the time profile of the losses assuming that any proton hitting the dummy septum blade is lost. Therefore, the losses detected by the BLM during the extraction process can be quantified as at the number of proton lost $\ell(t)$ per unit turn in the PS and as the number of proton per beamlets interacting with the septum blade per unit of its thickness (defined as $\Delta_s = \Delta x_s^+ - \Delta x_s^-$) during the rise up of the extraction kickers t_{int}. Thus the equality between these two terms can be written as:

$$\int \ell(t) d\tau_{\text{rev}} = \int_0^{t_{\text{int}}} dt \int_{\Delta x_s^-}^{\Delta x_s^+} d\hat{x_s} \eta \rho(\hat{x_s}, t), \tag{4.4}$$

where the parameter η is the efficiency of the MTE splitting process (sometimes also abbreviated as MTE efficiency). In perfect conditions its value should be 0.2 showing a perfect splitting process (equal division of the initial beam intensity among the five beamlets). In practise, a prefect splitting can not be obtained. For this reason, it is necessary to define a value of efficiency for the core and one for the islands. In the latter case, it is defined as the ratio between the average number of particles in the islands divided by the total beam intensity:

$$\eta_{\text{isl}} = \frac{< N_{\text{isl}} >}{N_p}, \tag{4.5}$$

while the MTE effiency for the core simply reads as $\eta_{\text{core}} = 1 - 4\eta_{\text{isl}}$. The nominal value of the MTE efficiency is 0.2, which means that the number of particles in one of the islands is the same as those in the core. It is possible to retrieve from Eq. 4.4 the mathematical expression defining the expected losses at the BLM as:

$$\ell(t) = \frac{t_{\text{int}}}{\tau_{\text{rev}}} \int_{\Delta x_s^-}^{\Delta x_s^+} \eta \rho(\hat{x_s}, t) d\hat{x_s}. \tag{4.6}$$

From the substitution on Eq. 4.1 into Eq. 4.6 it is possible to obtain:

$$\ell(t) = \frac{t_{\text{int}}}{\tau_{\text{rev}}} \frac{\eta N_p}{\sqrt{2\pi}\sigma_x} \int_{\Delta x_s^-}^{\Delta x_s^+} \exp\Big[-\frac{1}{2} \frac{(\hat{x_s} - \mu_x(t))^2}{\sigma_x^2} \Big] d\hat{x_s}. \tag{4.7}$$

The particle distribution was defined with respect to the centre of the dummy septum thickness. However, it is useful to refer it to the centre of the vacuum chamber, namely, the reference system co-moving with the reference particle, with respect to which any other particle is defined. Therefore, it is necessary to re-define the septum position x_s in the reference system of the reference particle. Variables with the hat refers to the reference system centred on the dummy septum while variables without the hat refers to the co-moving reference system. In this latter reference system the dummy septum position can be defined as:

$$\hat{x}_s = x_s - x_b - x_{co}, \tag{4.8}$$

where, x_s is the dummy septum position with respect to the zero closed orbit, x_b is the amplitude of the slow bumps and x_{co} is the value of the closed orbit. The latter two parameters are different between core and islands. To compute the interaction time between each beamlet and the septum, it is important to consider that losses only occur when the outermost edge of the distribution (usually set at 3σ) intercepts the inner blade of the septum. Therefore, the interaction time t_{int} can be evaluated as:

$$t_{\text{int}} = t_{\text{end}} - t_{\text{start}} = \mu_x^{-1}\big(x_s - x_b - x_{co} + 3\sigma\big) - \mu_x^{-1}\big(x_s - x_b - x_{co} - 3\sigma\big) \,, \tag{4.9}$$

where μ_x^{-1} is the inverse function of Eq. 4.2. All these quantities depend on whether the core or the islands are considered. From the substitution of Eq. 4.8 and Eq.4.9 into Eq. 4.7 and considering that the integration is always performed on the dummy septum thickness, the expected beam losses read as:

$$\ell(t) = \frac{t_{\text{int}}}{\tau_{\text{rev}}} \frac{\eta N_p}{\sqrt{2\pi}\sigma_x} \int_{x_s - \Delta_s/2}^{x_s + \Delta_s/2} \exp\Big[-\frac{1}{2} \frac{(x - x_b - x_{co} - \mu_x(t))^2}{\sigma_x^2} \Big] dx \tag{4.10}$$

The time evolution of the losses in Eq.4.10 can be simplified performing two approximations. The integral over the septum width can be replaced by the function evaluated in the centre of the integrating interval. The second approximation consists of replacing the sinusoidal function in the equation describing the rise of the kickers (see Eq. 4.2) with its argument. This approximation is

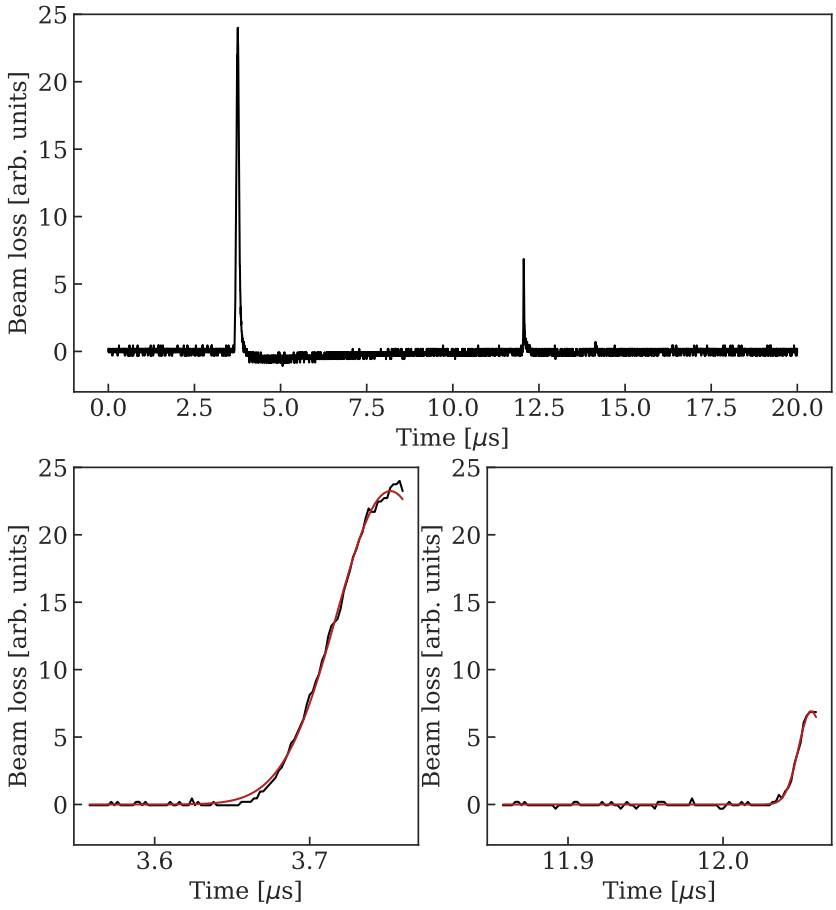

Figure 4.4: BLM signal acquired during the experimental campaign carried out in November 2017. On the top it is possible to observe the signal recorded by the BLM in SS15, above the dummy septum. At the bottom of the figure, a zoom of the two peaks is reported together with the Gaussian fit performed on the data, which is shown as the red curve.

based on the observation that losses actually occur during the linear part of the kicker's strength ramp (see Figure 4.2), thus when the outermost particles in the island, located at 3σ, collide with the septum and losses are over when the innermost particles in the islands, located at -3σ are on the other side of the dummy septum. Under these considerations, Eq. 4.10 reads as follows:

$$\ell(t) \approx \frac{t_{\text{int}}\Delta_s}{\tau_{\text{rev}}} \frac{\eta N_p}{\sqrt{2\pi}\,\sigma_x} \exp\Big[-\frac{1}{2}\frac{A^2 t^2}{\zeta^2 \sigma_x^2}\Big]. \tag{4.11}$$

In conclusion, from Eq. 4.11 it is possible to observe that measured losses have a Gaussian time profile that is a function of the beamlet spatial width σ_x, of the extraction kicker features ζ and of the orbit bumps provided by the slow bumpers prior to extraction A. It is useful to express Eq. 4.11 as a function of the time t^* at which the maximum losses, namely the peak, occur. The analytical expression for t^* can be determine by computing the derivative of the expected BLM losses from Eq. 4.10 using the approximation described above and performing a time shift

according to $\hat{t} = t - t^*$. In these conditions, the time at which the peak of the losses occur is defined as: $t^* = (x_s - A\pi/4)\zeta/A$ and the corresponding value of the losses is:

$$\ell_{\text{peak}} = \ell(\hat{t} = 0) = \frac{t_{\text{int}}\Delta_s}{\tau_{\text{rev}}} \frac{\eta N_p}{\sqrt{2\pi}\sigma_x}, \tag{4.12}$$

being A, σ_x, and η different for core and islands, different values of the peak are obtained for the two beam structures. Following a similar approach it is possible to determine the integrated value of the losses over the interaction period between beam and blade performing the integral in time of the losses described in Eq. 4.11 as:

$$\ell_{\text{tot}}(t) = \frac{t_{\text{int}}\Delta_s}{\tau_{\text{rev}}} \frac{\eta N_p}{\sqrt{2\pi}\sigma_x} \int_{-t^*}^{-t^* + \frac{\pi}{2}\zeta} \exp\Big[-\frac{1}{2}\frac{A^2\hat{t}^2}{\zeta^2\sigma_x^2}\Big] d\hat{t}, \tag{4.13}$$

where the lower and upper bound of the time integral are determined by performing the time shift $\hat{t} = t - t^*$ in the kickers time evolution reported in Eq. 4.2. Both the peak (Eq. 4.12) and the integrated losses (Eq. 4.13) are linearly dependent on the total number of particles in the beam before splitting N_p and on the MTE efficiency η, defined in Eq. 4.5. The peak and the cumulative time losses are also inversely proportional to the beam width σ_x. The mathematical relation among these quantities will be analysed in the following section.

4.3 Numerical simulations

From the previous section, the beam losses at the BLM are expected to be Gaussian. Moreover, from Figure 4.4, it is possible to observe that the measured losses at the BLM actually have a Gaussian profile, thus a fit of experimental data with a Gaussian curve seems to be feasible. Before moving to the analysis of the experimental data, it is important to check the dependence of the peak and total losses for the core and the island as a function of the beam intensity. From Figure 4.5 it is possible to observe that the peak of the measured losses at the BLM for both the core and the islands show a linear trend as a function of the total beam intensity. A similar observation can be performed also for the integrated value of the losses. This behaviour was expected since a linear dependence on the intensity N_p can be noted in Eq. 4.12 and Eq. 4.13. As explained before, the numerical value of the peak value is different among the two beam structures because of the different speeds with which they are extracted from the PS ring.

The reconstruction of the transverse emittance comes from the knowledge of the spatial width of the beam σ_x. The rationale of the fit procedure, consists in fitting the experimental BLM data with a Gaussian function:

$$f(a, \bar{t}, \sigma_t) = \frac{a}{\sqrt{2\pi}\sigma_t} \exp\Big(-\frac{1}{2}\frac{(t-\bar{t})^2}{\sigma_t^2}\Big), \tag{4.14}$$

where the amplitude a, the mean value $\bar{t}$ and the time width σ_t are the fitting parameters. Around 1000 experimental data have been collected during the measurement campaign carried

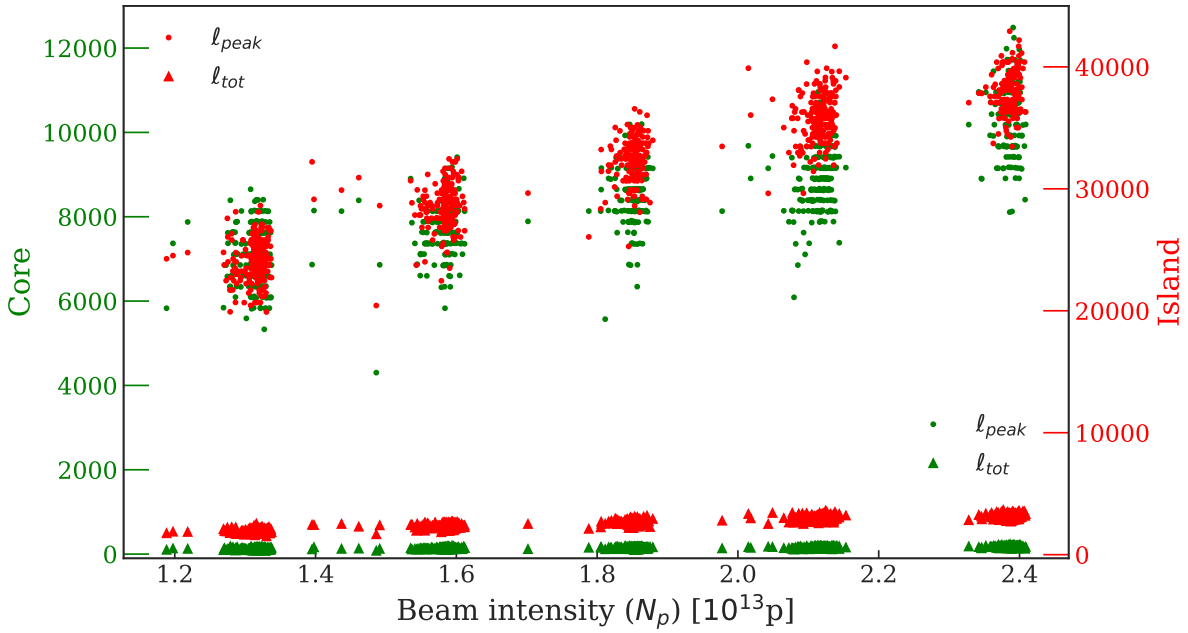

Figure 4.5: In green it is possible to observe the peak (dot) and the cumulated (triangle) losses recorded by the BLM. The same variables are reported in red for the core. Both quantities for the two beam structures are reported as a function of the total beam intensity.

out in November 2017. An example of the signal recorded during this campaign is shown in Figure 4.4. From the comparison between the fit function in Eq. 4.14 and the time dependent equation describing the losses in Eq. 4.11, it is possible to obtain an analytical relation between the time width σ_t and the space width σ_x of the beam:

$$\sigma_x = \frac{A}{\zeta}\sigma_t \,, \tag{4.15}$$

where ζ is defined as in Eq. 4.3. Furthermore, from the comparison of the two equations an additional scaling parameter to a has to be added to Eq.4.14 to make it equal to Eq.4.11:

$$b = \frac{A\tau_{\text{rev}}}{\zeta\Delta_s t_{\text{int}}}.$$

As explained in the previous section, the amplitude A, that the kickers have to provide to the core and to the island to enable their extraction, have been determined with the Twiss analysis, while the kickers parameters are input values, these variables are summarized in Table 4.1. Before performing the analysis of the experimental data, it is important to perform some remarks. The signal that is recorded by the BLM is not symmetric with respect to the peak because of an artefact introduced by the electronic systems. For this reason, only the raising part of the curve of the losses is fitted to a Gaussian function (as shown in Figure 4.4). Even though two BLM system have been installed in the PS ring [33, 47] only the experimental data of the BLM installed in

	A [mm]	τ_α **[ns]**	α **[-]**
Core	24.95	56	0.9
Island	31.61	350	0.9

Table 4.1: Key parameters to compute σ_x from σ_t.

SS15 (above the dummy septum) will be considered in the following analysis. In fact, it is not possible to exclude that the magnetic field of the extraction septa (in SS16) does not affect the time evolution of the secondaries therefore inducing a perturbation in the signal detected by the BLM.

4.4 Experimental data analysis

During the experimental campaign carried out in November 2017 around 1000 measurements were performed. The measurement consisted in extracting the beam with the MTE scheme and collecting the losses detected by the BLM. At the same time, also the MTE efficiency data, defined as in Eq. 4.5, have been collected. The rationale used to compute the beam transverse emittance has been described for the first time in Ref. [47] and in the following section it will be adopted to determine the core emittance. The determination of the island emittance requires more attention since the beam dynamics around its SFP is highly non-linear. Similarities and difference for the emittance calculation of the two beam structures will be described and highlighted in the next sections. The first step consists in removing the base line of the signal so that the noise value is set to zero, the resulting signal is as the one reported on the top of Figure 4.4. Then, the determination of the island and core time width σ_t is performed from the fit of the two peaks of the BLM data with a Gaussian curve, defined as in previous section and shown on the bottom of Figure 4.4. This procedure is performed for all the measurement performed in 2017, among these only 2 dataset were discarded because they detected only noise.

The results of this analysis are reported in the top of Figure 4.6. It is possible to observe in Figure 4.6 top left, that the value of time width σ_t for the core is almost four time smaller than the one of the island in Figure 4.6 top right. As proven in the previous section, there is a linear relation between the time width σ_t of the signal and the spatial width σ_x of the beam causing the losses, reported in Eq. 4.15. The beam width values are reported in Figure 4.6 bottom, the results of the core are shown on the left while those of the island are shown on the right. The factor four difference between core and island has disappeared, as expected. In fact, no significant difference in the spatial width σ_x is expected between core and islands being the splitting efficiency almost equal to the nominal value (0.2). The measured values of MTE efficiency are shown in Figure 4.7, where the values relative to the islands are shown with red dots, while those computed for the core are shown in green. The average efficiency of islands is larger than the nominal value of 0.2, as it can be observed in Figure 4.7, meaning that on average, islands have more particles than

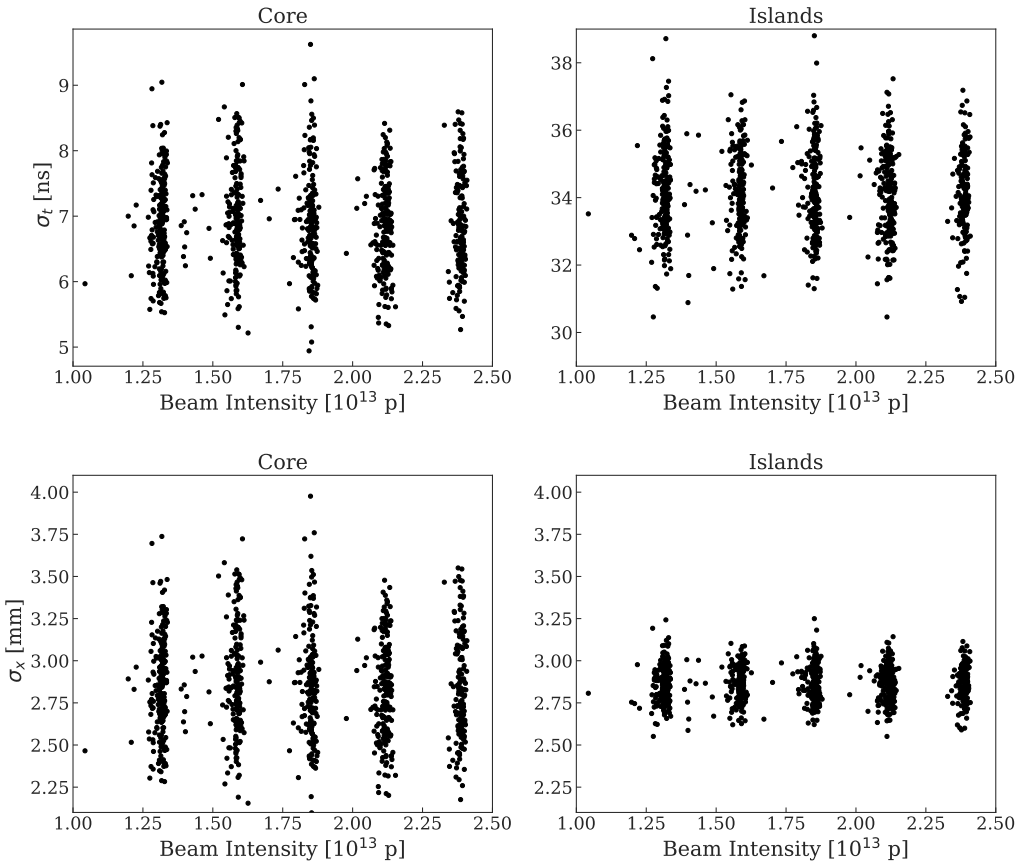

Figure 4.6: From the Gaussian fit procedure the value of σ_t is reported for the core (left) and for the islands (right) on the top part of the figure; while the computed value of beam width σ_x is shown on the bottom part.

those left in the core. As a consequence, this leads to a larger spread in the MTE efficiency values for the core and to an average value lower than the nominal one. It is now possible to determine the emittance of the beamlets (core and islands). It is important to note that the two structures have a completely different dynamics. The core is completely linear while the islands have a non-linear dynamics. Therefore the emittance calculation has been performed in two different ways. At first the core emittance calculation will be described and after the one relative to the islands.

4.4.1 Core emittance reconstruction

The emittance of the core can be computed knowing that for a beam in a linear beam dynamics regime the emittance is

$$\epsilon_{\mathrm{ph}} = \frac{\sigma_{\mathrm{x}}^2 - D_{\mathrm{x}}\sigma_{\mathrm{p}}^2}{\beta_{\mathrm{x}}}, \tag{4.16}$$

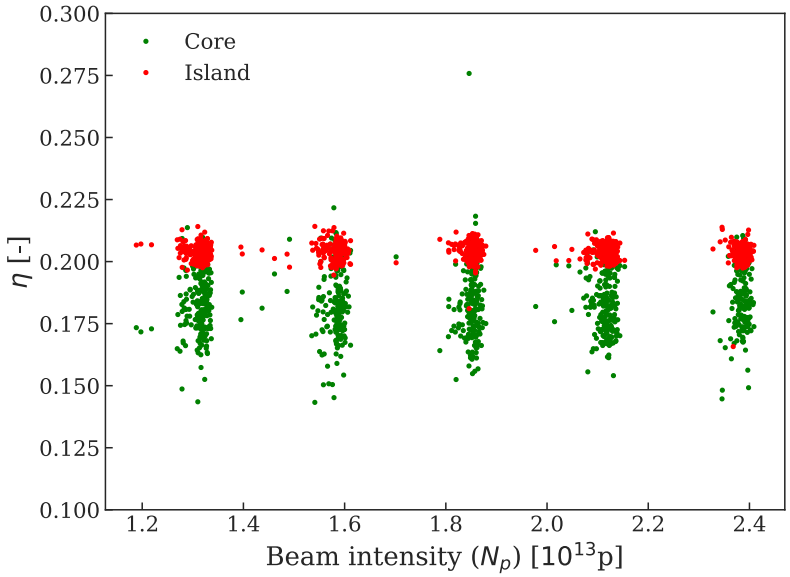

Figure 4.7: Measured MTE efficiency for the island in red and computed value for the core in green.

in accordance with the discussion performed in Section 2.2.1. The beam spatial width σ_x comes from the analysis of the experimental measurements, which results have been summarised in the lower part of Figure 4.6 left. The beta function β_{x} and the dispersion function D_{x} are characteristic values of the PS ring that have been determined with a Twiss analysis and their numerical values respectively reads as 20.460 m for the beta function and 2.293 m for the dispersion. The value of σ_{p} was retrieved from an internal report written during the experimental campaign, and its values is 0.5×10^{-3}. The physical emittance of the core can be computed applying Eq. 4.16 to the experimental data reported in Figure 4.6 (bottom left). Thus, the calculation of the core normalised emittance is performed multiplying the physical emittance times the relativistic Lorentz factors (β_{rel} and γ_{rel}), in accordance with the description in Section 2.2.1. The results of the analysis are shown in Figure 4.8 where the physical emittance is reported on the left and the normalised emittance on the right. Although the results obtained are in accordance with the expected values, it is important to notice that a quite large spread ($\approx 8\mu$m) in the values of emittance can be observed. The clear reasons of this behaviour are still under investigation, it is fundamental to highlight that this is the first case that this feature was observed; therefore, additional and detailed studies are necessary.

4.4.2 Islands emittance reconstruction

The reconstruction of the transverse emittance of the particles in the islands should be treated with care. In fact, even though the Twiss parameters are known for particles within the islands,

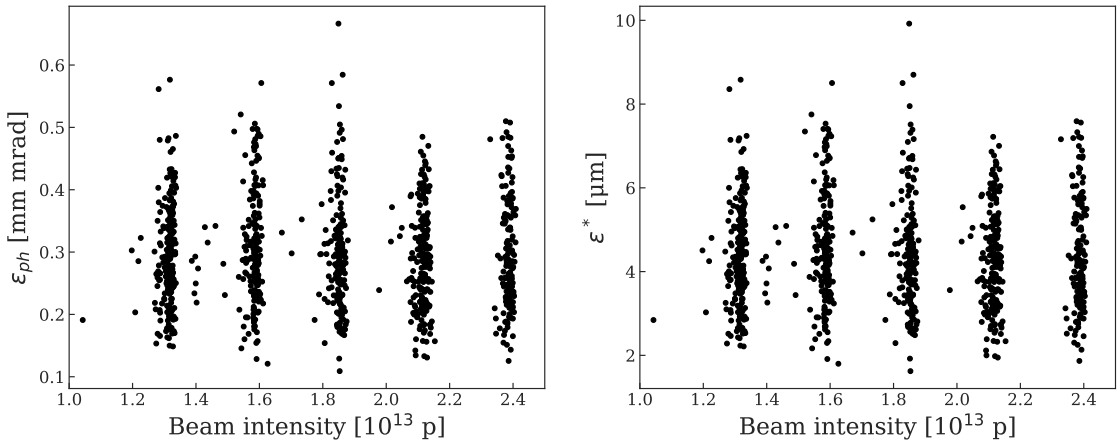

Figure 4.8: Physical (left) and normalised (right) core emittance. Each point refers to a different data set collected on November 2017, approximately 998 data are reported.

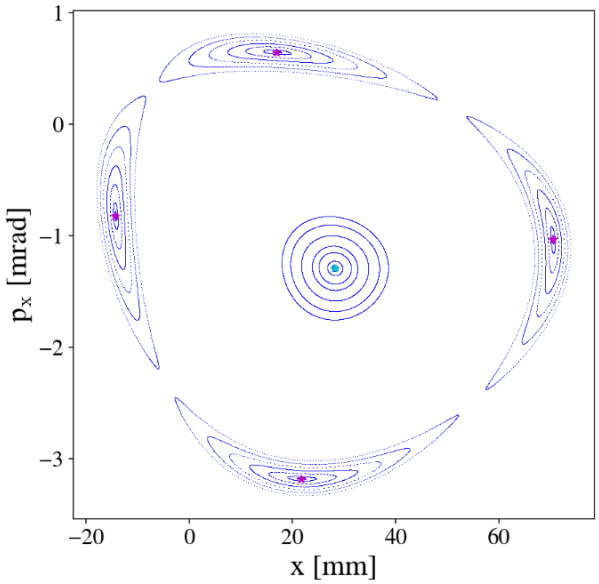

Figure 4.9: Core and islands phase space. The cyan and magenta dots represents the SFP of the core and islands respectively.

it is not possible to use Eq. 4.16 because it assumes linear dynamics of the particles. In Figure 4.9 it is possible to notice that the particles in the core have a circular orbit, highlighting the linear nature of the motion of the particles left in the core after the splitting process. Particles trapped in the islands have deformed orbits. In particular, those close to the island SFP (shown as a magenta dot in Figure 4.9) have an ellipse-like orbit while those rotating with a larger amplitude around the SFP have an elongated and curved ellipse. This feature shows that the beam dynamics around the island SFP is highly non-linear, thus, it is necessary to identify a way to compute the emittance of the islands. Following the description performed in Section

2.2.1, it is possible to identify two invariants of motion: the Courant-Snyder invariant and the action. The latest one will be used to compute the island emittance in order to compute the emittance of the island independently from the beam width σ_x measured by the BLM. In fact, the Courant-Snyder invariant allows the calculation of the emittance from the knowledge of the Twiss parameters at the SFP location and by properly averaging particle position and divergence, while the action is based on the average of the orbit area of every particle within the island itself. The calculation of the emittance as the average of the action enables to set one simulation for any beam width retrieved from the BLM measurements; while the use of the Courant-Snyder approach would need to prepare a simulation for every beam width. The island emittance has been computed performing the tracking of 2500 initial conditions linearly spaced between the location of the SFP of the island and the maximum dimension of the island itself, that is, the separatrix. Each condition has been tracked for 2048 turns, and for each turn, the position x and the momentum p_x have been recorded. An example of the turn-by-turn evolution of two initial conditions is shown in Figure 4.10. This is equivalent of considering two particles trapped in the island having x and p_x coordinates equal to those of the considered initial conditions, thus, Figure 4.10 shows the turn-by-turn evolution of their orbit. It is worth highlighting that the shape of the two orbits qualitatively describes the distance from the SFP at which they oscillate. In fact, since the particle orbit reported on the first line of Figure 4.10 is a rotated ellipse, it is clear that it is the closest to the SFP, while the other one has a deformed orbit, thus it rotates at a larger amplitude, further from the SFP. The orbit is not made up of an ordered sequence of points (as can be observed in the first column of Figure 4.10). In fact, as described in Section 2.2 and reported in Figure 2.5, a non-zero fractional part of the tune leads to a non-overlapping condition after $\lfloor Q \rfloor$ turns (see Eq. 2.18). Therefore, it is fundamental to order the particle's coordinate for increasing (or decreasing) momenta p_x before computing the area enclosed by the coordinate evolution, namely the particle orbit. The comparison between the particle orbit with ordered coordinates and without ordered coordinates can be observed at the centre of Figure 4.10. The area of the particle orbit is computed by implementing the triangulation procedure in Python. On the right-hand side of Figure 4.10 it is possible to observe that the triangulation procedure covers the area enclosed by the particle motion. The action calculation is straightforward if the area of the orbit is known, in fact, as defined in Eq. 2.35, it is necessary to divide it by 2π. Therefore, for every particle in the island the area enclosed by their orbit is computed and the calculation of the action comes from the division of the area by 2π. Thus, it is possible to evaluate the evolution of the action as a function of the distance of every particle from the SFP, being the initial conditions uniformly spaced from the SFP to the separatrix of the island. This result is shown in Figure 4.11. In a linear system, thus without the effect of non-linear magnetic components, the single-particle action is related to the transverse particle position according to [8, 22]:

$$J_x = \frac{(x - x_{SFP})^2}{2\beta_x}. \tag{4.17}$$

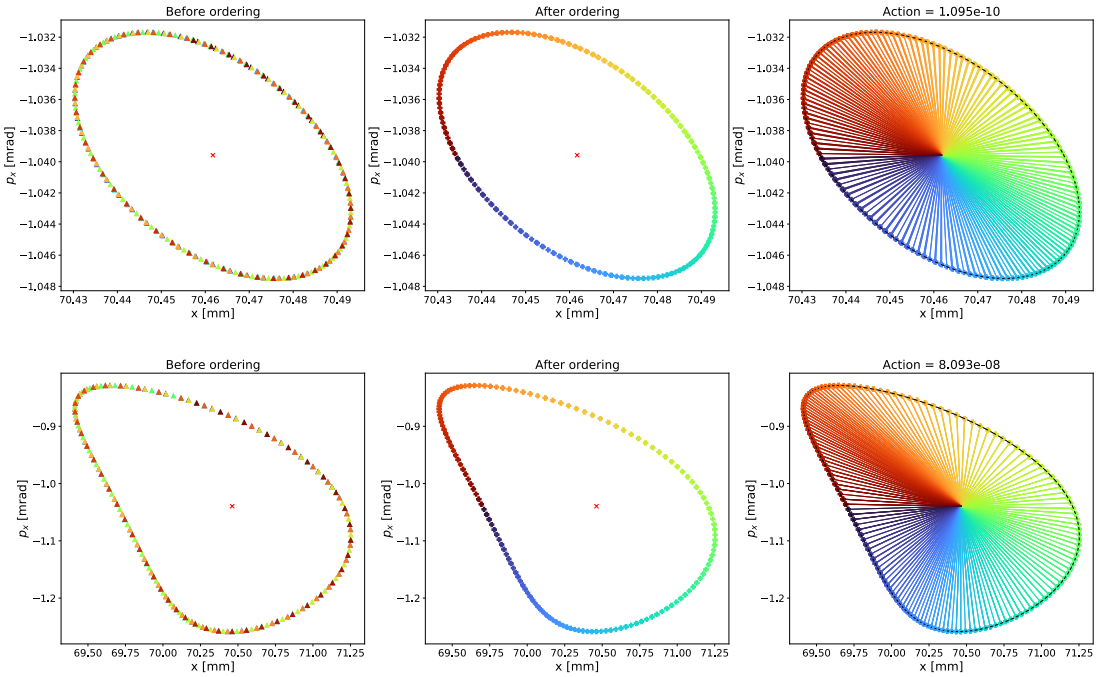

Figure 4.10: Two different particles rotating at different amplitudes: the top row refers to the particle closer to the SFP than the particle on the bottom. Along the three columns it is possible to observe the evolution of particles turn after turn before and after the ordering process.

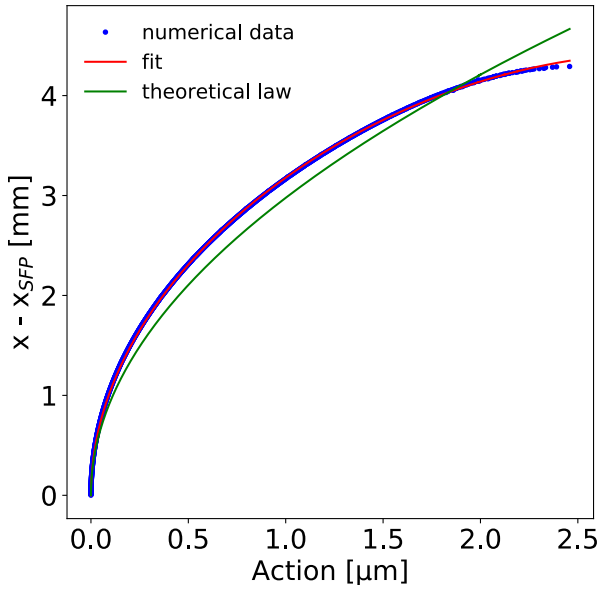

Figure 4.11: Distribution of actions as a function of distance from the SFP. In particular, in blue is reported the distribution provided from the analysis of the experimental data, while in green there is the theoretical law (Eq. 4.17) and in red the fit law (Eq. 4.18).

However, from the observation of Figure 4.11, it is possible to notice that the theoretical law (Eq. 4.17) represents well the experimental data only for small values of the action, thus in the close vicinity of the SFP, where the particle dynamics can be still approximated to be linear. In order to consider the actual non-linear behaviour of the particle motion inside the island, it is necessary to perform a fit of the numerical data. The fit law is such that for low values of actions the theoretical law (Eq. 4.17) is still valid, and for increasing values of actions it deviates from the theory. The function used for the fit is a polynomial expansion of the theoretical law:

$$x - x_{\mathrm{SFP}} = \sqrt{2\beta_{\mathrm{x}} J_{\mathrm{x}} + a_2 J_{\mathrm{x}}^2 + a_3 J_{\mathrm{x}}^3 + a_4 J_{\mathrm{x}}^4} = f(J_{\mathrm{x}}). \tag{4.18}$$

Figure 4.11 shows a very good agreement between the numerical data and the fit; this is also confirmed from the low value of the Chi-square test[3]: $\chi^2 = 4 \times 10^{-6}$. From the knowledge of the position distribution (assumed to be Gaussian Eq.4.1) it is possible to determine the action distribution knowing that $\rho(x)dx = \rho(f(J_{\mathrm{x}}))d(f(J_{\mathrm{x}}))$, therefore the action distribution reads as:

$$\rho(J_{\mathrm{x}}) = \frac{1}{\sqrt{2\pi}\sigma_{\mathrm{x}}} \exp\left(-\frac{1}{2}\frac{f(J_{\mathrm{x}})^2}{\sigma_{\mathrm{x}}^2}\right) \frac{d(f(J_{\mathrm{x}}))}{dx}. \tag{4.19}$$

From Eq. 4.19 it is possible to introduce the dependence on the beam width σ_{x} that was previously removed to perform a unique numerical simulation. For every value of the beam width, coming from the Gaussian fit of BLM data, it is possible to compute the emittance as the average of actions:

$$\epsilon = < J_{\mathrm{x}} > = \frac{\int_0^{J_{\mathrm{sep}}} J(x)\rho(J)dJ}{\int_0^{J_{\mathrm{sep}}} \rho(J)dJ}, \tag{4.20}$$

where J_{sep} is the maximum action value reached from the particle closest to the separatrix. The evaluation of the integral of the distribution is performed numerically by implementing the quadrature rule. A cross-check on the obtained value was performed by implementing a Monte Carlo code. The emittance of the islands is shown in Figure 4.12: the physical emittance is shown on the left-hand side of the plot and the normalised emittance is on the right-hand side. The normalised emittance is computed as the product between physical emittance and the relativistic Lorentz factors (β_{rel} and γ_{rel}), as described previously in Section 2.2.1. Also in this case is possible to observe a spread in the data. This is a direct consequence of the fact that the beam width σ_{x} itself has a spread (see Figure 4.6).

It is important to compare the normalised emittance of the two beam structures: core and islands. In Figure 4.13 the distribution of the normalised core emittance in green is compared with the one of the island shown in red. It is quite evident that the core emittance as a larger spread than the island one. As expected, the normalised emittance of the two beamlets is between 4μm and 6μm, on average; but there is an important spread in the data of the core. The reason of this behaviour is still under investigation because it was the first time that this feature was

[3]The chi-squared test is defined as the quadratic sum of the difference between the expected and the obtained data normalised to the expected data.

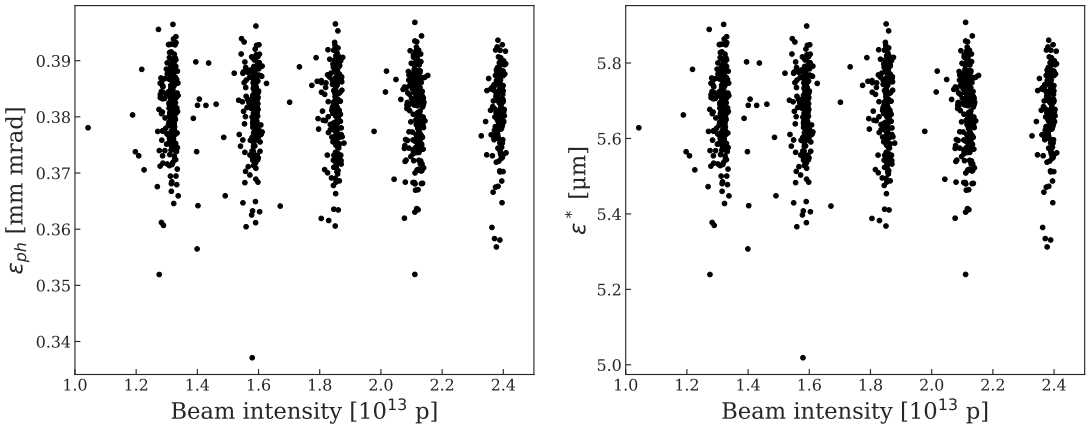

Figure 4.12: Physical (left) and normalised (right) island emittance as a function of the beam intensity.

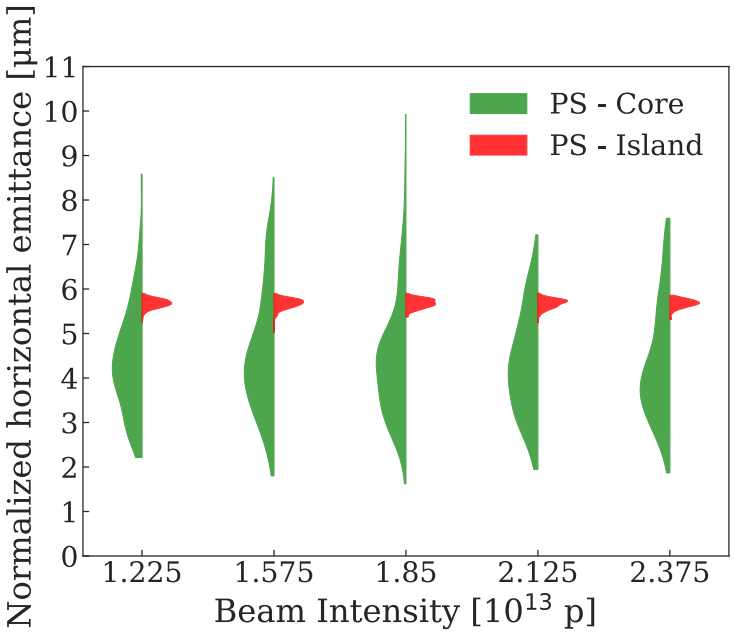

Figure 4.13: Comparison between the normalised emittance of the core (green) and island (red) as a function of the total beam intensity retrieved from the experimental data collected in November 2017.

observed. Moreover, it is evident that there is no dependence between the beamlets emittance and the beam intensity before the splitting. In fact, possible intensity dependent effects can be observed during the splitting process but not during the extraction one.

4.4.3 Remarks on the island transverse emittance reconstruction

As a final remark, it is worth comparing the results that could have been obtained if the emittance for the island would have been computed using the same approach as for the core, namely, assuming a linear beam dynamics. For this purpose, among the beam width values σ_x calculated from the BLM data, only one has been considered, the final considerations being true independently of the numerical value of the beam width used for the simulations. The simulation consisted of tracking for 2048 turns 6000 particles in the island and computing the emittance. The choice of the number of turns to be used comes from the observation that 2048 turns are enough to allow the complete filamentation of the particles in the island and so have a very good estimation of the emittance. For a similar reason, the choice of the number of particles to track is the result of a trade-off between minimising the time needed for the simulation and having a sufficiently high number of particles to have a good precision on the RMS emittance. In addition, to evaluate how the estimate of the emittance changes as a function of the beam width, a set of 18 simulations has been prepared. Each simulation tracks a particle beam with a width that is a fraction of the nominal one σ_x used for the following simulation. The particle distribution used in the tracking procedure is generated in the normalised phase-space, coordinates are then transformed into the physical phase-space, and then tracked for the desired number of turns. At the end of the tracking procedure the tune of each particle is computed and if it is the resonant one (0.25) the particle is considered to be trapped in the island and thus it will be used to compute the island emittance. The emittance is computed in two different ways: averaging the action values and in the statistical way, using the RMS definition (see Eq. 2.30). The results of this analysis are shown in Figure 4.14, where the y-axis on the left-hand side represent the value of the normalised emittance (computed as the product of the RMS or action emittance and the relativistic Lorentz factors) while the y-axis on the right-hand side show the discrepancy among these two quantity computed in terms of relative error:

$$\Delta\epsilon^*_{\%} = \frac{\left|\epsilon_{\mathrm{RMS}} - \epsilon_{\langle J\rangle}\right|}{\epsilon_{\langle J\rangle}}\ 100\ .$$

As the beam width increases, it is possible to notice an increasing discrepancy between the value of emittance computed with the RMS formula (blue dots) and the action average (magenta dots). However, this discrepancy is almost negligible for small values of beam width. This is a direct consequence of the beam dynamics of the island. In fact, close to the SFP the particle motion is almost linear while at larger distances the non-linearities become more and more important. Therefore, when a beam of particles with a small emittance is centred on the SFP of the island, its dynamics will be mainly linear. If the same beam would be centred on a different point, then

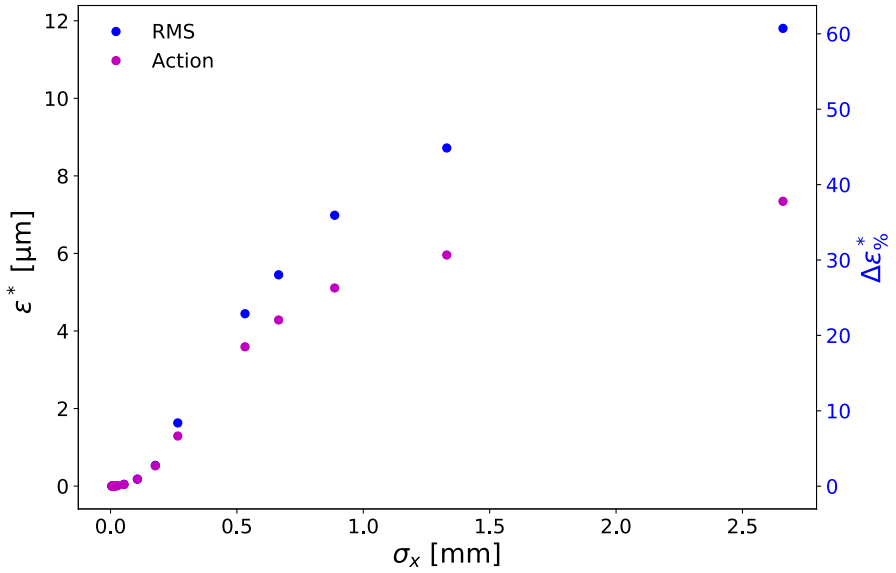

Figure 4.14: Comparison RMS emittance and Action for the reconstruction of the transverse emittance of the island

due to the phenomenon of injection mismatch previously explained in Section 2.2.1, filamentation occurs and its emittance will be larger than the initial value it had been generated with. The percent error between the action average and the RMS emittance is shown as a secondary y-axis in Figure 4.14. As expected for small beam width, thus in an almost linear case, the two methods provide almost the same value of emittance, but for increasing beam widths the discrepancy increases significantly. The maximum difference ($\approx 60\%$) is observed at the nominal value of σ_x used in these simulations (≈ 2.6mm). In conclusion, the use of the RMS emittance rather than the average of the action would cause an overestimation of the island emittance of $\approx 60\%$ for the nominal beam width. This type of error is unacceptable.

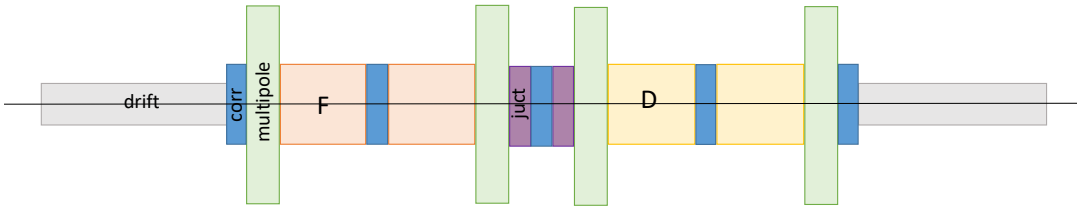

Figure 4.15: Sequence of magnetic elements used in MAD-X to describe the PS MUs. Elements with the same color represent the same type of magnetic component. In blue are shown the BLW, in green multipolar magnets, in orange the focusing half section, in purple the junction between focusing and defocusing section that is shown in yellow. The drifts at the beginning and at the end of the MU is reported in grey.

4.5 Sensitivity Analysis

A sensitivity analysis was performed to understand which PS parameters mostly affect the islands dynamics. The first step to perform, consists in the identification of the relevant parameters. The islands dynamics is mostly affect by non-linear elements that generate non-linear magnetic fields. Even though in the PS there are several families of sextupoles and octupoles (as described in Chapter 3), their role is limited to the control of island's parameters during the splitting and extraction process. It is important to analyse the contribution of the sextupolar and octupolar field components generated by the Main Magnetic Units (MUs) of the PS to the islands dynamics, being the island dynamics mostly non linear and thus, strongly dependent on the accuracy of the PS non-linear model. The aim of this study is to assess whether a change of the PS non-linear model parameters has an effect in the reconstruction of the island transverse emittance, and, if it has an effect, trying to estimate it. The sextupolar and octupolar magnetic field components of the PS main MUs are controlled by the PFW and the f8. As described in Section 3.2, the MUs are combined function magnets that focus the beam along the transverse planes while bending it. It is possible to model these magnets in MAD-X as a sequence of elementary magnetic elements, as reported in Figure 4.15. Even if there are several types of MUs, as reported in Table 3.2, it is possible to model them with the same sequence of elements. For magnets of type R and T the defocusing half-section is followed by the focusing one, thus the elements are symmetric with respect to those shown in Figure 4.15. For magnets of type S and U the sequence of elements is as shown in Figure 4.15. Finally, to account also for the different position of the yoke, the sign of the quadrupolar strength changes if an internal or external yoke is considered. As soon as the beam gets into one of the combined function magnets of the PS, it finds a Back-Leg-Winding (BLW), that corrects horizontally (or vertically) the beam orbit [48] (from here the label "corr", abbreviation of corrector, in Figure 4.15). Then a multipolar magnets aims at simulating the contribution of the PFW. It is possible to add and modify magnetic field component up to the sixth order (that corresponds to the contribution of a dodecapolar magnet), but in the PS non-linear model simulations, the fourth order component is the last one that can be changed, thus simulating the

effect of an octupole. Then the beam enters the focusing half-section (or defocusing one if MU of type R and T are considered) where it gets focused in the horizontal plane ad defocused along the vertical one (viceversa if a defocusing half-section is considered). At the end of this element the beam enters again in a multipole and then in the junction region between the focusing half-section and the defocusing one. Also in this case, between the junction magnets, a BLW is installed. Downwards the junction region, the beam enters the defocusing half-section where it will be defocused along the horizontal plane and focused along the vertical one. Before the end of the MU, the beam will enter another multipolar magnets and a corrector. In order to assess how the islands dynamics changes with respect to a change in the PS non-linear model, it is important to define which parameters are representative of the islands dynamics and which other parameters have to be changed in the non-linear model. As far as the first topic is concerned, three different physical quantities can be identified: the horizontal beta function β_{x} as well as the SFP position x_{SFP} are good indicators of the island dynamics and position; and the dispersion function D_{x} to account for off momentum particles. As far as the second topic is concerned, the non-linear parameters that will be changed in the analysis are the sextupolar and octupolar components in the multipoles of the PS main MUs. In particular each half-section (focusing or defocusing) is characterised by one variable representative of the sextupolar component of the multipole magnet and one variable for the octupolar one. These values might differ among the two types of half-sections. Thus there are four variables that can be changed. A first investigative and preliminary analysis was performed to understand the range within which the parameters could be varied, in particular, the contribution of the two setupolar and the two octupolar components has been increased and decreased at the same time to understand where to set the limits of the 4D hypercube. In this analysis only the position of the island SFP was considered since its variation is expected to be more sensitive to a change of the sextupolar and octupolar strengths. In particular, a variation above the ±1.5mm is considered to exceed the limits. The results of this analysis are shown in Figure 4.16. On the upper part of Figure 4.16 it is possible to observe how the position of the SFP changes as a function of the percentage difference of the sextupolar and octupolar strength with respect to their nominal conditions, where the zero corresponds to nominal conditions. It is possible to observe that even a reduction of the 25% leads to a change of the SFP position within the ±1.5mm deviation from nominal condition (represented by the black lines). A deviation larger than ±1.5 mm would lead the island to be too close to the dummy septum and thus have a fraction of the beam lost. It is also possible to observe that a 6% increase of the sextupolar and octupolar strengths would cause the SFP position to fall beyond the −1.5mm deviation. Therefore, the upper limit of set by the SFP position of on-momentum particles. It is important to perform a similar analysis for off-momentum particles because their closed orbit $x_{co}^{off-mom}$ is related to the one of on-momentum particles through:

$$x_{co}^{off-mom} = x_{co}^{on-mom} + D_x \frac{dp}{p}. \tag{4.21}$$

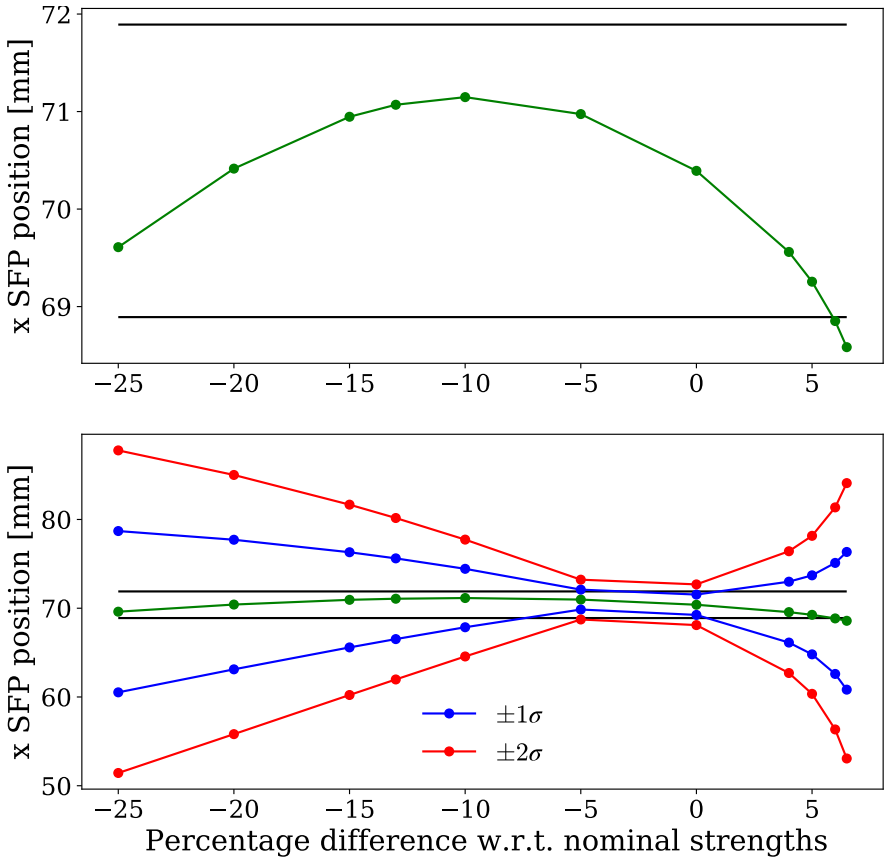

Figure 4.16: The top of the figure is dedicated to the SFP position while the bottom one considers off momentum particles with $\pm 1\sigma$ and $\pm 2\sigma$ deviation from nominal conditions. In both plots the continuous black lines represent a deviation of ± 1.5 mm of the SFP position in nominal conditions.

The bottom part of Figure 4.16 represents the closed orbit position for off-momentum particles, particles with $\pm 1\sigma$ deviation are reported in blue while those with $\pm 2\sigma$ are shown in red. In this case it is evident that even though on-momentum particle would allow a maximum deviation from nominal condition of -25%, it is actually not feasible because of the limitations imposed by off-momentum particles. In fact, both the upper and lower limit have to be reconsidered when off-momentum particles are considered. It was decided to limit the range within which the sextupolar and octupolar strenghts could vary to $\pm 2\%$ even though it is already possible to observe that a particle with a -2σ momentum deviation would have a closed orbit variation larger than the imposed tolerance. The reason of this choice is that so far only one single parameter, over the three relevant one, has been considered. To evaluate the precise variation of the SFP as well as of the β_x and D_x function a complete simulation is needed. However, it is expected that even within the $\pm 2\%$ variation some combination of parameters would provide unfeasible or unphysical conditions and thus they will have to be discarded. A Monte Carlo code has been used for the generation of 1000 non-linear quadruplets representing the four variables (two sextupolar

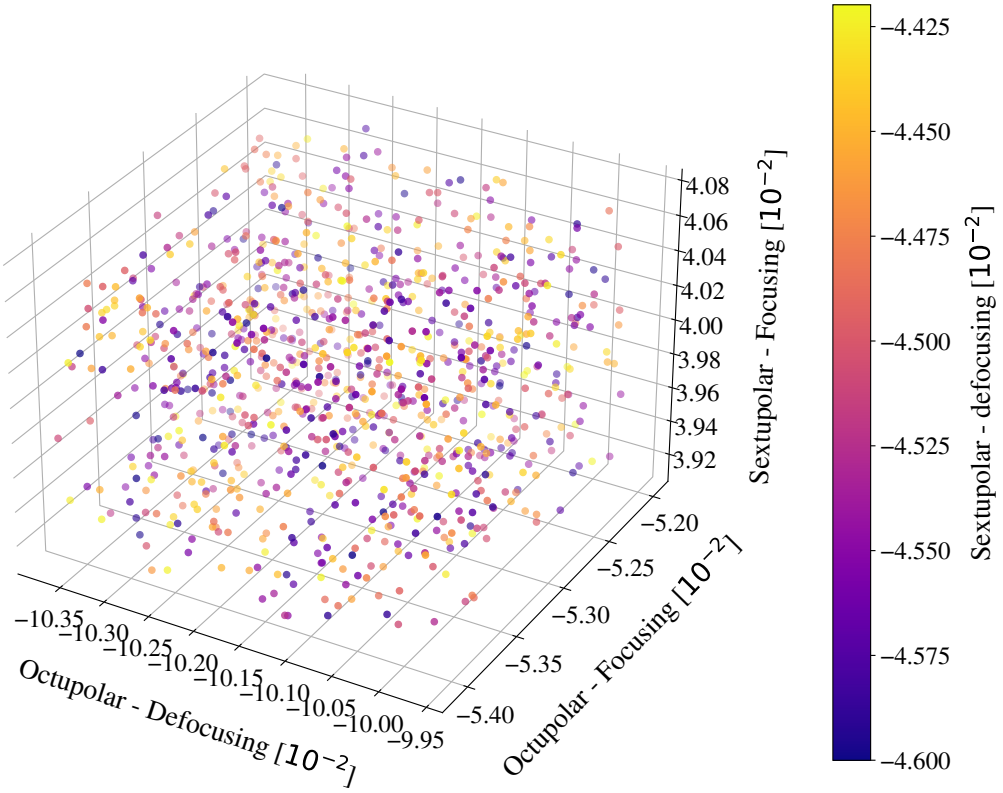

Figure 4.17: The hypercube shown the range within which the PS multipolar components can vary. Each side is centred on the nominal value of the multipolar components (thus, nominal configuration of the PS) and its maximum variation is ±2% with respect to the nominal value. There are in total 1000 dots and each dot represent one PS non-linear model and its coordinates as well as its color provide information on the value of the four multipolar components varied in the analysis.

and two octupolar) to be changed. These components are defined within an hypercube having dimensions corresponding to a variation of ±2% centred on the nominal value of every non-linear component. These conditions are shown in Figure 4.17 and they represent 1000 synthetic non-linear PS models. Each model has been used to perform a TWISS analysis to determine the β_x and D_x functions as well as the position of the island SFP. As it was explained in the previous section, in order to determine the island emittance independently from the beam width of each BLM measurement, a uniform distribution of 2000 initial conditions was generated from the SFP position to the separatrix. Each initial condition was tracked for 4096 turns to enable complete filamentation and thus determine which initial conditions have a resonant tune (and so are inside the island) and which ones are lost and should be discarded. Therefore, the action is computed only for those initial conditions within the island. This rationale is followed for every PS non-linear model and, for each model, the action distribution as a function of the island SFP position can be determined, a plot similar to Figure 4.11 is obtained for every PS non-linear

model. Thus, the fit of the numerical values to the fit function in Eq. 4.18 is performed and the fit coefficients (a_2, a_3 and a_4) are determined for every model. The good quality of the fit is ensured by the low value of the chi-square test which shows a mean value of $(7.02 \pm 0.87) \times 10^{-5}$. In order to compute the island emittance, it is necessary to introduce the dependence on the beam width σ_x following the procedure described in the previous section. Thus, for every polynomial expansion (see Eq. 4.18), that is characteristic of a specific PS non-linear model, it is possible to compute the action distribution as in Eq. 4.19. Therefore, the emittance is determined using Eq. 4.20. In order to determine whether the non-linear PS model is feasible or not, the dispersion function D_x, the beta function β_s and the island SFP position are evaluated for every configuration. These data are reported in Figure 4.18 as a function of Euclidean distance from the multipolar components at nominal strength. In order to determine what non-linear PS models represent actually feasible ones, it was necessary to impose constraints on the three variables analysed. In particular, as far as the dispersion and beta functions are concerned, the limit has been imposed to $\pm 10\%$ with respect to the nominal value, being the 10% the usual uncertainty on the value of optical functions. As far as the SFP position is concerned, the limit has been imposed to ± 1.5mm variation with respect to the nominal value, being this variation detectable in operation. Moreover, the nominal value of the beta function, dispersion function and SFP position is shown as a dashed line, while the bounds are reported with a continuous black line. Thus, in Figure 4.18 it is possible to find the feasible configurations as green dots while the unfeasible ones as red cross. Only 204 configurations can be accepted among the 1000 simulated. The major limitation that caused the high number or rejected models is imposed by the value of the dispersion function D_x, as shown in Figure 4.18, in fact, only 204 fall within the imposed limits. For the accepted non-linear models the value of emittance is reported in Figure 4.19. The black dots refers to the nominal values of the multipolar PS components (it is possible to find these values on the right hand side of Figure 4.12), while the color dots refers to the 204 non-linear models that have been considered as feasible in the previous analysis. It is possible to observe how the range within which the emittance varies remains unchanged as the simulated non-linear model varies. Moreover, it is worth highlighting that even if a large number of non-linear model had to be discarded, the remaining models are spread within the desired hypercube dimension, i.e., the sensitivity analysis of the accepted model is not simply a selection of the models around the nominal condition. It is interesting to make a projection of Figure 4.19 and show the emittance distribution as a function of the beam intensity, in analogy to Figure 4.12. It was chosen to show the result in terms of distribution of points to provide information on the mean value of the distributions as well as highlight possible spread of the data. This result is reported in Figure 4.20, where the distribution of island emittance as shown in Figure 4.12 is reported in red and the distribution of the emittance computed in the sensitivity analysis is shown in blue. It is possible to observe that both distributions have compatible values of the mean, the most probable value and the spread, meaning that the PS non-linear model is reliable and it can be used to

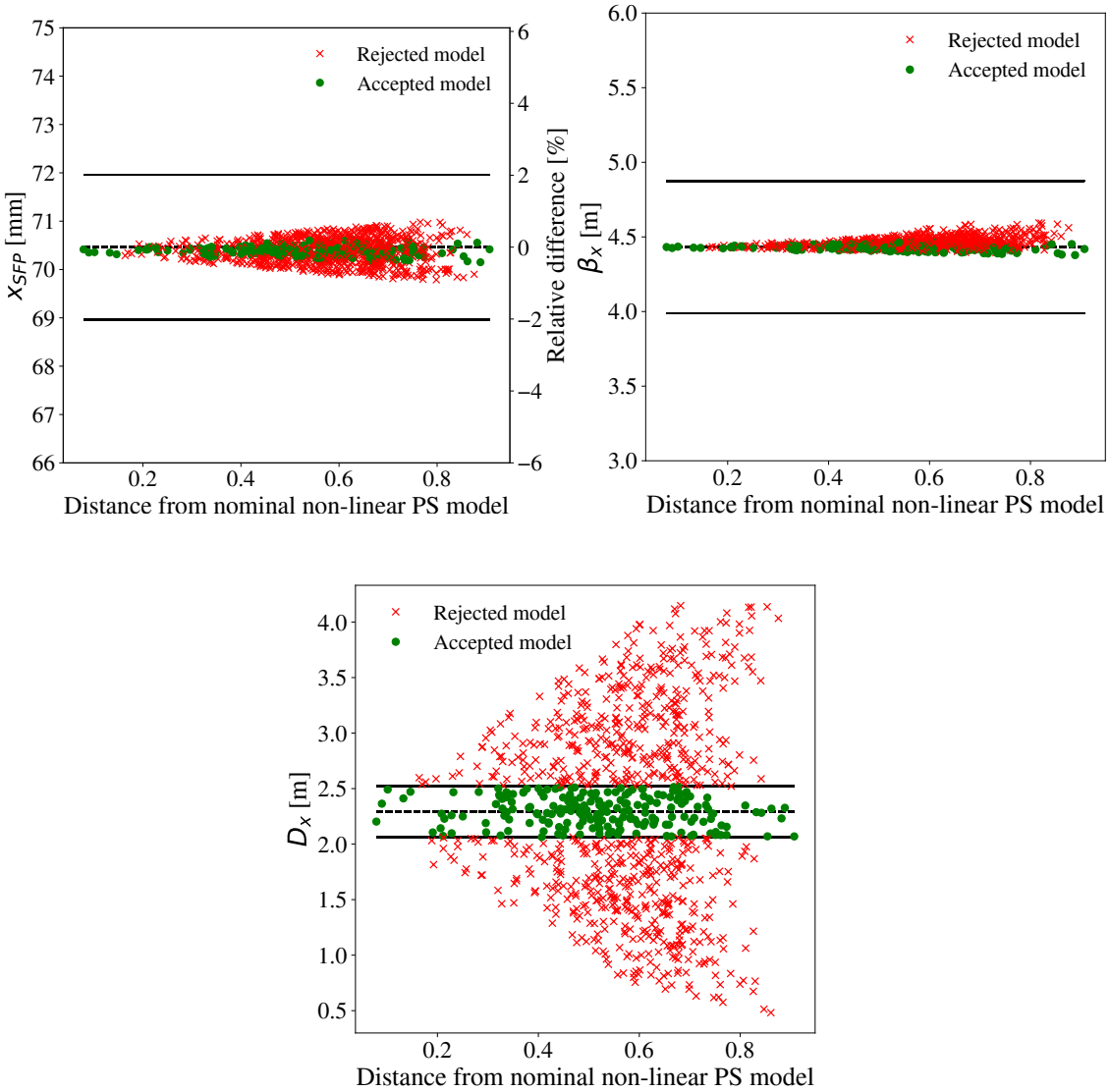

Figure 4.18: The position of the island SFP (top left), $\beta - x$ function (top right) and dispersion function (bottom) are shown as a function of the distance from the centre of the hypercube that corresponds to nominal conditions. Dashed lines represent the nominal value of the three variables, while black lines show the limits imposed to their values. A tolerance of ±10% is imposed to the optical functions, while a maximum variation of ±1.5mm is accepted for the SFP position.

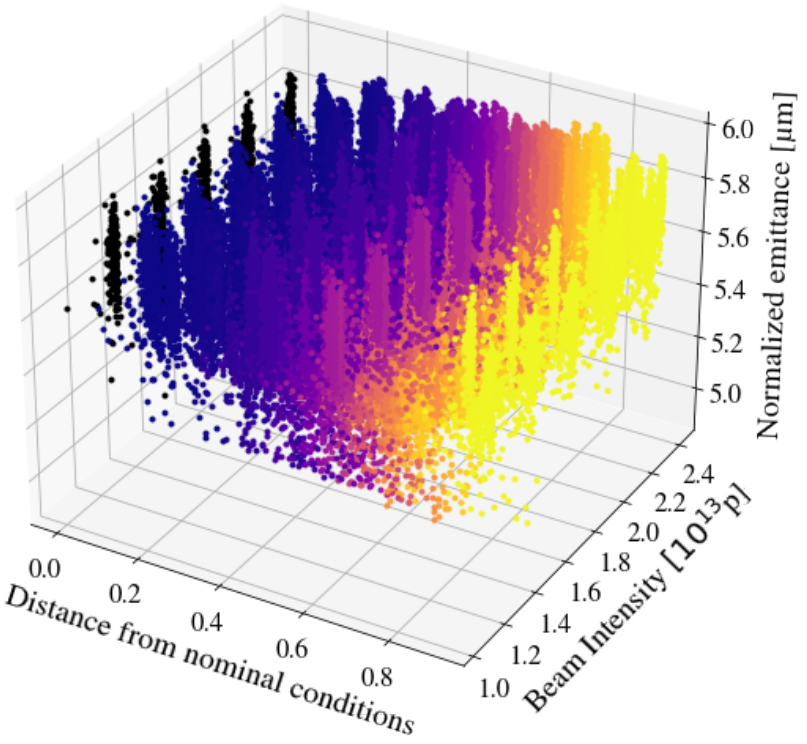

Figure 4.19: The island normalised emittance is shown as a function of the beam intensity and the euclidean distance from nominal operating conditions of the PS multipolar components. The black dots refers to the multipolar components at nominal conditions, while the colored points refers to the selected 204 non-linear model (each color refers to a different configuration).

reconstruct the island emittance.

In the context of the sensitivity analysis it was decided to consider only the effect of a variation of the sestupolar and octupolar non-linear components in the reconstruction of the island transverse emittance. The results have been presented and discussed in this section, it is possible to find additional details on which one has a larger effect with respect to the other in Appendix B. However, it is important to highlight that there are other parameters that might significantly affect the island emittance. In particular the tune of the machine is the fundamental one. A change in the tune, unavoidably causes changes in the number of particles trapped within the island as well as in the structure of the phase-space itself. In fact, the phase-space reported in Figure 4.9 as been determined for a horizontal tune of 6.267, which is the typical tune at which the PS ring works. Therefore, it is important to determine whether the tune has a relevant effect on the the shape of the island in phase-space. This discussion will be performed in Chapter 5 and

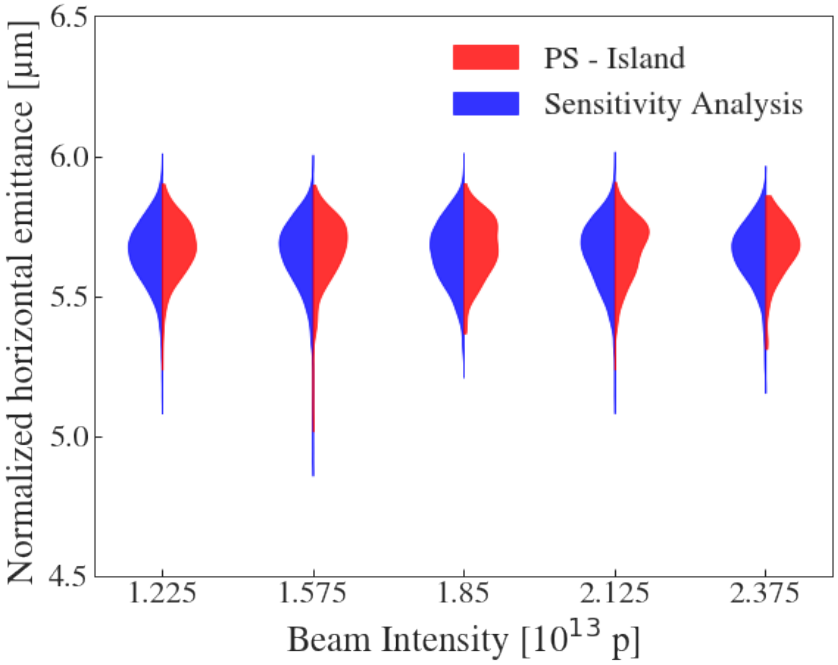

Figure 4.20: The distribution of island emittance coming from the analysis of the BLM data is shown in red, while the one coming from the results of the sensitivity analysis is reported in blue.

from the results presented it will be clear the need to develop new methods to compute the tune with a very high precision (the methods, their explanation and usage will be explained in detail in Chapter 6).

CHAPTER 5

THE IMPORTANCE OF ACCURATE TUNE DETERMINATION

The Proton Synchrotron ring at CERN was the very first accelerator to be constructed and that is still nowadays accelerating and delivering beams. For this reason it has undergone to numerous modifications and upgrades from the electronic, mechanical and beam physics point of view. The PS has a very key role in providing high-energy beams to its downstream experiments, as well as to the down stream accelerators (the SPS and the LHC, see Figure 1.1) and their experiments (as the fixed-target experiment at the SPS). Over the years, the PS ring has faced enormous changes, one of the most significant being the change in the extraction technique. The reasons of this choice are mainly explained by the need of reducing beam losses to enable the transfer of more intense beam and thus reduce the radiation levels at the extraction point. However, it is important to highlight that such a radical change in the PS has led to the need to assess whether the performance of the accelerator chain has been left unchanged. For this reason, several studies have been carried out to verify this key feature and numerous changes were needed in the upstream accelerators such as the PSB and the LINAC; additional and detailed information can be found in Ref. [36, 49]. In the following sections, several issues related to the implementation and operation of the MTE technique, the innovative PS extraction scheme, will be highlighted. The physics behind it and how it has overcome the limitations of the previous CT beam extraction scheme have been described in Chapter 3. However, there were issues related to the actual MTE operation that took a few years to be fully understood. A description of these phenomena will be provided in this chapter. Moreover, a comparison with the experimental campaign carried out in 2017, which have been used also to reconstruct the beam transverse emittance in Chapter 4, will be described. In conclusion, the description of particular, and still unclear observations will make clear the need of determining the tune with high precision.

5.1 MTE and tune fluctuations

The Multi-Turn-Extraction (MTE) was proposed for the first time in 2002. However, due to its complexity, it took about five years of studies and investigations to assess its feasibility. In 2006, feasibility studies were terminated and the design and construction of the hardware was started. This phase was rather fast, in fact in 2008 the hardware design and commissioning was over and the beam commissioning started shortly thereafter [49]. To avoid interrupting beam physics experiments and commissioning to the downstream accelerators, the CT was kept as a back-up extraction technique. In 2010, it was possible to gather confidence with the new extraction technique (MTE) testing its performance and its limitations. It was immediately evident that there were some phenomena that strongly limited the usage of MTE. In fact, after few weeks of measurements carried out in 2010, two major limitations have arised: high radiation levels were detected in the extraction region and it was possible to observe fluctuations in the MTE efficiency (defined as in Eq. 4.5) and in the extraction trajectories [50]. As the fluctuations varied from cycle to cycle, it was particularly difficult to identify the cause of the problem and possibly, solve it. In particular, this phenomenon strongly affected the transverse beam distribution as well as the intensity of the spills [50]. As a consequence, the beam transfer to and beam optimisation at the SPS were significantly limited and affected by these phenomena. Therefore, it was extremely important to solve it to make the MTE operational.

The former problem (high radiation levels in the extraction region) was solved installing a fictitious septum (called dummy septum) with a position and an orientation to actually shield the magnetic septum minimising, at the same time, the losses due to the interaction between the beam and the dummy septum itself. The installation inside the vacuum chamber further reduced the available space for the beam along the horizontal direction, leading to the need for a complete re-design of the beam optics at extraction [50].

The latter problem (unclear fluctuation in the MTE efficiency and in the beam orbit after extraction) required years of studies and investigations. During the experimental campaigns carried out in 2015, the phenomenology of this issue was understood and solved [50]. As described in Chapter 3, the PS working point is defined by the value that the horizontal and vertical tune, which are controlled by the Pole-Face-Windings (PFW) and the figure-of-eight (F8). At the same time, these magnets also power auxiliary magnets installed on the combined-function dipoles (the Main magnetic Units, MUs) that can generate higher-order magnetic field components (quadrupolar, sextupolar and octupolar). The power converters responsible for their operation have an operating frequency of 5 kHz and 2 kHz, respectively. From experimental measurements, it was possible to observe a current ripple at those frequencies [50]. In particular, the amplitude of the perturbation was bigger than expected and was non-constant in time. This latter effect is caused by a wrong synchronisation between the power converters of the different circuits. Thus, by properly synchronising them, the time-amplitude variation was solved. The effect of the current ripple actually translated into a change of the machine parameters and, therefore, had a

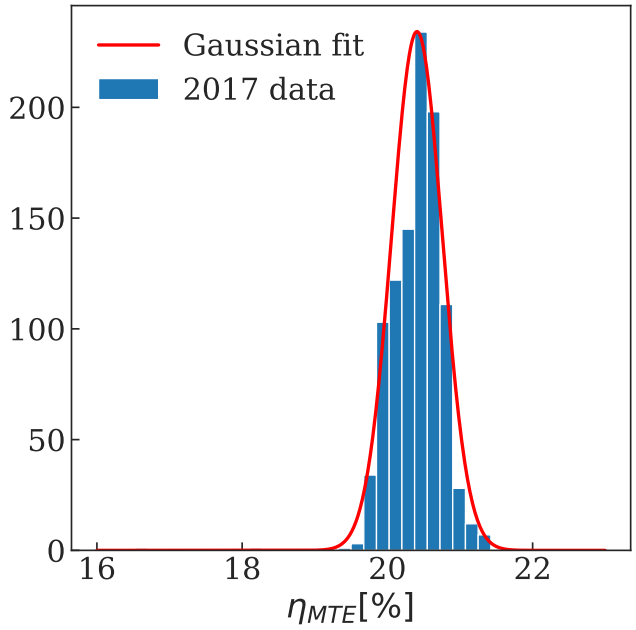

Figure 5.1: MTE efficiency distribution for the experimental campaign carried out on November 2017. The histogram of the MTE efficiency is then fit to a Gaussian function which is shown in red.

relevant effect on the beam manipulations performed during the MTE scheme. The solutions of MTE efficiency fluctuations as well as those of the beam orbit after extraction have been solved by damping the ripple contribution at those frequency, and by adjusting the synchronisation. The solution of this major issue was confirmed on September 2015 when the first beam with the desired properties was successfully extracted with the MTE scheme.

From an experimental point of view, the above described MTE efficiency fluctuations were clearly visible from cycle to cycle. A detailed analysis of those data can be found in Refs. [50, 51], where it is possible to observe that the MTE efficiency distribution in the uncorrected configuration (that is, with the frequency ripple still present) looks like a skew Gaussian distribution. Therefore, after the upgrades of the power converters, the distribution is expected to be Gaussian-like distribution. It is possible to consider again the experimental data analysed in Chapter 4 and verify whether the distribution of the MTE efficiency (defined as in Eq. 4.5) is a Gaussian. The result is reported in Figure 5.1. The distribution of the MTE efficiency histogram was fitted to a Gaussian curve (represented in red in Figure 5.1) that shows an average value of 20.4% with a standard deviation of 0.3%. From Figure 5.1 it is possible to observe that the expected Gaussian distribution is obtained and that its mean value is close to the theoretical expected value of splitting efficiency (namely of 20%).

During the investigations carried out to understand the MTE efficiency distribution, addi-

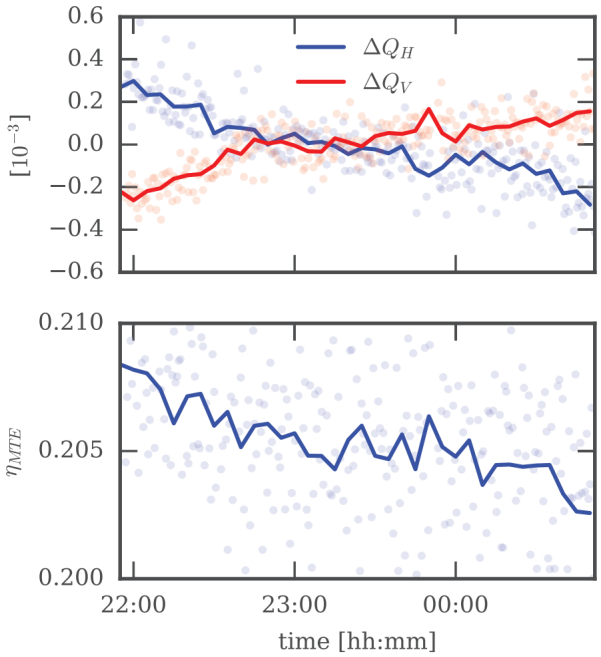

Figure 5.2: Tune fluctuations and MTE efficiency fluctuations as a function of the sampling period.

tional phenomena have been observed. In particular, high-frequency components such as the current ripples, have been fully understood and corrected; but minor deviations from the expected operative conditions were still observed and they were caused by slowly varying phenomena, as shown in Figure 5.2 [51]. The horizontal and vertical tune change in time and a quite evident relation between the horizontal tune Q_x and the MTE fluctuation is observed. Although the reasons behind this phenomenon are not clear, the tune fluctuations as a function of time can be adjusted by means of the PS tuning quadrupoles [51]. From Figure 5.2 a maximum tune shift of $\pm 6 \times 10^{-4}$ is observed. Even if it is possible to adjust the PS tune during operational conditions, it is of great interest to understand and determine the horizontal phase-space when such tune shift occurs. In fact, it is expected that uncorrected tune shift unavoidably leads to changes in the horizontal phase-space as, for example, an enlargement of the transverse phase-space and thus, a possible interaction between particles and vacuum chamber (or physical insertion within it). For this reason it was decided to study the evolution of the horizontal phase-space as a function of the horizontal tune when its value changes of $\pm 0.6 \times 10^{-3}$ with respect to its nominal value 6.267.

5.2 Phase-space portraits

The effect of a change in the PS working point is analysed in the following section. In particular, the nominal working point after beam splitting is defined by $Q_x = 6.267$ and $Q_y = 6.30$. It is possible to notice that the horizontal tune is not equal to the fourth-order resonance tune (thus

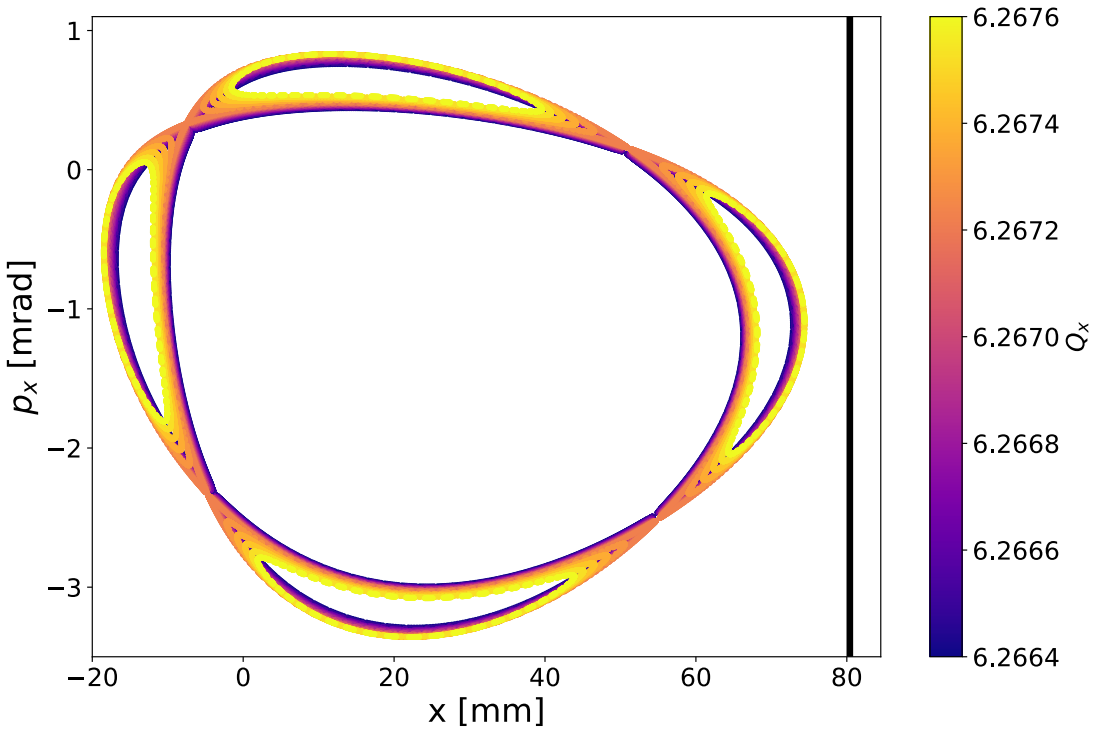

Figure 5.3: Islands horizontal phase-space representation as a function of the horizontal tune that has been varied within an interval centred on the PS nominal horizontal tune wide $\pm 6 \times 10^{-4}$.

6.25), the reason being to enhance the separation between the beamlets in the island prior to extraction. Numerical simulations have been prepared to evaluate how the horizontal phase-space changes as a function of the horizontal tune. The analysis is carried out in MAD-X [24], where the non-linear model of the PS is described. The horizontal tune is changed keeping the vertical one unchanged. As a first step, the Twiss analysis is performed to determine the position and momentum of the SFP. These parameters are used as input values for the tracking procedure. The determination of how the island parameters and features change as a function of the horizontal tune, is performed by tracking a limited number of initial conditions (1000, for this specif case) over a certain number of turns (2048). The initial conditions are generated as a uniform distribution from the SFP position to the separatrix, all of them with the same value of momentum (equal to the one of the SFP). After 2048 turns, the tune of each initial condition is evaluated with the Hanning method (it will be described in Section 6.1.3) and compared to the resonant tune 6.25. Only those initial conditions with a resonant tune are considered to be inside the island. It is also possible to observe the last stable condition and the SFP in Figure 5.3, where also the position of the dummy septum is reported with a black line. Note that as the tune deviates towards larger values with respect to the nominal tune, a right shift of the island position can be observed. This behaviour can be observed also in Figure 5.4, where the action evolution is reported as a function of the horizontal SFP position, where the colour refers to the

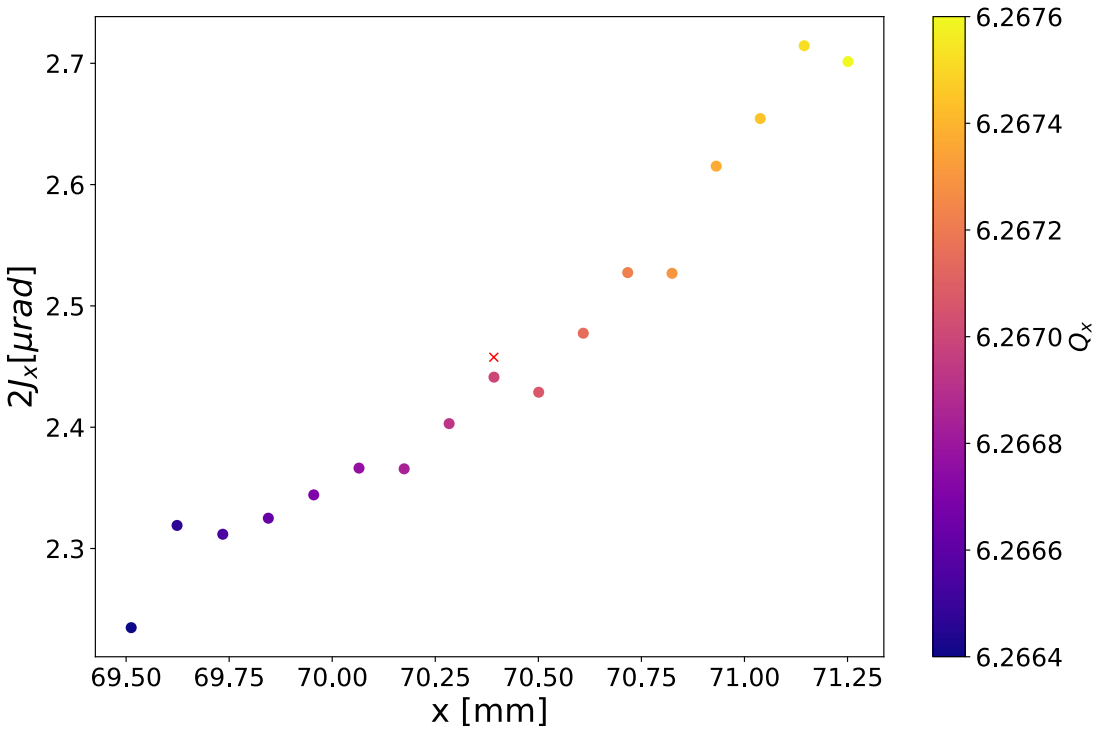

Figure 5.4: Island action as a function of the SFP position. The increase in the island action and the right-shift of the SFP position are caused by different horizontal tune values. The nominal working point configuration is reported with a red cross.

horizontal tune. The slight discrepancy in the action value computed at nominal condition (red cross in Figure 5.4) and the one computed in the present analysis is due to the reduced number of initial conditions (1000 versus 2500) and turns (1024 versus (2048) adopted compared to those used previously (see Section 4.4.2). Moreover, as the tune shifts to larger values (compared to the nominal one) the identification of the last stable particle before the separatrix gets more complicated since the time (or equivalently, the number of turns) needed to complete the orbit in the island increases enormously. Figure 5.4 shows how a reduction of the horizontal tune with respect to its nominal value (thus, moving towards pink-purple points) leads to a left-shift in the SFP position with a maximum reduction of -36% in the value of the island action. Although such a reduction is quite relevant, the most relevant deviations from nominal conditions (reported as a red dot in Figure 5.4) can be observed for positive tune shifts (thus, towards yellow points). In fact, for a maximum tune change of 6×10^{-4} with respect to the nominal horizontal tune, a $+10\%$ increase in the island action value is observed. However, the right-shift of the SFP position makes critical to operate the beam in this condition being the beam close to the dummy septum.

It is clear that the precise determination of the working point of an accelerator is fundamental, especially in conditions where non-linear fields have a relevant effect on the beam dynamics. In the next Chapter several methods for the very precise tune determination will be described and new innovative equations and methods will be introduced, discussed and numerically simulated.

CHAPTER 6

METHODS FOR HIGH PRECISION TUNE DETERMINATION

In accelerator physics is of great importance to know accurately the betatron tunes since they define the working point of the accelerator, they provide information on the beam stability as well as on the width of resonances[1] in non-linear machines [52]. Its evaluation can be performed in several ways depending if synthetic signals or real beam data are analysed. During the design phase and its related studies (such as the research and optimisation of the working point) tracking results from numerical simulations are used to evaluate the tune. In this configuration, the turn-by-turn signal, that describes the time evolution of the beam centroid can be analysed to determine the tune. During experimental measurements, its determination is performed with different techniques, among these it is worth mentioning the radio-frequency dipole (called, AC dipole) and conventional kickers used, for example, during the injection or extraction phase. Thus, the tune evaluation is performed on a signal whose amplitude may vary over time (depending on the technique adopted) and that may be affected by noise. Therefore, the methods to be used to compute the tune are a restricted selections of those available for the analysis of test signals.

As far as the AC dipole is concerned, it perturbs the beam with an RF field, introducing a forced oscillation that excites the coherent oscillations of the beam at the desired frequency (Q_d). Its usage is particularly interesting since the exciting frequency can be properly tuned and because the driven oscillations can be maintained for several thousands turns improving the reproducibility and the quality of the measurements. It is important to highlight that, setting the excitation frequency at the same value as the accelerator tune induces the excitation of a

[1] With the term "width of resonances" is meant the non-linear resonance produced by non-linear magnetic elements. For this type of resonances some particles in the beam might get unstable depending on their oscillation amplitude. These resonance are significantly different from linear resonances produced, for example, by gradient errors where stability or instability refers to the whole beam [8].

resonance that leads to the complete loss of the beam. In a similar way, higher-order multipoles might excite resonance of the type $NQ_d = p$ if the excitation frequency is set to a value too far from the accelerator tunes. Moreover, it is worth highlighting that the ramp up of the AC dipole has to be performed adiabatically, to prevent undesired phenomenon such as emittance blow up. Additional information on how to reliably operate an AC dipole can be found in Ref. [53].

As far as the use of kickers to perform tune measurements is concerned, their effect on the beam is completely different from that of an AC dipole. Any kicker already installed in the ring can be used for tune measurements, provided that it is possible to ramp it up and down within a single turn. Once the beam has been kicked, the betatron oscillation of every particle in the beam will start to decohere. At the end of the measurement the beam has to be dumped and a new beam has to be provided to the accelerator before another tune measurement, or any other measurement, can be performed. This is a relevant drawback compared to the AC dipole measurement, where the beam can be reused if the AC dipole has been turned on and off adiabatically.

Both tune measurement techniques use the Beam Position Monitors (BPMs) to record the time evolution of the beam centroid along the ring. Some accelerators, such as the PS ring, can also be equipped with other instruments such as the Base-Band tune (BBQ) measurement system. It is a system of capacitors and resistors able to filter orbit oscillations, thus providing the time evolution of betatron oscillations induced by the effect of kicker only; the measured quantity cannot be directly related to the beam position. Additional details on this instrument can be found in Ref. [54]. The number of turns over which the measurement is performed has to be long enough to have a sufficient number of samples to determine the tune.

The dependence of the tune accuracy on the number of turns will be discussed in detail in this chapter. The time evolution of the beam centroid position defines a time-dependent signal (whose amplitude and frequency evolution is determined by the physical phenomenon occurring within the particles of the beam) that can be analysed with several harmonic analysis methods to determine the tune. Among the different techniques available to determine the frequency of a signal only a selected number will be named and discussed in the context of this chapter: Average Phase Advance method (APA), Numerical Analysis of Fundamental Frequencies (NAFF) and the Fast Fourier Transform (FFT) are used to perform this analysis. The latter one will be covered in detail, the aim being to determine new analytical formulae for computing the tune.

In the context of this chapter, the properties of the beam will refer to its centroid; therefore, the single-particle approach will be used to describe the beam dynamics. The studies presented in the following section will concern the determination of new analytical formulae to compute the value of the tune as a function of the number of turns for different types of synthetic signals. Each presented and analysed signal is the synthetic version of a signal that can be obtained during beam measurements. The rationale of the work consisted in constructing an artificial signal with known properties (such as frequency, constant, or varying amplitude) and trying to determine its

features with different methods. Thus, testing a selection of methods on a variety of different signals with different features enabled the understanding of which method performs better than others in terms of accuracy in the estimation of the signal parameters. At the end of the chapter, the analysis of real beam data will be performed using some of the methods described in the next sections.

6.1 State of the art

As a first approximation, the evolution of the beam centroid position in absence of non-linearities and magnet errors, can be considered as a sinusoidal function that evolves as a function of the number of turns, n, in the accelerator. Its frequency is the tune ν_0, its amplitude may be constant or varying as a function of the number of turns. Using the complex variable $z(n) = x(n) - ip_x(n)$, it is possible to describe the turn-by-turn beam centroid evolution as:

$$z(n) = e^{2\pi i \nu_0 n} + \sum_k a_k e^{2\pi i \nu_0 n k}, \tag{6.1}$$

where $a_k = e^{-k}$ and $n \in \mathbb{N}$ with $n \in [1, N]$. In the context of current and future studies, the number of perturbative harmonics has been fixed to four ($k \in \mathbb{N}$ with $k \in [1, 4]$). Moreover, the complex-valued signal $z(n)$ has been constructed in such a way that its real part $x(n)$ and its imaginary part $p_x(n)$ are shifted in phase by $\pi/2$ and, except if explicitly stated, this phase shift is always kept constant. This type of signal represents well the dynamics of a particle in a circular accelerator where only linear magnetic elements are installed. As a first approximation, for non-linear machines the beam position can be described as a combination of cosinusoidal functions and a perturbation term. Although the discussions that will follow will refer to and analyse the signal $z(n)$ as defined in Eq. 6.1, it will be possible to extend the results and conclusions to the vertical plane, since the coordinates x and p_x can be replaced with y and p_y without loss of generality.

The determination of the frequency of a signal is a very well-known topic that has been studied and applied to many different areas ranging from astronomy and astrophysics, where the secular evolution of the planets orbit is analysed [55], to accelerator physics, where the betatron oscillation frequency (tune) of the beam is studied [56]. The determination of a signal frequency is based on the use of the discrete Fourier transform. Its application implies that the signal has a constant amplitude and a constant frequency over the sampling time. Cases where either the frequency or the amplitude, or both, vary over time, should be handled with care.

The knowledge of the tune with high precision is fundamental to determine whether the beam orbit is stable or chaotic, and it precisely determines the nominal working point of an accelerator in the tune diagram (see Figure 2.9). For this reason, during the past decades several analytical studies have been performed to increase and improve the precision of the tune calculation by proving analytical equations whose precision scales as an inverse power of the number of turns

N, namely,

$$\Delta\nu = |\nu_0 - \hat{\nu}_0| = \frac{1}{N^\alpha}, \tag{6.2}$$

with $\alpha \geq 1$, being $\alpha = 1$ already provided by the Fast Fourier Transform (FFT), $\hat{\nu}_0$ the value of the tune computed with the selected equation or method and ν_0 the one used for the generation of the test signal. The results of these studies can be found in Ref. [52]. In Sections 6.1.2 and 6.1.3 the main results of [52] will be reported and discussed since they will be used as a reference for performance comparison in the next studies.

It is important to make a final remark. The analytical tune equations that will be presented and derived in the next sections, will be determined for signal in Eq. 6.1 where the contribution of perturbative harmonics is neglected. The numerical simulations are performed over the signal defined in Eq. 6.1 (with the contribution of perturbative harmonics) where the tune is determined with the equation above mentioned. Therefore, because of the presence of perturbative harmonics, the tune ν_0 used for generating the signal will be different from the one retrieved numerically $\hat{\nu}_0$, and their difference depends on the accuracy of the considered analytical equation or method.

6.1.1 Average Phase Advance

The Average Phase Advance (APA), as the name suggests, is a method based on the average of the phase calculated between two successive iterations. It enables the calculation of the frequency (namely, the tune) of an orbit in the vicinity of an elliptic fixed point [52]. The use of this method on the signal in Eq. 6.1 allows to compute the tune as:

$$\nu_0 = \frac{1}{2\pi(N-1)} \sum_{n=1}^{N} (\theta_{n-1} - \theta_n), \tag{6.3}$$

where θ_n is the phase advance of the 2D orbit. Although its performance is quite poor compared to the methods that will be explained later, it is still among the fundamental methods used to compute the frequency of a system.

6.1.2 Interpolated FFT

Given the signal, as in Eq. 6.1, is possible to determine an analytical formulae for the tune starting from the Fourier transform of the signal itself without the contribution of perturbative harmonics. The FFT coefficients of the signal in Eq. 6.1 read as

$$\phi(\nu_j) = \frac{1}{N} \sum_{n=1}^{N} e^{2\pi i n(\nu_0 - \nu_j)}, \tag{6.4}$$

where $\phi(\nu_j)$ are the FFT coefficients, N is the number of turns at which the sampling has been interrupted (thus it is equivalent to the number of available samples if the sampling frequency is of one turn), ν_0 is the tune and $\nu_j = j/N$, with $j = 0, \ldots, N$. The Eq. 6.4 has to be rewritten to

obtain the tune value ν_0 as a function of the other parameters, namely the FFT coefficients and the number of turns N. Using the following identities

$$\sum_{n=0}^{N-1} e^{2\pi i f n} = \frac{1-e^{2\pi i f N}}{1-e^{2\pi i f}}, \qquad \sin(x) = \frac{e^{ix}-e^{-ix}}{2i}, \tag{6.5}$$

it is possible to simplify Eq. 6.4 as:

$$\left|\phi(\nu_j)\right| = \left|\frac{\sin(\pi N(\nu_0-\nu_j))}{N\sin(\pi(\nu_0-\nu_j))}\right|. \tag{6.6}$$

From the knowledge that the highest FFT peak occurs at the frequency of the signal, it is possible to define the frequency $\nu_k = k/N$ as the value that maximises the FFT coefficients. Using Eq. 6.4 as interpolating function between ν_k and $\nu_{k\pm1}$ it is possible to write three equations that, if properly combined with each other, enable to write a closed-form solution of the equation for the tune ν_0 that reads as:

$$\nu_0 = \frac{k}{N} \pm \frac{1}{\pi}\arctan\left(\frac{|\phi(\nu_{k\pm1})|\sin\frac{\pi}{N}}{|\phi(\nu_k)| + |\phi(\nu_{k\pm1})|\cos\frac{\pi}{N}}\right). \tag{6.7}$$

The first term on the right-hand side of Eq. 6.7 is the peak of the FFT, and thus the frequency value that would be provided by the FFT analysis, which is then corrected with the second term on the right-hand side of Eq. 6.7. The complete proof to obtain Eq. 6.7 can be found in Ref. [52]. The choice of sign in the correction term depends on the values of the FFT coefficients around the highest FFT peak ($|\phi(\nu_{k\pm1})|$). Therefore, if $|\phi(\nu_{k+1})| > |\phi(\nu_{k-1})|$ it means that the tune k/N has to be corrected with a positive term and that the FFT tune is underestimating its actual value. On the contrary, if $|\phi(\nu_{k+1})| < |\phi(\nu_{k-1})|$ a negative correction is needed. The tune can be computed with a precision that scales as $1/N^2$, as reported and proved in Ref. [52]. For the sake of simplicity and explanation, the number of turns in the following example is fixed to 1000. Therefore, from the comparison of the precision of Interpolated FFT with the one of the FFT, the former provides a tune uncertainty of 10^{-6} , while the latter of 10^{-3}. The improvement obtained with the Interpolated FFT is very significant.

6.1.3 Hanning filtered FFT

The determination of an analytical equation for the tune is carried out on an unperturbed signal, as the one reported in Eq. 6.1 where the contribution of perturbative harmonics is neglected. Prior to the analysis of the frequency spectrum, the signal can be filtered with the Hanning filter $w_H(n)$, shown in Figure 6.1 and defined in Eq. 6.8. Filtering a signal is a well-known procedure in signal processing that aims at reducing the contribution of discontinuities at the ends of a signal caused by the lack of smoothness as the signal has a finite length. The Hanning filter reads as

$$w_H(n) = 2\sin^2\left(\frac{\pi n}{N}\right), \tag{6.8}$$

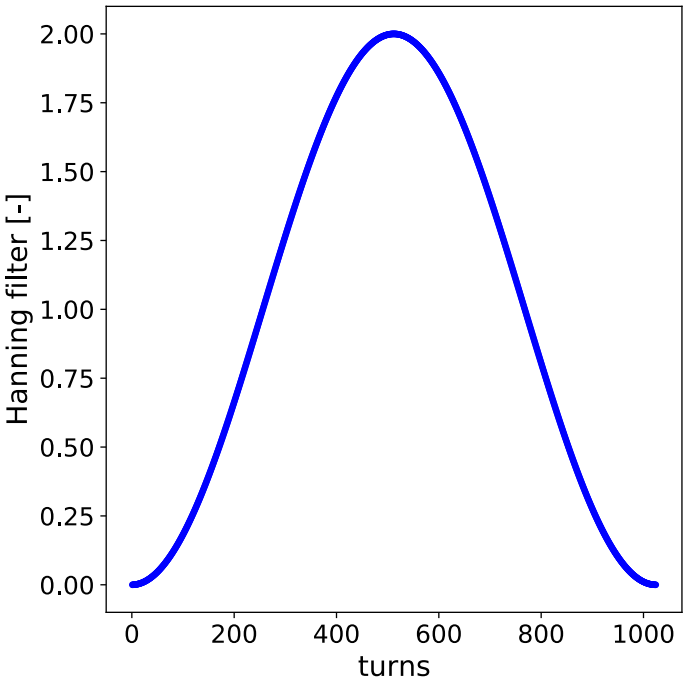

Figure 6.1: Hanning filter as a function of the number of turns for N fixed to 1024.

where N is the maximum number of sampling points and n is a linearly spaced vector that ranges between $n = 1,...,N$. There are many benefits in filtering the signal before performing the FFT analysis. If a signal with one frequency is analysed, the width of the main peak is increased, making its identification easier; however, a loss of resolution is also observed. In the current analysis, the analysed signal has perturbative harmonics located far from the main frequency, thus the filter increases the height of the main frequency peak and further reduces the contribution of the harmonics. These effects significantly increase the tune precision. Cases where perturbative harmonics or secondary frequencies are located close to the main frequency should be handled with care. Under these considerations, the unperturbed signal in Eq. 6.1 reads as:

$$z(n) = 2\sin^2\left(\frac{\pi n}{N}\right)e^{2\pi i \nu_0 n}, \tag{6.9}$$

and the FFT coefficients will read as:

$$\phi(\nu_j) = \frac{1}{N}\sum_{n=1}^{N} 2\sin^2\left(\frac{\pi n}{N}\right)e^{2\pi i n(\nu_0-\nu_j)}. \tag{6.10}$$

Using the relations in Eq. 6.5, is possible to rewrite Eq. 6.10 as a combination of sinusoidal and cosinusoidal functions, as reported in Eq. 6.11

$$\left|\phi(\nu_j)\right| = \left|\frac{\sin^2\left(\frac{\pi}{N}\right)\sin\left(\pi N\left(\nu_0-\nu_j\right)\right)\cos\left(\pi\left(\nu_0-\nu_j\right)\right)}{N\sin\left(\pi\left(\nu_0-\nu_j\right)\right)\sin\left(\pi\left(\nu_0-\nu_j+\frac{1}{N}\right)\right)\sin\left(\pi\left(\nu_0-\nu_j-\frac{1}{N}\right)\right)}\right|. \tag{6.11}$$

It is now possible to find an analytical equation for the tune assuming that the value of the frequency that maximises the FFT coefficients is $\nu_k = k/N$ and that it is possible to interpolate the peak ($|\phi(\nu_k)|$) with the two neighbours coefficients ($|\phi(\nu_{k+1})|$ and $|\phi(\nu_{k-1})|$). The analytical equation for the tune reads as:

$$\nu_0 = \frac{k}{N} + \frac{1}{2\pi}\arcsin\left(A(a,b,c)\sin\left(\frac{2\pi}{N}\right)\right), \tag{6.12}$$

where A is

$$A(a,b,c) = \begin{cases} \frac{-(a+bc)(a-b)+\sqrt{c^2(a+b)^2-2ab(2c^2-c-1)}}{a^2+b^2+2abc}, & |\phi(\nu_{k+1})| > |\phi(\nu_{k-1})| \\ \\ \frac{-(a+bc)(a-b)+\sqrt{c^2(a+b)^2-2ab(2c^2-c-1)}}{a^2+b^2+2abc}, & |\phi(\nu_{k+1})| < |\phi(\nu_{k-1})| \end{cases}$$

and the variables a, b and c reads respectively as:

$$a = |\phi(\nu_k)|; \qquad b = |\phi(\nu_{k\pm1})|; \qquad c = \cos\left(\frac{2\pi}{N}\right),$$

where the value of b depends on which one among $|\phi(\nu_{k+1})| > |\phi(\nu_{k-1})|$ and $|\phi(\nu_{k-1})| > |\phi(\nu_{k+1})|$ is satisfied. The complete mathematical proof can be found in Ref. [52] where the scaling law of $1/N^4$ is also retrieved. As performed at the end of the previous section, it is useful to consider a fixed number of turns to determine and compare the precision of different methods. Thus, in analogy to the previous consideration, the precision of the Hanning method is determined with $N = 1000$, that leads to a tune precision of 10^{-12}. This methods, compared to those already described, as the best tune precision.

6.2 Constant-amplitude signals

The first signals to be analysed are those that have a constant amplitude and a constant frequency during the sampling period. These signals represent, from an experimental point of view, the data obtained when a tune measurement with an AC dipole is performed, provided that the beam signal during the ramp-up and ramp-down of the magnet is neglected, since during this period the amplitude of the signal changes over time. The frequency spectrum of these signals can be analysed with the FFT as well as the analytical equations derived from the interpolation of FFT coefficients around the peak of the FFT, namely the interpolated FFT (briefly explained in Section 6.1.2) and the Hanning filtered FFT (that can be found in Section 6.1.3). Two additional methods will be discussed in the following section: the zero padding and the weighted Birkhoff average. The former is a very well-known technique in time series analysis that is often used to increase the signal length by adding zeros at the end of the signal [57], for this method a new analytical for the tune calculation equation will be proven. The latter is an approach developed in recent years [58] and for the first time applied to beam dynamics in the context of tune determination. In the following discussion it will be explained why an analytical approach is not feasible and only a numerical approach will be adopted and described.

6.2.1 Zero Padding

The zero padding technique consists in adding zeros at the end of a signal. It is a widely used technique in the analysis of time series for several different purposes; among these, the need to increase the length of a signal to the desired value (usually to match its length to the closest power of 2, since FFT algorithms have optimised performances for signals length equal to a power of 2) [59]. In Figure 6.2 the schematic representation of the zero padding technique and its effects is shown. In particular, the same signal is padded with different blocks of zeros, $l = 16$ for the red case (top) and $l = 32$ for the blue one (bottom), and each of them has $N = 128$ non-zero points. The effects on the frequency response are visible as a reduction of the bin size, or equivalently, as the increase in the number of points around the FFT peak (right plot in Figure 6.2). This procedure actually increases the length of the signal, therefore, causing a reduction of the bin size in the frequency spectrum. In fact, if the signal has a length equal to N, the bin size in the frequency domain is defined $1/N$. If l blocks of N zeros are added at the end of the signal, then the bin size becomes $1/(N(l+1))$. As a consequence, the number of available points around the main frequency is increased and it is possible to compute it more accurately. In this context, a new analytical equation has been determined for the calculation of the tune of a zero-padded signal. Consider a signal as in Eq. 6.1 without the contribution of perturbative harmonics, during the padding step l blocks of N zeros are added at the end of the signal, thus, the FFT coefficients read as:

$$\phi(\nu_j) = \frac{1}{N+lN} \sum_{n=1}^{N+lN} e^{2\pi i n(\nu_0-\nu_j)} = \frac{1}{N_1} \sum_{n=1}^{N_1} e^{2\pi i n(\nu_0-\nu_j)}, \tag{6.13}$$

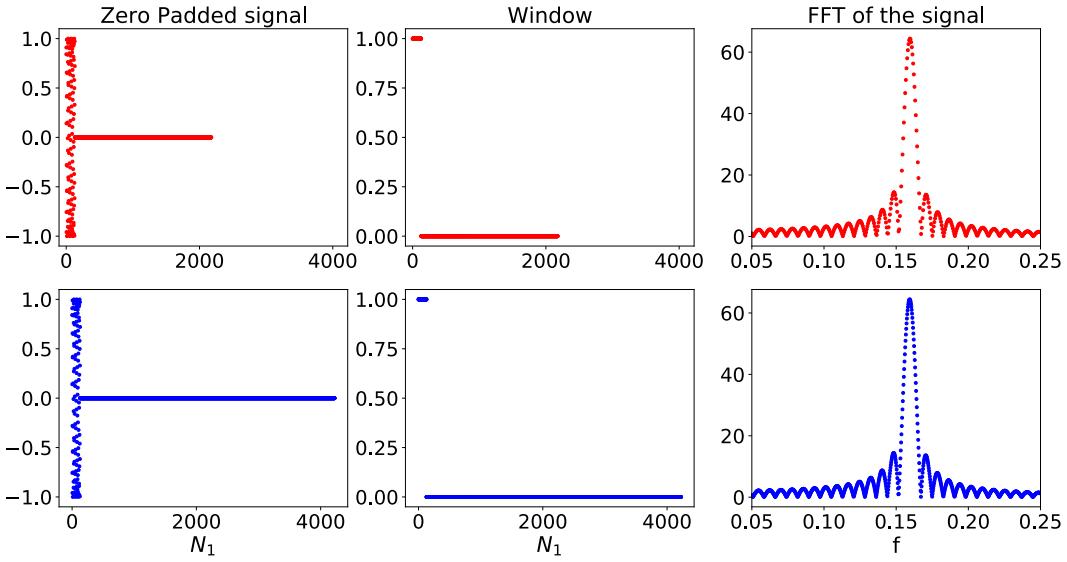

Figure 6.2: A signal with $\nu_0 = 0.15$ has been sampled with $N = 128$ points and has been padded with $l = 16$ (red case) and $l = 32$ (blue case). The total number of points of the signal is defined as $N_1 = N(l+1)$.

where $N_1 = N(l+1)$. It is possible to re-write Eq. 6.13 using the relation in Eq. 6.5 and thus, once the absolute value of the FFT coefficient is computed, it reads as

$$\left|\phi(\nu_j)\right| = \left|\frac{1}{N(l+1)}\frac{\sin\pi N(\nu_0-\nu_j)}{\sin\pi(\nu_0-\nu_j)}\right| . \tag{6.14}$$

The determination of a solution for Eq. 6.14 in terms of the tune ν_0, is performed by evaluating Eq. 6.14 at the frequency that maximises its value (namely $\nu_k = k/N_1$). In addition, using its neighbour values (located respectively at $\nu_{k\pm1}$) to evaluate the corresponding FFT coefficients ($|\phi(\nu_{k+1})|$ and $|\phi(\nu_{k-1})|$), it is possible to find the tune with a better precision than the FFT. To summarise, the solution of Eq. 6.14 for the tune ν_0 reads as:

$$\nu_0 = \frac{k}{N(l+1)} + \frac{1}{\pi}\arctan\left[\frac{(\alpha_{k+1}-\alpha_{k-1})\sin\frac{\pi}{N(l+1)}}{\alpha_{k+1}\left(\alpha_{k-1}\cos\frac{\pi}{l+1}-\cos\frac{\pi}{N(l+1)}\right)+\alpha_{k-1}\left(\alpha_{k+1}\cos\frac{\pi}{l+1}-cos\frac{\pi}{N(l+1)}\right)}\right], \tag{6.15}$$

where the variables $\alpha_{k\pm1}$ are defined as:

$$\alpha_{k\pm1} = \frac{\left|\phi(\nu_k)\right|}{\left|\phi(\nu_{k\pm1})\right|}. \tag{6.16}$$

The complete derivation can be found in Appendix C. The determination of the precision with which Eq. 6.15 determines the tune is performed considering the contribution of the perturbative term in the generation of the signal as defined in Eq. 6.1. Exploiting the linearity of the FFT, the FFT coefficients of the perturbed signal will be given by the sum of the unperturbed FFT

coefficients (defined as in Eq. 6.13) plus those of perturbative harmonics ψ, the FFT coefficients of the perturbed $\hat{\phi}$ signal evaluated at ν_k read as

$$\hat{\phi}(\nu_k) = \phi(\nu_k) + \frac{\psi(\nu_k)}{N(l+1)} = \phi(\nu_k) + \frac{\psi(\nu_k)}{N_1}. \tag{6.17}$$

Propagating this source of errors in all equations demonstrated in Appendix C, leads to the following scaling law:

$$\Delta\nu = \nu_0 - \hat{\nu}_0 = \frac{1}{N^2(l+1)^2} f\left(\cos\frac{\pi}{l+1}\right), \tag{6.18}$$

where f is a function that depends on $\cos\frac{\pi}{l+1}$ only, ν_0 is the the tune value used to generate the signal defined in Eq. 6.1 and $\hat{\nu}_0$ is the tune estimated from Eq. 6.15 where the FFT is performed on the perturbed signal defined in Eq. 6.1, thus in presence of perturbative harmonics. The Eq. 6.18 shows that the tune precision scales quadratically as a function of the number of non-zero samples as well as a function of the number of zero blocks l added at the end of the signal. If l would be equal to zero then the same scaling law as for the interpolated FFT (see Section 6.1.2) would be obtained, otherwise (for $l > 0$) a better precision than the interpolated is expected.

6.2.2 Weighted Birkhoff average

The behaviour of conservative systems with two or more degrees of freedom can be represented by multidimensional area-preserving maps. In the absence of perturbations, the dynamics of an integrable Hamiltonian system consists of periodic and quasi-periodic motion around a stable torus [58]. When the system is perturbed, some of these tori remain unperturbed, others are replaced by isolated periodic orbits or chaotic regions. As the perturbation strength increases, the resonance areas grow until they might even overlap and form a chaotic region. The weighted Birkhoff averages have recently been used in this context to distinguish between stable, resonant, or chaotic areas [58, 60]. For the first time, the use of the weighted Birkhoff average was applied to the study of transverse beam in Ref. [61], where the objective was to determine the tune of a test signal and estimate the precision of the method. Similarly to the procedure of filtering a signal prior to the FFT analysis (see Section 6.1.3), the weighted Birkhoff average is performed in two successive steps:

- the filtering step is performed at first by weighting the time series with the Birkhoff weights $w_B^\alpha(t,\beta)$ defined as

$$w_B^\alpha(t,\beta) = \exp\left(-\frac{1}{\beta t^\alpha(1-t^\alpha)}\right), \tag{6.19}$$

- then the weighted Birkhoff average $WB_N(f)$ is computed normalising the weighted time series by the sum of Birkhoff weights

$$WB_N(f) = \frac{1}{\sum_{n=1}^{N-1} w_B^\alpha(t,\beta)} \sum_{n=1}^{N-1} w_B^\alpha(t,\beta) f(z(n)), \tag{6.20}$$

where the weights $w_B^\alpha(t,\beta)$ have been defined in Eq. 6.19, $\beta \in \mathbb{R}$ is a coefficient, $\alpha \geq 1$ and $\alpha \in \mathbb{N}$, and $t = \frac{n}{N}$ is defined in the interval $]0,1[$ with $n = 1,...,N-1$ and $f(z(n))$ is a function of the signal $z(n)$ analysed.

The average defined as in Eq. 6.20 is performed for a fixed value of α and β. The Birkhoff weights are also defined in the normalised form $w^\alpha_{B,\text{Norm}}(t,\beta)$ according to:

$$w^\alpha_{B,\text{Norm}}(t,\beta) = \frac{w^\alpha_B(t,\beta)}{\sum_{n=1}^{N-1} w^\alpha_B(t,\beta)} \,. \tag{6.21}$$

The main result of the weighted Birkhoff average has been proven in Ref. [62] and states that:

$$\left| WB_N(f) - \lim_{N\to\infty} \frac{1}{N} \sum_{n=1}^{N-1} f(z(n)) \right| < C_k N^{-k}, \tag{6.22}$$

where C_k is a constant and $k \in \mathbb{N}$. Equation 6.22 means that the weighted Birkhoff average WB_N is super-convergent to the limit value of the time average of the function $f(z(n))$ with a precision that is proportional to $1/N^k$, thus in accordance to the required scaling law defined in Eq. 6.2. Before using this method on a signal, it is important to define the function $f(z(n))$ whose limit value has to converge to the value of the tune. From the state of the art section (see Section 6.1), it is possible to notice that the APA method (see Section 6.1.1) evaluates the phase advance between two successive iteration and its average (see Eq. 6.3) converges to the tune. Thus, if the value of $f(z(n))$ is the phase advance, then the weighted Birkhoff average $WB_N(f)$ converges to the tune of the signal analysed. In conclusion, the use of a filter such as the Birkhoff weights (and their normalised form) enables to remove any possible discontinuity of the signal at the ends and thus enhance the performance in the tune calculation.

Several combinations of coefficients α and β have been considered as a preliminary analysis, the aim being to understand whether it was possible to determine a couple of values $(\hat{\alpha},\hat{\beta})$ that provide the best performance in terms of tune calculation. In Figure 6.3 it is possible to observe how the distribution of normalised Birkhoff weights changes as a function of the parameters α and β. In particular, the normalised weight distribution increases its peak height and, obviously, reduces its widths for the smallest value of β. Although this feature seems to be promising because it could enable to strongly reduce the contribution of next-to-leading frequencies, in reality, this type of effect is not expected to be relevant when the reconstruction of the tune will be performed on the signal in Eq. 6.1, since its harmonics have been defined to be quite far from the tune ν_0. In Figure 6.3 it is also possible to observe that for large values of β the normalised weights distribution changes from a rectangular-like window (with the property of always being derivable infinity times at the ends, the name "rectangular-like" only refers to its shape and not to the properties of the actual rectangular window) to a wider Hanning-like window. The latter should be preferred since it is expected to perform better than the rectangular-like cases. Therefore, low values of α and β as well as high values of the same parameters (for example $\alpha = 4$ and $\beta = 350$) should be preferred than other combinations.

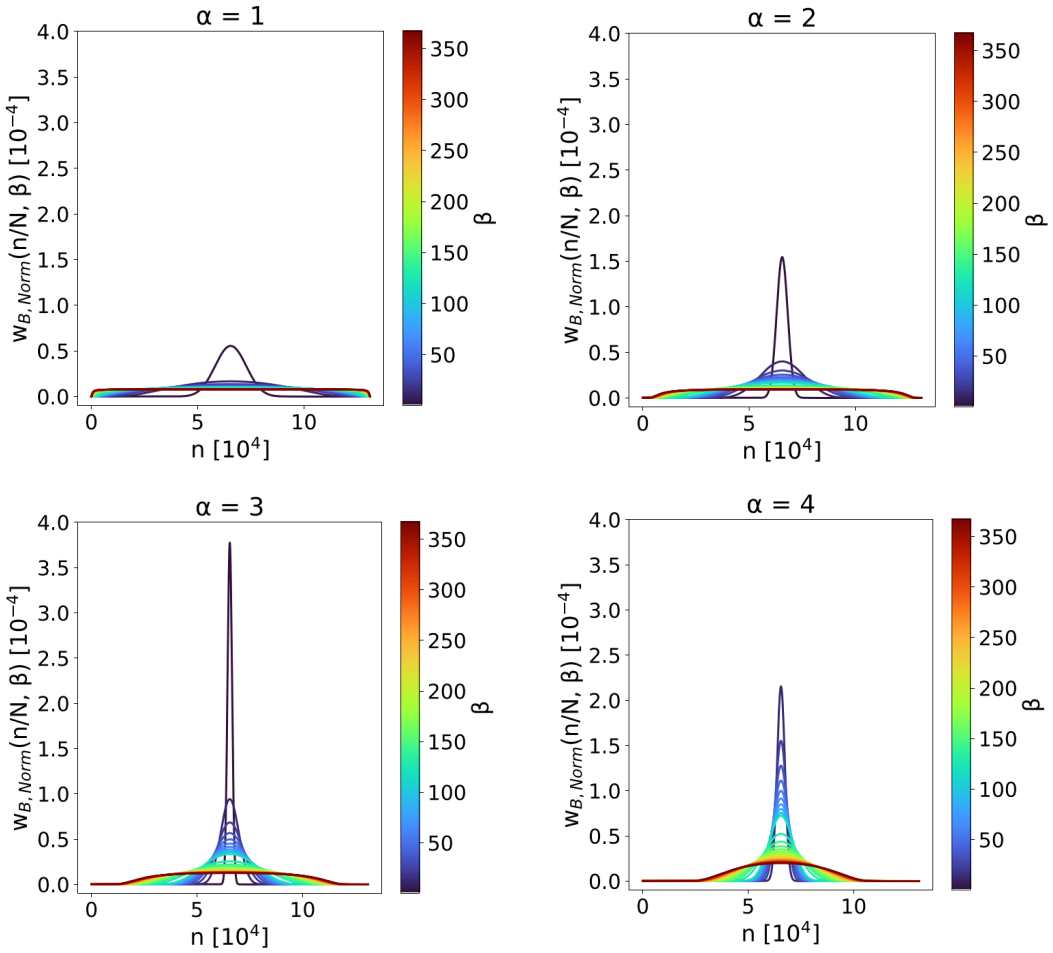

Figure 6.3: The normalised Birkhoff weights as a function of the parameters α (along the four plots) and β (which dependence is shown as a function of the colour) and for $N = 2 \times 10^5$.

6.2.3 Numerical simulation results

In the following section, the results of numerical simulations will be presented and discussed in detail. The section focuses on the analyses of the performances in the tune calculation for the time series in Eq. 6.1 using the methods discussed in the previous sections. At first, the performance of the methods described in the state-of-the-art section (see section 6.1) will be assessed. Then the zero-padding and the weighted Birkhoff average will be considered and discussed. The tune of the signal is computed with the above mentioned equations and methods on signal slices having increasing length. Thus, the tune error $\Delta\nu$ is computed as the absolute value of the difference between the tune value used to generate the signal and the one retrieved from the considered method. Moreover, the length matched a power of two being all the equations based on the FFT. This choice is justified by the fact that the FFT, and all the routines based on it, are optimised for signal length that matches a power of two.

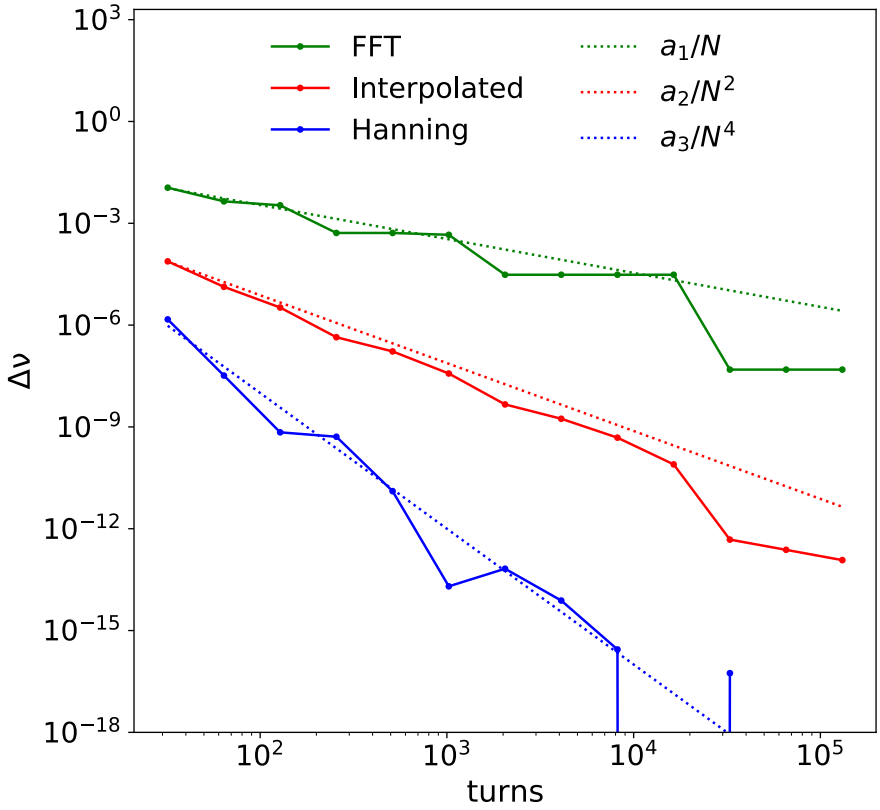

Figure 6.4: The discrete time series in Eq. 6.1 is analysed using the FFT method, shown in green, the Interpolated procedure, shown in red, and the Hanning filtering, reported in blue. The results of the fit of each method is reported with dotted line.

6.2.3.1 State of the art

The signal in Eq. 6.1, is evaluated for increasing integers values of n up to a maximum value N that has been fixed to 2×10^5 and the tune ν_0 has been fixed to 0.2612. The tune is then computed with the FFT, the Interpolated FFT (most of the time simply called Interpolated) and the Hanning filtered FFT (or simply Hanning). The tune error $\Delta\nu$ obtained from each method is shown in Figure 6.4. The FFT, Interpolated FFT and Hanning are shown in different colours (green, red, and blue, respectively). The numerical results of each method have been fitted to a/N^b, where b is equal to 1, 2 and 4 for the three aforementioned methods, respectively, the results of the fit are also shown in Figure 6.4 as dotted line. From the fit procedure, it is possible to obtain the coefficients a_1, a_2 and a_3, that read as $(17246.2 \pm 3.7) \times 10^{-5}$, $(379827.6 \pm 6.3) \times 10^{-7}$ and 1.00 ± 0.02, respectively. The use of the Hanning equation (Eq. 6.12) does not provide the value of tune error $\Delta\nu$ in three cases (number of turns larger than 10^4) because in those cases the machine precision has been hit.

The Interpolated FFT and Hanning methods will be considered as the references to compare the performance of new methods discussed in the next section. The FFT will not be considered as

reference since the aim is to determine new methods to compute the tune with an error $\Delta\nu$ that scales faster than the FFT.

6.2.3.2 Zero-Padding

The numerical results from the use of the zero-padding tune equation in Eq. 6.15 on a zero-padded signal are analysed. For the simulation, the signal in Eq. 6.1 has been generated with $\nu_0 = 0.28$ and $n = 1,...,N$, with $N = 8192$. Two different analysis have been performed on the signal:

- In order to estimate the effect of the number of non-zero points N on the tune estimation, the signal was cut into slices of increasing length (up to $N = 8192$), each of them equal to a power of 2. Then each slice was padded with $l = 32$ blocks of zeros, each of them containing as many zeros as the length of the considered slice. With this procedure, it was possible to check whether the scaling law of the tune error in Eq. 6.18 with l fixed was respected.

- The second analysis consisted of determining what the effect of an increasing number of zero-blocks l added at the end of the signal was on the determination of the tune. Therefore, the number of non-zero points N was fixed to 8192 and the number of blocks, each of them of length N, added at the end of the signal was varied between 1 and 128. Also in this case, the aim was to check whether the scaling law in Eq. 6.18 was retrieved.

The results from the application of the zero padding tune equation (see Eq. 6.15) for both analysis were compared with the standard FFT, the Interpolated FFT (Eq. 6.7) and the Hanning filter (in Eq. 6.12). The results are reported in Figure 6.5.

In Figure 6.5 left, the results from the first analysis, where the tune of the signal has been calculated for increasing length of the signals slices with a fixed number of zero blocks $l = 32$, is shown. The Interpolated FFT (shown in red) and Hanning (in blue) methods are not distinguishable and provide values comparable to those of the FFT (in green). This means that when these two methods are applied to a padded signal it is not possible to retrieve the typical scaling law defined in the previous sections ($1/N^2$ and $1/N^4$, respectively). Therefore, the use of the Interpolated FFT or the Hanning filtered method should not be used in the frequency analysis of a padded signal. The result of the zero padding method have been fitted to the expected scaling law a_1/N^2 where $a_1 = (26.23 \pm 1.36) \times 10^{-3}$.

In Figure 6.5 right, the tune precision is computed as a function of the number of zero blocks l with the number of non-zero points fixed $N = 8192$. In analogy to the previous case, the Interpolated and Hanning methods are superimposed and they provide tune values comparable to those of the FFT, thus, no improvement is observed with respect to the FFT itself. The zero padding equation scales as predicted in Eq. 6.18, in fact, the fit law is $a_2/(l+1)^2$ with $a_2 = (66.54 \pm 1.32) \times 10^{-6}$, while the oscillations are justified by the co-sinusoidal term in Eq. 6.18.

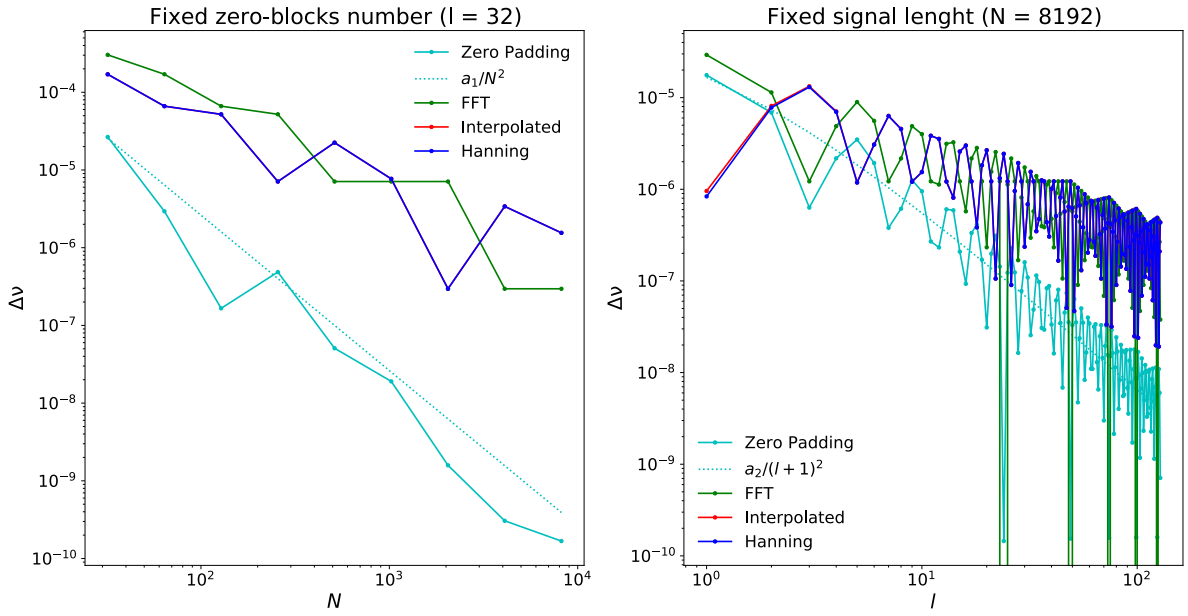

Figure 6.5: The dependence of the tune error on the number of non-zero points of the signal for a fixed value of zero blocks (N changing and l fixed) is shown on the left picture; while the dependence of the tune error on the number of zero blocks for a fixed number of non-zero points of the signal (l changing and N fixed) is shown on the right picture.

In conclusion, if there is the need to add zeros at the end of the signal before performing frequency analysis, it is convenient then to determine the tune with the zero padding equation in Eq. 6.15 rather than with one of the methods described in the state-of-the-art Section 6.1.

6.2.3.3 Weighted Birkhoff average

The tune determination for the signal in Eq. 6.1 is now performed with the weighted Birkhoff average method (described in Section 6.2.2) and the results are compared with the Interpolated and Hanning techniques. The signal in Eq. 6.1 was generated with $\nu_0 = 0.2612$ and it was sampled for $N = 2 \times 10^5$ turns. As previously discussed in Section 6.2.2, it was decided to compare the performances of four different values of the parameter α (ranging from 1 to 4) and 35 values of the parameter β from 0.1 to 360. The results of this analysis are reported in Figure 6.6.

As a first comment, it is important to highlight that the Interpolated and Hanning methods show the same trend as those obtained in the state-of-the-art (see Figure 6.4), thus $1/N^2$ and $1/N^4$, respectively. Moreover, their value does not change in the four plots because the analysis is performed on a signal that does not change its feature, what is changing are the parameters used in the Birkhoff weighted average.

As far as the results obtained from the use of the weighted Birkhoff averages are concerned:

- From the comparison of the results reported in Figure 6.6, there are particular combinations of α and β parameters for which the tune error $\Delta\nu$ scales faster than Hanning. For example,

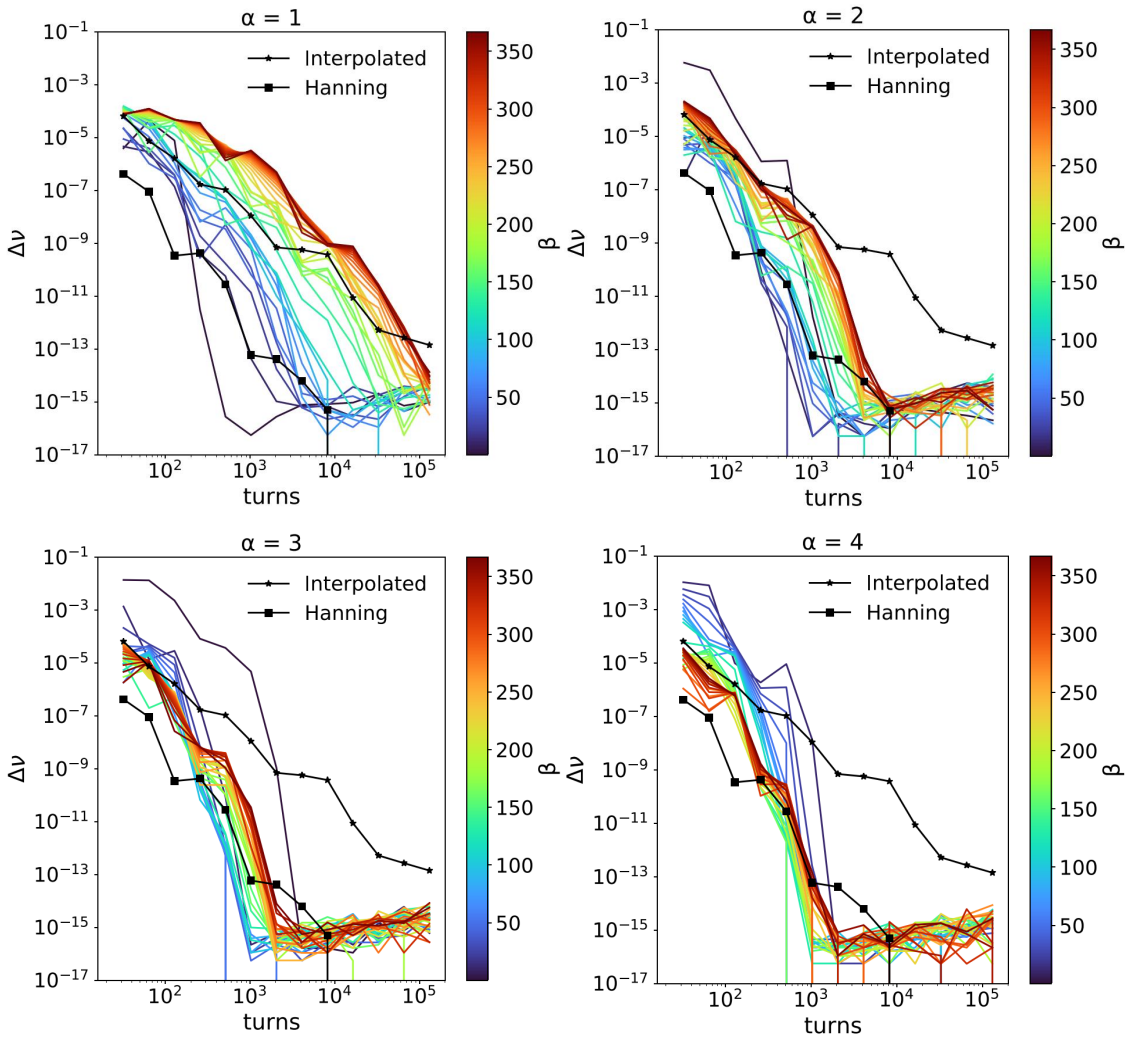

Figure 6.6: The tune of the signal was calculated using the weighted Birkhoff averages for $\alpha = 1,...,4$ and different values of the coefficient β. The results are then compared with the interpolated FFT (shown as black stars) and the Hanning filter method (black squares).

if the case with $\alpha = 1$ (Figure 6.6 top-left) is considered, then low values of β provide better tune estimation than high values of β. This is caused by the normalised weight distribution, as briefly explained in Section 6.2.2. In fact, a rectangular-like distribution uses similar (or equal) weights for points located at different distance from the main frequency. On the contrary, low values of β ensure a Hanning-like normalised weight distribution, thus, weighting the points closer to the main frequency more than those located further away and thus reducing the contribution of additional harmonics.

- This behaviour tends to invert as α increases. For example, for $\alpha = 4$ (Figure 6.6 bottom-right) it is not possible to identify a value of β, among the tested ones, for which the rectangular-like shape of the weights distribution is obtained. However, it is expected to

find a rectangular-like distribution for values of $\beta > 360$ (corresponding to the maximum tested value in these simulations). From Figure 6.3, the normalised Birkhoff weights distribution is comparable to a Hanning-like window for almost all the tested values of β. In particular, the lower the value of β the narrower is the distribution.

- For the cases with $\alpha \geq 2$, the weighted Birkhoff average reaches the machine precision ($\approx 10^{-16}$) for $N \geq 1024$, the larger the value of β the larger is the number of turns at which this saturation phenomenon occurs. In addition, it is possible to observe that this difference is less evident as α increases.

In conclusion, for $\alpha = 1$ and $\alpha = 2$ low values of β should be preferred because of the evident improvements in computing the tune with a better precision; for $\alpha = 3$ a relevant difference between the tested values of β can be observed at large number of turns (namely, $N > 512$) where low values of β allow for a tune error convergence to machine precision at 1024 turns rather than 2048 (achieved for large values of β); for $\alpha = 4$ larger values are clearly preferred. In order to determine the scaling law with which the tune is computed, only the set of the above described combination of parameters will be analysed. The result of the fit procedure can be observed in Figure 6.7. The fit law used in the analysis was a/N^b where both the exponent b and the proportionality coefficient a were fit to the data. For the tested values of $\alpha = 1, \ldots, 4$, the values of the exponent b obtained from the fit varies from a minimum value of (5.7 ± 0.3), for $\alpha = 1$, to a maximum value of (7.2 ± 0.4), for $\alpha = 4$.

Although it seems that the scaling law of the tune error increases its steepness as the value of α increases, it has been checked with numerical simulation that this behaviour saturates and that the actual maximum precision that can be obtained is $1/N^{8.7\pm0.2}$ for $\alpha = 7$. Moreover, it has to be taken into account that as soon as the value of α increases, significant changes occur in the distribution of the normalised weights; thus, a narrow peak around the main frequency. Although having a tune error that scales as $1/N^{8.7\pm0.2}$ seems to be very appealing, in reality it is not actually possible to exploit this feature. In fact, on the one hand it is possible to notice that the number of turns at which the saturation phenomenon occurs does not change significantly (it is always located ≈ 1024 turns). On the other hand, at smaller number of turn ($N < 1024$) the tune error is several order of magnitudes larger than the one provided by the Interpolated FFT (and thus also by Hanning and weighted Birkhoff averages with smaller values of α). As a consequence, the fastest scaling law is not achieved by the reach of machine precision at a lower number of turns, but rather from a larger tune error in that region. It is also worth mentioning, that as the value of α increases (above the maximum simulated, thus $\alpha > 4$) there are issues in the evaluation of the Birkhoff weights, defined in Eq. 6.19, due to numerical overflow or underflow. However, it has been demonstrated [58, 60, 62] that a possible way to overcome this issue would be to adopted extended precision.

From the studies and the analysis reported so far, one specific case seems to clearly emerge as a preferred one. From Figure 6.6 top-left, the case with $\alpha = 1$ and $\beta = 1$ emerges as the one

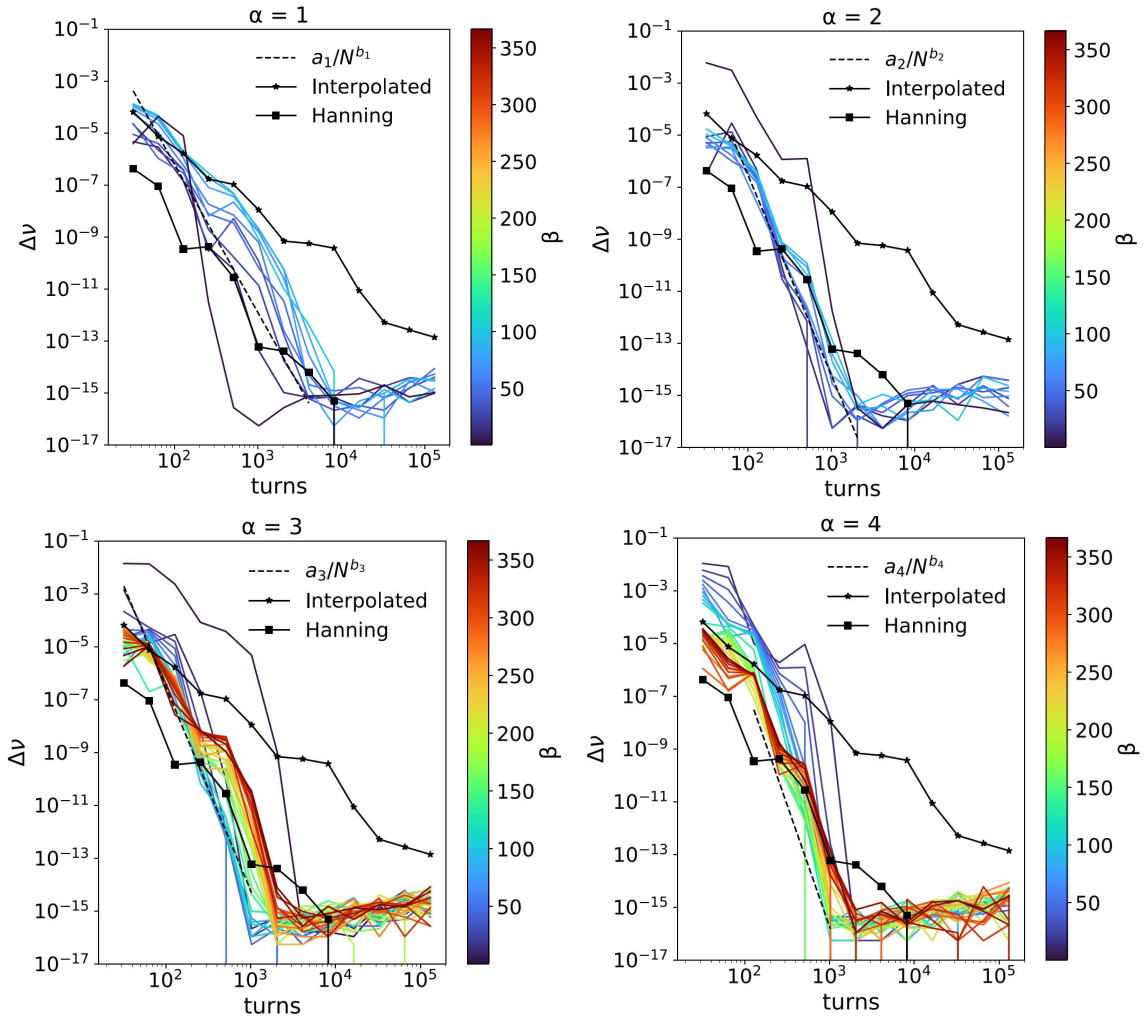

Figure 6.7: For the four different values of the parameter α, the fit procedure was performed over a limited set of the parameter β. The fit law is shown as a dashed black line.

with the fastest tune error scale, namely $1/N^7$. Thus, in the next studies, the weighted Birkhoff average will be performed with these values, except if explicitly stated.

6.2.4 Hénon map: analysis of a 4D dynamical system

The Hénon map is one of the simplest dynamical system featuring rich dynamical behaviours. It can be used to describe the 4D motion, in terms of (x, p_x, y, p_y), in a FODO lattice where a single sextupole has been installed. The Hénon map is defined as [52]:

$$\begin{cases} x_n = x_{n-1}\cos 2\pi\nu_{x,0} + \left(p_{x,n-1} + (x_{n-1}^2 - y_{n-1}^2)\right)\sin 2\pi\nu_{x,0} \\ p_{x,n} = -x_{n-1}\sin 2\pi\nu_{x,0} + \left(p_{x,n-1} + (x_{n-1}^2 - y_{n-1}^2)\right)\cos 2\pi\nu_{x,0} \\ y_n = y_{n-1}\cos 2\pi\nu_{y,0} + \left(p_{y,n-1} - 2x_{n-1}y_{n-1}\right)\sin 2\pi\nu_{y,0} \\ p_{y,n} = -y_{n-1}\sin 2\pi\nu_{y,0} + \left(p_{y,n-1} - 2x_{n-1}y_{n-1}\right)\cos 2\pi\nu_{y,0}\ . \end{cases} \tag{6.23}$$

The Hénon map can be used to determine the evolution of a particle orbit over N turns. Thus, from the definition of M initial conditions within the interval $[0,1]$ for the x and y variable, it is possible to cover the physical space (x, y). At the first step, thus when x and y have the values defined by the initial conditions, the momenta p_x and p_y are taken to be zero. Therefore, all the initial conditions are defined, and the turn-by-turn 4D Hénon map evolution can be determined. The number of turns has to be properly chosen. If the aim is to determine whether a certain condition is stable or not on the long term, the number of turns has to be high, usually values larger than 10^3 are chosen. In the context of the present discussion $N = 10^5$, $\nu_{x,0} = 0.28$, $\nu_{y,0} = 0.31$ and 1000 initial conditions along the x and y directions were generated; thus, in total 10^6 initial condition are studied. From a preliminary analysis it was observed that the interval $[0,1]$ had only unstable initial conditions for $x > 0.6$ and $y > 0.5$, thus it was decided to reduce the upper limit of the interval to 0.6 on both planes. This choice allowed to have more information on the stable conditions, keeping unchanged the number of conditions generated, that was previously fixed to 10^6. To determine whether the initial conditions are stable or not, the radius of the 4D hypersphere is computed for each of them at every turn as:

$$R(n) = \sqrt{x_n^2 + p_{x,n}^2 + y_n^2 + p_{y,n}^2}\ , \tag{6.24}$$

where the subscript n refers to the fact that the stability is evaluated at every turn n up to the maximum tracked turn N or until the stability is lost. From the knowledge that unstable conditions are characterised by having extremely large oscillation amplitudes due to the dominant contribution of the polynomials term in Eq. 6.23, it is possible to define the condition of stability as:

$$R(n) \leq 2 \quad \forall n \leq N\ , \tag{6.25}$$

where the value 2 is quite arbitrary. In fact, from the first results obtained it was seen that the stability zone was observed for $x < 0.6$ and $y < 0.5$, consequently, no stable condition will have oscillation amplitudes greater than 1 in the four simulated dimensions x, p_x, y and p_y. Therefore, considering 2 as the limit value for the distinction between stable and unstable conditions in Eq. 6.25, does not change the nature of the initial condition itself (if it is stable, it will be so regardless

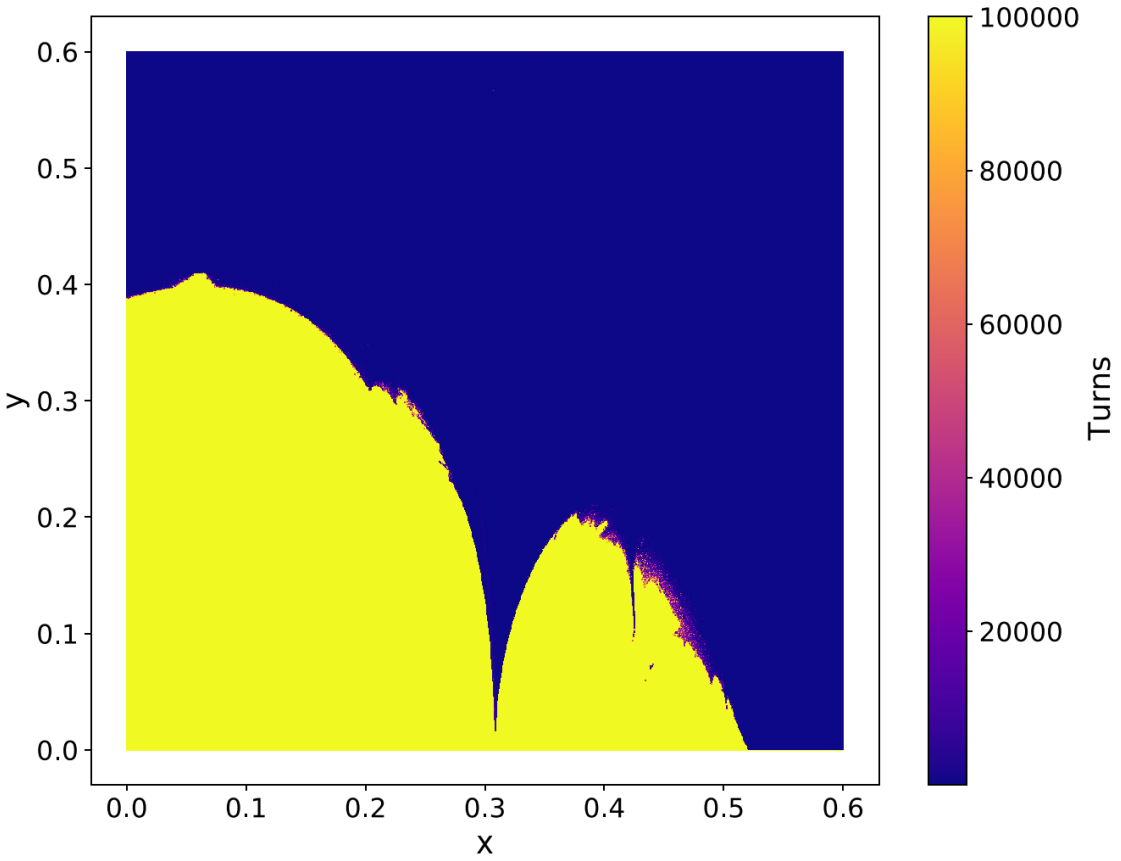

Figure 6.8: Stable and unstable initial conditions are shown as a function of the number of turns at which the stability is assessed.

of the value used in Eq. 6.25, the same is true for unstable conditions). As a consequence, the effects of the chosen value are noticed in the transition zone between stable and unstable initial conditions, the higher the chosen value, the more turns (therefore, more time) it will be necessary to see the instability of the analysed condition. The results of the tracking procedure are reported in Figure 6.8, where the colour of every initial condition refers to the turn at which the stability is lost. Thus, the yellow area refers to those conditions that after 10^5 turns were still stable, while the blue area refers to those that have been lost within the first turns, and thus are classified as unstable. Moreover, it is possible to observe that the region that separates stable from unstable conditions is made up by conditions whose stability is lost after some thousands turns. This phenomenon highlights the fact that the transition is quite sharp although a very thin intermediate region can be identified at $x \approx 0.45$. It is now of great interest to study further in detail the stable conditions. In fact, among these it is possible to identify resonant ones, thus particular combinations of (x, y) for which a resonant condition is satisfied. For the sake of

simplicity, even if the resonant condition can be found in Eq. 2.40, it is reported here as well:

$$\ell \nu_x + m \nu_y = p \ , \tag{6.26}$$

where ℓ, m, and p are integer coefficients and the first two respect the following condition $|\ell| + |m| = N_{\text{res}}$, where N_{res} is the order of the resonance. To determine what stable conditions are resonant, it is necessary to compute the horizontal ν_x and vertical ν_y tunes with one of the methods described before. In particular, it was decided to perform this analysis using the Hanning filtered FFT and the weighted Birkhoff average (with $\alpha = 1$ and $\beta = 1$), being these methods those with the fastest scaling law for the determination of the tune error. Thus, the resonant condition in Eq. 6.26 is computed until the 10^{th} order (meaning $N_{\text{res}} = 1, \ldots, 10$) and all those initial conditions for which

$$0 \leq \ell \nu_x + m \nu_y - p \leq \epsilon \ , \tag{6.27}$$

with $\epsilon = 10^{-2}$, is satisfied are considered resonant conditions. To assess how these methods perform as a function of the number of turns, the tune is calculated for $N = 1024$ and $N = 32768$. Moreover, it is expected to observe a difference in the number of resonant conditions detected by the two methods being their precision quite different ($1/N^4$ for Hanning and $1/N^7$ for Birkhoff).

6.2.4.1 Numerical simulation results for constant frequency Hénon map

The results from the application of the Hanning method in the determination of resonant conditions are reported in Figure 6.9, where only the stable conditions up to 10^5 turns have been displayed (yellow area, in accordance with the colour notation of Figure 6.8), unstable conditions have not been reported to simplify the identification of resonant conditions. In Figure 6.9, resonant initial conditions (on the right) and their corresponding vertical and horizontal tune (left) are shown in the physical space (x, y) and the tune diagram, respectively. The colour of each resonant condition refers to the distance ϵ from the resonant line.

Three peculiar regions can be identified. In fact, on Figure 6.9 right, for $x \approx 0.05$ and $y \approx 0.38$, $x \approx 0.18$ and $y \approx 0.3$, $x \approx 0.45$ and $y \approx 0.15$ three regions very close to a resonance appear, as the colour highlights. From the comparison of the results obtained for $N = 1024$ (top) and those obtained for $N = 32768$ (bottom), it appears that all three regions are more populated by resonant conditions. This observation is in accordance with the ability of the Hanning method to better estimate the tune when the signal is evaluated for a larger number of turns and thus, possibly increase the number of resonant conditions.

From the comparison of the results obtained with the Hanning method (in Figure 6.9) and the weighted Birkhoff average (in Figure 6.10), the resonant conditions computed with the latter method appear to be almost the same as those computed with the former. The major difference is in the on-resonant region located at $x \approx 0.05$ and $y \approx 0.38$ previously identified as such by the Hanning method. Using the weighted Birkhoff averages over an orbit length of 1024 (Figure

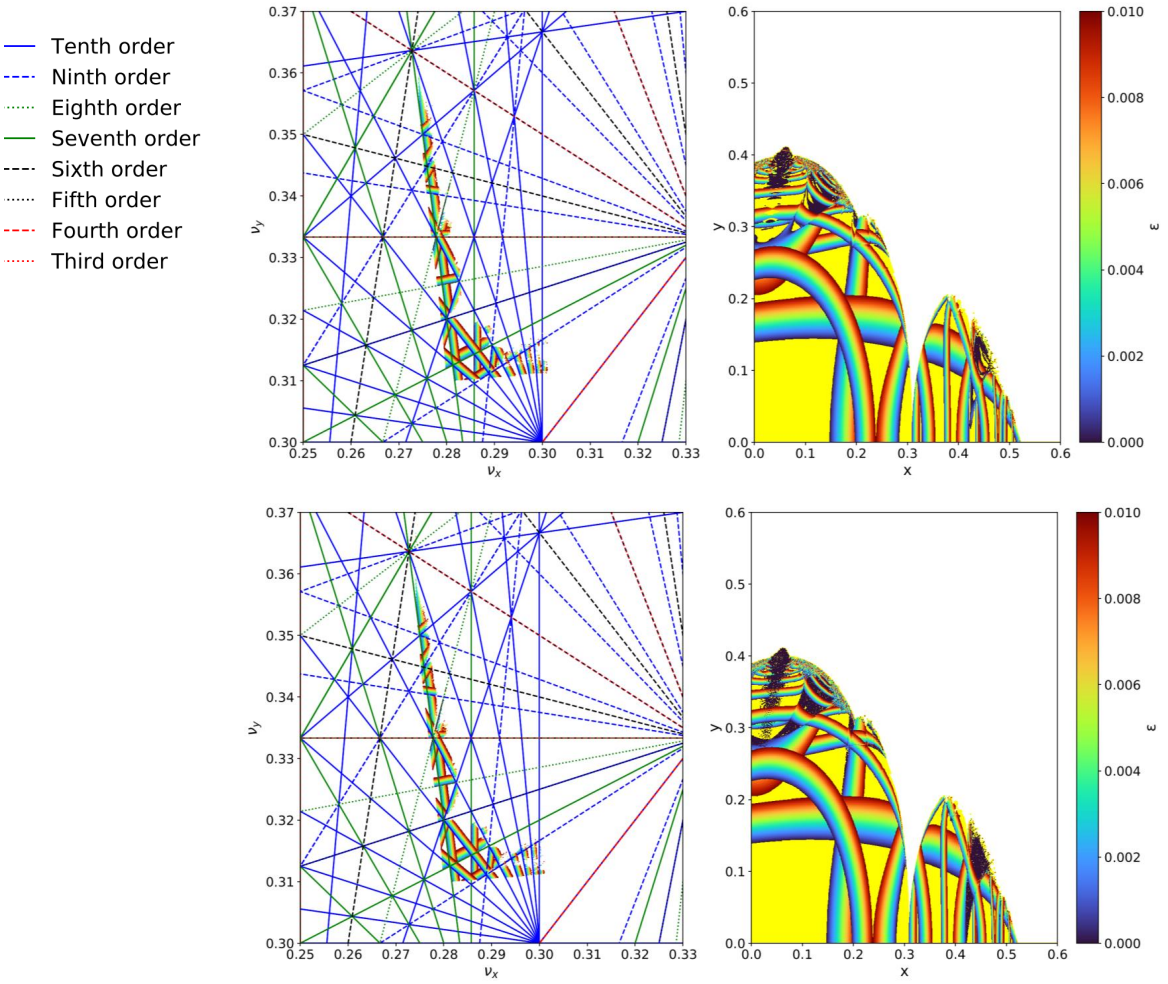

Figure 6.9: The tune computed with the Hanning method for $N = 1024$ (top) and $N = 32768$ (bottom) enables the determination of resonant conditions (right) and their corresponding tunes (left). The colour of the resonant conditions identifies the distance to the resonance line.

6.10 top) and 32768 (Figure 6.10 bottom), it is possible to notice that the outermost and the central on-resonance regions (thus those located at $x \approx 0.45$ and $y \approx 0.15$ and $x \approx 0.18$ and $y \approx 0.3$, respectively) are composed of resonant conditions very close to resonance lines, and, as previously observed with Hanning, the number of resonant conditions increases when the tune is computed over a longer signal slice (namely, 32768 rather than 1024). On the contrary, the innermost region (located at $x \approx 0.05$ and $y \approx 0.38$) is actually composed of resonant conditions located at different distances from the resonant lines, as highlighted by the multitude of different colours. In fact, in Figure 6.10 left, those conditions correspond to the new horizontal-like line that appears in the tune diagram compared to the Hanning tune diagram (Figure 6.9 left). Even though those conditions do not appear as resonant bands in the initial condition diagram (Figure 6.10 right) but rather as a chaotic region, it is clear from the tune estimation at $N = 32768$ (Figure 6.10 right-bottom) that a more regular structure appears compared to the one retrieved for $N = 1024$

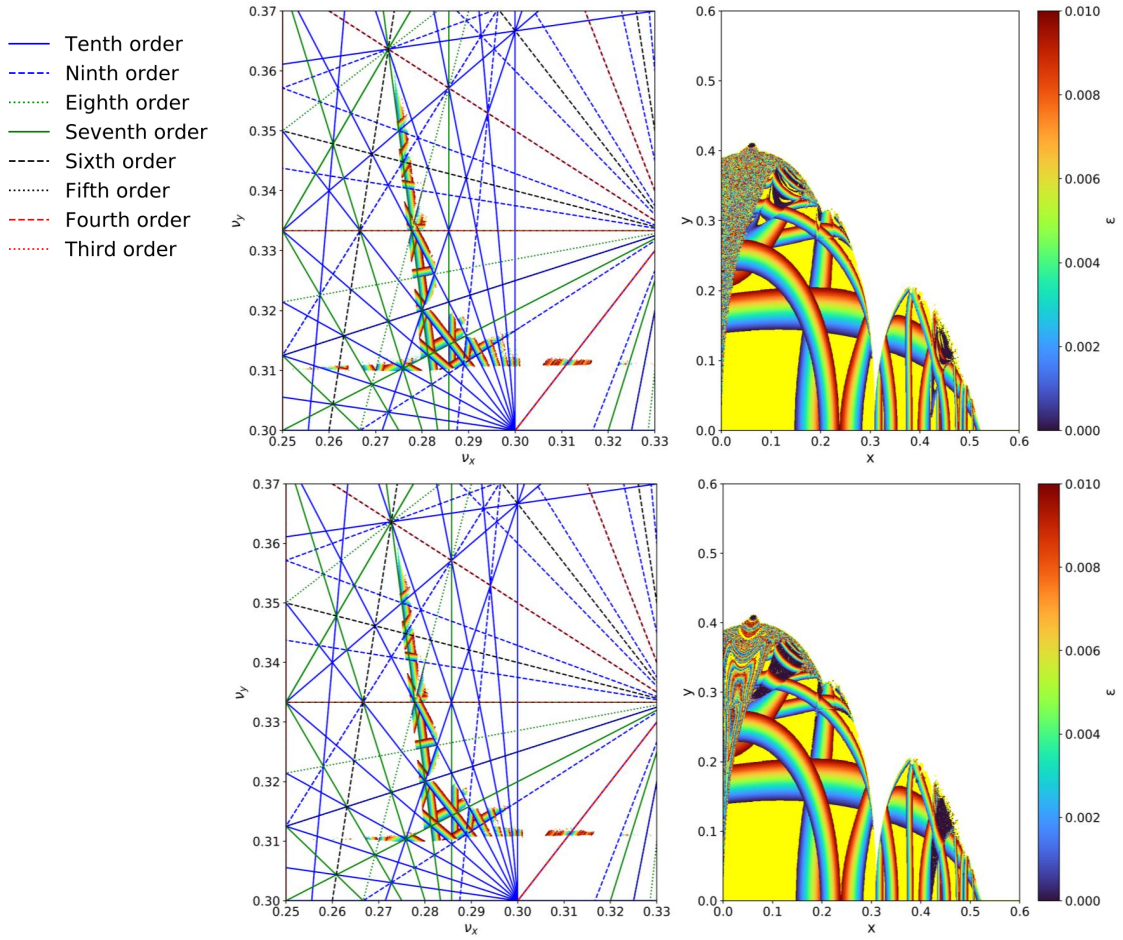

Figure 6.10: The tune computed with the weighted Birkhoff average for $N = 1024$ (top) and $N = 32768$ (bottom) enables the determination of resonant conditions (right) and their corresponding tunes (left). The colour of the resonant conditions identifies the distance to the resonance line.

(comparison Figure 6.10 bottom and top). In fact, curved lines made of conditions at the same distance from a resonant line clearly appear.

From the comparison of Figure 6.9 and Figure 6.10 it is clear how Birkhoff identifies resonant conditions that were not detected by Hanning. Therefore, highlighting the strength of the method.

An additional way to observe similarities and discrepancies between the two methods and if, for the selected method, peculiar behaviours emerge as a function of the number of turns is looking at the tune distance (TD) defined as:

$$TD = \log_{10} \sqrt{(\nu_x(0:N-1) - \nu_x(N:2N-1))^2 + \left(\nu_y(0:N-1) - \nu_y(N:2N-1)\right)^2}\,, \tag{6.28}$$

with N fixed to 1024 first, and then to 32768. The results are reported in Figure 6.11, where the tune distance for the Hanning method is reported on the top while that computed with Birkhoff is on the bottom. The colour of each point is the ten-based logarithm of the tune distance. Therefore, for a given resonant initial condition, the closer the horizontal and vertical tunes (evaluated on

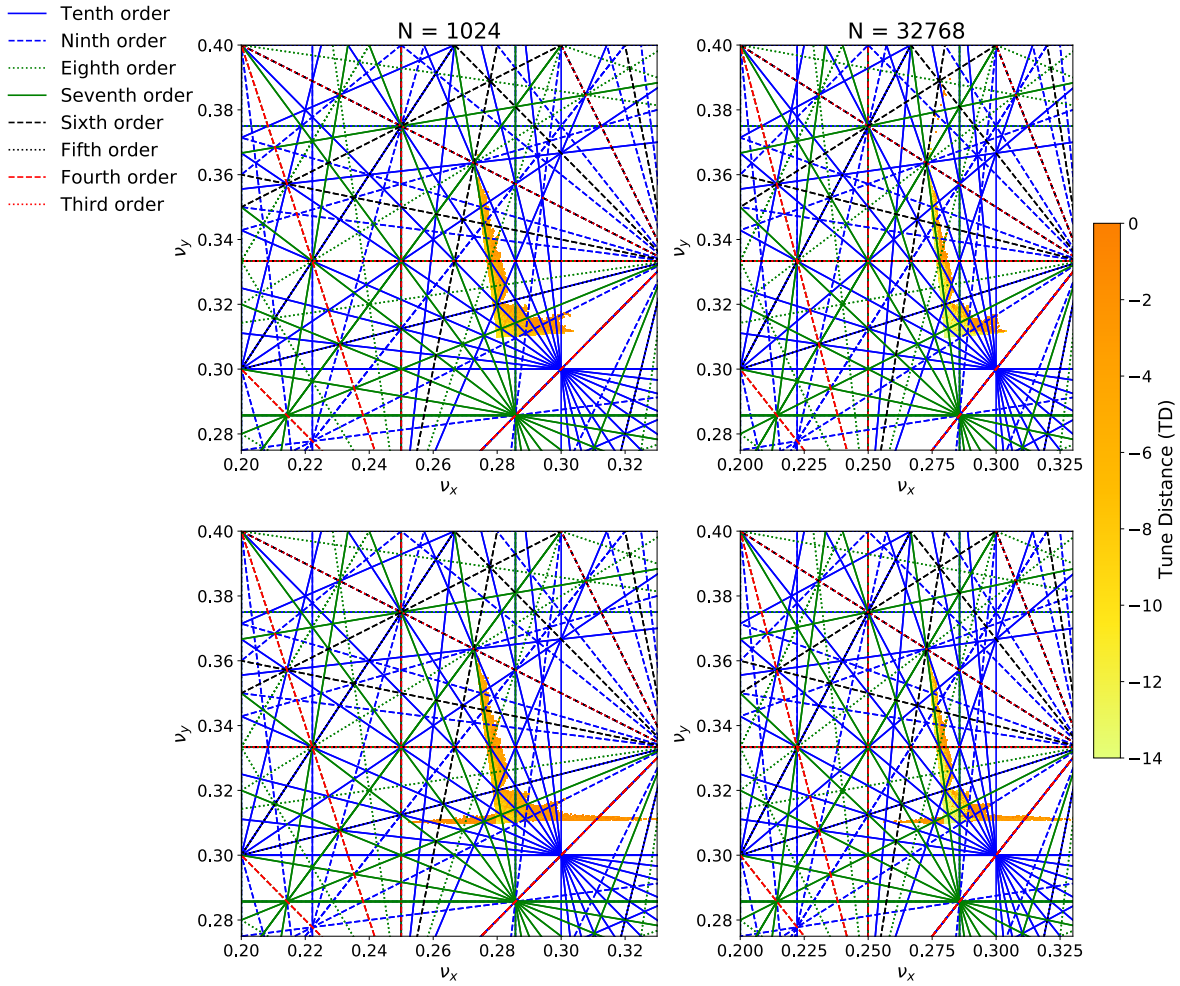

Figure 6.11: The tune distance for $N = 1024$ (left) and $N = 32768$ (right) computed with the Hanning method (top) and with Birkhoff averages (bottom). The tune distance reduces (thus the colour moves from the orange to the yellow) as the values of the tunes get closer between two consecutive slices of the signal of length N. Thus when $N = 32768$ is considered a wider yellow area emerges.

two successive signal slices of length N) are, the smaller the tune distance is, thus the colour goes towards the yellow. From Figure 6.11 it can be observed that as the number of turns, over which the tune (horizontal and vertical) is evaluated, increases from left $N = 1024$ to right $N = 32768$, the yellow area also increases for both methods. This means that the tune distance in Eq. 6.28 decreases, i.e. the difference in the frequency evaluated on two successive slices of the signal, each of them with length N, decreases.

Both methods have a precision that scales (in different ways) as a function of the number of turns, consequently it was expected that as the number of turns increases (by comparing the left plot with the right one in Figure 6.11) the difference between the two tunes diminished.

In order to better comprehend whether the Hanning method provides a better tune estimation

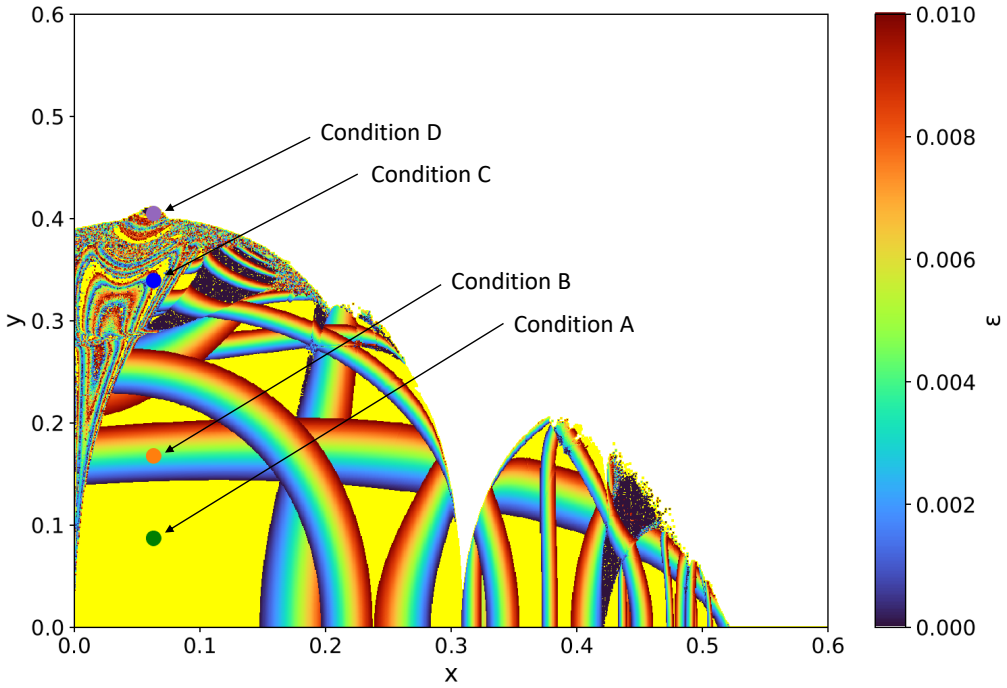

Figure 6.12: In the physical space space the resonant conditions have been computed with Birkhoff for $N = 32768$ and the four selected orbits have been highlighted.

than the weighted Birkhoff average in the region with $x < 0.1$ over a wide range of y ($0.3 < y < 0.4$), or whether the opposite holds true or if both methods will converge to a different situation on a long term, thus with $N > 10^5$; studies on particular initial conditions have been carried out. In particular, for x fixed to ≈ 0.630, four different orbits have been selected. In Figure 6.12, the four conditions are reported in the physical-space diagram, where it is possible to note that the four conditions have been picked to be in the stable non-resonant region (the condition will be named A), in the stable resonant band (the condition will be named B), then a condition in the chaotic region identified by both Hanning and Birkhoff has been picked (the condition will be named C) and finally a condition in the region very close to resonance located at $y \approx 0.4$ has been selected (the condition will be named D). These four orbits hare reported in Figure 6.13 (for conditions A and B) and Figure 6.14 (for conditions C and D) , where, for each condition, the four projections of x, p_x, y, p_y evolution are reported on the left, while on the right the 4D evolution can be observed. The orbit of Condition A and B show their regularity in Figure 6.13, and their projections on the (x, p_x) plane as well as the one on (y, p_y) plane show the characteristic circular path. However, conditions C and D, in Figure 6.14 show significant distortions, up to the limit of having three loops (for condition D).

A set of 10 conditions around Condition A, B, C and D have been selected to determine the evolution of the horizontal and vertical tune as a function of the number of turns. In fact, it is of great interest to understand similarities and discrepancy of the Hanning and Birkhoff methods

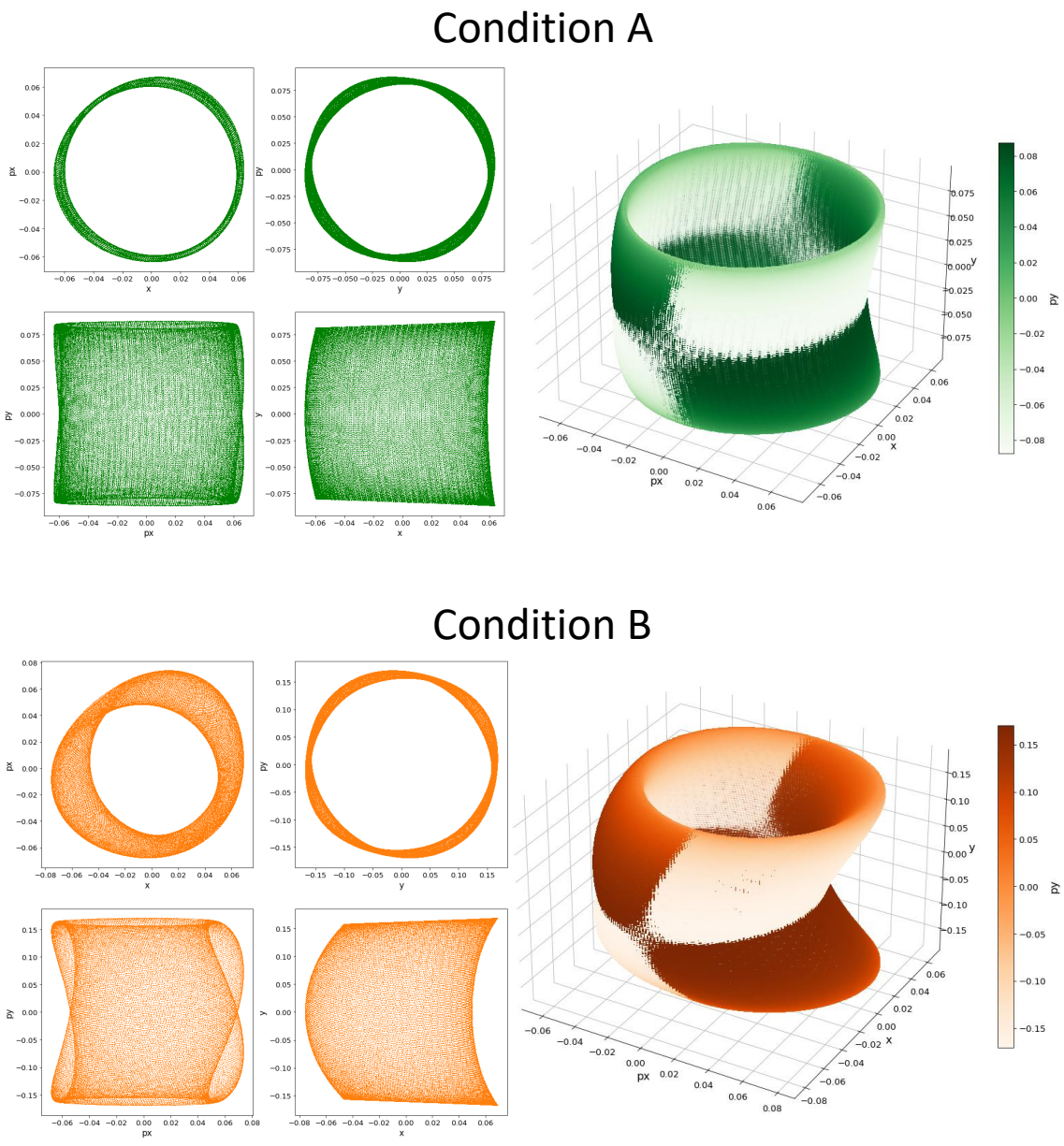

Figure 6.13: Stable non-resonant (condition A) and resonant (condition B) orbits. The orbit projections are reported on the left while the 4D evolution of the orbit itself is shown on the right.

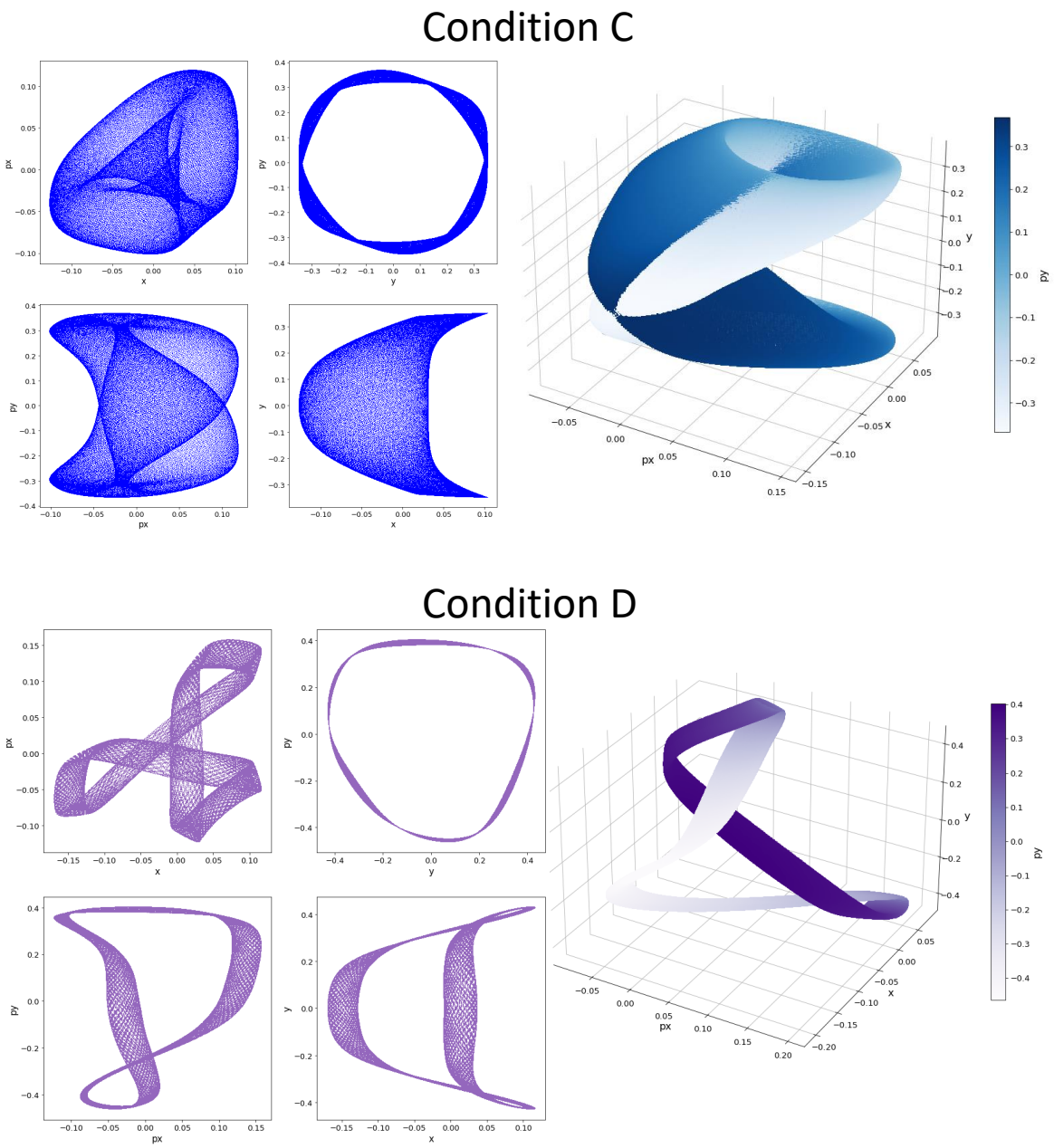

Figure 6.14: Stable resonant orbit in the chaotic region (condition C) and a stable resonant orbit very close to resonance (condition D). The orbit projections are reported on the left while the 4D evolution of the orbit itself is shown on the right.

in the four selected regions, where major discrepancies have been observed (see for reference Figure 6.9 and Figure 6.10). The tune analysis for the ten conditions around each selected orbit is reported in Figure 6.15. For the selected orbits around the Condition A the horizontal and vertical tune in Figure 6.15 is computed up to machine for both methods, but the weighted Birkhoff averages reaches a better precision (on both planes) at a halved number of turns smaller than Hanning (16×10^3 for Birkhoff versus 32×10^3 of Hanning). However this behaviour is partially lost when orbits around condition B are considered. In fact, on the vertical plane the same features highlighted before are still observed, while on the horizontal plane, both methods scale linearly as a function of the number of turns. This behaviour could be partially explained observing the orbit in Figure 6.13, the major difference is detected on the projections on the horizontal phase-space (x, p_x). As soon as the orbit shows small distortions (as Condition B and Condition C in figure 6.13 bottom and Figure 6.14 top, respectively) or significant orbit distortion highlighted by the presence of loops (as Condition D in Figure 6.14 bottom), the tune calculation becomes more complicated. A possible explanation has been found in the way the two methods compute the tune. The Hanning method retrieves the tune from the FFT spectrum, while the Birkhoff ones relies on the evaluation of the average phase advance between two consecutive turns. Therefore, possible issues related to the evaluation of the phase advance in presence of orbit distortion could be expected. However, additional studies to determine the final shape of resonant conditions are foreseen. In particular, a longer tracking for $N > 10^5$ to understand the long term convergence of the resonant conditions located at $x < 0.1$ and over a wide range of y should be the first step to complete this analysis. In fact, at the moment it is not possible to conclude whether the system will converge to a configuration more similar to the one determined by Hanning or by the one determined by Birkhoff. It is also necessary to consider the possibility that the convergence will be different than the one described by the methods.

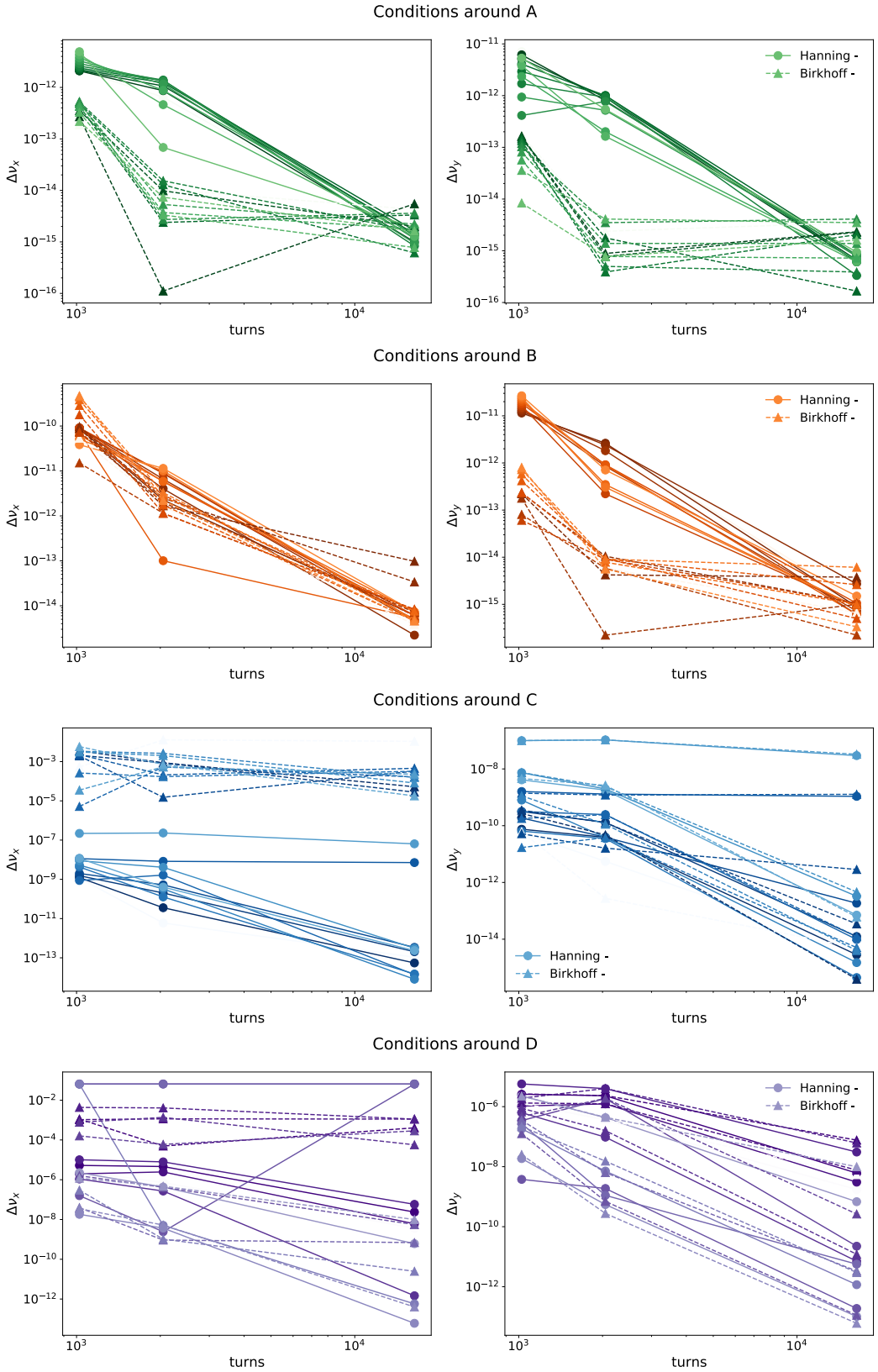

Figure 6.15: Comparison of the performance in the horizontal (left) and vertical (right) tune calculation as a function of the number of turns for the Hanning and Birkhoff methods in the four selected regions of the Henon map.

k	Ω_k	$\epsilon_k[10^{-4}]$
1	$2\pi/868.12$	1.000
2	$2\Omega_1$	0.218
3	$3\Omega_1$	0.708
4	$6\Omega_1$	0.254
5	$7\Omega_1$	0.100
6	$10\Omega_1$	0.078
7	$12\Omega_1$	0.218

Table 6.1: Tune modulation parameters

6.2.4.2 Numerical simulation results for modulated Hénon map

A similar analysis is performed in presence of tune modulation. In this case, the Hénon map defined in Eq. 6.23 has tunes ν_x and ν_y that change as a function of the number of turns according to [63]:

$$\begin{aligned} \nu_x(n) &= \nu_{x,0}\left(1+\epsilon_{\text{mod}}\sum_{k=1}^{7}\epsilon_k\cos\Omega_k n\right) \\ \nu_y(n) &= \nu_{y,0}\left(1+\epsilon_{\text{mod}}\sum_{k=1}^{7}\epsilon_k\cos\Omega_k n\right), \end{aligned} \tag{6.29}$$

where $\nu_{x,0}$ and $\nu_{y,0}$ are the nominal tunes used in the previous analysis, 0.28 and 0.31, respectively. The tune perturbation in Eq. 6.29 has $\epsilon_{\text{mod}} = 10$ and the other parameters are defined in Table 6.1 [63]. Similarly to what has been performed before, the same 10^6 initial conditions, used for the constant tune analysis case, have been used in this case as well. The Hénon map defined in Eq. 6.23 with the tunes in Eq. 6.29 has been tracked for 10^5 turns and the stability of each condition is evaluated as in Eq. 6.24. As previously explained, the choice of the values (namely, 4) used to determine whether an initial condition is stable or not, does not affect its stability, but rather the time (or equivalently, the number of turns) needed for an unstable particle to get lost. As a consequence, to enable a direct comparison of the stable conditions diagrams with and without frequency modulation, the same equation (namely, Eq. 6.24) has been used to evaluate the stability condition. Stable and unstable conditions are shown in Figure 6.16. From the comparison between Figure 6.8 and Figure 6.16, the region that divides stable from unstable conditions is not as thin as it was in the absence of tune modulation. An increased number of initial conditions becomes unstable, with a reduction of 9.13% in the actual number of stable conditions. The tune of stable conditions is computed using two methods (Hanning and Birkhoff) and slicing the signal at two different lengths (1024 and 32768). The results of this analysis can be found in Figure 6.17 and Figure 6.18, for Hanning and Birkhoff respectively.

In Figure 6.17 right, the identification of resonant conditions with the Hanning method is reported in the tune diagram whereas the same is shown in physical space on the left, and the colour refers to the distance from the resonant line. The horizontal and vertical tunes of

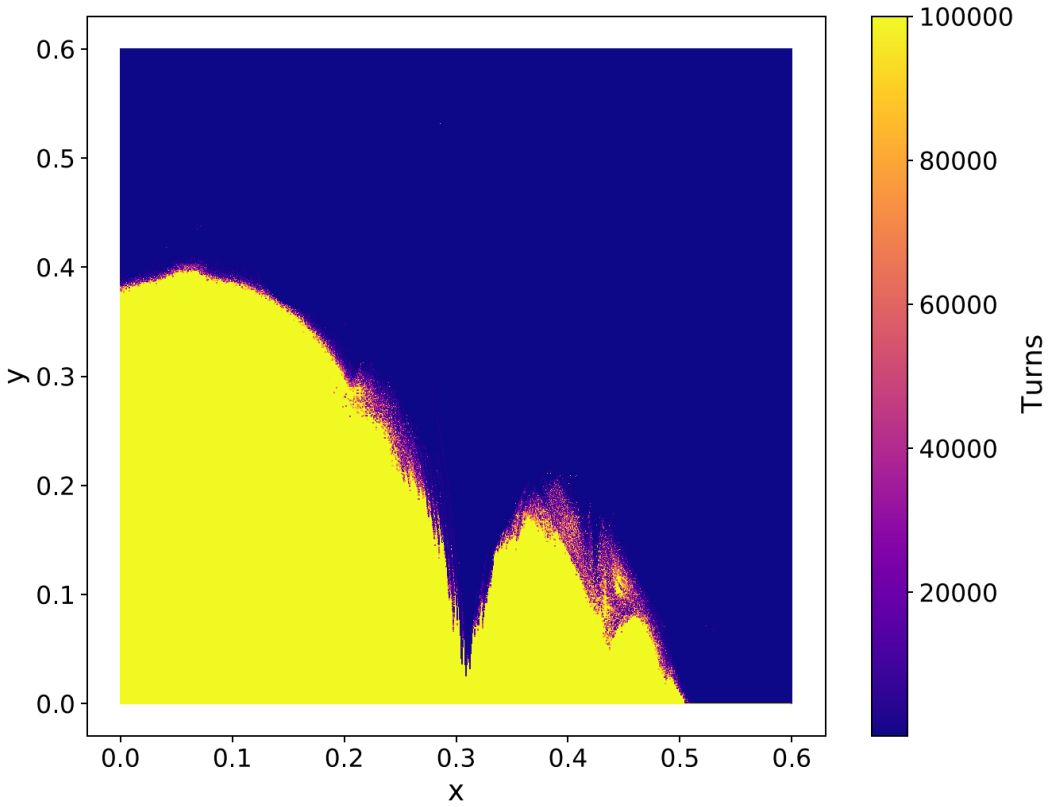

Figure 6.16: Stable conditions are shown in yellow while unstable ones have a colours that directly refer to the turns at which the stability is lost. Due to the frequency modulation introduces in the Hénon map, the transition from stable to unstable region is more gradual.

these conditions are reported in the tune diagram, in Figure 6.17 left. On the rows the analysis differentiate for the number of turns over which the tune is computed: 1024 on the top and 32768 on the bottom. Resonant conditions close to the edge of the stable region as well as those located close to the intersection of two different resonant lines show a blurred effect which becomes more evident when the signal length increases. Thus, a loss of smoothness in the evolution of coloured resonant conditions bands close to unstable region can be observed. From the comparison of the results obtained with constant tunes (refer to Figure 6.9) and those obtained in presence of tune modulation (Figure 6.17) few differences can be noticed. The blurred effect on some resonant conditions is more evident. In particular, this phenomenon is also observed at the intersection between points close to different resonance ($x \approx 0.2$ and $y \approx 0.27$), and it is even more evident for $N = 32768$ (bottom of Figure 6.17). In addition, the on-resonance region (located at $x \approx 0.05$ and $y \approx 0.35$) that was clearly visible in Figure 6.9 is now divided into two main regions. As a consequence of the frequency modulation a new set of resonant conditions can be identified close to the origin of the physical space (x, y), however, as the number of turns increases, their tunes are better calculated and they fall beyond the maximum distance from the resonant line $\epsilon = 10^{-2}$

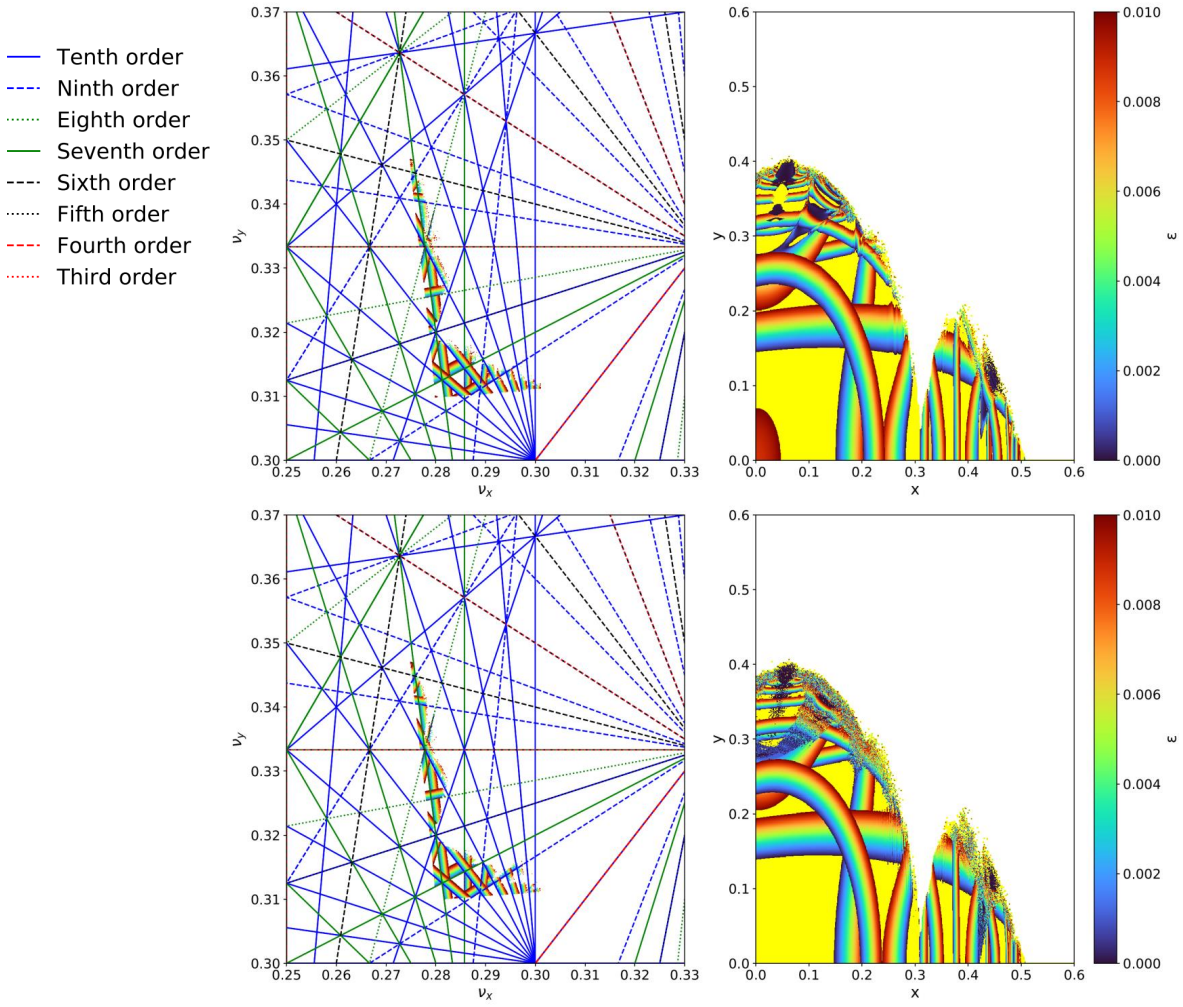

Figure 6.17: Tune and initial conditions diagram, where the resonant conditions are coloured as a function of their distance from the resonant line. The analysis is performed with the Hanning method for two different signal slice lengths: 1024 on the top and 32768 on the bottom.

and thus are classified as stable conditions.

The results obtained with the weighted Birkhoff average are reported in Figure 6.18. The same new region in proximity of the origin of the physical space is detected by Birkhoff too; and, also in this case, the conditions are classified as stable non-resonant conditions when the tune is evaluated over a longer signal slice. The blurred effect in the tune diagram (Figure 6.18 right) is more relevant for those conditions closer to the unstable region and in close proximity of the intersection between conditions on different resonant lines. Moreover, this effect seems to be more evident when a longer signal is analysed, in accordance with what has been observed from Hanning results. In fact, in Figure 6.18 top, the tune evaluation is performed on a slice of the signal made of 1024 samples, while on the bottom 32768 have been selected. In comparison to the results obtained in absence of frequency modulation (see Figure 6.10) the initial conditions

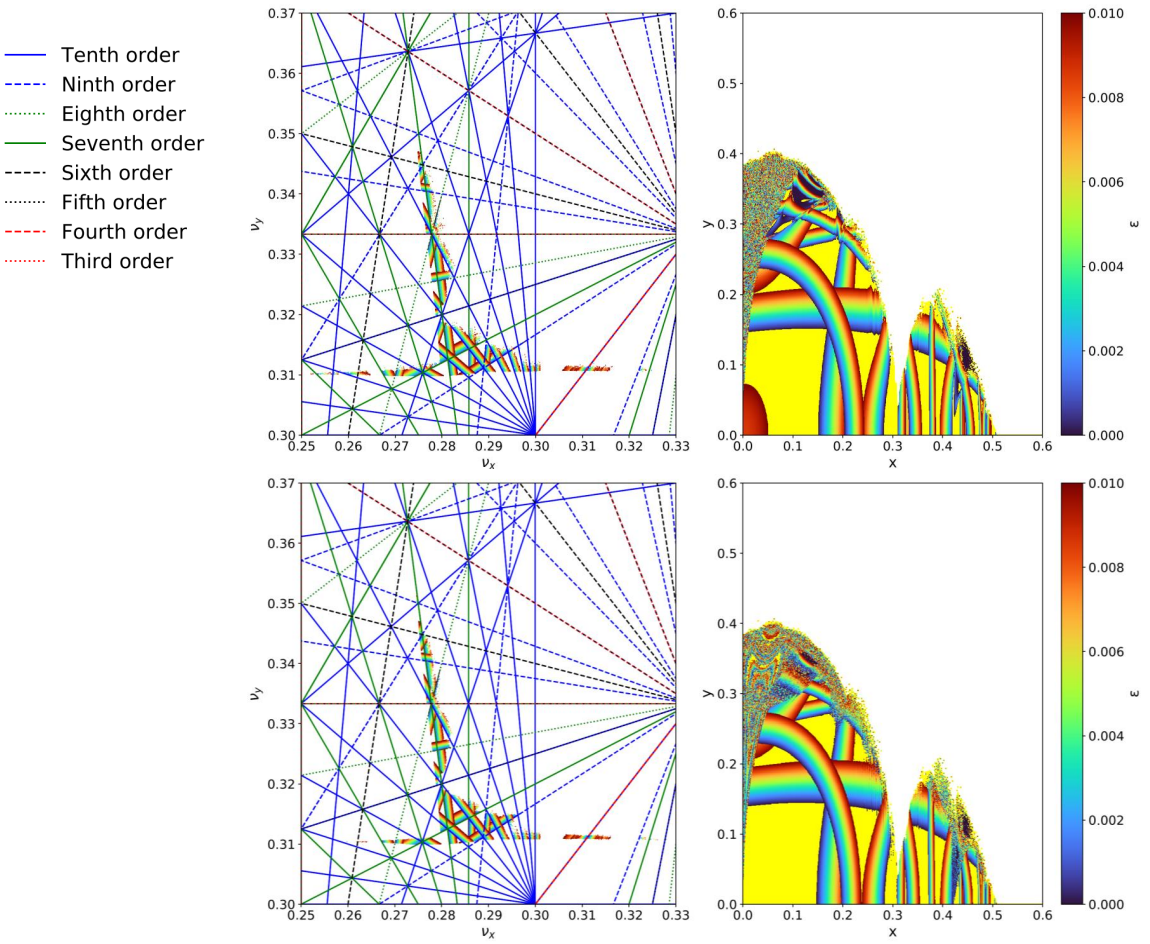

Figure 6.18: The horizontal and vertical tune are calculated with the weighted Birkhoff averages for two different Hénon map slices lengths: 1024 on the top and 32768 on the bottom.

on-resonance are left almost unperturbed by the frequency modulation, although a blurred effect is still visible at the edge of each resonant band. Major differences can be observed in the other subset of initial conditions close to resonance (located at $x \approx 0.18$ and $y \approx 0.31$), although its identification is performed also for a smaller signal length ($N = 2014$ on Figure 6.18), as a larger slice is considered ($N = 32768$ on the bottom of the same plot) a larger number of resonant conditions is identified. This can be observed fro the thickening of the line at the edge of the stable conditions, thus in the vicinity of the unstable region.

Thus in presence of frequency modulation both methods seems to provide different results than those obtained in absence of frequency modulation. As far as the chaotic region detected by Birkhoff for $x < 0.1$ and over a wide range of y is concerned, few elements can be identified. As a first consequence of the increased length of the signal slice, the dimension of the chaotic region is increased. Moreover, a clearer identification of a diagonal line above the first horizontal band of resonant conditions can be performed, especially if compared to the case in the absence

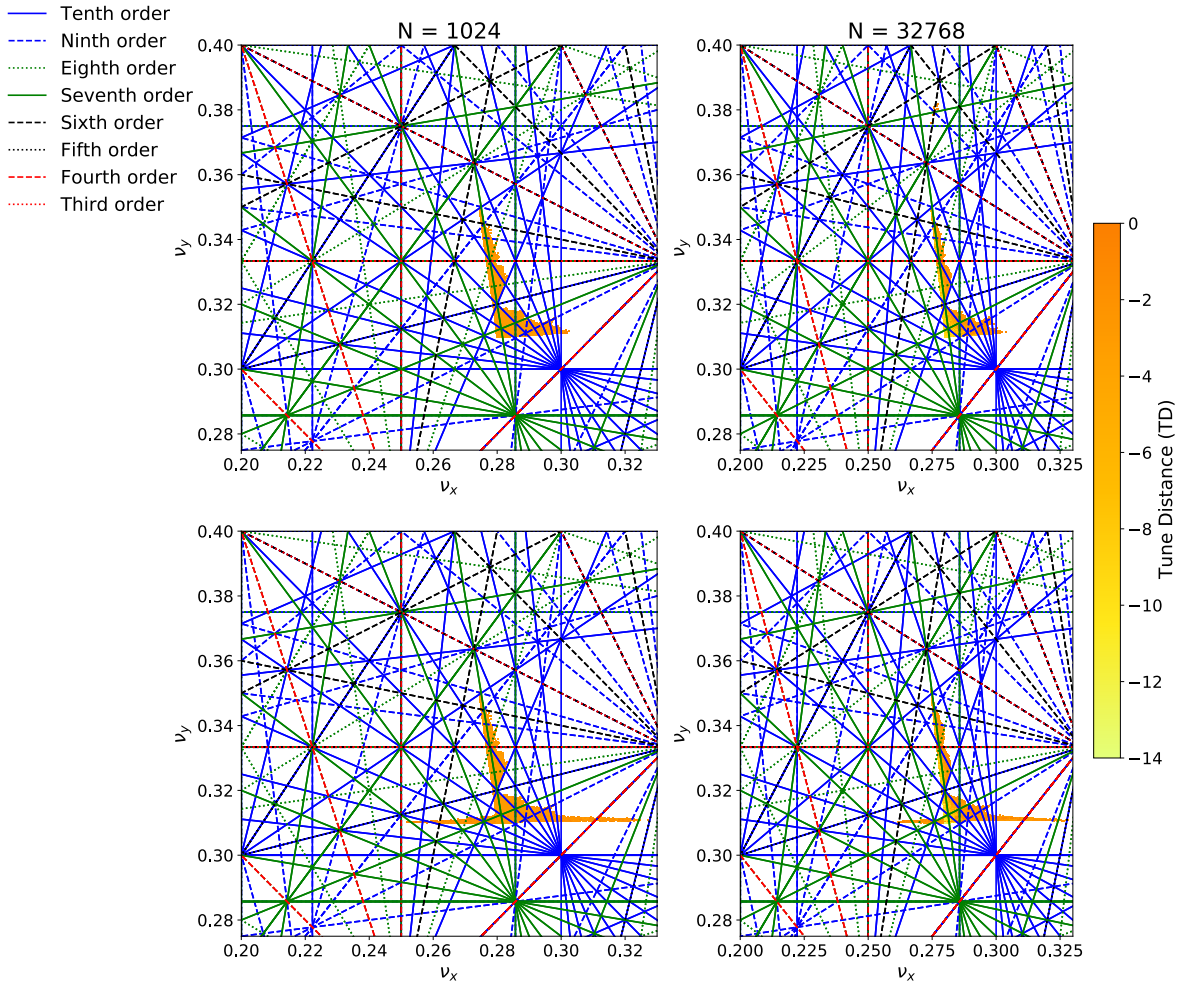

Figure 6.19: The tune distance for $N = 1024$ (left) and $N = 32768$ (right) computed with the Hanning method (top) and with Birkhoff averages (bottom). The tune distance slowly reduces (thus the colour moves from the orange to yellow) as the values of the tunes get closer between two consecutive slices of the signal of length N. The dominant colour is the orange highlighting the relevant contribution of the frequency modulation that does not allow for a convergence of the tune to the same value between to consecutive signal slices.

of perturbation in Figure 6.10. This line thickness becomes more evident when the tunes are evaluated on a higher number of revolutions (32768, Figure 6.18 bottom). Furthermore, it is important to highlight that, in accordance with what happened in the absence of frequency modulation (see the comparison between Figure 6.9 and Figure 6.10), the greater precision with which Birkhoff is able to determine the horizontal and vertical tunes allows for considering the points of the chaotic band closest to $x \approx 0$ as resonant points belonging to different resonant lines.

As a final study, the tune distance defined as in Eq. 6.28 is computed for the case with frequency modulation. The results are reported in Figure 6.19. To enable for the comparison

with the case without frequency modulation, the colour scale has been left unchanged. From the comparison of Figure 6.11 and Figure 6.19, where tune modulation is introduced, the tune computed at two successive signal slices (each of length N) changes significantly. In fact, both Hanning (Figure 6.19 top) and Birkhoff (bottom of the same figure) evaluated with $N = 1024$ have blue as the dominant colour, meaning that the tunes evaluated between 0 and $N-1$ and between N and $2N-1$ do not differ significantly from each other. Slight improvements can be observed for $N = 32768$, where a reduction of the tune distance of almost two order of magnitude can be observed.

In conclusion, the study of the Hénon map enabled for the understanding of the Hanning method and the weighted Birkhoff average performances on a 4D dynamical system. In the absence of frequency modulations, the use of the Birkhoff method enabled the identification of a chaotic resonant region that was not visible with Hanning. Moreover, being these conditions close to a fourth-, fifth- and sixth-order resonance, their identification is of fundamental importance to prevent their possible and unwanted excitation. Even if the Hénon map represents a very simple accelerator model where only a single sextupole is installed, the identification of resonant conditions that were not detected by the Hanning method, opens the possibility to study the space of stable conditions for a generic accelerator with Birkhoff rather than with Hanning. Both methods show the same almost unchanged results with and without frequency modulation. However, their discrepancies (especially in the identification of on-resonance and chaotic region) persist in both cases. In the tune distance diagrams, the variation of the tune as a function of the number of turns makes its identification more critical in the lower number of samples case.

6.3 Constant amplitude signals in presence of noise

The presence of noise, meant as unwanted and uncontrolled fluctuations that interfere with the signal, is unavoidable when real signals are analysed. The noise does not add any information to the signal and it is present in whenever a signal is recorded, transmitted and/or processed. There are multiple sources of noise and several classifications are possible. In the present discussion, the effect of the noise on constant amplitude signals is a fundamental study to carry out for the determination of the performance of the methods described in the previous section.

The constant-amplitude signal defined in Eq. 6.1 has been generated over $N = 10^5$ turns and with a tune $\nu_0 = 0.261$. The contribution of the noise is quantified by the Signal-to-Noise Ratio (SNR) defined as:

$$\mathrm{SNR} = \left(\frac{\sigma_s}{\sigma_n}\right)^2 , \tag{6.30}$$

where σ_s represents the RMS of the signal and σ_n stands for noise RMS. From Eq. 6.30, the smaller the contribution of the noise the larger is the value of SNR. Several SNR, for several different σ_n, have been considered ranging from a minimum value of 10 (that corresponds to $\sigma_n = 10\%$) to a maximum value of 10^9 (for a $\sigma_n = 0.001\%$). Thus the noise has been generated by taking N random samples from a Gaussian distribution having zero mean value and a width equal to half the RMS noise σ_n. This step has been performed twice in order to determine a complex-valued noise with zero mean and a standard deviation of σ_n, to be added to the original signal. For each value of RMS noise σ_n, 200 different Gaussian noises have been generated. Therefore, 200 noise signal were available for the tune analysis. The tune of the noisy signals has been evaluated using the Interpolated FFT, the Hanning filtered FFT and the weighted Birkhoff average (for $\alpha = 1$ and $\alpha = 2$, both having β fixed to 1).

The results of this analysis are reported in Figure 6.20, where for the sake of comparison, also the tune error for the pure signal (namely., in absence of noise) is reported with a black line. As the RMS noise decreases, the tune error reduces as well. In particular, for the Interpolated FFT noise levels of 0.1% or smaller converge to the not noisy tune error. Thus, in the analysis of real beam data with noise levels compatible with the simulated ones, it would be possible to obtain a tune error that scales as $1/N^2$ as the not noisy signal. As far as the other methods are concerned, some similarities and discrepancy with respect to the Interpolated FFT can be noted. At first, none of the precise methods shows the same precision it had in the absence of noise. In fact, even the least noisy configuration does not have a tune error that scales as $1/N^4$ for Hanning or $1/N^7$ for Birkhoff. Although, as the noise RMS reduces, the initial value of tune error reduces approaching the black line, thus the values in absence of noise. According to the initial values of tune error and to the noise RMS, a convergence to the not noisy tune error can be observed. This is due to the fact that in the presence of noise, it is not possible to obtain a tune error smaller than the one retrieved in the absence of noise. Therefore, for the Hanning filtered FFT this occurs for $N < 128$ and a RMS noise of 0.001%. For Birkhoff this behaviour occurs at smaller

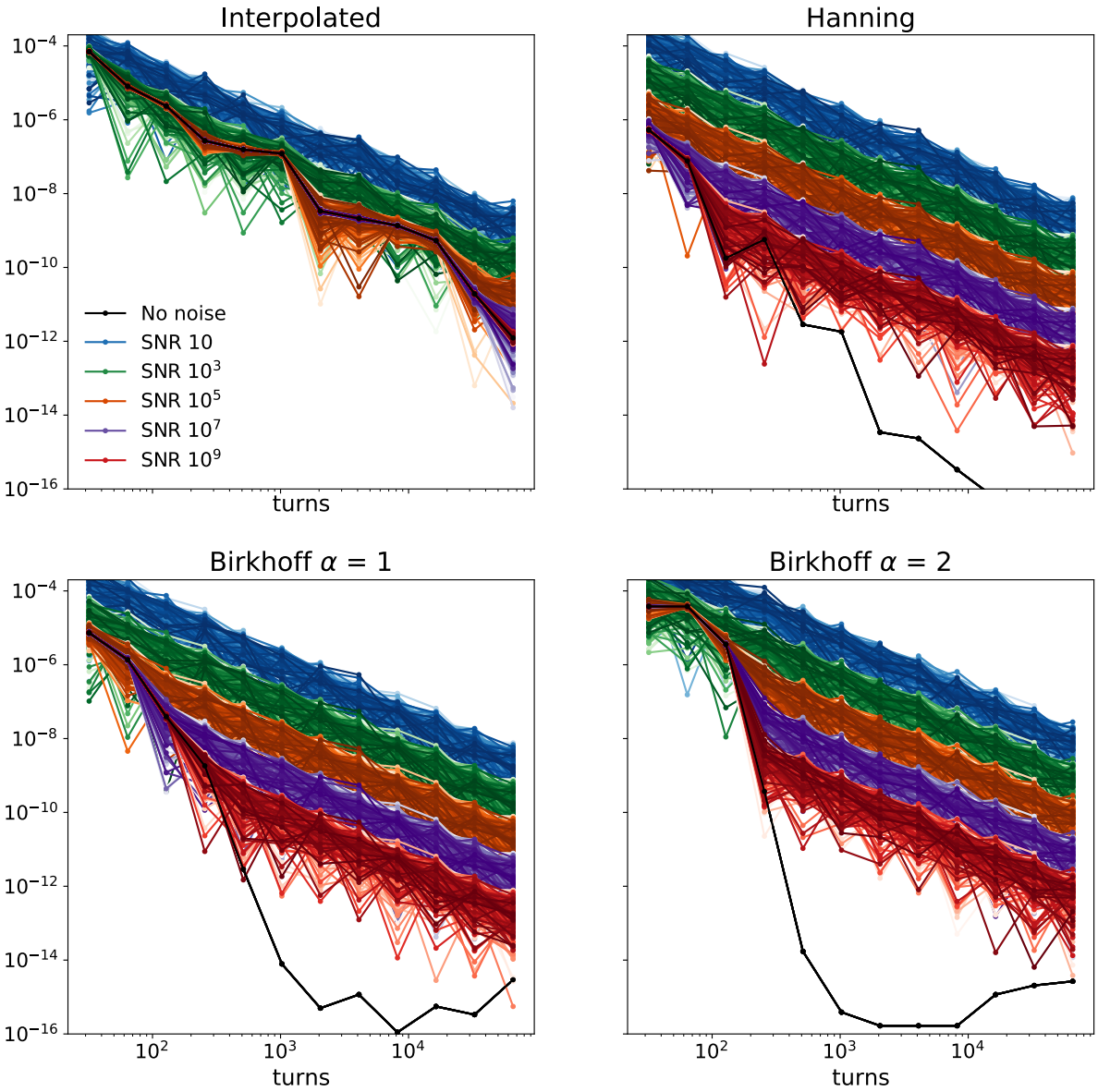

Figure 6.20: The tune analysis for a constant-amplitude signal perturbed with a Gaussian noise has been performed with the Interpolated FFT (top left), Hanning filtered FFT (top right) and the weighted Birkhoff average with $\alpha = 1$ (bottom left) and $\alpha = 2$ (bottom right). The tune error in absence of noise is displayed in black for the four methods, while the different values of SNR have been represented with different colours, ranging from red (for the largest SNR, namely 10^9, or equivalently the smallest contribution of noise) to blue (for the smallest SNR, namely 10).

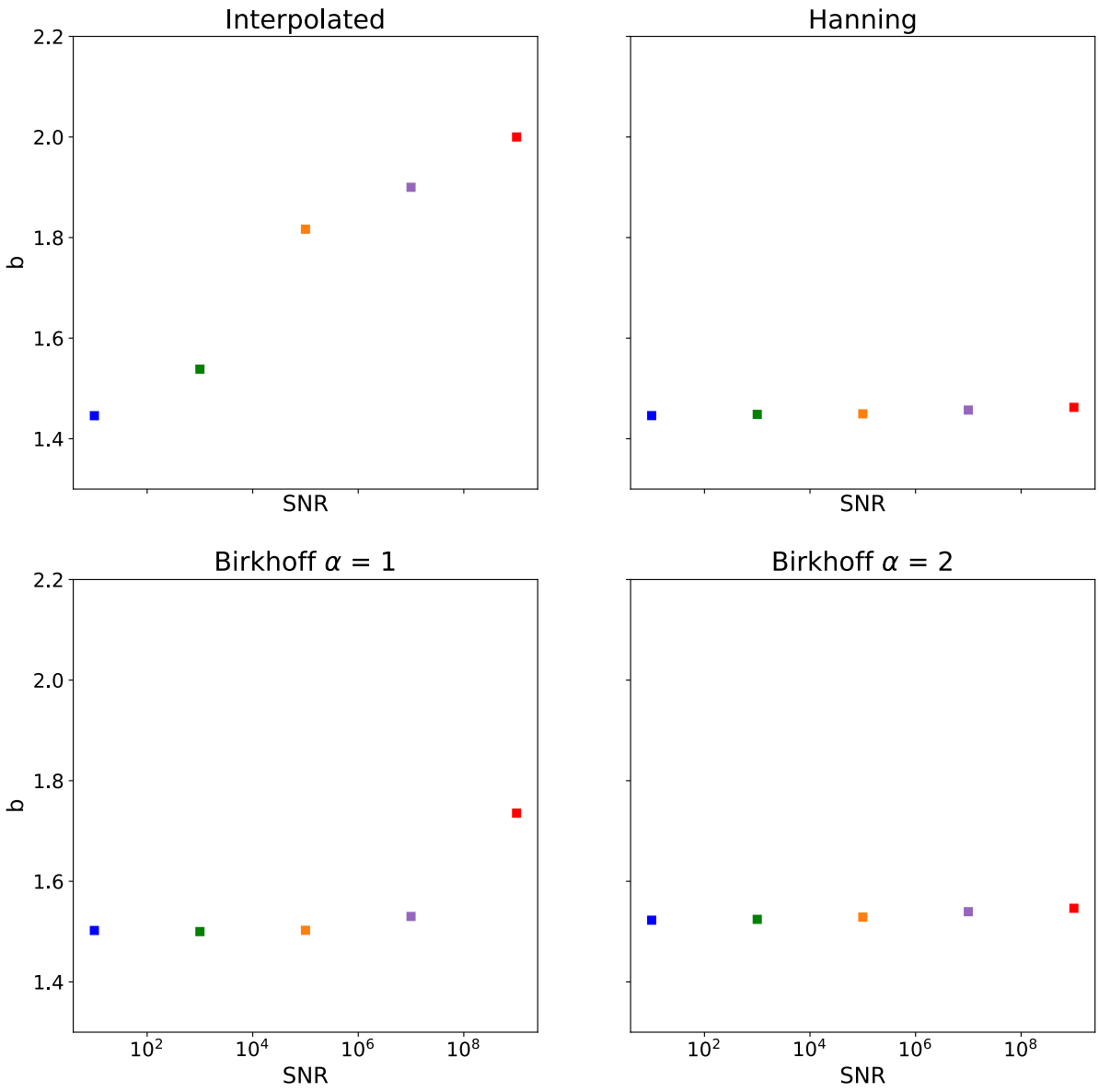

Figure 6.21: The exponent b of the fit a/N^b is reported for the four tested methods (Interpolated FFT, Hanning filtered FFT, and weighted Birkhoff average) as a function of the noise RMS.

noise RMS, in particular 0.01% for $\alpha = 1$ and 0.1% for $\alpha = 2$. From the observation of the results obtained with the Interpolated FFT, it is expected that if the RMS noise is further reduced the more precise methods (namely, Hanning and Birkhoff) will show the same convergence that the Interpolated showed. To determine the effect of noise on the methods performance, for each RMS noise condition the tune errors have been fit to a/N^b where both the proportionality coefficient a and the exponent b, that determines the scaling law of each noisy condition, has been fit to the data. The results are shown in Figure 6.21. As expected, the Interpolated FFT shows an increase in the b as the RMS noise reduces. This is in agreement with the results reported in

Figure 6.20, where a convergence was observed to the non-noisy tune error when the RMS noise is reduced. As far as the Hanning method is concerned, an average value of 1.45 ± 0.01 is obtained to no improvement as the RMS noise reduces. However, some improvements can be observed for the Birkhoff methods. For $\alpha = 1$, an average value of 1.51 ± 0.01 is obtained, except for the smallest noise level where $b = 1.735 \pm 0.002$. Also in this case, this result is in agreement with the tune error displayed in Figure 6.21. Minor improvements are observed for the weighted Birkhoff average with $\alpha = 2$ where an average value of 1.53 ± 0.01 is obtained.

Although the weighted Birkhoff average is based on the average of the phase advance between two successive iteration, it does not improve its performance when the SNR reduces. In fact, contrary to the initial expectations, the perturbative terms directly related to the noise are a function of the number of turns and their mean value does not go to zero. Therefore, it is not possible to expect any significant improvement.

In conclusion, when a real signal is analysed it is important to estimate at first the SNR. For this specific application where the frequency of the signal is estimated, the Interpolated FFT is the best method to use since for noise levels compatible with those of an experimental measurement can provide a tune error that scales as in absence of noise, namely a/N^2.

6.4 Varying amplitude signals

Amplitude-modulated signals comprehend a wide variety of signals ranging from communication purposes (such as local citizen radio) to accelerator physics (such as tune measurements). The frequency analysis of these signals should be handled with care, as the direct application of the FFT (and its related methods) would possibly lead to uncorrect results. In fact, the FFT is based on three main assumptions:

1. that the signal shows its periodicity within the sampling period;
2. that its sampling frequency is constant;
3. that it has been sampled in N intervals of time.

Any complex-valued signal can be decomposed as a sum of varying amplitude and phase signals. According to the time evolution of the varying amplitude signal, it is not always possible to perform an analytical analysis and thus, possibly find a closed equation whose solution is the tune. Among all possible ways the amplitude of a signal can vary, the damped exponential was considered as a first study-case, it is defined as:

$$z(n) = e^{-\lambda n}\left(e^{2\pi i \nu_0 n} + \sum_k a_k e^{2\pi i \nu_0 n k}\right), \tag{6.31}$$

where $a_k = e^{-k}$ with $k = 1,...,4$. The damped exponential defined as in Eq. 6.31 is the easiest to deal with from a mathematical point of view and, from a physical point of view, it represents the evolution of a beam of charged leptons (such as electrons) after it has been kicked. The dynamics of current[2] proton beams is significantly different from that of electron beams. Among the many differences, it is worth highlighting the different way they behave after they have been kicked. As far as protons are concerned, the beam position and angle is centred on the reference system, as shown on Figure 6.22 right, after it has been kicked (a kick equal to $\Delta x'$ causes the beam angle to move of a quantity equal to the kick itself) the centroid of the beam filaments until it returns at the centre of the reference system. The mathematical details of this phenomenon can be found in Ref. [64]. Moreover, the decoherence of proton beams will be analysed in the context of this thesis in Section 6.5. In the presence of imperfections (such as magnetic errors) the proton beam will evolve turn after turn and it will tend to occupy an annular region in trace space, as shown in Figure 6.22 right. As a consequence of this type of perturbation, the proton beam occupies an area in trace-space larger than the original one. On the contrary, electron beams emit part of their energy as photons while they circulate in the accelerator, this phenomenon is known as synchrotron radiation. The loss of energy observed from the photon emission is characteristic

[2]Although LHC proton beams lose part of their energy due to synchrotron radiation, their dynamics is not strongly dominated by this effect as it happens for electron beams. Future proton beams for FCC-hh will emit even more synchrotron radiation due to their higher energy. Thus, this consideration is valid up to LHC beams energy.

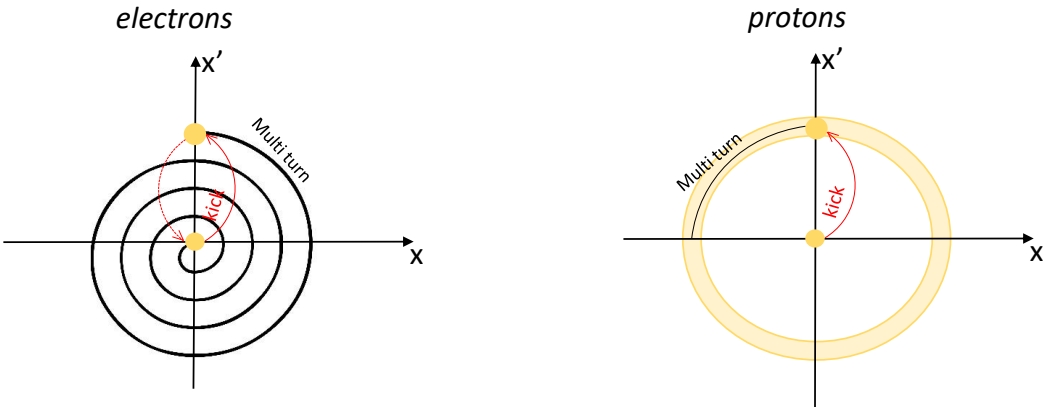

Figure 6.22: Comparison proton and electron response to kick.

of any charged particle moving on a curved path, thus it occurs also for proton beams, but the fraction of energy loss is significantly larger for electrons than for protons[3]. Therefore, after an electron beam has been kicked, different phenomena occurs at the same time among this the energy loss because of synchrotron radiation always plays a key role. On the one hand, the synchrotron radiation can excite transverse and longitudinal oscillations; on the other hand, its damping effect brings the beam to a new equilibrium condition [66]. As shown on Figure 6.22 left, the electron beam returns to the centre of the trace space due to the turn-by-turn damping effect provided by the synchrotron radiation.

In the following section, new analytical formulae will be demonstrated for the determination of the tune for an exponentially damped signal defined as in Eq. 6.31. In 2015, preliminary studies on the possibility to determine an analytical tune equation for the damped exponential signal were performed [67]. Those results will be used as starting point and thus the performance of the method will be taken as the reference. Moreover, additional considerations and results will be demonstrated and described. Then, a new analytical equation that exploits the properties of the Hanning filter will be discussed and numerically tested. As a final theoretical topic, the Hilbert Transform will be introduced as an innovative method to analyse varying amplitude signals and retrieve their properties. At the end of the chapter, the numerical simulation results will be described and the performance of the different methods will be compared.

[3]At the LHC, where two proton beams at 6.8 TeV are brought into collision, the energy loss per turn due to synchrotron radiation is approximately 7 keV per beam ($\approx 0.00001\%$). At the Synchrotron Radiation Source (SRS) at the Daresbury Laboratory in Cheshire (UK) electron beams at 2 GeV are accelerated, and the energy loss for synchrotron radiation is 0.25 MeV ($\approx 0.0125\%$) [65]

6.4.1 Interpolated FFT

For the signal defined in Eq. 6.31, the FFT coefficients read as:

$$\phi(\nu_j) = \frac{1}{N}\sum_{n=1}^{\mathrm{N}} e^{2\pi i(\nu_0-\nu_j)-\lambda n}\ , \tag{6.32}$$

Using the relations in Eq. 6.5 and taking the absolute value of the resulting complex number, Eq. 6.32 becomes:

$$\left|\phi(\nu_j)\right|^2 = \frac{1}{N^2}e^{-\lambda(N+1)}\frac{\sin^2\left(\pi N(\nu_0-\nu_j)\right)+\sinh^2\frac{\lambda N}{2}}{\sin^2\left(\pi(\nu_0-\nu_j)\right)+\sinh^2\frac{\lambda}{2}}\ . \tag{6.33}$$

It is possible to identify in the frequency range swapped by ν_j where $j = 0,\ldots,N-1$, the value of ν_k that maximises the FFT coefficient. At that frequency, the FFT coefficient is $|\phi(\nu_k)|$ and interpolating its value with its left and right neighbours (namely, $|\phi(\nu_{k-1})|$ and $|\phi(\nu_{k+1})|$, respectively) a solution for the tune can be found and it reads as:

$$\hat{\nu}_0 = \frac{k}{N}+\frac{1}{\pi}\arctan\left[\frac{1}{\tan\frac{\pi}{N}}\left(\frac{\eta+1}{\eta-1}\pm\sqrt{\left(\frac{\eta+1}{\eta-1}\right)^2+\tan^2\frac{\pi}{N}}\right)\right]\ , \tag{6.34}$$

where,

$$\eta = \frac{\chi_+-1}{\chi_--1}\ , \qquad \chi_\pm = \frac{|\phi(\nu_k)|^2}{|\phi(\nu_{k\pm1})|^2}\ , \tag{6.35}$$

Moreover, an analytical equation for the determination of the damping factor λ, used in the generation of the signal in Eq. 6.31, can be found by properly combining the FFT coefficients defined above:

$$\lambda = 2\mathrm{arcsinh}\sqrt{\frac{|\phi(\nu_{k+1})|^2\sin^2\left(\pi(\nu_0-\nu_k)\mp\frac{\pi}{N}\right)-|\phi(\nu_k)|^2\sin^2\pi(\nu_0-\nu_k)}{|\phi(\nu_k)|^2-|\phi(\nu_{k+1})|^2}}\ . \tag{6.36}$$

From the analysis of the right-hand side of Eq. 6.34, the first term represents the peak of the FFT that is then corrected for with the second term. The tune is corrected with a negative or a positive term according to which one between $|\phi(\nu_{k+1})|$ and $|\phi(\nu_{k-1})|$ is larger. In fact, if $|\phi(\nu_{k+1})| > |\phi(\nu_{k-1})|$ it means that the FFT tune estimation is actually underestimating the tune itself, thus the negative term on the RHS of Eq. 6.34 has to be selected being $\eta < 1$. The opposite holds true as well. Although numerical simulations were performed to determine the precision with which the tune and the damping factor are computed [67]; the analytical determination of the scaling law has been performed for the first time in the context of this research. From a mathematical point of view, the FFT coefficients are perturbed with a known source of error, thus they read as:

$$\tilde{\phi}(\nu_k) = \phi(\nu_k)+\frac{\psi(\nu_k)}{N}. \tag{6.37}$$

Applying this perturbation to both Eq. 6.34 and Eq. 6.36, it is possible to show that both equations provide a precision that scales as $1/N^2$. The complete derivation can be found in Appendix D.

6.4.2 Hanning FFT

Similarly to what has been performed in Section 6.1.3, the aim is to verify whether it is possible to determine an analytical equation for the calculation of the tune (and possibly of the damping factor λ) for the signal defined in Eq. 6.31 filtering it with the Hanning filter (see Eq. 6.8, Figure 6.1). In the following section the most important mathematical steps will be reported and described. Additional details and explanations can be found in Appendix E. After the signal in Eq. 6.31 has been filtered, it will look like:

$$z(n) = 2e^{-\lambda n}\left(e^{2\pi i \nu_0 n} + \sum_k a_k e^{2\pi i \nu_0 n k}\right)\sin^2\left(\frac{\pi n}{N}\right) , \tag{6.38}$$

where N is the number of turns at which the sampling has been stopped. Performing the FFT on the signal defined in Eq. 6.38 but removing the contribution of perturbative harmonics, the FFT coefficients read as:

$$\phi(\nu_j) = \frac{2}{N}\sum_{n=1}^{N} e^{2\pi i(\nu_0-\nu_j)n-\lambda n}\sin^2\frac{\pi n}{N} . \tag{6.39}$$

The Eq. 6.39 can be rewritten and simplified if the sinusoidal function (the Hanning filter) is written using the exponential notation and if the relations reported in Eq. 6.5 are applied:

$$\phi(\nu_j) = \frac{ie^{-N\lambda}\sin^2\frac{\pi}{N}\cot\left(\pi(\nu_0-\nu_j)+\frac{i\lambda}{2}\right)\left(-e^{\lambda N}+e^{2i\pi(\nu_0-\nu_j)N}\right)}{N\left(\cos\frac{2\pi}{N}-\cos(2\pi(\nu_0-\nu_j)+i\lambda)\right)} . \tag{6.40}$$

The mathematical expression in Eq. 6.40 can be further simplified introducing the following complex variable:

$$\theta_j(\lambda) = \pi(\nu_0-\nu_j)+i\frac{\lambda}{2} , \text{ where } \theta_j(\lambda)\in\mathbb{C} \tag{6.41}$$

Thus, the FFT coefficients in Eq. 6.40 read as

$$\phi(\nu_j) = \frac{ie^{-N\lambda}\sin^2\frac{\pi}{N}\cot\,\theta_j(\lambda)\left(-e^{\lambda N}+e^{2i\pi(\nu_0-\nu_j)N}\right)}{N\left(\cos\frac{2\pi}{N}-\cos(2\theta_j(\lambda))\right)} . \tag{6.42}$$

In order to determine an analytical equation for the tune, it is necessary to evaluate the FFT coefficient in Eq. 6.42 at the frequency $\nu_k = k/N$ that maximises its values. In this condition, Eq. 6.42 is a complex equation in the complex unknown $\theta_k(\lambda)$, where also $\theta_j(\lambda)$ has been evaluated at ν_k. Writing the corresponding equations for $\phi(\nu_{k\pm1})$, and combining them together, allow for the definition of the following variables:

$$\chi_\pm \equiv \frac{\phi(\nu_k)}{\phi(\nu_{k\pm1})} = \frac{\cos(\theta_k(\lambda))\sin(\theta_k(\lambda)\mp\frac{2\pi}{N})}{\sin(\theta_k(\lambda)\pm\frac{\pi}{N})\cos(\theta_k(\lambda)\mp\frac{\pi}{N})} . \tag{6.43}$$

Thus, a second-order trigonometric equation in the unknown $2\theta_k(\lambda)$ defined as:

$$2\theta_k(\lambda) = 2\pi(\nu_0-\nu_k)+i\lambda , \tag{6.44}$$

can be written, and it reads as

$$a_{\pm}\sin^2 2\theta_k(\lambda) + b_{\pm}\sin 2\theta_k(\lambda) + c_{\pm} = 0\ , \tag{6.45}$$

which solutions can be expressed as

$$\sin 2\theta_k(\lambda)\Big|_{1,2,3,4} = \frac{-b_{\pm} \pm \sqrt{b_{\pm}^2 - 4a_{\pm}c_{\pm}}}{2a_{\pm}}\ , \tag{6.46}$$

where the complex coefficients $a_{\pm}, b_{\pm}, c_{\pm}$ are defined as

$$a_{\pm} = (\chi_{\pm}^2 + 1 - 2\chi_{\pm}\cos\frac{2\pi}{N})\ ,\ b_{\pm} = \pm 2\sin\frac{2\pi}{N}(\chi_{\pm}+1)\left(\chi_{\pm} - \cos\frac{2\pi}{N}\right)\ ,\ c_{\pm} = \sin^2\frac{2\pi}{N}\chi_{\pm}(\chi_{\pm}+2)\ .$$

The choice of the sign of the coefficients $a_{\pm}, b_{\pm}, c_{\pm}$ depends on whether $|\phi(\nu_{k+1})|^2 > |\phi(\nu_{k-1})|^2$ or if the opposite holds true. For similar reasons, the positive sign in Eq. 6.46 is considered when the relation above is verified, otherwise the negative sign is picked. Being $a_{\pm}, b_{\pm}, c_{\pm}$ complex numbers and being the unknown $\theta_k(\lambda)$ a complex variable as well, the right-hand side of Eq. 6.46 must be a complex number too. Thus, to simplify the notation that will follow, it will be referred to as z and its real and complex components will be x and y, respectively. The solutions of Eq. 6.45 can be found using the formula 4.4.37 in Ref. [68] that defines the inverse sine function of a complex number as:

$$\arcsin(z) = \arcsin(x+iy) = k\pi + (-1)^k \arcsin\beta + (-1)^k i\ln\left(\alpha + \sqrt{(\alpha^2+1)}\right)\ , \tag{6.47}$$

where k is an integer or it is zero (this latter value has been chosen, $k=0$) and,

$$\alpha = \frac{1}{2}\sqrt{\left((x+1)^2+y^2\right)} + \frac{1}{2}\sqrt{\left((x-1)^2+y^2\right)}\ ,$$

and

$$\beta = \frac{1}{2}\sqrt{\left((x+1)^2+y^2\right)} - \frac{1}{2}\sqrt{\left((x-1)^2+y^2\right)}\ .$$

In conclusion, the real component of Eq. 6.47 is equal to the real part of Eq. 6.44 providing a closed-form equation for the tune determination. In analogy the imaginary part enables the determination of the damping factor. Thus the tune equation and the damping factor equation respectively read as:

$$\nu_0 = \frac{k}{N} + \frac{1}{2\pi}\arcsin\beta\ , \tag{6.48}$$

and

$$\lambda = \ln\left(\alpha + \sqrt{(\alpha^2+1)}\right)\ . \tag{6.49}$$

Because of the difficulties of their definition, it was not possible to determine analytically the precision of Eq. 6.48 and Eq. 6.49, thus only the numerical evidence will be provided. In analogy to what has been performed in Section 6.1.3, it is possible to first assume, and then numerically verify, that both equations will provide a scaling law of $1/N^4$. In fact, the scaling law is not

determined by the time evolution of the signal but rather from the method used to analyse it. Therefore, considering that the scaling law $1/N^4$ characteristic of the Hanning filter has been mathematically proved for the constant amplitude signal in Section 6.1.3, it is expected that also in this case the same scaling law will be found in numerical simulations. The numerical results will be shown in Section 6.4.5.1.

6.4.3 Hilbert Transform

The Hilbert transform (HT) is one of the most powerful methods to use when determining the modulation of the amplitude of a signal. It is widely used in signal processing when the analysed signals has properties (such as amplitude, frequency and statistical properties as the mean) that vary over time [69, 70]. In the following section, a brief description of the main features of the Hilbert Transform will be reported and described. Moreover, the extension of these definitions for complex-valued signals will be provided, since they will be exploited in the next sections.

Thus, given a generic real-valued signal $u(t)$ continuous in time, the Hilbert transform of the signal is defined as:

$$HT(u(t)) = -\frac{1}{\pi} p.v. \int_{-\infty}^{+\infty} \frac{u(\tau)}{t-\tau}\, d\tau \ , \tag{6.50}$$

where $p.v.$ is the Cauchy Principal Value integral. An alternative way to define the Hilbert transform for a discrete time series $x(n)$ is with the Fast Fourier Transform (FFT) and its inverse (IFFT) [69]:

$$HT(x(n)) = IFFT(-i\ sgn(v_j)\ FFT(x(n))) \ . \tag{6.51}$$

Equation 6.51 defines the Hilbert transform of the signal $x(n)$ as the Inverse Fourier Transform (IFFT) of the FFT coefficients each shifted in phase by $\pi/2$ (due to the presence of the imaginary unit i) and multiplied times the sign function of the frequency. Thus, the Hilbert Transform does not change the domain of the signal, meaning that if the signal is a time-series the HT will exist in the time domain. The same does not happen for the FFT where, if the signal exists in the time domain, the FFT is a linear transformation of the signal in the frequency domain. It is very important to notice that the HT is defined for real signals only, as a result, the HT provides a complex signal, whose real part is the original signal and the imaginary part is the HT of the signal itself, this complex signal is known as analytic signal $o(n)$ and it is reported in Eq. 6.52.

$$o(n) = x(n) + i\ HT(x(n)) \ , \tag{6.52}$$

where $x(n)$ is a real-valued signal. The absolute value of the analytic signal has a very special property: it is the envelope of the analysed signal, and its definition is reported in Eq. 6.53.

$$e(n) = |o(n)| = |x(n) + i\ HT(x(n))| \ . \tag{6.53}$$

From the knowledge of the envelope it is possible to normalise the original signal obtaining a constant-amplitude signal, defined as:

$$x_N(n) = \frac{x(n)}{e(n)} \ , \tag{6.54}$$

where the subscript N means that the signal has been normalised with respect to the HT envelope. It is important to generalise some concepts when the HT is applied to a complex-valued signal $z(n)$ defined as in Eq. 6.55.

$$z(n) = x(n) - i\ p_x(n)\ , \tag{6.55}$$

where the real $x(n)$ and imaginary part $p_x(n)$ are defined as the position and momentum of a particle orbit, as previously done in Section 6.1. Being the HT a linear operator, it can be applied to the real part and to the imaginary one separately, and for each of them the definition of the analytic signal is reported in Eq. 6.56 and Eq. 6.57, respectively.

$$o_R(n) = x(n) + i\ HT(x(n))\ , \tag{6.56}$$

$$o_I(n) = p_x(n) + i\ HT(p_x(n))\ . \tag{6.57}$$

It is straightforward to generalise the concept of envelope for the real and imaginary parts starting from Eq. 6.53. In particular, for each of the two components of the complex-valued signal, the normalisation step can be performed considering each component separately and determining the envelope as the absolute value of Eq. 6.56 and Eq. 6.57, respectively, for each of them. In conclusion, given the complex-valued signal defined in Eq. 6.55, the effect of amplitude modulation can be removed by performing the HT on the real and imaginary part independently. The resulting constant-amplitude signal $z_N(n)$ reads as

$$z_N(n) = \frac{x(n)}{e_R(n)} - i\ \frac{p_x(n)}{e_I(n)} = x_N(n) - i\ p_{x,N}(n)\ , \tag{6.58}$$

where $e_R(n)$ is the envelope of the real part of the complex-valued signal defined as the absolute value of Eq. 6.56. Similarly for the imaginary part, where the envelope $e_I(n)$ is defined as the absolute value of the analytic signal defined in Eq. 6.57. Two aspects are of fundamental importance:

- The normalised signal $z_N(n)$ in Eq. 6.58 has a real and imaginary part which amplitude varies within the $[-1,1]$ interval, but their combination does not necessarily lead to a signal whose amplitude varies within the same interval. However, being $x(n)$ and $p_x(n)$ shifted in phase by $\pi/2$, the normalisation of the signal as defined in Eq. 6.58 holds true and the signal will have a constant amplitude.

- For complex-valued signals in which there is not a linear relation between the real and imaginary part, the definition of the normalised signal as in Eq. 6.58 does not hold true anymore. A generalisation of the concept of envelope and thus of the normalised signal needs the use of quaternions. Additional information on this topic can be found in Ref. [71, 72].

The use and applications of the HT are much wider than those described in this section, and additional applications can be found in Ref. [69, 70].

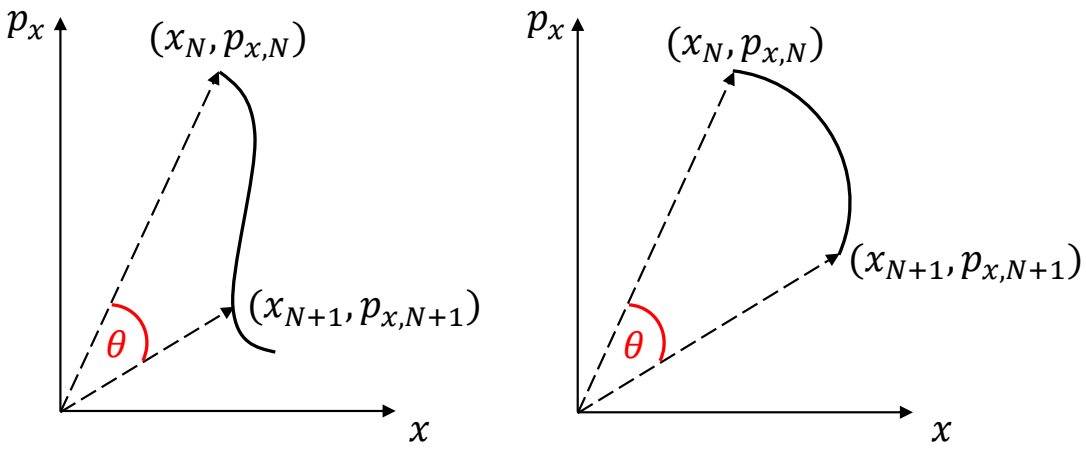

Figure 6.23: The phase defined as the angle between two vectors is shown for vectors of different lengths (left) and of equal length (right).

6.4.4 Remarks on the use of weighted Birkhoff averages on amplitude modulated signals

As discussed in Section 6.2.2 the use of weighted Birkhoff averages exploits its super-convergence to determine the tune value with a precision that scales as $1/N^7$. In particular, this method relies on the proportionality between the phase advance and the tune. From a physical point of view, the phase advance is defined as the angle between two vectors described by the x and p_x coordinates of the particle between two successive iterations as reported in the schematic representation in Figure 6.23. On Figure 6.23 left, the phase θ defined for an amplitude modulated signal. Between iteration N and iteration $N+1$, the amplitude of the signal changes, thus does the length of the vectors. On Figure 6.23 right, a generic circular path is drawn, and it is possible to observe that the length of the vectors remains unchanged between the two consecutive turns. Therefore, it is expected that the weighted Birkhoff average still shows its super-convergent behaviour also when applied to amplitude modulated signals. From a mathematical point of view, it is possible to prove this behaviour considering a generic amplitude modulated signal in the form

$$z(n) = a(n)e^{2\pi i \nu_0 n} \,. \tag{6.59}$$

The calculation of the average phase advance θ is performed computing the phase at each iteration and then summing all the values computed over the $M-1$ sampled turns, where each of them is weighted with the normalised Birkhoff weights. At every turn, the phase is computed as the inverse cosine function of the scalar product between the two vectors defined by the particle

coordinates at that turn and the one before. Thus, the average phase is computed as:

$$\theta = \sum_{N=1}^{M-1} \arccos\left(\frac{x_N x_{N+1} + p_{x,N} p_{x,N+1}}{\sqrt{(x_N + p_{x,N})^2 (x_{N+1} + p_{x,N+1})^2}}\right) sign\left(x_N p_{x,N+1} - x_{N+1} p_{x,N}\right) w^{\alpha}_{B,\mathrm{Norm}}(t,\beta) \,, \tag{6.60}$$

where $w^{\alpha}_{B,\mathrm{Norm}}(t,\beta)$ are the normalised defined as in Eq. 6.21, where t slightly changes notation and is defined as $t = N/M$ where N ranges in $1,\ldots,M-1$, and the variables x_N, x_{N+1}, $p_{x,N}$, $p_{x,N+1}$ are defined as:

$$\begin{aligned} x_N &= a(N)\cos(2\pi\nu_0 N) \\ x_{N+1} &= a(N+1)\cos(2\pi\nu_0 (N+1)) \\ p_{x,N} &= a(N)\sin(2\pi\nu_0 N) \\ p_{x,N+1} &= a(N+1)\sin(2\pi\nu_0 (N+1)) \,. \end{aligned} \tag{6.61}$$

By the substitution of Eq. 6.61 into Eq. 6.60, with some algebra is found that the amplitude dependence cancels out. In conclusion, it is expected that the use of the weighted Birkhoff averages converges with its characteristic scaling law (see Section 6.2.2) to the value of tune for any amplitude modulated signal $a(n)$ and for any value of the parameters α and β of the of the Birkhoff weights.

6.4.5 Numerical simulation results

In the following section, the results of the numerical simulation will be presented and discussed in detail.

At first, the exponential damped amplitude-modulated signal, defined in Eq. 6.31 will be considered. The performance of different methods will be compared. In particular, it will be shown how the methods developed for constant amplitude signal (such as those described in Section 6.1 and in Section 6.2) behave when an amplitude modulated signal is considered. Moreover, the precision of the Interpolated method will be numerically assessed while it will be determined for the Hanning methods, both developed for the damped exponential signal that have been described in Section 6.4.1 and Section 6.4.2.

As a second case study, the chromatic decoherence will be analysed. The mathematical model developed in the 1980s will be described and explained. From the mathematical description of the amplitude modulation of this type of signal, it will be clear that it can not be treated analytically, thus it is not possible to find a close-form solution of the tune equation. Therefore, it has to be analysed using the Hilbert transform, described in Section 6.4.3. The normalised chromatic signal will be analysed with the techniques developed for constant amplitude signals, and described in Section 6.1 and in Section 6.2. The same methods will be also used to analyse the original (thus, amplitude-modulated) signal. From the comparison of the results it will possible to understand which method performs better (in terms of precision in the tune determination).

6.4.5.1 Damped exponential

For the damped exponential signal reported in Eq. 6.31, the numerical simulations were performed for different values of the damping factor λ. The results that will follow have been obtained for a signal as in Eq. 6.31 where the tune ν_0 was set to 0.28 and the number of maximum turns used in the generation of the signal was chosen to be 2×10^5. The precision of the Interpolated equation reported in Section 6.4.1 was verified for both the tune equation (Eq. 6.34) and the damping factor one (Eq. 6.36). As far as the case where the damped exponential signal is filtered with the Hanning window (see for reference Section 6.4.2), the precision with which the tune and the damping factor can be retrieved, is expected to scale as $1/N^4$, and it will be assessed in the following numerical simulations.

In order to determine the scaling law of the different methods, the tune and the damping factor (only using the methods described in Section 6.4.1 and Section 6.4.2) are computed on slices of signal of increasing length up to the total signal length. Each slice is equal to a power of 2 being the above mentioned methods based on the FFT. Thus, the relative error, computed as the absolute value of the difference between the retrieved tune value and the one used in the signal generation, is calculated.

Two different values of damping factor λ are considered, the signals and the results are shown in Figure 6.24. In particular, the top row in Figure 6.24 refers to $\lambda = 5 \times 10^{-5}$ while the bottom one to $\lambda = 5 \times 10^{-4}$. The first plot on the Figure 6.24 left, shows in blue the damped exponential computed as in Eq. 6.31, the black curve is the envelope computed by means of the Hilbert Transform and, following the procedure explained in Section 6.4.3, the normalised signal is retrieve and it is reported in red, its amplitude varies between $[-1, 1]$ as expected. The two damped signals considered in the analysis were truncated when the amplitude of the signal decreased by 95% with respect to the nominal value. That is, it has been considered that a signal amplitude value equal to 5% of the nominal one is comparable with the noise levels that generally occurs in signals taken from experimental measurements.

The two damped signals have been analysed using the equations described in Section 6.4.1 and in Section 6.4.2, thus the set of equations that can be used to determine the tune and the damping factor of an exponential modulated signal. At first, the tune is determined for both signals and the results are shown on the plot at the centre of Figure 6.24. For both cases the Hanning filter approach (Eq. 6.48) provides better a better precision, with respect to the Interpolated method (Eq. 6.34) as expected. The numerical results have been fitted to the following scaling law a_1/N^2 for the Interpolated and a_2/N^4 for Hanning. The following values of coefficients have been obtained:

- For $\lambda = 5 \times 10^{-5}$: $a_1 = (5.53 \pm 0.71) \times 10^{-2}$ and $a_2 = 1.022 \pm 0.010$;
- for $\lambda = 5 \times 10^{-4}$: $a_1 = (2.15 \pm 0.76) \times 10^{-2}$ and $a_2 = 1.018 \pm 0.010$.

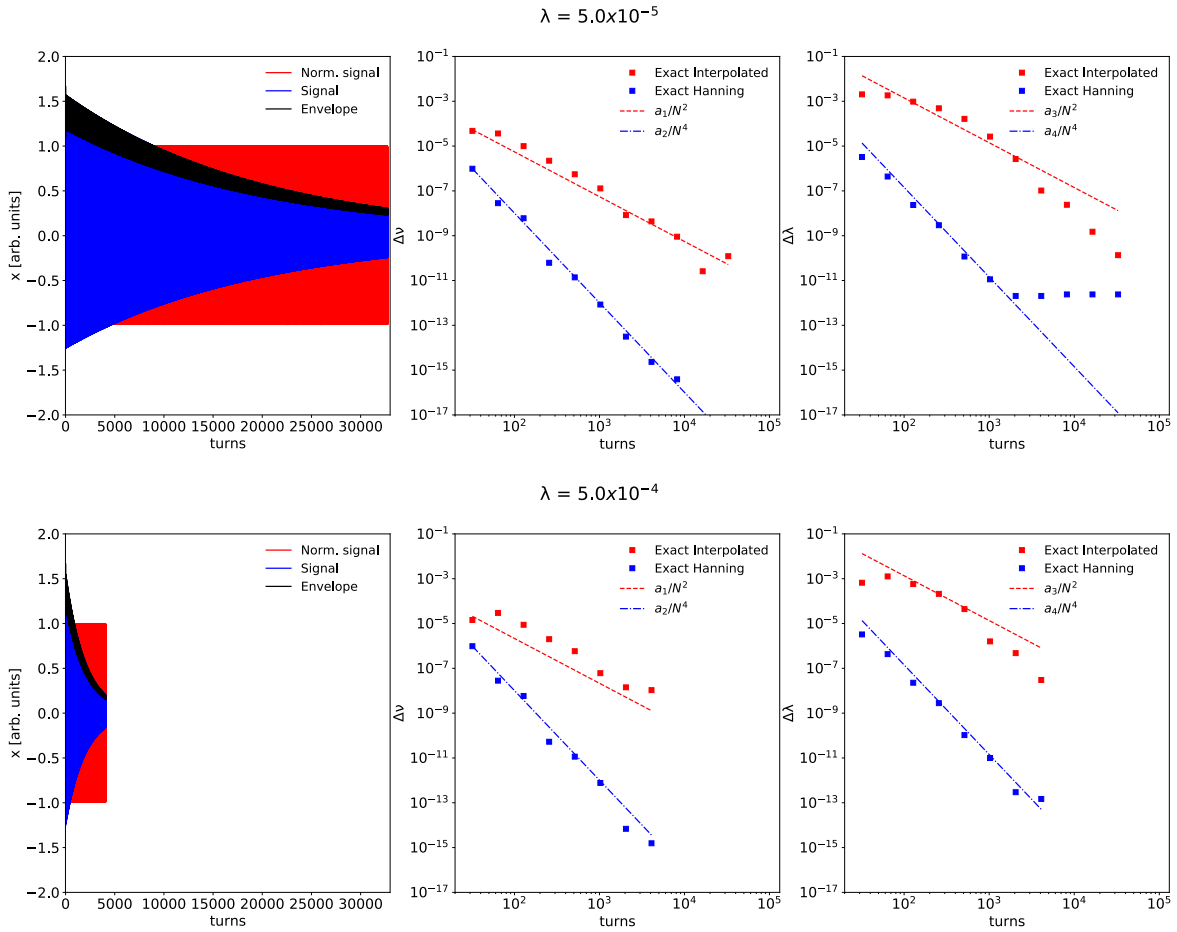

Figure 6.24: The numerical results of the damped exponential signal are shown for two different values of the damping factor λ. On the top $\lambda = 5 \times 10^{-5}$, while on the bottom $\lambda = 5 \times 10^{-4}$. On the first column the real part of the signal is reported in blue, the reconstruction of the envelope with the Hilbert Transform in black and the normalised signal in red. Then, the tune error and the damping factor error are shown with their scaling law on the second and third column, respectively.

Similarly, using the equations to determine the damping factor with the Interpolated and Hanning method (Eq. 6.36 and Eq. 6.49, respectively) the error can be estimated, it is reported on Figure 6.24 right. Also in this case the fit of the numerical data was performed with the scaling laws characteristic of the two methods and the coefficients are:

- For $\lambda = 5 \times 10^{-5}$: $a_1 = (14.11 \pm 0.12)$ and $a_2 = 14.30 \pm 0.02$;
- for $\lambda = 5 \times 10^{-4}$: $a_1 = (13.58 \pm 0.12)$ and $a_2 = 14.23 \pm 0.02$.

It is important to notice that in the reconstruction of the damping factor λ a saturation phenomenon can be observed for $\lambda = 5 \times 10^{-5}$ while it seems to be absent for $\lambda = 5 \times 10^{-4}$. The reason is that during the evaluation of the damping factor machine precision is hit. In fact, the value of

lambda error at which saturation occurs is $\approx 10^{-12}$, if the value of lambda $\lambda = 5 \times 10^{-5}$ is added, then it is clear that the machine precision has been reached. From this observation it is expected that a similar phenomenon occurs also for $\lambda = 5 \times 10^{-4}$, but the number of turns over which the evaluation is performed is not high enough to actually show the saturation. As a consequence, it is also possible to notice that the smaller the value of the damping factor λ, the smaller is the value of turns at which the saturation is reached (for $\lambda = 5 \times 10^{-5}$ saturation occurs ≈ 2048, while for $\lambda = 5 \times 10^{-4}$ it is expected for turns larger than ≈ 8192).

The same signals have been analysed with the methods described in Section 6.1 and Section 6.4. In particular, being these methods developed for constant amplitude signals, the comparison of their performance when used on the Hilbert normalised signal will be discussed (red signal in Figure 6.24) together with the discussion of the results obtained when the same methods are used on the original damped signal (blue one in Figure 6.24). The results of these analysis are reported in Figure 6.25. In particular, the analysis shows the results obtained for the tune estimation only, in fact for these methods it is not possible to determine the damping factor λ.

As a first comment, it is worth to notice that the tune analysis on the signal with larger λ has been performed over a lower number of turns because, as previously explained, the signal was truncated when the amplitude has reached the 5% of the initial value. The value of the number of turns at which truncation occurs is the same as the previous analysis, as it can be noticed from the comparison of Figure 6.24 and Figure 6.25. The results of the methods applied on the original damped signal are reported on the Figure 6.25 left, while their application to the Hilbert normalised signal has lead to the results shown on Figure 6.25 right. At first sight, the results of the different methods are compatible for the two values of damping factor λ. In fact, it is not possible to find a method that performs differently for the two cases.

As far as the use of the constant amplitude methods on the original signal is concerned, the results are reported on Figure 6.25 left, and two main points can be discussed. At first, it is clear that the use of the Interpolated method (see Section 6.1.2) and the Hanning one (see Section 6.1.3) leads to an estimation of the tune that increases as a function of the number of turns rather than decreasing. This behaviour is quite evident if the results from the FFT analysis (green cross line) is compared with the above-cited methods (red and blue cross lines). On the contrary, the weighted Birkhoff average can determine the tune to machine precision with 1024 (512) samples for $\alpha = 1$ ($\alpha = 2$) and the characteristic scaling law of $1/N^7$ is retrieved. FFT-based methods show their strong limitations when used on a amplitude modulated signal; while the super-convergence of the weighted Birkhoff average is not affected by the amplitude modulation of the signal, as proved in Section 6.4.4.

As far as the analysis of the Hilbert normalised signal is concerned, additional comments and conclusions can be drawn. The FFT provides the very similar results as those obtained when the method was applied to the original damped exponential signal. The Interpolated FFT (thus the use of Eq. 6.7) on the Hilbert normalised signal enables to retrieve the tune with the expected

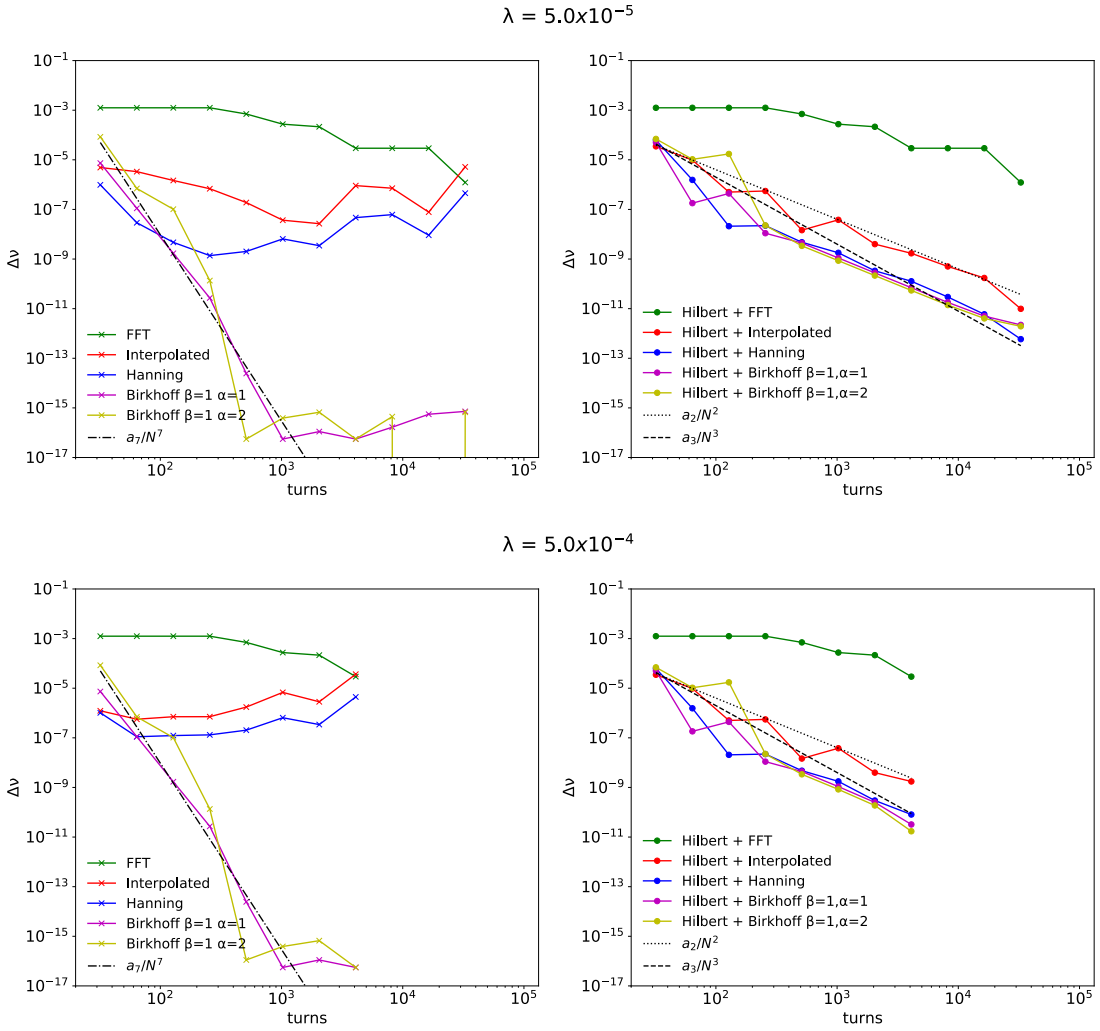

Figure 6.25: The methods developed for a constant amplitude signal are applied on the Hilbert normalised signal (left) and on the original damped exponential one (right). The analysis is performed for two values of the damping factor: $\lambda = 5 \times 10^{-5}$ on the top and $\lambda = 5 \times 10^{-4}$ on the bottom. Where possible, numerical data are fit and the characteristic scaling law of some methods is retrieved.

precision, in fact the tune error scales as $1/N^2$, as shown from the dotted line in Figure 6.25. On the contrary, it is not possible to conclude the same for the Hanning method (see Section 6.1.3) and Birkhoff (see Section 6.2.2). For both method a tune precision of $1/N^4$ and $1/N^7$, respectively, was expected while a scaling law of $1/N^3$ was obtained. The reason might be that the use of the Hilbert Transform on amplitude modulated signal could cause a modulation of the instantaneous frequency that limits the determination of the frequency by the subsequent harmonic analysis, as reported in Ref. [73]: *"[...] Clearly, the amplitude has introduced a* 1.5% *instantaneous frequency modulation around the mean of the carrier frequency. This frequency modulation should not be a surprise, equation (3.11) has already indicated that amplitude variations could cause a frequency*

fluctuation, but not a change of the mean. [...]". Therefore, a possible explanation for the reduction in performance of the Hanning and Birkhoff methods could be explained in this way.

In conclusion, from this analysis two methods seems to clearly emerge as the preferred ones. The Hilbert method developed for the purpose of analysing a damped exponential signal shows the expected precision and enables the determination of the tune as well as the damping factor of the signal. In the same way, the weighted Birkhoff average confirmed the expected scaling law even when applied on an amplitude modulated-signal. However, although the weighted Birkhoff average ensures a faster tune error scaling law compared to the exact Hanning formula, the former does not provide any information on the damping coefficient, that can be retrieved from the latter. They might be used together to precisely determine the tune with the weighted Birkhoff average and retrieve information on the damping factor from the Hanning analytical equation.

6.4.5.2 Chromatic decoherence

Chromatic decoherence have been first described in Ref. [64]. The evolution of the centroid of a proton beam after it has been kicked is described considering the effect of coupling between energy spread and transverse tune through the chromaticity [64]. It is possible to demonstrate that the energy spread does not actually cause a change in the betatron tune of the centroid, but rather a periodic amplitude modulation of the centroid is observed. Following the demonstration reported and described in Ref. [64], the turn-by-turn evolution of the beam centroid is:

$$x(n) = e^{-\frac{\alpha(n)^2}{2}} \cos 2\pi \nu_0 n \ , \tag{6.62}$$

where the coefficient α is defined as

$$\alpha(n) = 2\frac{\sigma_s \zeta}{\nu_s} \sin \pi \nu_s n \ , \tag{6.63}$$

and where σ_s, ν_s and ζ are the bunch length, the synchrotron tune, and the chromaticity, respectively. The generalisation of this description using a complex-value signal $z(n)$ is straightforward if the real part x is given by the average beam centroid position defined in the Eq. 6.62, and its imaginary part p_x is the average centroid momentum of the beam defined as:

$$p_x = e^{-\frac{\alpha(n)^2}{2}} \sin 2\pi \nu_0 n \ . \tag{6.64}$$

To further generalise the description, the signal has an initial amplitude a given by the kick and the contribution of $k = 1,...,4$ perturbative harmonics is added. Thus, the complex-valued signal $z(n)$ that describes the chromatic decoherence reads as follows:

$$z(n) = a e^{-\frac{\alpha(n)^2}{2}} \left(e^{2\pi \nu_0 n} + \sum_k e^{-k} e^{2\pi i n k \nu_0} \right) . \tag{6.65}$$

The amplitude modulation of the chromatic signal in Eq. 6.65 is fully determined by:

$$a \ \exp\left(-\frac{\alpha(n)^2}{2} \right) \tag{6.66}$$

known as decoherence factor. Trying to find an analytical expression for the tune by solving the FFT coefficient equation (or a combination of FFT coefficient equations around the peak) in terms of the frequency is not feasible. Thus, the way that has been adopted to determine the tune of the chromatic signal is to normalise it with the Hilbert Transform and analyse the resulting constant-amplitude signal with the methods described so far. For the sake of completeness, also the results obtained when the methods are applied on the original (thus, the non-normalised) signal will be reported and described. Three synchrotron tune values have been chosen to perform the analysis, in particular $\nu_s = 6.33 \times 10^{-5}$, $\nu_s = 1.21 \times 10^{-4}$ and $\nu_s = 2.51 \times 10^{-4}$ are those analysed and reported in Figure 6.26. The signal has been generated with a tune $\nu_0 = 0.261$, a chromaticity $\zeta = 20$ and a longitudinal beam sigma $\sigma_s = 1.33 \times 10^{-5}$; it has been sampled for a maximum

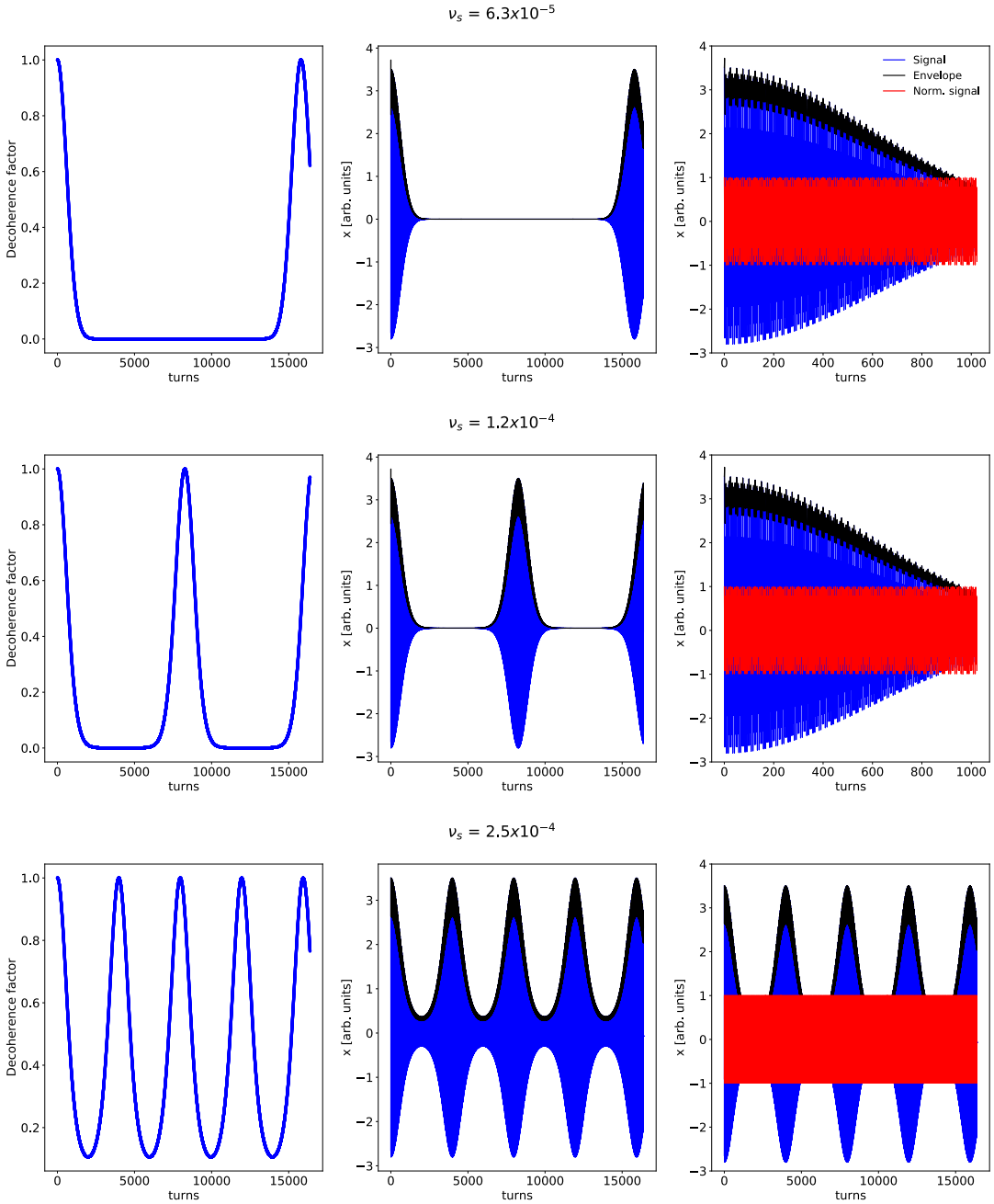

Figure 6.26: Three synchrotron tune values ν_s have been chosen to generate and analyse the chromatic signal. From left to right, it is possible to find: the decoherence factor; the signal (in blue) and the envelope (black) reconstructed with the Hilbert transform; the portion of the signal used for the tune determination where in red the Hilbert normalised signal is shown.

number of turns of 2×10^4. The characteristic features of the signal are reported in Figure 6.26. From top to bottom, the signals for the three synchrotron tunes are shown, while from left to right the decoherence factor is reported on the first plot. Its definition can be found in Eq. 6.66, and different decoherence and re-coherence behaviours can be observed according to the value of the synchrotron tune and the number of turns over which the signal has been sampled. For $\nu_s = 6.3 \times 10^{-3}$, the decoherence occurs within the first 2500 turns, then, after a period where no decoherence is observed, the recoherence occurs. According to the description performed in Ref. [64], chromatic phenomenon in absence of any type of error are periodic and their periodicity is determined by the synchrotron tune. In fact, as shown in Figure 6.26, the number of times the beam centroid re-coheres changes as a function of the synchrotron tune. The plots in the central column of Figure 6.26 represent the actual beam centroid evolution x, defined as in Eq. 6.62, as a function of the number of turns. Overlapped to it the envelope of the signal determined with the Hilbert Transform is shown in black. On Figure 6.26 right, the portion of the signal that has been used to compute the tune is displayed, in blue. Then, the envelope and the Hilbert normalised signal are reported in black and red respectively. It is possible to notice that for the first two signals (with $\nu_s = 6.3 \times 10^{-3}$ and $\nu_s = 1.2 \times 10^{-4}$) only a portion of the original signal as well as the normalised one as been reported and thus analysed. The reason is that when the amplitude of the signal reduces of the 95% with respect to the initial value, the remaining part of the signal is considered to be compatible with noise values that usually occur during measurement. Thus, also the re-coherence part is discarded, being it detected after a significant noise level. For this reason the value $\nu_s = 2.5 \times 10^{-4}$ of the synchrotron tune was chosen. It decoheres and recohere several times during the sampling period without reaching the noise level. Therefore, the analysis of these signals enables the understanding of how the different tune methods perform. Note that the portion of the signal analysed for the tune determination for the first two values of synchrotron tune (namely, 6.3×10^{-5} and 1.2×10^{-4}) is the same, the reason being that decoherence and re-coherence phenomena occur with a periodicity that is fully determined by the synchrotron tune itself. Thus, being 1.2×10^{-4} almost twice 6.3×10^{-5}, the former will show a complete re-coherence and decoherence behaviour where the latter will be compatible with 0, as shown in Figure 6.26.

As far as the tune analysis is concerned, the signals reported in Figure 6.26 right, were analysed and the results are reported in Figure 6.27. In particular, the results obtained from the analysis of the original chromatic signal are shown on Figure 6.27 left, while those obtained analysing the Hilbert normalised signals are reported on Figure 6.27 right .

As far as the analysis of the amplitude-modulated signal is concerned, it is possible to notice that the Interpolated FFT as well as the Hanning filtered FFT behave in the same way for the three considered signals. The tune retrieved from these methods leads to a tune error that increases as a function of the number of turns. This type of results confirm that FFT-based methods cannot be used on amplitude modulated signals, as it has already been observed for the damped exponential signal (see Figure 6.25). Two weighted Birkhoff averages for $\alpha = 1$ and

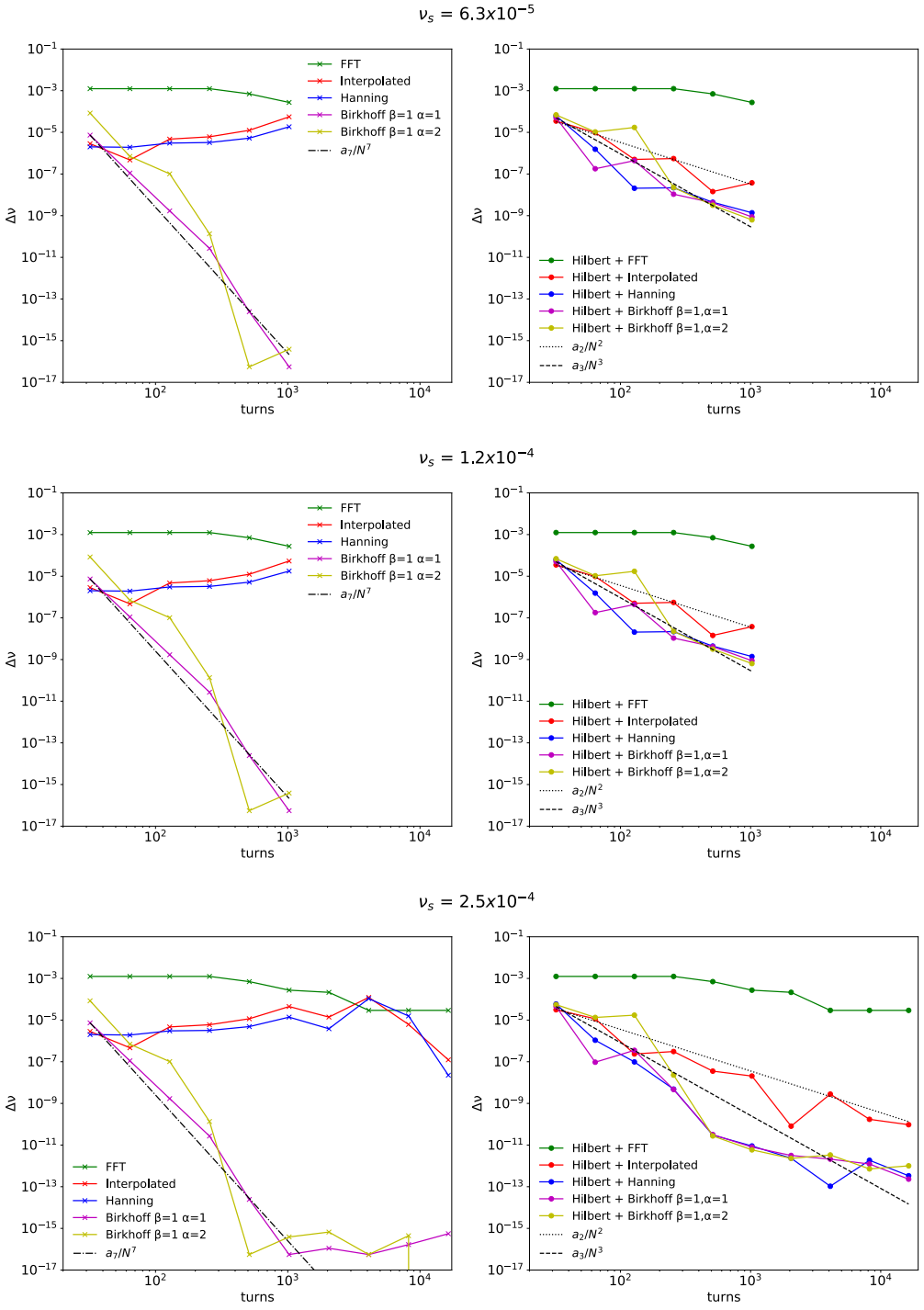

Figure 6.27: The tune analysis on the three chromatic signal is performed. The results obtained when the chromatic signal is analysed are reported on the left, while on the right those relative to the analysis of the Hilbert normalised signals are shown. Where possible the fit of the numerical data is performed and displayed.

$\alpha = 2$ have been performed on the chromatic signal. For both cases, it is possible to note that the characteristic scaling law of the method $1/N^7$ is observed. Also in this case, the feature highlighted in Section 6.4.4 (namely, the unchanged performances in terms of scaling law even when the method is applied to a varying amplitude signal) is verified for the chromatic amplitude modulated signal.

When the constant-amplitude chromatic signals (generated normalising the original signal by the Hilbert envelope) are analysed, two main features can be highlighted. At first the FFT and the Interpolated FFT show their characteristic scaling law of $1/N$ and $1/N^2$, respectively. However, the Hanning filtered FFT as well as the two weighted Birkhoff averages show an incredible worsening of their performances, since all of them scale as $1/N^3$ rather than $1/N^4$ and $1/N^7$, respectively. As already discussed earlier, the reason of this unexpected behaviour could be explained with Ref. [73], where a frequency modulation is observed when an amplitude modulated signal is analysed by means of the Hilbert transform.

In conclusion, also from the analysis of the chromatic signal, the weighted Birkhoff averages seem to emerge as the most promising methods to compute the tune with high precision.

6.4.6 Applications of the Hilbert transform on amplitude-modulated signals

In the previous sections, results on the use of the Hilbert transform on amplitude modulated signals have been shown and discussed. It has been found that for both a damped exponential signal as well as for the chromatic one, the tune analysis by means of the Hilbert normalised signal has led the most powerful methods, namely the Hanning filtered FFT and the Birkhoff averages, to a strong reduction in their performances. Therefore, even if this is a critical aspect of the Hilbert transform, the fact that it can reconstruct the envelope of an amplitude modulated signal is a very interesting feature to be further exploited. In fact, apart from the use of the envelope as a normalisation function (as described in Section 6.4.3 and exploited in Section 6.4.5.1 and Section 6.4.5.2), it could be used to retrieve machine parameters. The idea behind this innovative approach is to:

- generate a test signal simulating a possible measured beam signal with known properties;
- determine the envelope using the Hilbert Transform;
- fit the envelope to the physical model that explain the physics behind the evolution of the simulated signal;
- determine and compare the physical parameters obtained from the fit procedure with those used in the generation of the signal.

It was decided to test this approach on the chromatic signal, whose physics has been briefly explained in Section 6.4.5.2 but additional detail can be found in [64] where also the description of non-linear decoherence is carried out. The physics as well as the data analysis of non-linear

decoherence will be described in detail in Section 6.5, while the analysis on chromatic signal will be performed in this section. The analysis has been carried out on three test signals generated on 8000 turns with a chromaticity $\zeta = 20$, a longitudinal tune equal to $\nu_s = 6.33 \times 10^{-5}$, $\nu_s = 1.21 \times 10^{-4}$ and $\nu_s = 2.51 \times 10^{-4}$, a longitudinal beam size of $\sigma_s = 1 \times 10^{-5}$ and a betatron tune of $\nu_0 = 0.261$. The signal as been generated as defined in Eq. 6.65 with the parameter defined above. They are reported in Figure 6.28, where chromatic signal is shown in red, blue and green for the three values of synchrotron tune, respectively. For each of them the envelope is reported with a light-coloured version of the signal colour. Each envelope is then fit to the physical model described by Eq. 6.66.

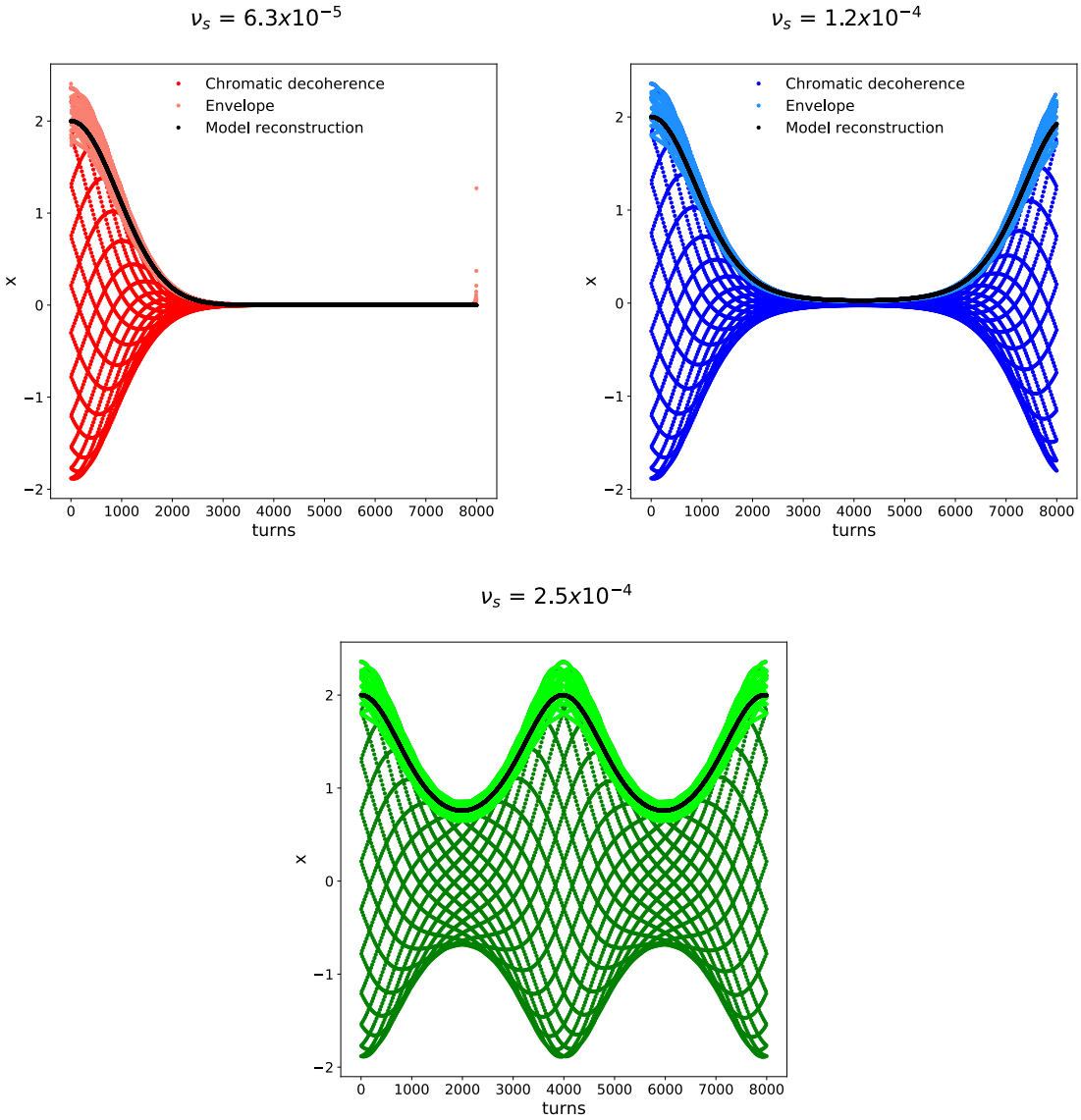

Figure 6.28: The chromatic signal and the envelope are shown for three different values of the synchrotron tune. The reconstruction of the physical model is then shown as a black line.

	$\nu_s = 6.33 \times 10^{-5}$	$\nu_s = 1.21 \times 10^{-4}$	$\nu_s = 2.51 \times 10^{-4}$
Chromaticity ζ	19.56 ± 0.04	19.77 ± 0.02	19.64 ± 0.02
Synchrotron tune ν_s	$(5.0 \pm 0.6) \times 10^{-5}$	$(1.21 \pm 0.0003) \times 10^{-4}$	$(2.51 \pm 0.0009) \times 10^{-4}$

Table 6.2: Results of the fit procedure applied on the Hilbert envelope.

In order to determine how many and which parameters among the synchrotron tune, the chromaticity and the longitudinal beam size were supposed to be considered as fit parameters to the model, several combinations and tests were performed. In these considerations, it is important to take into account the physics of the phenomenon. The experimental determination of the longitudinal beam length σ_s is not difficult while it is more critical to determine the chromaticity and the synchronous tune. The determination of the chromaticity ζ and the longitudinal beam size σ_s from the fit procedure was quite critical and their uncertainty was high compared to their nominal values. In fact, in Eq. 6.66, ζ and σ_s are multiplied by each other, thus the fit tends to optimise their product rather than the single variable. If the synchrotron tune ν_s and the longitudinal beam length σ_s are determined from the fit procedure, the latter is correctly determined for the three configurations. However, the former is determined correctly only for the last two chromatic configurations while an error of $\approx 40\%$ is obtained for the chromatic configuration where no re-coherence occurs within the $N = 8000$ tracked turns, namely $\nu_s = 6.33 \times 10^{-5}$. For these reasons and for the considerations discussed above, the final set of parameters that have been used in the fit procedure were the chromaticity ζ and the synchronous tune ν_s. The results of the fit procedure and the error associated at each variable are reported in Table 6.2. Also in this case, the chromatic configuration where no re-coherence is observed, shows the highest error in the determination of the synchrotron tune. Thus, it is possible to conclude, that a correct determination of the synchrotron tune for the fit procedure is strongly limited in the absence of re-coherence phenomenon. These values have been used to reconstruct the amplitude modulation of the chromatic signal according to Eq. 6.66. The reconstructed model is shown as the black line in Figure 6.28. As it is possible to observe from the results reported in Table 6.2, the chromaticity and the synchrotron tune are compatible with the one used in the generation of the signal.

This approach seems to enable the determination of fundamental machine parameters such as the chromaticity and the synchrotron tune. Therefore, from this preliminary but promising results, it was decided to use this approach on real beam data that are based on a different theoretical model. The analysed signal has a Gaussian amplitude modulation which comes from the model describing the amplitude detuning phenomenon. The analysis as well as the discussion on different approaches to reconstruct the amplitude detuning will be the main focus of the next Sections.

6.5 Real beam data analysis: non-linear decoherence

Non-linear effects have a direct impact on the beam life-time. There are some special conditions where non-linear effects are wanted and exploited: one application has been discussed in Chapter 4 where sextupolar and octupolar non-linear magnetic fields are used to generate a fourth-order resonance that splits the beam into five beamlets that are then extracted and sent to the downstream accelerator. On the contrary, it is more common to investigate and study to minimise their effect and their contribution, thus improving accelerator performance.

There are multiple non-linear effects that affect the beam dynamics. On the one hand, the tune spread of the beam might increase because of the beam-beam interactions, space charge and amplitude detuning [22]; on the other hand, unwanted excitation of resonances might occur because of non-proper tuning of multipoles; thus the available space in the tune diagram to accommodate the beam within resonance lines reduces. As a consequence, it has become more and more important to evaluate the tune during machine operations to increase beam life-time. Numerical simulations and experimental measurements benchmark are needed to assess the impact of non-linear effects on the beam stability.

Their contribution is experimentally evaluated perturbing the beam with a kick and observing the tune changes. Repeating this measurement for different kick amplitudes enables the evaluation of the tune as a function of the amplitude of the single-particle emittance, namely the amplitude detuning. Due to the intrinsic coupling[4] between the horizontal and vertical transverse planes, a perturbation in one of the two planes unavoidably propagates to the other plane. After a proton beam has been kicked in one plane, it is possible to observe a decoherence of the betatron oscillation of the beam particles on a turn-by-turn basis. From a physical point of view, this is explained considering that the beam filaments occupying a larger area in phase-space, as schematically shown on Figure 6.22 right. Turn after turn, the betatron oscillations of every particle in the beam decohere, thus also the beam centroid position evolves until it reaches the zero-amplitude. Once this condition is reached, the beam filamentation is completed and the beam centroid is back on the zero orbit.

The mathematical description of this phenomenon has been carried out for the first time by Meller et al. in Ref. [64]. The model is based on two main assumptions: the beam has a Gaussian distribution (this is representative of the actual beam distribution in the majority of the cases) and the tune changes as a quadratic function with respect to the betatron amplitude.

In the context of this section, the Meller model will be briefly reported and discussed since one of its major results will be used at the end of this section to suggest a new and innovative method to compute the amplitude detuning. At first, experimental data will be analysed and the results will be benchmarked against the actual state-of-the-art for the amplitude detuning

[4]There are several phenomenon that cause a coupling between the transverse planes, among these it is worth highlighting the presence of non-linear magnetic elements, such as sextupoles, octupoles and higher-order magnets; magnets misalignments and imperfections.

measurements procedure. Then, it will be shown as this method can provide information on the amplitude detuning factor, separating the first- to the second-order contribution.

6.5.1 Meller model description

The Meller model described in Ref. [64], considers a Gaussian beam with transverse beam size equal to σ_x and emittance ϵ_x and assumes that the nominal tune ν_0 changes quadratically with the normalised kick amplitude a, following

$$\nu = \nu_0 - \mu a^2 \,, \tag{6.67}$$

where μ is called decoherence factor and a is defined as

$$a = \frac{\sqrt{\beta_x \epsilon_x}}{\sigma_x} \,, \tag{6.68}$$

where ϵ_x is the single-particle emittance (thus, the following equality holds true $\epsilon_x = 2J_x$), and β_x is the horizontal beta function. Under these conditions, it is possible to write the beam distribution in terms of the amplitude a and phase ϕ coordinates. If a kick Z with intensity normalised[5] to the beam size

$$Z = \frac{\beta \Delta x'}{\sigma_x} \,, \tag{6.69}$$

is applied to the beam, then, it is possible to write the distribution of the kicked beam, and it will read as:

$$\rho(a,\phi) = \frac{1}{2\pi} a \, \exp\left[-\frac{1}{2} \left(a^2 + Z^2 - 2aZ\cos\phi \right) \right] \,. \tag{6.70}$$

From the knowledge of the tune shift reported in Eq. 6.67, it is possible to determine the phase shift as:

$$\Delta\phi(a,n) = -2\pi\mu a^2 N \,. \tag{6.71}$$

Considering that particles have different betatron amplitudes and considering the entire phase domain ($\phi \in [0, 2\pi]$), it is possible to integrate the distribution of a kicked beam reported in Eq. 6.70 and thus obtain the turn-by-turn evolution of the beam centroid:

$$x(N) = \sigma_x Z A(N) \cos\left(2\pi\nu_0 n + \Delta\phi(N) \right) \,, \tag{6.72}$$

where N is the number of turns over which the signal has been sampled, thus the number of turns over which the decoherence is observed. The coefficient $A(N)$ is the amplitude decoherence factor defined as

$$A(N) = \frac{1}{1+\theta^2} e^{-\frac{Z^2}{2}\frac{\theta^2}{1+\theta^2}} \,, \tag{6.73}$$

where θ is defined as

$$\theta = 4\pi\mu N \,. \tag{6.74}$$

[5] Note that following the description by Meller, it is possible to prove that $a = Z$ since the kick is defined as $\Delta x' = \sqrt{\epsilon_{x,ph}/\beta_x}$, where $\epsilon_{x,ph}$ is the physical beam emittance.

For $Z >> 1$ a Gaussian decoherence is obtained and the amplitude decoherence factor reads as:

$$A_G(N) = e^{-\frac{1}{2}(4\pi\mu ZN)^2} \ . \tag{6.75}$$

This case is particularly interesting since in experimental measurements the beam is usually kicked at amplitudes significantly larger than the beam size (thus the condition $Z >> 1$ is verified). Therefore, when observing real beam data a Gaussian decoherence is expected to be found.

6.5.2 Experimental data analysis

As already briefly explained, the determination of the amplitude detuning, thus the tune as a function of the kick amplitude, is one of the procedures used to determine the contribution of non-linear effects. Even if the contribution of non-linear fields is minimised during the accelerator design, it is not possible to completely remove their effects. In fact, during construction and installation additional source of non-linearities can be created (such as imperfections during manufacturing or alignments problems during installation). For this reason their experimental determination and later on their minimisation is fundamental to improve the accelerator performance.

In 2012 an extensive campaign has been carried out to determine the contribution of LHC non-linearities by measuring several observables, relative to local or global properties of the ring: amplitude detuning, non-linear chromaticity and dynamic aperture. Measurements of dynamic aperture is of fundamental importance to understand the actual limits in phase-space beyond which particles are lost. The loss might occur because of physical limitation inside the vacuum chamber or because of resonance lines that actually limit the available transverse space the beam can occupy, thus losses occur because particle orbits become unstable. The effect of non-linear chromaticity is similar to the one of amplitude detuning. The former considers a tune change due to the relative deviation of the particle momentum from the nominal value, the latter considers a tune deviation as a function of the single particle emittance, namely the Courant-Snyder invariant. In 2012, the three methods have been applied in details and the results can be found in Ref. [74]. In the context of this section only the amplitude detuning results will be analysed and discussed.

The change of tune as a function of the single-particle emittance is known as amplitude detuning. It is possible to quantify it as the Taylor expansion in the vicinity of the unperturbed tune:

$$\nu_x(\epsilon_x,\epsilon_y) = \nu_{x,0} + \frac{\partial\nu_x}{\partial\epsilon_x}\epsilon_x + \frac{\partial\nu_x}{\partial\epsilon_y}\epsilon_y + \frac{1}{2}\left(\frac{\partial^2\nu_x}{\partial\epsilon_x^2}\epsilon_x^2 + 2\frac{\partial^2\nu_x}{\partial\epsilon_x\partial\epsilon_y}\epsilon_x\epsilon_y + \frac{\partial^2\nu_x}{\partial\epsilon_y^2}\epsilon_y^2\right) , \tag{6.76}$$

where ϵ_x and ϵ_y refer to the single-particle emittance in the horizontal and vertical plane, respectively. Equation 6.76 can be written also for the vertical tune by replacing ν_x and $\nu_{x,0}$ with ν_y and $\nu_{y,0}$, respectively. Following the description in Ref. [75], a normal octupole induces a linear effect in the tune change as a function of the single-particle emittance thus it induces a linear

amplitude detuning. However, higher-order dependence can arise from higher-order multipoles. From the Meller model, the following series of identities can be derived:

$$a = \frac{\sqrt{\beta_x \epsilon_x}}{\sigma_x} \longrightarrow a^2 = \frac{\beta_x 2J_x}{\sigma_x^2} = \frac{2J_x}{\epsilon_{x,ph}} \,, \tag{6.77}$$

from which it is deduced that the quadratic dependence on the kick intensity a is nothing but a linear proportionality with the action $2J_x$.

The amplitude detuning is measured in several steps. After the beam has been kicked, the BPMs record the position of the beam centroid on a turn-by-turn basis. Thus, at the end of the measurement, a signal sampled over N turns is available for analysis. FFT-based techniques, such as NAFF, are used to determine the tune. From the average of the tune values, computed analysing every BPM signal, it is possible to obtain an average value of the tune and its error, determined as the standard deviation on the tune values. Repeating the measurements and the frequency analysis for different kick amplitudes it is possible to obtain the tune as a function of the single-particle emittance. The single-particle emittance $2J_x = \epsilon_x$ and the kick amplitude Z are related according to the following equality:

$$Z = \frac{\beta_x \Delta x'}{\sigma_x} = \sqrt{\frac{\epsilon_x}{\epsilon_{x,ph}}} \,, \tag{6.78}$$

where $\epsilon_{x,ph} = \sigma_x^2/\beta_x$ is the physical emittance of a Gaussian beam, as the one considered in these analysis. From Eq. 6.78 it is clear that the kick is normalised with respect to the physical beam emittance. A fit of the experimental data is then performed to determine the relative change of tune with respect to a kick in a certain direction, and thus the partial derivative terms in Eq. 6.76 are determined.

Even though this procedure is well established and provides useful information on the amplitude detuning, its knowledge comes from tune measurements for increasing single-particle emittance. It would be very interesting to be able to directly evaluate or measure the amplitude detuning since it provides information on the optical properties of the ring lattice. For a given Gaussian beam, the Meller model provides a mathematical model of the phenomenology that can be exploited to directly measure the amplitude detuning following a free-kick perturbation to the beam. This topic will be described in detail in the next subsection. Moreover, amplitude detuning measurements are destructive measurements in the sense that after the beam has been kicked and it has filamented, it is necessary to dump it and create a new one before the next measurement can be performed. Thus it is a very time consuming measurement and it has to be repeated twice for both beams in the LHC.

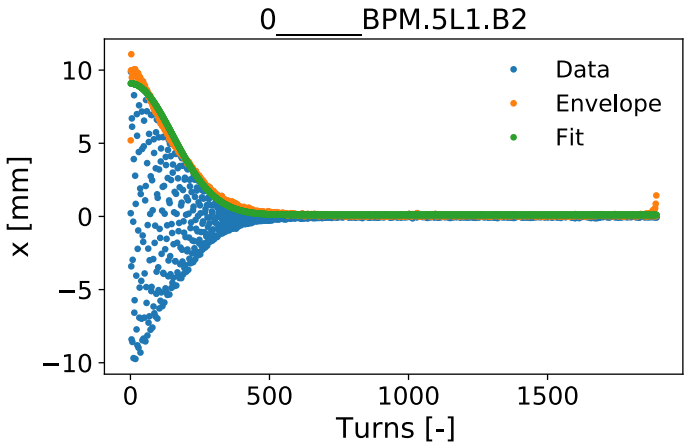

Figure 6.29: The turn-by-turn position of the beam centroid is shown in blue. The envelope computed with the Hilbert transform is shown in orange, and the result of the fir procedure is reported in green.

6.5.2.1 Benchmark against 2012 measurements

A new innovative approach to determine the amplitude detuning will be discussed. There are few drawbacks in the approach used for amplitude detuning measurements. The tune evaluation of the turn-by-turn BPM signal with the NAFF (or any FFT-based approach) is intrinsically not corrected. In fact, the BPM signal has an amplitude that changes over time due to the decoherence phenomenon described in Ref. [75] and mathematically derived by Meller in Ref. [64]. An example of LHC signal acquired during 2012 measurements is reported in Figure 6.29, where the amplitude decreases during the sampling period according to the Gaussian modulation predicted by Meller in Ref. [64] and reported in Eq. 6.75. The NAFF technique is an FFT-based method that assumes the amplitude of the signal to be constant during the sampling period. The suggested approach aims at determining the tune and the amplitude detuning coefficient following these steps:

- The envelope of every BPM signal is reconstructed by means of the Hilbert transform (see Section 6.4.3). In Figure 6.29 the envelope is reported in orange;
- The envelope is then used to normalise the signal. Thus, the tune is computed with the Interpolated FFT (see Section 6.1.2).
- The envelope is fitted with a Gaussian function

$$y_{Fit}(n) = Ae^{-\lambda n^2}\ , \tag{6.79}$$

where the factor λ and the amplitude A are the fit parameters, and the number of turns n ranges from 1 to N. The result of the fit procedure for the BPM in Figure 6.29 is shown in

green. From the comparison of Eq. 6.79 and Eq. 6.75 the amplitude detuning coefficient μ is computed as:

$$\mu = \pm \frac{\sqrt{2\lambda}}{4\pi Z} \ . \tag{6.80}$$

This procedure is then repeated for every BPM. The tune and amplitude detuning coefficient values are obtained as the average of the values from the analysis of every BPM signal, and the associated error is estimated as the standard deviation. The results obtained from this procedure are compared with those obtained with the previous method and reported in Ref. [74].

In particular, during 2012 the amplitude detuning was determined in two LHC configurations: the uncorrected configuration where no adjustment was performed and thus it enables the determination of the nominal non-linear components; and a corrected configuration where the strengths of specific non-linear elements was adjust in order to minimise the effects of non-linear fields. Additional details on the setup of the two configurations can be found in Ref. [74].

The results from the analysis of the two data set is shown in Figure 6.30, where the uncorrected configuration is shown in red while the corrected one is shown in blue. Moreover, Figure 6.30 shows the tune along the vertical (top) and horizontal (bottom) plane as a function of a horizontal (left) and vertical (right) perturbation. In particular, the analysis of the experimental data is shown as a dot with the corresponding vertical and horizontal error bar for the tune and action, respectively. Thus the data are fitted with:

$$Q_u(2J_u) = Q_{u,0} + a_1 2J_u + \frac{1}{2} a_2 (2J_u)^2 \ , \tag{6.81}$$

where the subscript u refers to x, y and their proper combination, according to the plane where the tune is measured and to the plane where the perturbation occurs. The linear ($a_2 = 0$) or parabolic fit (Eq. 6.81) of the data is shown with a continuous line, and its error is shown with a coloured area. The dashed black curve as well as its grey error area refers to the fit and its error obtained in 2012 with the previous methodology (thus tune calculation by means of the NAFF technique on the Gaussian amplitude-modulated BPM signal), which details can be found in Ref. [74].

From the comparison of the results obtained with the two methodologies, it is possible to observe that the uncorrected configuration (in red) is in agreement with the previous analysis and a reduction of the fit uncertainty is also observed. The only discrepancy can be observed for amplitude detuning in the vertical plane (top right plot). However, this deviation is only relevant and observable at high values of actions (above 0.4) where no measurement has been performed. Below this threshold, where the linear term is dominant, the maximum discrepancy in the fit parameters is $\approx 7\%$, which is within the deviation $\pm 10\%$ usually accepted in experimental measurements. As far as the corrected configuration (blue curve) is concerned, the uncertainty associated to the fit it is larger than the one retrieved from the previous method. However, the fit curve represents well the experimental data, this observation is also confirmed from the value of the reduced chi-square test. All the results of the fit procedure, such as the coefficients in Eq. 6.81

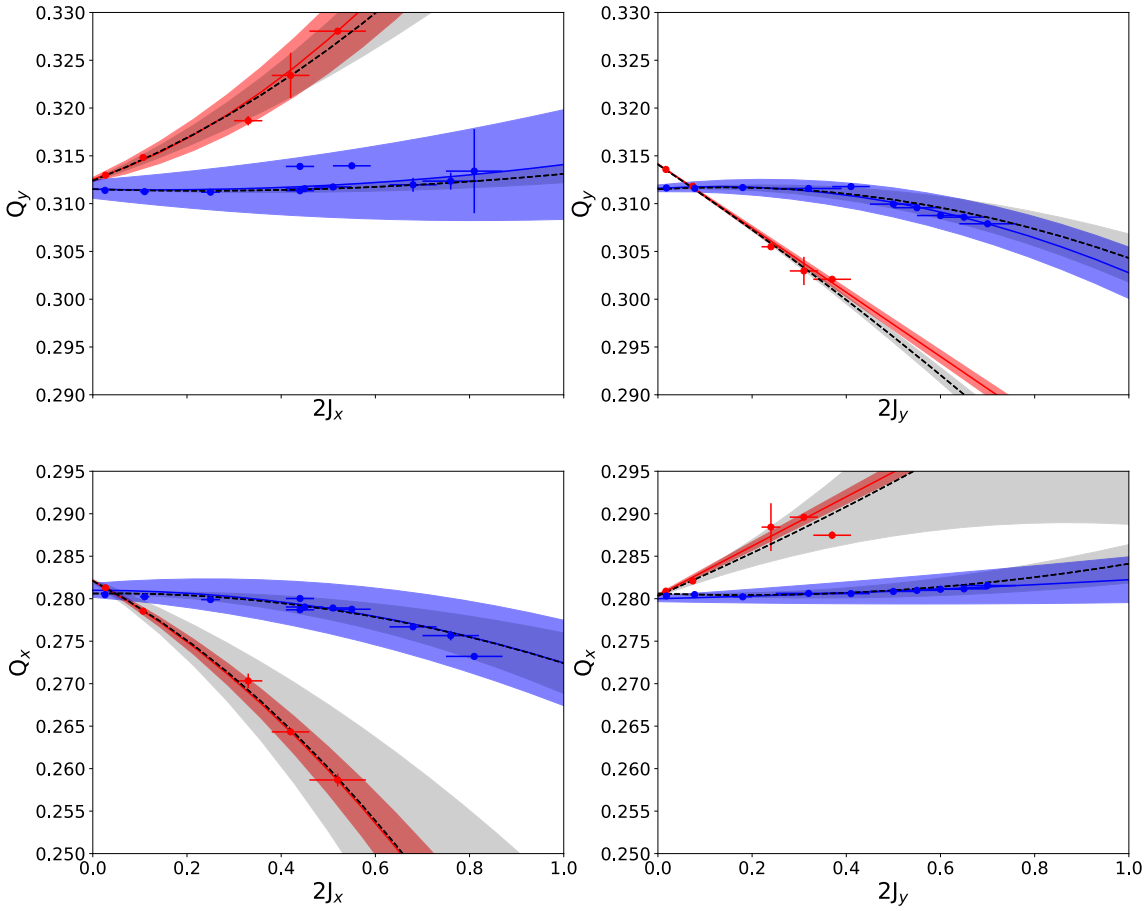

Figure 6.30: The experimental data collected during the 2012 experimental campaign at LHC have been analysed using the Hilbert normalisation approach. The red data and the corresponding fit refer to the non-corrected LHC configuration, while the blue ones refer to the corrected one. The results obtained in 2012 are shown in black and grey. The picture shows the change of the vertical (horizontal) tune on the first (second) row as a function of a horizontal (vertical) kick on the first (second) column, thus, namely, the amplitude detuning.

and the reduced chi-square test, are reported in Table 6.3. From the results reported in Table 6.3, the largest uncertainty are related to the determination of the first-order coefficient a_1 in the corrected configuration, however, the low value of the chi-square test ensures the good quality of the fit. In conclusion, although some discrepancy in the reconstruction of the detuning, it is possible to observe from Figure 6.30, a quite good agreement with the results obtained in 2012 (see Ref. [74] for additional information). The discrepancies between the two methods might be several; among these, it is worth citing the different way of computing the tune. In particular, in 2012 FFT-based methods to determine the tune were adopted on an amplitude-modulated signal. This limitation is solved in the proposed methodology. This innovative method in the reconstruction of amplitude detuning from experimental data seems to provide promising results.

	Uncorrected configuration			
	Q_y vs $2J_x$	Q_y vs $2J_y$	Q_x vs $2J_x$	Q_x vs $2J_y$
$Q_{u,0}$	$0.3125 \pm 2 \times 10^{-4}$	$0.31415 \pm 3 \times 10^{-5}$	$0.28211 \pm 8 \times 10^{-5}$	$0.2804 \pm 2 \times 10^{-4}$
a_1	$(1.6 \pm 0.7) \times 10^4$	$(-3.4 \pm 0.1) \times 10^4$	$(-3.0 \pm 0.3) \times 10^4$	$(2.9 \pm 0.2) \times 10^4$
a_2	$(5.3 \pm 0.1) \times 10^{10}$	–	$(-5.8 \pm 1.1) \times 10^{10}$	–
χ^2	0.02	0.02	0.09	0.01
	Corrected configuration			
$Q_{u,0}$	$0.3115 \pm 9 \times 10^{-4}$	$0.3116 \pm 3 \times 10^{-4}$	$0.2810 \pm 8 \times 10^{-4}$	$0.2800 \pm 3 \times 10^{-4}$
a_1	$(-0.96 \pm 47) \times 10^3$	$(3 \pm 2) \times 10^3$	$(-1 \pm 4) \times 10^3$	$(1 \pm 2) \times 10^3$
a_2	$(7.1 \pm 0.1) \times 10^9$	$(-2.4 \pm 0.1) \times 10^{10}$	$(-1.7 \pm 0.1) \times 10^{10}$	$(1.7 \pm 0.1) \times 10^9$
χ^2	2.0×10^{-4}	5.0×10^{-4}	5.0×10^{-4}	2.0×10^{-5}

Table 6.3: Results of the fit on the tune as a function of the single particle emittance.

From the BPM signal normalisation by means of the Hilbert transform, the amplitude detuning coefficient as in Eq. 6.80 can be retrieved. Following the same rationale adopted for the evaluation of the average value of the tune, the amplitude detuning coefficient is computed for every BPM signal, thus the mean value and the standard deviation over all the BPM is determined. The results are shown in Figure 6.31. The amplitude detuning factor is fitted to the following curve:

$$\mu_u(2J_u) = a_{1,N} + a_{2,N}(2J_u) \,, \tag{6.82}$$

where the subscript u refers to the horizontal x, vertical y direction and the subscript N refers to the fact that those coefficients are normalised with respect to the physical emittance of the beam $\epsilon_{u,ph}$. Thus from the comparison of Eq. 6.82 with the derivative of Eq. 6.81 with respect to the single-particle emittance $2J_u$, the following identities can be retrieved:

$$a_{i,N} = a_i \epsilon_{u,ph} \,, \tag{6.83}$$

where the subscript i is either 1 or 2 if the constant or linear term are considered, respectively. As a consequence of the measurement procedure, the points reported in Figure 6.31 are a linearisation of the actual amplitude detuning coefficient (whose functional form is not known) in the proximity of the single-particle emittance at which the measurement is performed. For this reason, knowing its value at different kick strength allows for the understanding of whether there is an evolution of the parameter as a function of the kick amplitude and, if so, its mathematical shape (constant or linear).

The amplitude detuning can be determined in different ways:

1. The fit of the Hilbert envelope, provides, for the first time, a direct measurement of the amplitude detuning. The values obtained for increasing kick intensities can be fit with Eq. 6.82, to estimate if a constant or linear relation exists with the single-particle emittance. Since Eq. 6.80 does not provide information on the sign of the amplitude detuning μ, its

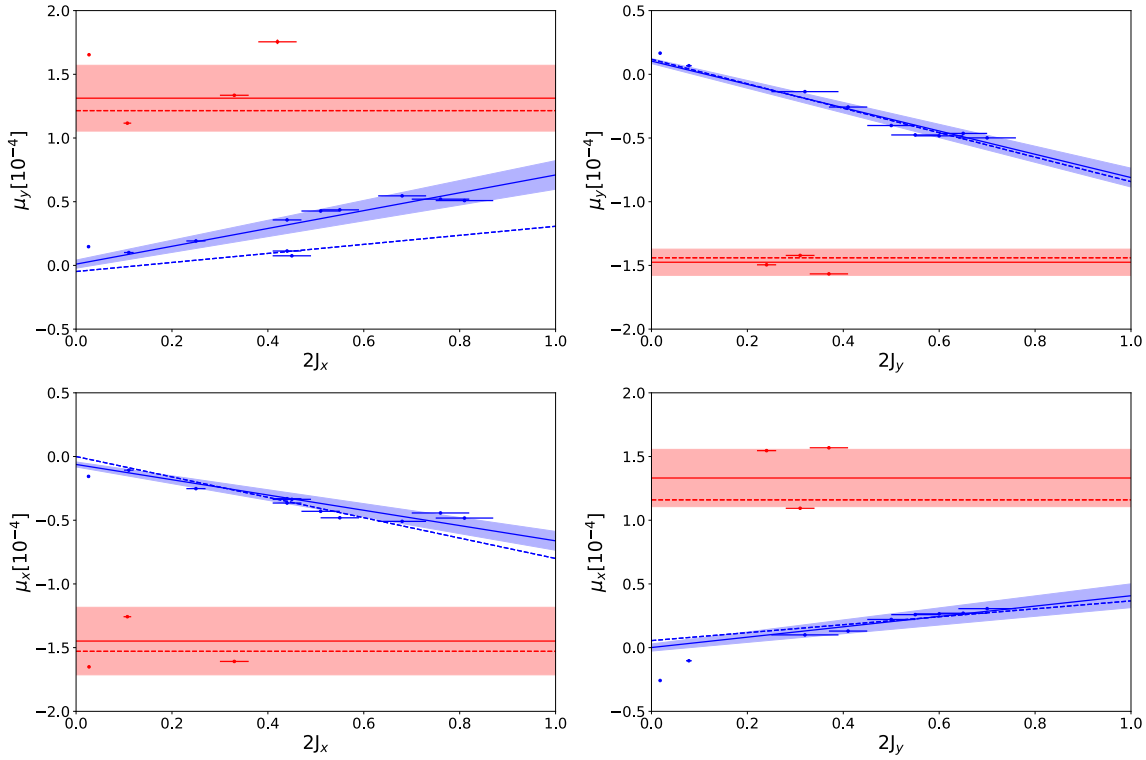

Figure 6.31: The amplitude detuning in the horizontal and vertical planes is reported as a function of the horizontal and vertical single-particle emittance for the uncorrected (red) and corrected (blue) configurations analysing the LHC data collected in 2012. The results of the fit procedure (continuous line) using Eq. 6.82 and the fit error are shown with a coloured bar. The dashed lines refer to the amplitude detuning evaluated as the derivative of the curve fitting the tune versus the action in Figure 6.30.

determination comes from the observation of how the tune changes as a function of the kick amplitude.

2. The amplitude detuning can be also obtained from tune measurements and thus:

   a) the tune can be computed on the Hilbert normalised signal (according to the new procedure just described);

   b) using the NAFF technique on the amplitude-modulated signal (as was performed in 2012).

3. For the uncorrected it is also possible to estimate the amplitude detuning using the LHC model in MAD-X, thus obtaining its value from tracking data. For the corrected one, the MAD-X model has been matched to the experimental data, thus it is not possible to obtain an additional independent model against with bench-marking the results.

The results obtained from these different approaches will be described, compared and displayed in Figure 6.31.

Figure 6.31 shows the comparison between the amplitude detuning retrieved from the Gaussian fit of the Hilbert envelope (point 1. above) and evaluated as the derivative of the tune fit curve (thus the derivative of Eq. 6.81 with respect to the action) when the tune is computed with the Interpolated FFT on the Hilbert normalised signal (point 2.a above). As reported in Figure 6.31 the uncorrected configuration has an amplitude detuning that does not depend on the action. On the one hand, the tunes in the horizontal and vertical planes due to a vertical kick, in Figure 6.31 top and bottom right, change linearly as a function of the single-particle emittance on the vertical plane itself, thus the amplitude detuning was expected to be constant. On the other hand, a clearly parabolic behaviour was observed for the vertical and horizontal tunes when the beam is kicked horizontally. From a closer look to Figure 6.31, it is possible to observe that one experimental point on the vertical plane and two on the horizontal one, have been removed from the analysis. The reason being that at the largest kick amplitude ($\approx 0.5\mu$m), the beam was kicked at such an amplitude that it was partially trapped into resonance islands. Therefore, from the measurements it was not possible to distinguish the contribution of the beam undergoing filamentation in the linear region of the phase-space from the one trapped in the islands. Islands were detected also in the vertical plane. Thus both points (horizontal and vertical tunes) have been removed for the largest kick amplitude. For the same reason, the second largest kick amplitude was removed from the analysis. However, on the vertical plane no islands have been observed, therefore, the point has not been removed from the analysis. The turn-by-turn beam centroid evolution for these cases can be found in Figure 6.35, where the presence of the islands has been highlighted. For these cases, after the removal of these critical points, a linear fit of the tune as a function of the action has been performed, thus, the constant dashed line in Figure 6.31 is justified.

The corrected configuration shows a linear trend of the amplitude detuning coefficients on all the planes independently on the plane where the perturbation occurs. The largest discrepancy can be observed for the vertical amplitude detuning as a consequence of an horizontal kick. The results of the fit procedure with the corresponding uncertainty on the fit coefficients are reported in Table 6.4 for the constant term $a_{1,N}$ and in Table 6.5 for the linear term $a_{2,N}$, where also the reconstruction of the amplitude detuning from 2012 analysis and with the LHC MAD-X model is reported. Note that during 2012 measurement, the horizontal and physical beam emittance have been measured and their value is 0.005μm and 0.004μm, respectively.

This is the first time where information on the amplitude detuning coefficients are retrieved from the analysis of individual series of orbit data. From the comparison of the constant and linear term in Table 6.3 and Table 6.5, respectively, several conclusions can be drawn:

- The new innovative approach allows for the determination of the amplitude detuning from the fit of the envelope with a Gaussian curve (first column) and from the observation of the

$a_{1,N}$ [10^{-4}]		**Fit envelope**	**Fit tune-action**	**Fit tune-action (2012)**	**LHC MAD-X**
μ_y vs $2J_x$	Unc.	(1.3 ± 0.3)	(1.2 ± 0.2)	(0.76 ± 0.12)	(0.88 ± 0.06)
	Corr.	(-0.01 ± 0.03)	(-0.05 ± 0.02)	(-0.07 ± 0.02)	–
μ_y vs $2J_y$	Unc.	(-1.5 ± 0.1)	(-1.44 ± 0.02)	(-1.64 ± 0.02)	(-1.53 ± 0.04)
	Corr.	(0.10 ± 0.02)	(0.12 ± 0.09)	(0.12 ± 0.04)	–
μ_x vs $2J_x$	Unc.	(-1.5 ± 0.2)	(-1.5 ± 0.3)	(-1.16 ± 0.03)	(-1.08 ± 0.03)
	Corr.	(-0.06 ± 0.01)	(-0.01 ± 0.02)	(-0.04 ± 0.05)	–
μ_x vs $2J_y$	Unc.	(1.3 ± 0.2)	(1.16 ± 0.06)	(1.0 ± 0.2)	(0.88 ± 0.06)
	Unc.	(0.01 ± 0.03)	(0.06 ± 0.02)	(0.08 ± 0.03)	–

Table 6.4: The abbreviations "Corr." and "Unc." refers to the corrected and uncorrected configurations, respectively. Results of the fit on the amplitude detuning as a function of the single-particle emittance. The table reports the value of the constant term $a_{1,N}$ computed from the four above-described methods: the fit of the envelope with a Gaussian curve (first column), the derivative of the curve fitting the tune vs. the action, where the tune is determined with the Hilbert normalised signal (second column), from the same method but when the tune is computed on the Gaussian amplitude-modulated signal (third column) and from the LHC MAD-X model (fourth column). For the corrected configuration the LHC MAD-X model has been matched to experimental data, thus it is not possible to have an independent value.

$a_{2,N}$ [10^{2}]		**Fit envelope**	**Fit tune-action**	**Fit tune-action (2012)**	**LHC MAD-X**
μ_y vs $2J_x$	Unc.	N.A.	N.A.	(1.4 ± 0.4)	(0.68 ± 0.32)
	Corr.	(0.7 ± 0.1)	(0.35 ± 0.1)	(0.30 ± 0.05)	–
μ_y vs $2J_y$	Unc.	N.A.	N.A.	(-0.7 ± 0.2)	(-0.2 ± 0.20)
	Corr.	(-0.91 ± 0.05)	(-0.97 ± 0.1)	(-0.8 ± 0.1)	–
μ_x vs $2J_x$	Unc.	N.A.	N.A.	(-2.4 ± 1.2)	(-0.56 ± 0.12)
	Corr.	(-0.60 ± 0.05)	(-0.80 ± 0.1)	(-0.90 ± 0.25)	–
μ_x vs $2J_y$	Unc.	N.A.	N.A.	(0.44 ± 1.4)	(-0.40 ± 0.36)
	Corr.	(0.40 ± 0.07)	(0.30 ± 0.1)	(0.44 ± 0.12)	–

Table 6.5: The abbreviations "Corr." and "Unc." refers to the corrected and uncorrected configurations, respectively. Results of the fit on the amplitude detuning as a function of the single-particle emittance. The table reports the value of the linear term $a_{2,N}$ computed from the four above-described methods: the fit of the envelope with a Gaussian curve (first column), the derivative of the curve fitting the tune vs. the action, where the tune is determined with the Hilbert normalised signal (second column), from the same method but when the tune is computed on the Gaussian amplitude-modulated signal (third column) and from the LHC MAD-X model (fourth column). For the corrected configuration the LHC MAD-X model has been matched to experimental data, thus it is not possible to have an independent value. The acronym "N.A." stands for "Not Applicable" and it refers to the cases where a linear fit of the tune-action data or a constant fit on the amplitude detuning has been performed, thus the linear term $a_{2,N}$ does not contribute.

tune change as a function of the single-particle emittance (second column). The methods are independent from each other, and the fact that both approach lead to compatible values of the constant $a_{1,N}$ and linear term $a_{2,N}$, already provides a good benchmark. Major discrepancies can be observed for the determination of the vertical amplitude detuning from an horizontal kick in the corrected configuration. However, in that condition, two tune values were quite outside the trend of the other experimental points.

- The comparison of the amplitude detuning obtained from the tune evaluation on the Hilbert-normalised signal (second column) and the Gaussian amplitude modulated signal (third column) allows for benchmarking the results of the new approach against a well-established technique. In fact, a part from the two cases of the uncorrected configuration were few experimental points have been removed (namely, first and third row, thus vertical and horizontal detuning from an horizontal kick), all the other combinations show values compatible with those obtained in 2012.

- In the end, it is possible to further compare the results with the values provided by the LHC MAD-X model. Also from this comparison, the results are compatible with those retrieved from the numerical model.

By looking at Figure 6.31, where in each plot the amplitude detuning in the uncorrected configuration (red) is compared with the one obtained in the corrected configuration (blue), significant improvements can be observed. Although, in the uncorrected configuration a constant amplitude detuning is obtained as assumed by the Meller model (see Section 6.5.1), a large spread in the data is also visible. When the LHC octupole contribution is corrected, the amplitude detuning is linearly varying with the single-particle emittance. In conclusion, although a linearly changing amplitude detuning might not be the expected result, the fact that in the corrected LHC configuration the amplitude detuning is well controlled allows to obtain significant improvements. Among these, it is worth mentioning a strong increase of the time (or, equivalently, turns) needed for the betatron oscillations to decohere. As an example, in Figure 6.32 the comparison of the signal recorded by the same BPM in the uncorrected (left) and corrected (right) configuration is displayed for the same kick intensity, thus $\approx 2J_x = 0.1\mu$m. Note that even though the two signals have the same sampling time, the oscillations in the uncorrected case (left) are completely damped in the first 100 turns, while in the corrected configuration (right) the betatron oscillations are damped in $1250 - 1500$ turns. Thus, the correction has actually increased the period needed by the betatron oscillations to decohere, obtaining the desired result.

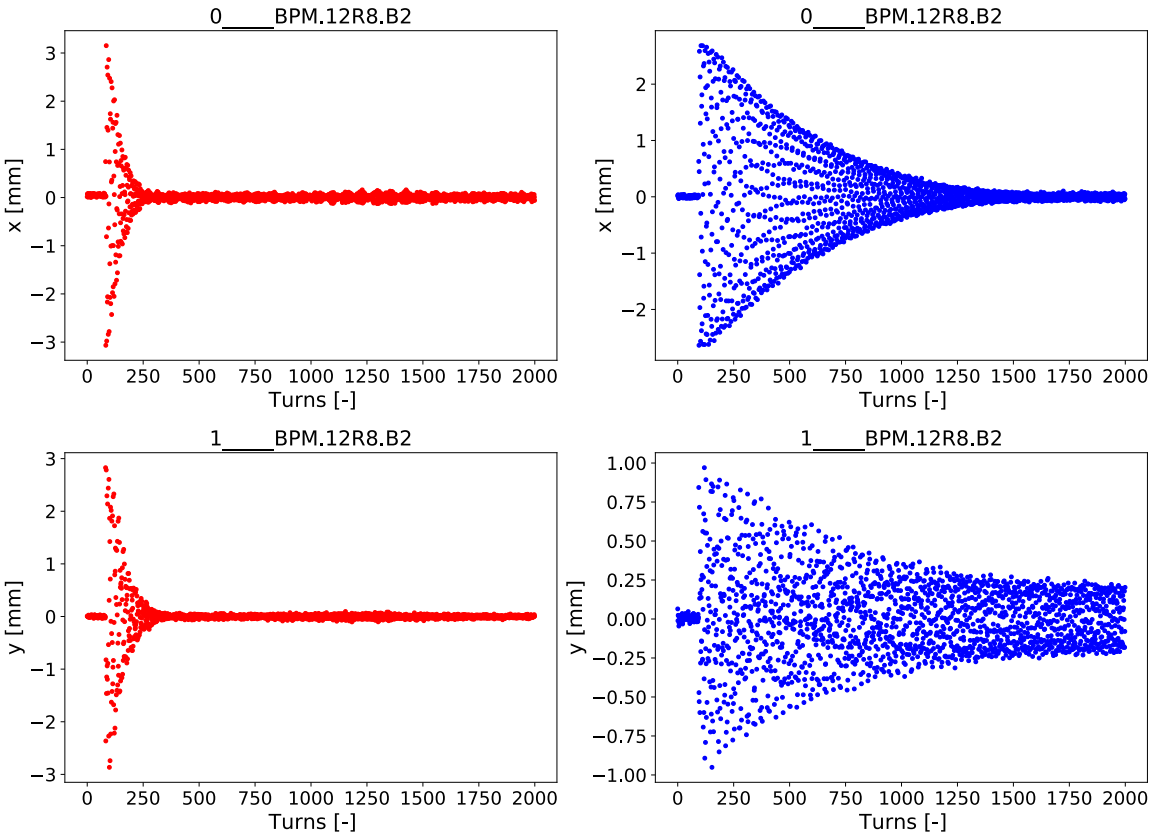

Figure 6.32: Turn-by-turn signal detected by the same BPM (BPM.12R8) when the beam is kicked at $2J_x \approx 0.1\mu$m in the uncorrected (left, in red) and corrected (right, in blue) LHC configuration on both the horizontal (top) and vertical (bottom) plane. The number of turns over which the decoherence of betatron oscillations occurs is longer in the corrected configuration.

6.5.2.2 Amplitude detuning measurement for other accelerators

Amplitude detuning measurements allow for the determination of non-linear fields. For some accelerators, such as LHC, a magnetic model is available and, as shown in the previous section, it provides values of amplitude detuning compatible with experimental data. On the contrary, there are other accelerators, such as the PS ring, for which the magnetic model is difficult to determine. Although the non-linear PS fields are determined by sextupoles, octupoles and correctors installed around the ring, a non-negligible contribution is also provided by the PFWs and the F8 (see Chapter 3 for detailed description) installed on the main combined-function magnets. The numerical simulation of these last two elements is particularly difficult since the position of their wires is quite uncertain. Thus, the construction of a magnetic model for the PS is particularly limited by the uncertainty associated to these components. For accelerators where a well benchmarked magnetic model is not available, it would be of great interest to have a procedure for the determination of the amplitude detuning from which the reconstruction of the magnetic model can be performed.

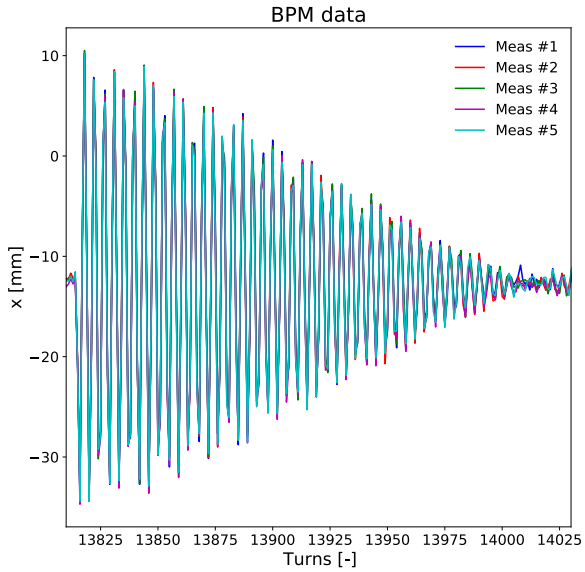

Figure 6.33: The data collected on the 18$^{\text{th}}$ of May 2022 at the PS are reported. For the five measurements, the turn-by-turn horizontal beam centroid position is displayed for the BPM installed in the SS 0.

During 18$^{\text{th}}$ of May 2022, a few measurements have been taken parasitically at the PS. In particular, the beam has been kicked once and the turn-by-turn data have been recorded by the BPMs. The measurement has been performed at the PS injection energy, namely 2 GeV/c (kinetic energy) and a kick of $2J_x = (18 \pm 2)$ μm has been imparted to the beam. Five different data sets (for a single kick value) are available and they are shown in Figure 6.33. In the PS ring, 43 BPMs are installed, from which it is possible to retrieve information on the turn-by-turn beam centroid position. Statistical analysis for the determination of the tune error $\Delta\nu$ and the damping factor error $\Delta\lambda$ can be carried out. Note that during the fit procedure for the determination of the damping factor λ the uncertainty related to the orbit measurement has been taken into account. Therefore, the damping factor error takes into account the uncertainty of the fit as well as the one of the measurement itself. For each measurement the weighted average of tune and damping factor has been reported in Table 6.6 and the corresponding error has been computed as the error associated to the weighted mean. The results reported in Table 6.6 show that the values of the damping factor as well as those of the tune are compatible with each other. In particular, the tune values show a spread smaller than the damping factor values. To complete the analysis it is possible to use the average damping factor to provide an estimate of the amplitude detuning μ for the tested configuration by applying Eq. 6.80. The normalised kick intensity Z is computed according to Eq. 6.78, where the PS physical emittance is $\epsilon_{x,ph} = (0.67 \pm 0.11)$ μm, thus $Z = 5.2 \pm 1.6$. The amplitude detuning and its error are reported in Table 6.6. No information can be retrieved on the sign of the amplitude detuning for two main reasons: Eq. 6.80 provides information on the absolute value of the amplitude detuning, the sign is determined from the

λ [10^{-5}]	$\Delta\lambda$ [10^{-5}]	ν	$\Delta\nu$	μ [10^{-4}]	$\Delta\mu$ [10^{-4}]
6.074	0.004	0.23295	0.00007	1.69	0.51
5.925	0.004	0.23304	0.00007	1.67	0.51
6.111	0.004	0.23292	0.00008	1.70	0.52
5.969	0.004	0.23295	0.00008	1.68	0.51
6.051	0.004	0.23300	0.00009	1.69	0.51

Table 6.6: Damping factor λ, tune ν, amplitude detuning μ and their error from the BPM data analysis collected on the 18^{th} of May 2022 at the PS ring.

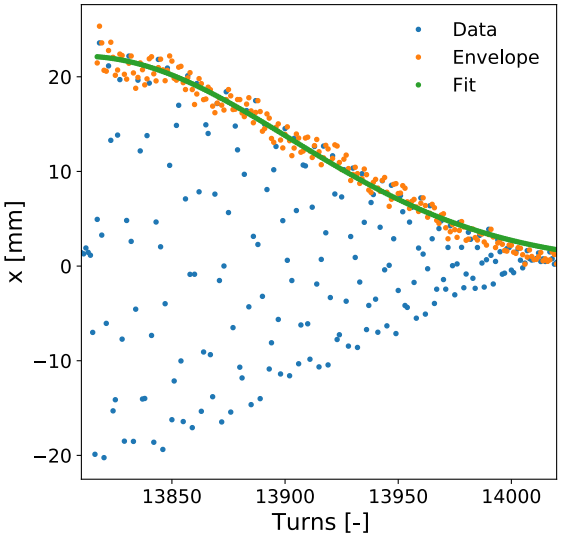

Figure 6.34: The BPM signal on the horizontal plane is shown in blue, while in orange and green it is possible to observe the envelope obtained with the Hilbert transform and the Gaussian fit, respectively.

tune estimation for different values of single-particle emittance; the second, trivial, reason is that a single measurements has been performed, therefore, there are not sufficient information to determine the sign of the amplitude detuning.

For the sake of completeness, in Figure 6.34 an example of the analysed signal has been shown. In blue, the original BPM signal on the horizontal plane is reported. The envelope of the signal can be retrieved from the Hilbert transform and it is shown in orange. Thus the fit of the envelope with a Gaussian curve allows for the determination of the damping factor, the result of the fit is reported in green. In conclusion, from this preliminary analysis and its results, it is possible to put the basis for a more detailed investigation and experimental campaign for the reconstruction of the amplitude detuning at the PS ring and thus, allow for the determination of a precise magnetic model that considers also the effect of the PFWs and the F8.

6.5.2.3 Tune calculation for the beam trapped in the islands

After a beam has been transversely kicked, its betatron oscillations start decohering until the beam has filamented completely. During this time, the centroid of the beam evolves according to Eq. 6.72, whose amplitude is a Gaussian-like function, as shown and described by the Meller model in Section 6.5.1. However, from the analysis of the LHC data collected in 2012, it was observed that during the frequency spectrum analysis, two major peaks were detected. At first, one located at ≈ 0.26, namely the LHC tune; and a second one located at ≈ 0.25 highlighting the presence of a fourth-order resonance structure. The behaviour occurred for few kick amplitudes that have brought the beam particularly close to a fourth order resonance, leading to a partial trapping of the beam in the islands, while the remaining part has been left in the linear core region. Although these combinations of data sets have been removed from the analysis for the determination of the amplitude detuning, they can be exploited for different analysis. In Figure 6.35, the discarded data are reported, where the four different colours highlight the presence of islands. In particular, the two largest values of single-particle emittance on the horizontal plane were identified as critical. The same BPM (namely, 12RB measuring the LHC Beam 2 centroid position) has been considered for the comparison. For every BPM in the ring, the relative position between the islands as well as the position around which the four lines oscillate is different and depends on the local orientation and configuration of the transverse phase-space. It is also fundamental to notice that as soon as the beam is kicked it is not possible to distinguish the four islands, meaning that the non-linear decoherence (thus the amplitude detuning) is dominant over any other phenomenon during that period of time. But as soon as the beam has filamented completely the four islands emerge clearly. In Figure 6.35 the value of horizontal action changes from ≈ 0.4 μm, on the top, to ≈ 0.5 μm on the bottom; the evolution of the beam centroid on the horizontal plane is reported on the left while the vertical one is shown on the right. The horizontal plane shows the presence of islands for both values of action, while on the vertical plane only the largest value of action leads to a partial beam trapping in the islands. The coherent part of the signal, after the decoherence of betatron oscillations has terminated, can be analysed to determine the frequency with which particles rotate within the islands. The results relative to the analysis of the data set obtained at the smaller value of action, namely $2J_x \approx 0.4$ μm, will be referred to as "Configuration A", the other one (for the largest value of action $2J_x \approx 0.5$ μm) will be referred to as "Configuration B". The frequency analysis of the coherent part of the signal has been performed for the horizontal plane. For the signals in Figure 6.35, the coherent part has been considered to start after 100 turns for both action values. Being the coherent signal a constant-amplitude signal, its frequency analysis can be performed with the methods described in Section 6.1.2. The Interpolated FFT has been chosen, being also the one able to provide the better tune estimation in the presence of noise (see Section 6.3). For every BPM in the LHC, the frequency analysis of the four coherent signals (one for every island) has been performed. Thus, the average tune and its standard deviation have been determined, the results are reported in

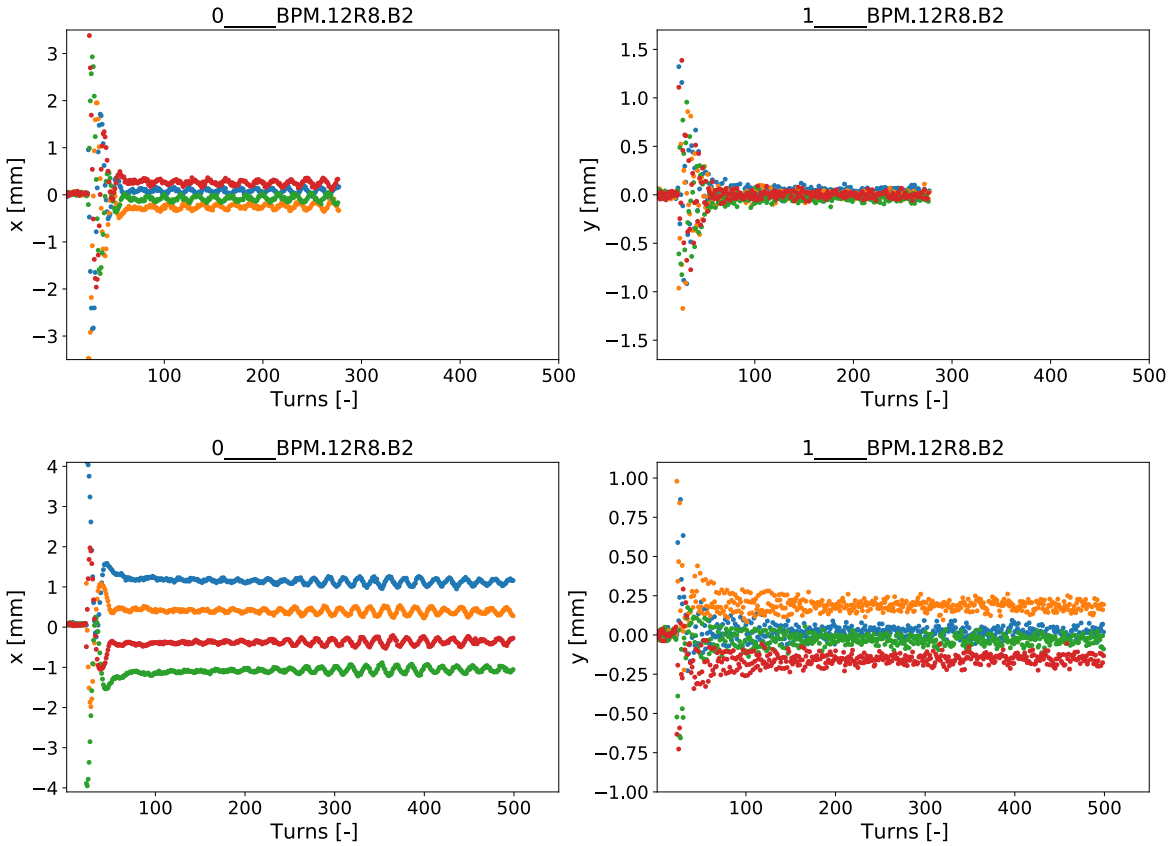

Figure 6.35: For the same BPM is shown the horizontal (left) and vertical (right) beam centroid position at the second-largest (top) and largest value of horizontal action (bottom) of the uncorrected LHC configuration.

Configuration A	Configuration B
$(6.58 \pm 0.08) \times 10^{-2}$	$(5.0 \pm 2.0) \times 10^{-2}$

Table 6.7: Frequency of oscillation of the particles within the islands, for the two LHC configurations (namely, $2J_x \approx 0.4$ μm reported in Configuration A and $2J_x \approx 0.5$ μm for Configuration B) that showed the presence of resonant islands during 2012 measurements.

Table 6.7. As expected, the islands have compatible values of frequency. Due to the large spread of tune values obtained in the "Configuration B", the one at the largest value of kick, the mean value is shifted to values lower than expected. As a consequence, the associated error is quite large, of the same order of magnitude as the frequency itself. However, considering the value of the frequency in both configurations and their errors, the values are compatible with each other, as expected.

For the sake of completeness, a numerical simulation has been performed. In fact, the phenomenology behind the partial trapping of the beam within the islands is very well-known

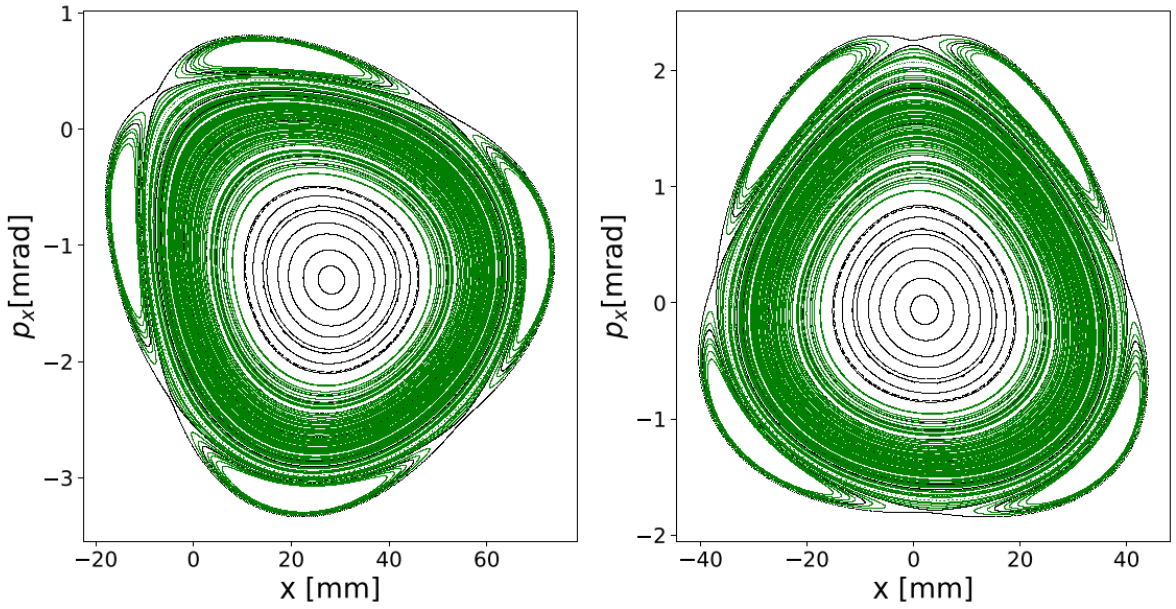

Figure 6.36: The horizontal phase space is shown at two different locations (extraction region on the left and initial section of the PS ring on the right). The filamented beam (green) is shown on the phase-space of the ring (black) after the filamentation process has terminated.

[76] and it occurs whenever the beam is kicked to a too big amplitude in the close vicinity of a fourth-order resonance. The PS ring has been used to numerically simulate this behaviour with MAD-X. In Figure 6.36 the transverse phase-space of the PS ring at two longitudinal positions (namely, the extraction area, SS15, and the start of the ring, SS0) is reported in black. The difference among the two phase-space sections consists of a rotation of the islands due to the phase advance between the two observation points and a shift of the beam to higher values of x in SS15, because in that area the dummy septum is approached. Thus, a bi-Gaussian beam with $\sigma_x = 6\sigma_{p_x} = 3.5$mm and composed of 1500 particles is injected in $s = 0$ and tracked for 6000 turns. The chosen number of turns enables to obtain a complete filamentation of the non-matched beam (see Section 2.2.1 for reference). The beam widths have been chosen so that its initial dimension would lead to a minimum number of particle loss (only 114 particles have been lost over the initial 1500 used to generate the distribution). Moreover, the bi-Gaussian beam has not been injected in $s = 0$ for $x = p_x = 0$mm, but to allow for a partial trapping of the particles in the islands it has been injected in $x = 0$ mm and $p_x = 1.5$ mrad, this non-matched beam will filament over the 6000 turns. From Figure 6.36 the filamented bi-Gaussian beam is reported in green. Thus, it is shown how some particles have been trapped in the islands while other remains at the centre of the phase-space, in the linear region. The turn-by-turn evaluation of the beam centroid is reported in Figure 6.37 for the two locations (SS15 on the left while SS0 on the right). The comparison of the two average centroid positions is shown in Figure 6.37, shows that at the beginning of the filamentation process, the centroid evolves and the typical Gaussian amplitude modulation can

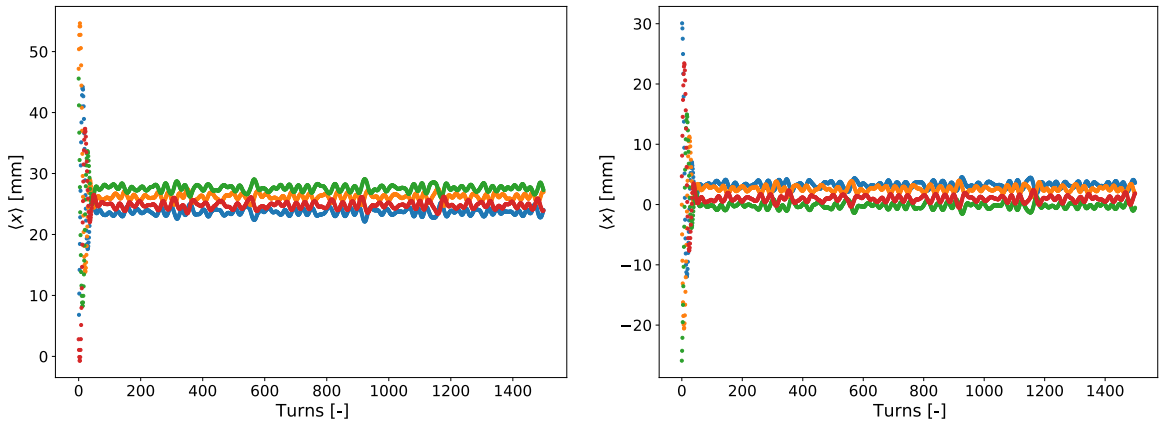

Figure 6.37: The beam centroid is evaluated on a turn-by-turn basis and different colours are used every other four turns to highlight the presence of islands.On the left side the extraction regions (SS15) is shown, while the SS) is reported on the right side.

be recognise. Moreover, as observed on the experimental data in Figure 6.35, it is not possible to clearly identify the four islands. After ≈ 50 turns, the amplitude reaches the zero value and then four parallel lines emerge. Thus, at the end of the betatron oscillation decoherence phenomenon part of the beam has been trapped within the islands.

In conclusion, the comparison of the LHC turn-by-turn data in Figure 6.32 and the simulated beam centroid evolution in Figure 6.37, shows a quite good agreement. This further confirms, that the reason of the observed island detection during some LHC measurements in 2012, is caused by the larger strength of the kick that brought part of the beam to be trapped inside the islands.

CHAPTER 7

CONCLUSIONS AND OUTLOOK

In the context of the present thesis several non-linear beam dynamics aspects of circular accelerators have been investigated and analysed. The PS ring at CERN plays a key role in the acceleration of proton and ion beams for experiments and for LHC physics. Therefore, the analysis of its performance and optimisation are fundamental to reaching more intense and energetic beams. Both studies described in this thesis (reconstruction of the transverse emittance for a split beam in Chapter 4 and the precise tune determination in Chapter 6) are of fundamental importance to understand and improve the PS performance, although their range of applicability is much wider. In fact, the transverse beam emittance reconstruction described in Chapter 4 can be applied in any circular accelerator that exploits a stable resonance of order n to transversely split a beam. However, some considerations on the beam energy and the available instrumentation are necessary before using this approach. Similarly, the methods described and proved in Chapter 6 are applicable for any simulated beam signal, as no assumptions have been made on the accelerator. The knowledge of the tune is fundamental to precisely determine the working point of an accelerator. As shown from the analysis of the Hénon map with and without frequency modulation, the precise tune determination is fundamental to distinguish, for example, stable resonant conditions from stable non-resonant ones. Thus, these methods are extremely powerful during the accelerator design phase, where the working points are defined for several different operational conditions. However, their application is not only theoretical. In fact, from the analysis of the experimental data, it was possible to determine the tune of the amplitude-modulated signals, overcoming the limitation imposed by FFT-based methods.

7.1 Conclusions

Several interesting conclusions can be drawn at the end of this research. As far as the reconstruction of the beam transverse emittance is concerned, it is possible to conclude that:

- For the first time, it was possible to reconstruct the transverse beam emittance of a split beam distinguishing between the core and the islands. Although in the past several attempts have been performed to determine the emittance of such beams, there was a strong intrinsic limitation with those approaches: the emittance was strongly dependent on the relative orientation of the islands with respect to themselves and to the one of the core in phase-space. It is important to further remark that in order to carry out this type of analysis, a precise knowledge of the non-linear model of the considered accelerator is fundamental.

- The sensitivity analysis carried out at the end of the experimental data analysis allowed to confirm that the non-linear PS model accurately describes the non-linear dynamics in the ring. Therefore, it can be used to reconstruct the island emittance.

To complete the analysis on the PS ring, a set of simulations that aimed at evaluating changes in the horizontal phase-space as a function of the horizontal tune have been performed. It was noticed that a change in the working point of the PS (see Chapter 5) leads to an enlargement of the phase-space (i.e., the absolute value of the four stable fixed points shifted to higher values) and thus to a right-shift towards the dummy septum. Therefore, the need to be able to determine the tune with high precision becomes evident.

The discussion of the results obtained from the analysis of the methods for high precise tune determination can be divided into a first theoretical one and a second one where experimental beam data have been analysed. As far as the theoretical part is concerned:

- Two new methods have been derived and described for determining the tune. Among these two methods, one is for constant amplitude signals (Zero padding, see Section 6.2.1) and one for an exponentially damped signals (Hanning filtered FFT, see Section 6.4.2). This latter method also provides information on the damping factor used during the generation of the amplitude modulation. Both methods have been tested on synthetic signals to determine numerically the speed with which the tune error (the absolute value of the difference between the tune used to generate the signal and the one retrieved from the application of the method) converges to zero as a function of the number of turns (namely, their scaling law $1/N^{\alpha}$, where α is larger than 1, being 1 already provided by the conventional FFT) and compare them with those obtained theoretically. As expected, the two scaling laws (theoretical and numerical) are identical. Their performances have been compared to those provided by the state-of-the-art methods and the former turned out to be the best.

- The weighted Birkhoff averages, although well-known in the study of quasi-periodic maps, find completely new applications in the field of accelerator physics, in particular for tune determination. There are two results that have to be highlighted. At first, the characteristic scaling law of weighted Birkhoff averages is $1/N^7$ (for $\alpha = 1$and $\beta = 1$). It is significantly better than the best state-of-the-art method (Hanning) that ensures a tune precision that scales as $1/N^4$. Moreover, even faster scaling laws can be obtained for specific combinations of the parameters α and β. The second aspect concerns tune precision of the weighted Birkhoff average method on amplitude modulated signal, for which it was shown that the scaling law is not affected by the signal amplitude modulation. The reason being that the Birkhoff average computes the tune from the knowledge of the phase advance between two successive turns, and the phase-advance, thus the angle between two vectors, is independent of the magnitude of the vectors themselves. This is a very significant and relevant difference with respect to FFT-based methods. They assume that the signal has a constant amplitude, and when used on a varying-amplitude signal fail in the detection of the frequency.

Several different signals have been analysed with the different methods and their performance has been compared. The conclusion being that for constant-amplitude signals the weighted Birkhoff average ensures the better tune precision, i.e., the tune error reaches machine precision within one or a few thousand turns. Moreover, it is among the best methods to be used also for amplitude-modulated signals. However, other ad-hoc developed methods (such as the Hanning-filtered FFT for exponentially damped signals) are equally interesting because they can retrieve the tune together with the damping factor, that is responsible for the amplitude modulation. Therefore, by performing the frequency analysis, it is possible to gain the knowledge not only on the frequency itself of the signal but also on its amplitude modulation, namely the damping coefficient. An extension of this idea led to the introduction of a new way of using and exploiting the Hilbert transform:

- At first the Hilbert transform has been used to normalise the amplitude of an amplitude-modulated signal to determine its frequency using the tune methods developed for constant amplitude signals. Its application is particularly interesting whenever a complete analytical approach is not feasible, thus for complex amplitude modulations as the one described in Section 6.4.5.2, where chromatic amplitude modulation has been analysed.

- Any beam data signal has an amplitude modulation that depends on the measurement conditions. For example, a beam perturbed with an AC dipole will produce a constant amplitude signal; a kicked beam will lead to a signal whose amplitude has a Gaussian shape. Thus, from the knowledge of the physical phenomenon that caused a specific type of signal and from the knowledge of the signal envelope by means of the Hilbert transform, it is possible to fit the physical model to the envelope and retrieve physical parameters of

the ring, such as chromaticity, synchrotron tune, or amplitude detuning. This approach can provide, for the first time, a direct measurements of these physical parameters. This aspect is relevant and interesting since the determination of amplitude detuning or chromaticity is usually performed indirectly, thus by measuring other parameters.

This latter idea has been tested on several types of signals (such as the synthetic chromatic one and the real beam turn-by-turn non-linear signal in Section 6.4.6 and Section 6.5.2.1, respectively). In particular:

- Chromatic decoherences have been tested on synthetic signals only, but it was the fundamental step that enabled to actually understand the feasibility of this approach. In fact, as described in Section 6.4.6, the input parameters are precisely reconstructed, with an error several orders of magnitude smaller than the parameter itself.

- LHC data collected in 2012 have been used to test this approach on real data. In this case, non-linear decoherences have been analysed, the final aim being to determine the amplitude detuning. At first, the tune is determined by exploiting the envelope as a normalisation factor for the amplitude. Thus, the tune is computed by means of the Interpolated FFT. The results have been compared with those obtained in 2012 (where a completely different approach was adopted to compute the tune), and the benchmark of the results obtained with this approach against 2012 results was achieved. From the fit of the Hilbert envelope the amplitude detuning coefficient was determined, as described by the Meller model in Section 6.5.1, and thus, for the first time a direct measurement of this parameter was performed. It is important to highlight that in the past the knowledge on the amplitude detuning coefficient was experimentally gained only as a consequence of tune measurements for a beam kicked at different amplitudes. In this case, the experimental procedure to know the amplitude detuning coefficient is still the same (thus kicking the beam at larger and larger amplitude), but the knowledge on the parameter comes from the study of the envelope of the turn-by-turn beam signal. In fact, if a set of measurements is performed, it is possible to distinguish between the first and the second-order amplitude detuning coefficient, therefore this enables the understanding of which set of multipoles (sextupoles and octupoles for the first-order and higher-order ones for the second-order) have to be properly adjusted.

For the sake of completeness, it is worth highlighting that Hanning and Birkhoff have not been used on real beam data signals because the level of noise leads to a strong reduction of their performance.

7.2 Outlook

In conclusion, the results obtained during this PhD work open the possibility to perform additional studies as well as applying the obtained results to other domains.

As far as the theoretical studies on the determination of new analytical formulae for the tune calculation are concerned, additional studies might be performed on amplitude-modulated signals and/or frequency modulated signals; provided that the amplitude and frequency modulation of the signal can be treated analytically. At the moment, several attempts to determine an analytical equation for the tune and for the damping factor on a Gaussian amplitude-modulated signal have been performed. However, several critical points have been detected due to difficulty in finding closed form solutions of Gaussian integrals.

It would be definitely interesting to continue the studies on the Hilbert transform to both improve its performance for the tune calculation but, above all, to retrieve interesting beam features. In fact, after the several benchmarks obtained for the amplitude detuning, it would be interesting to determine the chromaticity for real beam signals (so far only a numerical approach has been tested) and on combined chromatic and amplitude modulated beam signals. This interesting feature of the Hilbert transform might be used to plan an extensive experimental campaign at the PS to retrieve information on the magnetic model. Moreover, it might be used in any (present or future) circular accelerator to benchmark the magnetic model itself or to perform amplitude detuning measurements. Another different application, might be to electron rings. For this case, the Hilbert transform can be used to determine the envelope of the exponentially damped beam centroid position. But, it is worth to highlight, that in the present thesis a new analytical formulae for the determination of the tune and the damping factor of an exponentially damped signal has been proved. Therefore, its usage might find several applications in the possible change and optimisation of the working point for electron rings, as well as, an additional method against which benchmark the results provided by the application of the Hilbert transform to determine amplitude modulation of the electron beam centroid. Additional and different types of particle rings, such as antiprotons, ions, muon machines and the Future Circular Collider (FCC) might find useful the application described above for the Hilbert transform, but also the use of weighted Birkhoff average to precisely determine the tune during the design phase. However, an additional possible application of the weighted Birkhoff average for any of the above cited machines, could be to exploit its super-converges to estimate different beam properties. In fact, apart from the tune, which is estimated from the phase-advance, if other observables, whose mean value converges to a beam property, are identified, their behaviour could be studied using the weighted Birkhoff average.

As a last topic, the performance of the methods to determine the tune have been tested in presence of noise. Their limitations have been highlighted and this opens the possibility to perform additional studies to assess whether their performance can be improved by considering the effect of noise during the determination of new analytical formulae for the tune.

APPENDIX A

APPENDIX A: DERIVATION OF THE EQUATIONS OF MOTION IN THE LONGITUDINAL DIRECTION

Before performing the derivation of the motion equation in the longitudinal direction, it is important to define some quantities, namely, time t, phase Φ, and energy W, for a generic particle with respect to the synchronous one:

$$\Delta t = t - t_s \tag{A.1}$$

$$\varphi = \Phi - \Phi_s = \omega_{RF}(t - t_s) \tag{A.2}$$

$$w = W - W_s \tag{A.3}$$

Therefore, the first step consists in computing the energy gain per unit path for the synchronous particle:

$$\frac{dW_s}{dz} = \frac{1}{dz}\left(\frac{1}{2}mv_s^2\right) = \frac{1}{dt}\left(mv_s\right) = eE_s sin(\Phi_s) \tag{A.4}$$

Where in the second last passage the following expression has been substituted:

$$\frac{d}{dt} = \frac{dz}{dt}\frac{1}{dz} = v\frac{1}{dz} \tag{A.5}$$

The energy gain of a generic particle is expressed as:

$$\frac{dW}{dz} = eE_s\Big(sin(\Phi_s + \varphi) - sin(\Phi_s)\Big) = \frac{dw}{dz} \tag{A.6}$$

Performing the difference between the sinusoidal functions in Eq. A.6:

$$sin(\Phi_s + \varphi) - sin(\Phi_s) = 2cos\left(\frac{\Phi_s + \varphi + \Phi_s}{2}\right) \cdot sin\left(\frac{\Phi_s + \varphi - \Phi_s}{2}\right) = 2cos\left(\Phi_s \frac{\varphi}{2}\right) \cdot \frac{\varphi}{2} \tag{A.7}$$

The relative change of the phase per unit of the longitudinal path reads as:

$$\frac{d\varphi}{dz} = \omega_{RF}\left(\frac{dt}{dz} - \frac{dt_s}{dz}\right) = \omega_{RF}\left(\frac{1}{v} - \frac{1}{v_s}\right) \tag{A.8}$$

It is useful to write the explicit form for w to find an equation for the phase that does not depend on the velocity of the late/in advanced particle:

$$w = \frac{1}{2}m(v^2 - v_s^2) = \frac{1}{2}m(v+v_s)(v-v_s) \approx \frac{1}{2}m2v_s(v-v_s) = mv_s(v-v_s) \tag{A.9}$$

Thus, using Eq. A.9, it is possible to write Eq. A.8 as:

$$\frac{d\varphi}{dz} = \omega_{RF}\frac{v_s - v}{v \cdot v_s} \tag{A.10}$$

However, Eq. A.10 can be also written as:

$$v \cdot v_s = \frac{w + mv_s^2}{m}$$

Therefore, it is possible to obtain:

$$\frac{d\varphi}{dz} = -\frac{\omega_{RF} \cdot w}{mv_s^3} \tag{A.11}$$

When $\varphi << \Phi_s$, a simplified form of Eq. A.6 can be obtained and it reads as:

$$\frac{dw}{dt} = qE_s\varphi cos(\Phi_s) \tag{A.12}$$

Deriving Eq. A.10 with respect to the longitudinal position and using Eq. A.11, it is possible to obtain:

$$\frac{d^2\varphi}{dz^2} + \frac{\omega_{RF}}{mv_s^3}\Big(qE_s cos(\Phi_s)\Big)\varphi = 0 \tag{A.13}$$

The Eq. A.13 can be written as:

$$\frac{d^2\varphi}{dz^2} + \Omega^2\varphi = 0 \quad \text{where} \quad \Omega^2 = \frac{\omega_{RF}}{mv_s^3}\Big(qE_s cos(\Phi_s)\Big) \tag{A.14}$$

In this way, it is easier to observe that Eq. A.14 has the same form of an harmonic oscillator. A real solution of the equation has to be found to have a physical (thus, feasible) solution of the system. This means that the coefficient that multiplies the variable φ has to be positive:

$$\Omega^2 = \frac{\omega_{RF}}{mv_s^3}\Big(qE_s cos(\Phi_s)\Big) > 0 \rightarrow cos(\Phi_s) > 0 \tag{A.15}$$

Giving a graphical representation of the energy gain ΔE versus the phase difference φ (as shown in Figure **??**) it is possible to obtain circular trajectories that have the synchronous particle at their centre. When the assumption of $\varphi << \Phi_s$ is removed, then the circumference is deformed and the well known bucket shape is obtained. It is still possible to observe the circular path near the synchronous particle, while moving towards the separatrix the non-linear effects get more and more important and the circumference is deformed.

APPENDIX B

Appendix B: Remarks on the contribution of the sextupolar and octupolar components on the island emittance reconstruction

In Chapter 4 a detailed discussion on the sensitivity analysis results has been performed. In particular, the island normalised emittance has been computed for 204 non-linear PS models. Each model was characterised by a different quadruplet of focusing and defocusing sextupolar and octupolar components of the main combined function magnets. The determination of the quadruplet has been performed with a Monte Carlo code where these components have been varied around ±2% of their nominal values. In order to determine whether there is a clear dependence of one (or more) non-linear components on the reconstruction of the island emittance, the value of the normalised emittance is plot as a function of the four non-linear components where the color shows the distance from the nominal conditions (shown in red). This results is reported in Figure B.1. On the top of Figure B.1 the sextupolar (left) and octupolar (right) focusing strengths are shown, while the defocusing ones are reported on the bottom.

The distributions of normalised emittance discussed in Chapter 4 are reported in the four diagrams in Figure B.1 where the colour refers to the distance from nominal PS conditions; thus the same distribution will appear in the four diagrams with the same colour and the position along the $x-$axis depends on the value of the considered non-linear component used in the simulation of the model.

The focusing and defocusing sextupolar components show a fairly symmetric distribution around their nominal values. In fact, it is possible to observe that the emittance distributions obtained for quadruplets combination far from nominal conditions (yellow-like points) are located at the extremities of the focusing and defocusing sextupolar strengths. Similarly, the normalised distribution obtained for quadruplet values close to the nominal conditions is located on both

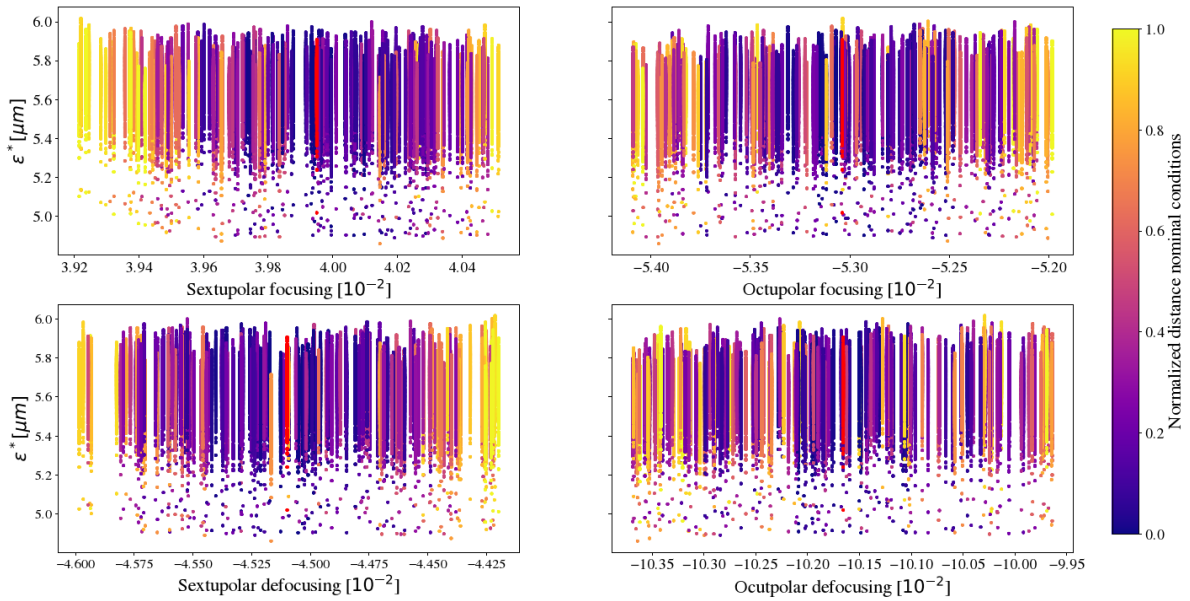

Figure B.1: The island normalised emittance is shown as a function of the sextupolar (left) and octupolar (right) focusing (top) and defocusing (bottom) components of the PS non-linear model. The colour refers to the distance from nominal conditions which is reported in red. Thus, emittance distributions are shown in the four plots with the same colour.

sides of the distribution obtained at nominal conditions.

As far as the distribution of normalised emittance as a function of octupolar strengths is concerned, it is not possible to notice such a clear division among distributions obtained close or far from the nominal conditions. In fact, if for example the focusing octupola rstrenghts is concerned, it is possible to observe on the left-hand side of the distribution obtained at nominal condition a red-orange line that was approximately obtained for a normalised distance from nominal condition of ≈ 0.8.

APPENDIX C

APPENDIX C: DERIVATION OF THE ZERO-PADDING TUNE EQUATION

Given the complex valued signal:

$$z(n) = e^{2\pi i \nu_0 n}, \tag{C.1}$$

sampled over N turns, it is possible to pad it with l blocks of N zeros. After the padding is performed, the signal $z_P(n)$ will read as:

$$z_P(n) = \begin{cases} z(n), & n \leq N \\ 0, & n > N \text{ and } n \leq lN \end{cases}, \tag{C.2}$$

and it will have a length equal to $N_1 = N(l+1)$. Performing the FFT of the padded signal in Eq. C.2, the FFT coefficients read as:

$$\phi(\nu_j) = \frac{1}{N(l+1)} \sum_{n=1}^{N(l+1)} e^{2\pi i n(\nu_0 - \nu_j)} = \frac{1}{N_1} \sum_{n=1}^{N_1} e^{2\pi i n(\nu_0 - \nu_j)} = \frac{1}{N_1} \sum_{n=1}^{N} e^{2\pi i n(\nu_0 - \nu_j)}, \tag{C.3}$$

where $\nu_j = j/(N(l+1))$. It is possible to simplify Eq. C.3 using:

$$\sum_{n=0}^{N_1-1} e^{2\pi i f n} = \frac{1 - e^{2\pi i f N_1}}{1 - e^{2\pi i f}} \ . \tag{C.4}$$

In particular, using the relation in Eq. C.4, it is possible to simplify the summation term in Eq. C.3 that will read as:

$$\phi(\nu_j) = \frac{1}{N(l+1)} e^{2\pi i(\nu_0 - \nu_j)} \sum_{n=0}^{N-1} e^{2\pi i(\nu_0 - \nu_j)n} = \frac{1}{N(l+1)} e^{2\pi i(\nu_0 - \nu_j)} \frac{1 - e^{2\pi i N(\nu_0 - \nu_j)}}{1 - e^{2\pi i(\nu_0 - \nu_j)}}. \tag{C.5}$$

The last term of Eq. C.5 can be written as the difference of two exponential functions that then can be further simplified as:

$$\phi(\nu_j) = \frac{1}{N(l+1)} e^{2\pi i(\nu_0 - \nu_j)} e^{\pi i(\nu_0 - \nu_j)} e^{\pi i N(\nu_0 - \nu_j)} \frac{\sin \pi N(\nu_0 - \nu_j)}{\sin \pi(\nu_0 - \nu_j)} \tag{C.6}$$

Taking the absolute value of Eq. C.6, the FFT coefficient read as:

$$\left|\phi(\nu_j)\right| = \frac{1}{N(l+1)}\left|\frac{\sin\pi N(\nu_0-\nu_j)}{\sin\pi(\nu_0-\nu_j)}\right|. \tag{C.7}$$

The value of the frequency that maximises the FFT coefficient is $\nu_k = k/(N(l+1))$ and the corresponding FFT coefficient is $\left|\phi(\nu_k)\right|$. In order to determine the analytical equation for the tune, it is possible to evaluate the FFT coefficients at ν_k (the value of the frequency that maximises the FFT coefficient) and at its neighbours values. These quantities read as:

$$\left|\phi(\nu_k)\right| = \frac{1}{N(l+1)}\frac{\sin\pi N(\nu_0-\nu_k)}{\sin\pi(\nu_0-\nu_k)}, \tag{C.8}$$

$$\left|\phi(\nu_{k+1})\right| = \frac{1}{N(l+1)}\frac{\sin\pi N(\nu_0-\nu_{k+1})}{\sin\pi(\nu_0-\nu_{k+1})} = \frac{1}{N(l+1)}\frac{\sin\left[\pi N(\nu_0-\nu_k)-\frac{\pi}{l+1}\right]}{\sin\pi(\nu_0-\nu_{k+1})}, \tag{C.9}$$

$$\left|\phi(\nu_{k-1})\right| = \frac{1}{N(l+1)}\frac{\sin\pi N(\nu_0-\nu_{k-1})}{\sin\pi(\nu_0-\nu_{k-1})} = \frac{1}{N(l+1)}\frac{\sin\left[\pi N(\nu_0-\nu_k)+\frac{\pi}{l+1}\right]}{\sin\pi(\nu_0-\nu_{k-1})}, \tag{C.10}$$

It is possible to define the parameter

$$\alpha_{k\pm1} = \frac{\left|\phi(\nu_k)\right|}{\left|\phi(\nu_{k\pm1})\right|}\ , \tag{C.11}$$

and the explicit expression for the $\alpha_{k\pm1}$ reads as:

$$\alpha_{k+1} = \frac{\left|\phi(\nu_k)\right|}{\left|\phi(\nu_{k+1})\right|} = \frac{\sin\pi(\nu_0-\nu_{k+1})}{\sin\pi(\nu_0-\nu_k)}\frac{\sin\pi N(\nu_0-\nu_k)}{\sin\left(\pi N(\nu_0-\nu_k)-\frac{\pi}{l+1}\right)}\ , \tag{C.12}$$

$$\alpha_{k-1} = \frac{\left|\phi(\nu_k)\right|}{\left|\phi(\nu_{k-1})\right|} = \frac{\sin\pi(\nu_0-\nu_{k-1})}{\sin\pi(\nu_0-\nu_k)}\frac{\sin\pi N(\nu_0-\nu_k)}{\sin\left(\pi N(\nu_0-\nu_k)+\frac{\pi}{l+1}\right)}\ . \tag{C.13}$$

For both Eq. C.12 and Eq. C.13, it is possible to focus on the second multiplicative term on the right hand side of the equations. In particular, considering the denominator and performing the difference (or sum, respectively) of the angles in the sine function, it is possible to obtain:

$$\alpha_{k+1}\frac{\sin\pi(\nu_0-\nu_k)}{\sin\pi(\nu_0-\nu_{k+1})} = \frac{\sin\pi N(\nu_0-\nu_k)}{\sin\pi N(\nu_0-\nu_k)\cos\frac{\pi}{l+1}-\cos\pi N(\nu_0-\nu_k)\sin\frac{\pi}{l+1}} \tag{C.14}$$

$$\alpha_{k-1}\frac{\sin\pi(\nu_0-\nu_k)}{\sin\pi(\nu_0-\nu_{k-1})} = \frac{\sin\pi N(\nu_0-\nu_k)}{\sin\pi N(\nu_0-\nu_k)\cos\frac{\pi}{l+1}+\cos\pi N(\nu_0-\nu_k)\sin\frac{\pi}{l+1}} \tag{C.15}$$

Performing some algebra that aims at dividing the terms that depend on $\pi N(\nu_0-\nu_k)$ from those that only depend on $\pi(\nu_0-\nu_k)$, it is possible to obtain the following equations:

$$\left(\alpha_{k+1}\cos\frac{\pi}{l+1}-\frac{\sin\pi(\nu_0-\nu_k)}{\sin\pi(\nu_0-\nu_{k+1})}\right)\sin\pi N(\nu_0-\nu_k) = \alpha_{k+1}\sin\frac{\pi}{l+1}\cos\pi N(\nu_0-\nu_k) \tag{C.16}$$

$$\left(\alpha_{k-1}\cos\frac{\pi}{l+1}-\frac{\sin\pi(\nu_0-\nu_k)}{\sin\pi(\nu_0-\nu_{k-1})}\right)\sin\pi N(\nu_0-\nu_k) = -\alpha_{k-1}\sin\frac{\pi}{l+1}\cos\pi N(\nu_0-\nu_k) \tag{C.17}$$

Dividing both the right- and the left-hand side of Eq. C.16 and C.17 times the term in brackets and dividing again times the $\cos \pi N(\nu_0 - \nu_k)$, it is possible to obtain an equation in $\tan \pi N(\nu_0 - \nu_k)$ on the left hand side of the equations and all the other terms on the right hand side.

$$\tan \pi N(\nu_0 - \nu_k) = \frac{\alpha_{k+1} \sin \frac{\pi}{l+1}}{\alpha_{k+1} \cos \frac{\pi}{l+1} - \frac{\sin \pi(\nu_0 - \nu_k)}{\sin \pi(\nu_0 - \nu_{k+1})}} \tag{C.18}$$

$$\tan \pi N(\nu_0 - \nu_k) = -\frac{\alpha_{k-1} \sin \frac{\pi}{l+1}}{\alpha_{k-1} \cos \frac{\pi}{l+1} - \frac{\sin \pi(\nu_0 - \nu_k)}{\sin \pi(\nu_0 - \nu_{k-1})}} \tag{C.19}$$

The left-hand side of Eq. C.18 and C.19 are the same, thus equating the two equations enable to write a single equation in the unknown ν_0, the tune, that reads as:

$$\frac{\alpha_{k+1} \sin \frac{\pi}{l+1}}{\alpha_{k+1} \cos \frac{\pi}{l+1} - \frac{\sin \pi(\nu_0 - \nu_k)}{\sin \pi(\nu_0 - \nu_{k+1})}} = -\frac{\alpha_{k-1} \sin \frac{\pi}{l+1}}{\alpha_{k-1} \cos \frac{\pi}{l+1} - \frac{\sin \pi(\nu_0 - \nu_k)}{\sin \pi(\nu_0 - \nu_{k-1})}} \tag{C.20}$$

Performing some algebra , it is possible to find:

$$\tan \pi(\nu_0 - \nu_k) = \frac{(\alpha_{k+1} - \alpha_{k-1}) \sin \frac{\pi}{N(l+1)}}{\alpha_{k+1}\left(\alpha_{k-1} \cos \frac{\pi}{l+1} - \cos \frac{\pi}{N(l+1)}\right) + \alpha_{k-1}\left(\alpha_{k+1} \cos \frac{\pi}{l+1} - cos \frac{\pi}{N(l+1)}\right)} \tag{C.21}$$

The solution of Eq. C.21 for the tune is now trivial, and it reads as:

$$\nu_0 = \frac{k}{N(l+1)} + \frac{1}{\pi} \arctan \left[\frac{(\alpha_{k+1} - \alpha_{k-1}) \sin \frac{\pi}{N(l+1)}}{\alpha_{k+1}\left(\alpha_{k-1} \cos \frac{\pi}{l+1} - \cos \frac{\pi}{N(l+1)}\right) + \alpha_{k-1}\left(\alpha_{k+1} \cos \frac{\pi}{l+1} - cos \frac{\pi}{N(l+1)}\right)} \right], \tag{C.22}$$

C.1 Demonstration of the tune error scaling law

The determination of the tune error scaling law is performed by perturbing the FFT coefficients as follows:

$$\left|\hat{\phi}(\nu_k)\right| = \left|\phi(\nu_k)\right| + \frac{\left|\psi(\nu_k)\right|}{N(l+1)}, \tag{C.23}$$

where $\psi(\nu_k)$ are the FFT coefficients of the perturbation source (for example additional harmonics to be added to the signal). In Eq. C.23 the linearity of the FFT has been exploited to write the perturbed FFT coefficients as the sum of the unperturbed term $\phi(\nu_k)$, which mathematical form is reported in Eq. C.8, and the perturbative term $\psi(\nu_k)$. Both the FFT coefficients (the one relative to the unperturbed signal and the one relative to the perturbation source) have been evaluated at ν_k, being this value the one that maximises the value of the unperturbed FFT coefficients. Thus the perturbed $\hat{\alpha}_{k\pm1}$ will read as:

$$\hat{\alpha}_{k\pm1} = \frac{\left|\hat{\phi}(\nu_k)\right|}{\left|\hat{\phi}(\nu_{k\pm1})\right|}. \tag{C.24}$$

From the substitution of Eq. C.23 into Eq. C.24, it is possible to obtain an expression that shows the dependence between the unperturbed $\alpha_{k\pm1}$ coefficients and the perturbed ones $\hat{\alpha}_{k\pm1}$:

$$\hat{\alpha}_{k\pm1} = \frac{|\phi(\nu_k)| + \frac{|\psi(\nu_k)|}{N(l+1)}}{|\phi(\nu_{k\pm1})| + \frac{|\psi(\nu_{k\pm1})|}{N(l+1)}} = \frac{|\phi(\nu_k)|}{|\phi(\nu_{k\pm1})|}\left(1 + \frac{|\psi(\nu_k)|}{|\phi(\nu_k)|N(l+1)}\right)\left(1 - \frac{|\psi(\nu_{k\pm1})|}{|\phi(\nu_{k\pm1})|N(l+1)}\right) . \tag{C.25}$$

The first multiplicative term on the right-hand side of the second equal sign is clearly the unperturbed $\alpha_{k\pm1}$ coefficients as defined in Eq. C.12 and Eq. C.13. All the other terms are perturbative terms that can be collected together according to their dependence on the number of non-zero samples N and the number of zero blocks l added at the end of the signal. Thus the perturbed $\hat{\alpha}_{k\pm1}$ coefficients read as

$$\hat{\alpha}_{k\pm1} = \alpha_{k\pm1}\left(1 + \frac{c_{1,\pm}}{N(l+1)} + \frac{c_{2,\pm}}{N^2(l+1)^2}\right) , \tag{C.26}$$

where, $c_{1,\pm}$ and $c_{2,\pm}$ are coefficients that depend only on combinations of perturbed $\psi(\nu_k)$, $\psi(\nu_{k\pm1})$ FFT coefficients and unperturbed ones $\phi(\nu_k)$, $\phi(\nu_{k\pm1})$. The most compact way to define the perturbed $\hat{\alpha}_{k\pm1}$ coefficients is:

$$\hat{\alpha}_{k\pm1} = \alpha_{k\pm1}(1 + \delta_{\pm}) , \tag{C.27}$$

where $\delta_{\pm}$ contains the dependence on the number of turns. The propagation of this perturbation into the tune Eq. C.22 allows for the determination of the tune equation precision. The rationale is similar to the one described above, thus, after the substitution of Eq. C.27 into Eq. C.22, the argument within the arc-tangent has to be written as:

$$\arctan[a(1+b)] , \tag{C.28}$$

which Taylor expansion is

$$\arctan[a(1+b)] \approx \arctan(a) + a\frac{b}{1+a^2} , \tag{C.29}$$

where a represent the unperturbed term of the arc-tangent defined as in Eq. C.22 and b contains all the perturbative components. From the definition of the following auxiliary variables:

$$\begin{aligned} t_1 &= (\alpha_{k+1} - \alpha_{k-1})\sin\frac{\pi}{N(l+1)} , \\ t_2 &= \alpha_{k+1}\left(\alpha_{k-1}\cos\frac{\pi}{l+1} - \cos\frac{\pi}{N(l+1)}\right) , \\ t_3 &= \alpha_{k-1}\left(\alpha_{k+1}\cos\frac{\pi}{l+1} - cos\frac{\pi}{N(l+1)}\right) , \end{aligned} \tag{C.30}$$

the perturbed tune equation will read as:

$$\hat{\nu_0} = \frac{k}{N} + \frac{1}{\pi}\arctan\left[\frac{t_1}{t_2+t_3}(1 + \delta_1 - \delta_2 - \delta_1\delta_2)\right] , \tag{C.31}$$

where δ_1 and δ_2 read as:

$$\delta_1 = \frac{\alpha_{k+1}\delta_+ - \alpha_{k-1}\delta_-}{\alpha_{k+1} - \alpha_{k-1}} , \tag{C.32}$$

and

$$\delta_2 = \frac{t_2\left(\delta_+ + \frac{\delta_+\alpha_{k-1}\delta_-\cos\frac{\pi}{l+1}+\alpha_{k-1}\delta_-\cos\frac{\pi}{l+1}}{t_2}\right)+t_3\left(\delta_- + \frac{\delta_-\alpha_{k+1}\delta_+\cos\frac{\pi}{l+1}+\alpha_{k+1}\delta_+\cos\frac{\pi}{l+1}}{t_3}\right)}{t_2+t_3} . \tag{C.33}$$

If the Taylor series in Eq. C.29 is applied to Eq. C.31, then the perturbed tune reads as

$$\hat{\nu_0} = \frac{k}{N} + \frac{1}{\pi}\arctan\left[\frac{t_1}{t_2+t_3}\right] + \frac{t_1}{t_2+t_3}\frac{\delta_1-\delta_2-\delta_1\delta_2}{1+\left(\frac{t_1}{t_2+t_3}\right)^2} , \tag{C.34}$$

where it is possible to recognise the first two terms on the right-hand side of equation as the unperturbed tune described in Eq. C.22 (after the terms in Eq. C.30 have been substituted into Eq. C.34). Thus, the tune error scaling law is determined as the series expansion of the third term in Eq. C.34:

$$\Delta\nu \approx \frac{1}{N^2(l+1)^2}\, f\left(\cos\frac{\pi}{l+1}\right) , \tag{C.35}$$

where $\Delta\nu = |\hat{\nu_0} - \nu_0|$.

APPENDIX D

APPENDIX D: EXPONENTIALLY DAMPED SIGNAL: TUNE AND DAMPING FACTOR ERROR

Considering a damped exponential signal with frequency ν_0 defined as:

$$z(n) = e^{-\lambda n} e^{2\pi i \nu_0 n} \,, \tag{D.1}$$

where n represents the number of turns over which the signal has been sampled and that varies in $1,...,N$. A possible way to determine a closed equation to retrieve the tune, consists in determining the FFT coefficients and solve the equation for the tune. Thus at first, it is possible to write the FFT coefficients as:

$$\phi(\nu_j) = \frac{1}{N} \sum_{n=1}^{\mathrm{N}} e^{2\pi i(\nu_0 - \nu_j) - \lambda n} \,, \tag{D.2}$$

where the frequency $\nu_j = j/N$ and the principal frequency ν_0 has changed notation and became $\hat{\nu_0}$ in Eq. D.2 to highlight the fact that if that equation can be solved for the tune, then the obtained value is a reconstruction of the value ν_0 used to generate the signal.Using the following identities:

$$\sum_{n=0}^{N_1-1} e^{2\pi i f n} = \frac{1 - e^{2\pi i f N_1}}{1 - e^{2\pi i f}}, \tag{D.3}$$

Eq. D.2 can be written in a simplified form that reads as

$$\left|\phi(\nu_j)\right|^2 = \frac{1}{N^2} e^{-\lambda(N+1)} \frac{\sin^2\left(\pi N(\nu_0 - \nu_j) \mp \pi\right) + \sinh^2 \frac{\lambda N}{2}}{\sin^2\left(\pi(\nu_0 - \nu_j) \mp \pi\right) + \sinh^2 \frac{\lambda}{2}} \,. \tag{D.4}$$

Thus, it is possible to solve Eq. D.4 in terms of the tune and the damping factor by using the frequency ν_k that maximises its value, with the FFT coefficients evaluated at the neighbour frequencies $\nu_{k\pm1}$. The tune equation reads as

$$\nu_0 = \frac{k}{N} + \frac{1}{\pi} \arctan\left[\frac{1}{\tan\frac{\pi}{N}} \left(\frac{\eta+1}{\eta-1} \pm \sqrt{\left(\frac{\eta+1}{\eta-1}\right)^2 + \tan^2\frac{\pi}{N}}\right)\right] \,, \tag{D.5}$$

and the equation to retrieve the damping factor λ reads as

$$\lambda = 2\text{arcsinh}\sqrt{\frac{|\phi(\nu_{k+1})|^2 \sin^2\left(\pi(\hat{\nu}_0 - \nu_k) \mp \frac{\pi}{N}\right) - |\phi(\nu_k)|^2 \sin^2 \pi(\hat{\nu}_0 - \nu_k)}{|\phi(\nu_k)|^2 - |\phi(\nu_{k+1})|^2}} \,, \tag{D.6}$$

where the parameter η and χ are defined as

$$\eta = \frac{\chi_+ - 1}{\chi_- - 1} \,, \qquad \chi_\pm = \frac{|\phi(\nu_k)|^2}{|\phi(\nu_{k\pm1})|^2} \,. \tag{D.7}$$

Additional details of the determination of Eq. D.5 and Eq. D.6 can be found in [67]. The determination of the precision with which Eq. D.5 and Eq. D.6 can compute the tune and the damping factor, respectively, is performed by perturbing the FFT coefficients of the unperturbed signal. The perturbed FFT coefficient will read as:

$$\hat{\phi}(\nu_j) = \phi(\nu_j) + \frac{\psi(\nu_j)}{N} \,. \tag{D.8}$$

Taking the absolute value of Eq. D.8 and substituting it into Eq. D.5 and Eq. D.6, it is possible to obtain a perturbed version of the tune and damping factor equation, respectively. In particular, the perturbed variables $\hat{\chi}_\pm$ and $\hat{\eta}_\pm$ read as:

$$\hat{\chi_\pm} = \chi_\pm + \frac{c_i}{N^i}, \qquad \hat{\eta} = \eta(1+\delta) \,, \tag{D.9}$$

where the subscript $i = 1,2$ in the coefficient c refers to the different powers of N (ranging from 1 to 2) and δ contains the dependence on this polynomials. To determine the precision of the tune and damping factor equations, all the terms that depend on the unperturbed coefficients only are collected together. The aim is to write the perturbed version of Eq. D.5 and Eq. D.6 as the product of the unperturbed term and a perturbed one. Thus, for the damping factor equation, it is possible to write:

$$\hat{\lambda} = 2\text{arcsinh}\sqrt{\frac{|\phi(\nu_{k+1})|^2 \sin^2\left(\pi(\hat{\nu}_0 - \nu_k) \mp \frac{\pi}{N}\right)(1+\delta_1) - |\phi(\nu_k)|^2 \sin^2 \pi(\hat{\nu}_0 - \nu_k)(1+\delta_2)}{(|\phi(\nu_k)|^2 - |\phi(\nu_{k+1})|^2)(1+\delta_3)}} \,, \tag{D.10}$$

where δ_1, δ_2 and δ_3 are the perturbative terms of the numerator (for the first two variables) and denumerator (for the last one). After some algebraic operations, it is possible to rewrite Eq. D.10 as:

$$\hat{\lambda} = 2\text{arcsinh}\sqrt{\frac{|\phi(\nu_{k+1})|^2 \sin^2\left(\pi(\hat{\nu}_0 - \nu_k) \mp \frac{\pi}{N}\right) - |\phi(\nu_k)|^2 \sin^2 \pi(\hat{\nu}_0 - \nu_k)}{|\phi(\nu_k)|^2 - |\phi(\nu_{k+1})|^2} \frac{1+\delta_4}{1+\delta_3}} \,, \tag{D.11}$$

where

$$\delta_4 = \frac{|\phi(\nu_{k+1})|^2 \sin^2\left(\pi(\hat{\nu}_0 - \nu_k) \mp \frac{\pi}{N}\right)\delta_1 - |\phi(\nu_k)|^2 \sin^2 \pi(\hat{\nu}_0 - \nu_k)\delta_2}{|\phi(\nu_{k+1})|^2 \sin^2\left(\pi(\hat{\nu}_0 - \nu_k) \mp \frac{\pi}{N}\right) - |\phi(\nu_k)|^2 \sin^2 \pi(\hat{\nu}_0 - \nu_k)} \,. \tag{D.12}$$

The substitution of Eq. D.6 into Eq. D.11 and the definition of the variable

$$\Delta\lambda = |\hat{\lambda} - \lambda| \,, \tag{D.13}$$

enables the determination of the damping factor precision as

$$\Delta\lambda \approx \frac{C_\lambda}{N^2} \,, \tag{D.14}$$

which is based on the series expansion of the $\operatorname{arcsinh}(x+\delta x)$ function with respect to $\delta x \longrightarrow 0$ truncated to the third order. A similar approach can be adopted also for the tune equation which, on the contrary, exploits the series expansion of $\arctan(x+\delta x)$ for $\delta x \longrightarrow 0$. In this case, the tune error scaling law can be computed as:

$$\Delta\nu = \frac{C_\nu}{N^2} \,. \tag{D.15}$$

APPENDIX E

Appendix E: Derivation of the tune Hanning equation for the exponentially damped signal

For the Hanning filtered damped exponential signal described as

$$z(n) = 2e^{-\lambda n}\left(e^{2\pi i \nu_0 n} + \sum_k a_k e^{2\pi i \nu_0 n k}\right)\sin^2\left(\frac{\pi n}{N}\right), \tag{E.1}$$

it is possible to determine an analytical equation to retrieve the tune and the damping used in the generation of the signal itself. The FFT coefficient reads as:

$$\phi(\nu_j) = \frac{2}{N}\sum_{n=1}^{N} e^{2\pi i(\nu_0-\nu_j)n-\lambda n}\sin^2\frac{\pi n}{N}, \tag{E.2}$$

that can be simplified using:

$$\sum_{n=0}^{N_1-1} e^{2\pi i f n} = \frac{1-e^{2\pi i f N_1}}{1-e^{2\pi i f}}. \tag{E.3}$$

In particular, at first the sinusoidal term in Eq. E.2 is converted into an exponential using the second relation in Eq. E.3, then the sum term in Eq. E.2 is solved using the first expression in Eq. E.3. Thus, the FFT coefficient read as:

$$\phi(\nu_j) = \frac{i e^{-N\lambda}\sin^2\frac{\pi}{N}\cot\,\theta_j(\lambda)\left(-e^{\lambda N}+e^{2i\pi(\nu_0-\nu_j)N}\right)}{N\left(\cos\frac{2\pi}{N}-\cos(2\theta_j(\lambda))\right)}, \tag{E.4}$$

where $\theta_j(\lambda)$ is a complex variable defined as:

$$\theta_j(\lambda) = \pi(\nu_0-\nu_j) + i\frac{\lambda}{2}, \text{ where } \theta_j(\lambda)\in\mathbb{C}. \tag{E.5}$$

Evaluating Eq. E.4 at the frequency $\nu_k = k/N$ that maximises its values, the FFT coefficient reads as:

$$\phi(\nu_k) = \frac{i e^{-N\lambda}\sin^2\frac{\pi}{N}\cot\,\theta_k(\lambda)\left(-e^{\lambda N}+e^{2i\pi(\nu_0-\nu_k)N}\right)}{N\left(\cos\frac{2\pi}{N}-\cos(2\theta_k(\lambda))\right)}, \tag{E.6}$$

where also $\theta_j(\lambda)$ has to be evaluated at ν_k, thus it is defined as:

$$\theta_k(\lambda) = \pi(\nu_0 - \nu_k) + i\frac{\lambda}{2} \,. \tag{E.7}$$

The neighbour values of the FFT peak in Eq. E.6 are defined as:

$$\phi(\nu_{k\pm1}) = \frac{ie^{-N\lambda}\sin^2\frac{\pi}{N}\cot\left(\theta_k(\lambda)\mp\frac{\pi}{N}\right)\left(-e^{\lambda N}+e^{2i\pi(\nu_0-\nu_k)N\mp 2\pi i}\right)}{N\left(\cos\frac{2\pi}{N}-\cos(2\theta_k(\lambda)\mp\frac{2\pi}{N})\right)} \,, \tag{E.8}$$

and the ratio between Eq. E.6 and Eq. E.8 leads to:

$$\chi_\pm \equiv \frac{\phi(\nu_k)}{\phi(\nu_{k\pm1})} = \frac{\cos(\theta_k(\lambda))\sin(\theta_k(\lambda)\mp\frac{2\pi}{N})}{\sin(\theta_k(\lambda)\pm\frac{\pi}{N})\cos(\theta_k(\lambda)\mp\frac{\pi}{N})} \,, \tag{E.9}$$

where the variable $\chi_\pm$ has been introduced and defined to simplify the notation. It is possible to use the sum rule of trigonometric functions to obtain a simplified version of Eq. E.9 that reads as:

$$\chi_\pm = \frac{\sin\mp\frac{2\pi}{N}+\sin(2\theta_k(\lambda)\mp\frac{2\pi}{N})}{\sin\pm\frac{2\pi}{N}+\sin 2\theta_k(\lambda)} \,. \tag{E.10}$$

Equation E.10 is an equation with complex coefficients in the complex unknown $\theta_k(\lambda)$. Equation E.10 can be also written as:

$$(\cos\frac{2\pi}{N}-\chi_\pm)\sin 2\theta_k(\lambda)\mp\sin\frac{2\pi}{N}\cos 2\theta_k(\lambda) = \pm\sin\frac{2\pi}{N}(\chi_\pm+1) \,. \tag{E.11}$$

Writing the cosine function in Eq. E.11 in terms of the sine leads to a second order equation:

$$(\chi_\pm^2+1-2\chi_\pm\cos\frac{2\pi}{N})\sin^2 2\theta_k(\lambda)\pm 2\sin\frac{2\pi}{N}(\chi_\pm+1)\left(\chi_\pm-\cos\frac{2\pi}{N}\right)\sin 2\theta_k(\lambda)+\sin^2\frac{2\pi}{N}\chi_\pm(\chi_\pm+2)=0 \,, \tag{E.12}$$

to simplify the notation it is possible to define the following variables:

$$a = (\chi_\pm^2+1-2\chi_\pm\cos\frac{2\pi}{N}) \,,\; b = \pm 2\sin\frac{2\pi}{N}(\chi_\pm+1)\left(\chi_\pm-\cos\frac{2\pi}{N}\right) \,,\; c = \sin^2\frac{2\pi}{N}\chi_\pm(\chi_\pm+2) \,.$$

Thus, Eq. E.12 reads as:

$$a\sin^2 2\theta_k(\lambda)+b\sin 2\theta_k(\lambda)+c=0 \,. \tag{E.13}$$

Equation E.13 is a second-order equation that can be easily solved and which solutions look as:

$$\sin 2\theta_k(\lambda)\Big|_{1,2} = \frac{-b\pm\sqrt{b^2-4ac}}{2a} \,, \tag{E.14}$$

where it is important to highlight that all the mathematical operations in Eq. E.14 occur between complex number, thus they should be properly performed. When the FFT coefficient evaluated at the ν_{k+1} frequency term is larger than the one evaluated at ν_{k-1} (thus, $|\phi(\nu_{k+1})| > |\phi(\nu_{k-1})|$) the positive sign in Eq. E.14 is chosen, the opposite holds true. In order to determine the tune and the damping factor it is necessary to determine the inverse sine function of a complex number. It

is possible to find its definition in Ref. [68] using the formula 4.4.37 that is reported here below for the sake of completeness:

$$\arcsin(z) = \arcsin(x+iy) = k\pi + (-1)^k \arcsin\beta + (-1)^k i \ln\left(\alpha + \sqrt{(\alpha^2+1)}\right) , \tag{E.15}$$

where k is either an integer or $k = 0$ (this last value has been considered in the following calculations) and,

$$\alpha = \frac{1}{2}\sqrt{\left((x+1)^2+y^2\right)} + \frac{1}{2}\sqrt{\left((x-1)^2+y^2\right)}$$

and

$$\beta = \frac{1}{2}\sqrt{\left((x+1)^2+y^2\right)} - \frac{1}{2}\sqrt{\left((x-1)^2+y^2\right)}$$

The complex number $z = x + iy$ in Eq. E.15 corresponds to the right-hand side of Eq. E.14, where x and y are the real and imaginary components, respectively, of the complex number. Thus:

$$z = x + iy = \Re\frac{-b \pm \sqrt{b^2-4ac}}{2a} + i\Im\frac{-b \pm \sqrt{b^2-4ac}}{2a} \tag{E.16}$$

In conclusion, the real and the imaginary part of Eq. E.15 with $k = 0$ are related to the tune and the damping factor of the signal in Eq. E.1 with Eq. E.7 and Eq. E.14. Thus, from the following equality

$$2\pi(\nu_0 - \nu_k) + i\lambda = \left(\arcsin\beta + i\ln\left(\alpha + \sqrt{\alpha^2+1}\right)\right) , \tag{E.17}$$

the tune equation reads as

$$\hat{\nu}_0 = \frac{k}{N} + \frac{1}{2\pi}\arcsin\beta , \tag{E.18}$$

while the one for the damping factor is

$$\hat{\lambda} = \ln\left(\alpha + \sqrt{\alpha^2+1}\right) . \tag{E.19}$$

BIBLIOGRAPHY

[1] Nobelprize.org. The Nobel Prize in Physics 1979. https://www.nobelprize.org/prizes/physics/1979/summary/, 2022.

[2] Carlo Rubbia. Experimental observation of some of the properties of the intermediate vector bosons. 1986.

[3] Nobelprize.org. The Nobel Prize in Physics 1984. https://www.nobelprize.org/prizes/physics/1984/summary/, 2022.

[4] Peter W. Higgs. Broken symmetries and the masses of gauge bosons. *Phys. Rev. Lett.*, 13:508–509, Oct 1964.

[5] S. Chatrchyan et all. Observation of a new boson at a mass of 125 gev with the cms experiment at the lhc. *Physics Letters B*, 716(1):30–61, 2012.

[6] G. Aad et all. Observation of a new particle in the search for the standard model higgs boson with the atlas detector at the lhc. *Physics Letters B*, 716(1):1–29, 2012.

[7] Nicholas Stoffle, Lawrence Pinsky, Martin Kroupa, Son Hoang, John Idarraga, Clif Amberboy, Ryan Rios, Jessica Hauss, John Keller, Amir Bahadori, Edward Semones, Daniel Turecek, Jan Jakubek, Zdenek Vykydal, and Stanislav Pospisil. Timepix-based radiation environment monitor measurements aboard the international space station. *Nuclear Instruments and Methods in Physics Research Section A: Accelerators, Spectrometers, Detectors and Associated Equipment*, 782:143–148, 2015.

[8] M. J. Syphers D. A. Edwards. *An introduction to the physics of high energy accelerators*. Wiley-VCH, 1993.

[9] Ewa Lopienska. The CERN accelerator complex - January 2022. Complexe des accélérateurs du CERN - Janvier 2022. Feb 2022. General Photo.

[10] Ulrich W Heinz and Maurice René Michel Jacob. Evidence for a New State of Matter: An Assessment of the Results from the CERN Lead Beam Programme. Technical report, CERN, Geneva, Feb 2000.

[11] K. Aamodt et al. The ALICE experiment at the CERN LHC. *JINST*, 3:S08002, 2008.

[12] G. Aad et al. The ATLAS Experiment at the CERN Large Hadron Collider. *JINST*, 3:S08003, 2008.

[13] S. Chatrchyan et al. The CMS Experiment at the CERN LHC. *JINST*, 3:S08004, 2008.

[14] Valerie Gibson. The LHCb experiment. In *22nd Lake Louise Winter Institute: Fundamental Interactions*, pages 60–79, 2007.

[15] M Chanel. LEIR: The low energy ion ring at CERN. *Nucl. Instrum. Methods Phys. Res., A*, 532:137–143. 9 p, Jun 2002.

[16] Andrea Latina, Hannes Bartosik, Nicolo Biancacci, Roberto Corsini, Davide Gamba, Simon Hirlaender, and Alexander Huschauer. Electron Cooling Simulation and Experimental Benchmarks at LEIR. page TUPAF039. 4 p, 2018.

[17] G.B. et all Andresen. Confinement of antihydrogen for 1000 seconds. Confinement of antihydrogen for 1,000 seconds. *Nature Phys.*, 7:558–564. 7 p, Apr 2011. Advance online publication.

[18] Frank Tecker. Longitudinal Beam Dynamics in Circular Accelerators. Technical report, Nov 2020. 17 pages, contribution to the CAS - CERN Accelerator School: Introduction to Accelerator Physics. arXiv admin note: substantial text overlap with arXiv:2004.11908, arXiv:1601.04901.

[19] Ernest D. Courant, M. Stanley Livingston, and Hartland S. Snyder. The strong-focusing synchroton—a new high energy accelerator. *Phys. Rev.*, 88:1190–1196, Dec 1952.

[20] Jean-Paul Burnet, Christian Carli, Michel Chanel, Roland Garoby, Simone Gilardoni, Massimo Giovannozzi, Steven Hancock, Helmut Haseroth, Kurt Hübner, Detlef Küchler, Julian Lewis, Alessandra Lombardi, Django Manglunki, Michel Martini, Stephan Maury, Elias Métral, Dieter Möhl, Günther Plass, Louis Rinolfi, Richard Scrivens, Rende Steerenberg, Charles Steinbach, Maurizio Vretenar, and Thomas Zickler. *Fifty years of the CERN Proton Synchrotron: Volume 1*. CERN Yellow Reports: Monographs. CERN, Geneva, 2011.

[21] M Martini. An introduction to transverse beam dynamics in accelerators. Technical report, CERN, Geneva, Mar 1996.

[22] S. Y. Lee. *Accelerator Physics - second edition*. World Scientific Publishing Co. Pte. Ltd., 2004.

[23] Stuart Turner. CAS - CERN Accelerator School : 5th General Accelerator Physics Course: Jyväskylä, Finland 7 - 18 Sep 1992. CAS - CERN Accelerator School : 5th General Accelerator Physics Course. Geneva, 1994. CERN, CERN. 2 volumes, consecutive pagination.

[24] MAD - methodical accelerator design. https:/mad.web.cern.ch/mad/.

[25] F Schmidt, E Forest, and E McIntosh. Introduction to the polymorphic tracking code: Fibre bundles, polymorphic Taylor types and "Exact tracking". Technical report, CERN, Geneva, Jul 2002.

[26] R Cappi and Massimo Giovannozzi. Novel Method for Multi-turn Extraction: trapping charged Particles in Islands of Phase Space. *Phys. Rev. Lett.*, 88:104801. 8 p, Dec 2001.

[27] Y. Wang et al. Effects of tune modulation on particles trapped in 1D resonance islands. *Phys. Rev. E*, 49:5697–5705, 1994.

[28] M Ball, B Brabson, J I Budnick, C M Chu, D D Caussyn, J Collins, V P Derenchuk, G East, M Ellison, D L Friesel, K M Fung, B Hamilton, W C Hsi, W P Jones, S Y Lee, A Riabko, Terence Sloan, H Huang, D Li, K Y Ng, and X Pei. Beam motions near separatrix. Apr 1999.

[29] Mariusz Juchno. Electromagnetic FEM analysis of the CERN Proton Synchrotron main magnetic unit, 2009. Presented on 21 Jan 2009.

[30] L Badano, Michael Benedikt, P J Bryant, M Crescenti, P Holy, A T Maier, M Pullia, S Rossi, and P Knaus. *Proton-Ion Medical Machine Study (PIMMS), 1.* Mar 1999.

[31] Bernhard Holzer. CAS - CERN Accelerator School: Beam Injection, Extraction and Transfer. Geneva, Dec 2018. CERN.

[32] Massimo Giovannozzi, M J Barnes, O E Berrig, A Beuret, J Borburgh, P Bourquin, R Brown, Jean Paul Burnet, Friedhelm Caspers, J M Cravero, T Dobers, T Fowler, S S Gilardoni, M Hourican, Willi Kalbreier, T Kroyer, F Di Maio, M Martini, V Mertens, E Métral, K D Metzmacher, C Rossi, J P Royer, L Sermeus, R Steerenberg, G Villiger, and T Zickler. *The CERN PS multi-turn extraction based on beam splittting in stable islands of transverse phase space: Design Report*. CERN Yellow Reports: Monographs. CERN, Geneva, 2006.

[33] Alexander Huschauer. Beam Dynamics Studies for High-Intensity Beams in the CERN Proton Synchrotron, May 2016. Presented 17 Jun 2016.

[34] L Sermeus, M J Barnes, and T Fowler. The Kicker Systems for the PS Multi-turn Extraction. Jun 2010.

[35] C Bertone, J Borburgh, D Bodart, R Brown, S Burger, S Damjanovic, P Demarest, R Fernandez Ortega, JA Ferreira Somoza, D Gerard, S Gibson, S Gilardoni, M Giovannozzi, G Le Godec, C Hernalsteens, M Hourican, N Jurado, J M Lacroix, S Mataguez, G Métral, C Pasquino, E Perez-Duenas, S Persichelli, B Salvant, R Steerenberg, and P Van Trappen. Studies and implementation of the PS dummy septum to mitigate irradiation of magnetic septum in straight section 16. Technical report, CERN, Geneva, Apr 2014.

[36] Alexander Huschauer, Jan Borburgh, Sanja Damjanovic, Simone Gilardoni, Massimo Giovannozzi, Michael Hourican, Karsten Kahle, Olivier Michels, Guido Sterbini, Cedric Hernalsteens, and Gilles Le Godec. Transverse beam splitting made operational: Recent progress of the multi-turn extraction at the CERN proton synchrotron. page MOPR009. 6 p, Jul 2016.

[37] M Vadai, A Alomainy, H Damerau, S Gilardoni, M Giovannozzi, and A Huschauer. Barrier bucket and transversely split beams for loss-free multi-turn extraction in synchrotrons. *EPL*, 128:14002. 7 p, 2019.

[38] R Jones, M Gasior, T Lefevre, H Schmickler, and K Wittenburg. Introduction to beam instrumentation and diagnostics. page 38 p, 2014. Comments: 38 pages, contribution to the CAS - CERN Accelerator School: Advanced Accelerator Physics Course, Trondheim, Norway, 18-29 Aug 2013.

[39] Gian Luca Orlandi et al. Wire-Scanners with Sub-Micrometer Resolution: Developments and Measurements. In *39th International Free Electron Laser Conference*, page WEB02, 2019.

[40] Tino Giacomini and P Forck. Ionization profile monitors - ipm @ gsi *. 2011.

[41] Peter Forck. Minimal invasive beam profile monitors for high intense hadron beams. *IPAC 2010 - 1st International Particle Accelerator Conference*, 01 2010.

[42] K Wittenburg. Beam loss monitors. 2009.

[43] FLUKA. https://https://fluka.cern/.

[44] C. Zamantzas. Blm installations at eyets: Ecr comments. Geneva, Switzerland, january 2017. LIU - Planning and Installation meeting.

[45] Edoardo Bossini and Nicola Minafra. Diamond Detectors for Timing Measurements in High Energy Physics. *Front. Phys.*, 8:248, 2020.

[46] CIVIDEC instrumentation gmbh. https://https://cividec.at/index.php.

[47] A Huschauer, H Bartosik, S Cettour Cave, M Coly, D Cotte, H Damerau, G P Di Giovanni, S Gilardoni, M Giovannozzi, V Kain, E Koukovini-Platia, B Mikulec, G Sterbini, and F Tecker. Advancing the CERN proton synchrotron multiturn extraction towards the high-intensity proton beams frontier. *Phys. Rev. Accel. Beams*, 22:104002. 13 p, 2019.

[48] V Chohan. Computer controlled beam local radial perturbation and rotation in CERN PS. *IEEE Trans. Nucl. Sci.*, 26:3334–3336. 3 p, Feb 1979.

[49] S et al. Abernethy. Operational performance of the CERN injector complex with transversely split beams. *Phys. Rev. Accel. Beams*, 20:014001. 21 p, 2017.

[50] J et al. Borburgh. First implementation of transversely split proton beams in the CERN Proton Synchrotron for the fixed-target physics programme. *Europhys. Lett.*, 113:34001. 6 p, 2016.

[51] A Huschauer, M Giovannozzi, O Michels, A Nicoletti, and G Sterbini. Analysis of performance fluctuations for the CERN Proton Synchrotron multi-turn extraction. *J. Phys.: Conf. Ser.*, 874:012072. 8 p, 2017.

[52] R Bartolini, A Bazzani, Massimo Giovannozzi, Walter Scandale, and Ezio Todesco. Tune evaluation in simulations and experiments. *Part. Accel.*, 52:147–177. 29 p, Oct 1995.

[53] R Tomás, S Fartoukh, and J Serrano. Reliable Operation of the AC Dipole in the LHC. page 4 p, Aug 2008.

[54] M Gasior and R Jones. The principle and first results of betatron tune measurement by direct diode detection. Technical report, CERN, Geneva, Aug 2005. revised version submitted on 2005-09-16 09:23:15.

[55] J Laskar. Secular evolution of the solar system over 10 million years. *Astronomy and Astrophysics*, 198:341–362, 1988.

[56] Jacques Laskar. Frequency analysis for multi-dimensional systems. global dynamics and diffusion. *Physica D: Nonlinear Phenomena*, 67(1):257–281, 1993.

[57] D.S.G. Pollock. Chapter 15 - the fast fourier transform. In D.S.G. Pollock, editor, *Handbook of Time Series Analysis, Signal Processing, and Dynamics*, Signal Processing and its Applications, pages 427–456. Academic Press, London, 1999.

[58] E. Sander and J.D. Meiss. Birkhoff averages and rotational invariant circles for area-preserving maps. *Physica D: Nonlinear Phenomena*, 411:132569, oct 2020.

[59] Peter Bloomfield. *Fourier Analysis of Time Series*. Probability and statistics. Wiley, 2000.

[60] Suddhasattwa Das, Yoshitaka Saiki, Evelyn Sander, and James A Yorke. Quantitative quasiperiodicity. *Nonlinearity*, 30(11):4111–4140, oct 2017.

[61] Giulia Russo, Giuliano Franchetti, and Massimo Giovannozzi. New Techniques to Compute the Linear Tune. NEW TECHNIQUES TO COMPUTE THE LINEAR TUNE. *JACoW IPAC*, '21:4142–4145. 4 p, 2021.

[62] Suddhasattwa Das and James A Yorke. Super convergence of ergodic averages for quasiperiodic orbits. *Nonlinearity*, 31(2):491–501, jan 2018.

[63] Massimo Giovannozzi, Walter Scandale, and Ezio Todesco. Dynamic Aperture Extrapolation in Presence of Tune Modulation. *Phys. Rev. E*, 57:3432. 24 p, Sep 1997.

[64] R. E. Meller, A. W. Chao, J. M. Peterson, Stephen G. Peggs, and M. Furman. Decoherence of Kicked Beams. 5 1987.

[65] R P Walker. Synchrotron radiation. 1994.

[66] A. W. Chao. Evaluation of Beam Distribution Parameters in an Electron Storage Ring. *J. Appl. Phys.*, 50:595, 1979.

[67] Ignacio Fabre. Betatron Tune Determination: Interpolation Formulas. Aug 2015. Summer Student Report.

[68] Milton Abramowitz and Irene A. Stegun. *Handbook of Mathematical Functions with Formulas, Graphs, and Mathematical Tables*. Dover, New York City, ninth dover printing, tenth gpo printing edition, 1964.

[69] Stefan L. Hahn. *Hilbert transform in signal processing*. Artech House, Boston, 1996.

[70] Norden E. Huang, Zheng Shen, Steven R. Long, Manli C. Wu, Hsing H. Shih, Quanan Zheng, Nai-Chyuan Yen, Chi Chao Tung, and Henry H. Liu. The empirical mode decomposition and the hilbert spectrum for nonlinear and non-stationary time series analysis. *Proceedings: Mathematical, Physical and Engineering Sciences*, 454(1971):903–995, 1998.

[71] Nicolas Le Bihan and Stephen J. Sangwine. The hyperanalytic signal, 2010.

[72] Nicolas Le Bihan, Stephen J. Sangwine, and Todd A. Ell. Instantaneous frequency and amplitude of orthocomplex modulated signals based on quaternion fourier transform. *Signal Processing*, 94:308–318, jan 2014.

[73] Norden Huang, Zheng Shen, Steven Long, M.L.C. Wu, Hsing Shih, Quanan Zheng, Nai-Chyuan Yen, Chi-Chao Tung, and Henry Liu. The empirical mode decomposition and the hilbert spectrum for nonlinear and non-stationary time series analysis. *Proceedings of the Royal Society of London. Series A: Mathematical, Physical and Engineering Sciences*, 454:903–995, 03 1998.

[74] E. H. Maclean, R. Tomás, F. Schmidt, and T. H. B. Persson. Measurement of nonlinear observables in the large hadron collider using kicked beams. *Phys. Rev. ST Accel. Beams*, 17:081002, Aug 2014.

[75] Hamish Maclean Ewen. Modelling and correction of the non-linear transverse dynamics of the LHC from beam-based measurements, 2014.

[76] S. Gilardoni, M. Giovannozzi, M. Martini, E. Métral, P. Scaramuzzi, R. Steerenberg, and A.-S. Müller. Experimental evidence of adiabatic splitting of charged particle beams using stable islands of transverse phase space. *Phys. Rev. ST Accel. Beams*, 9:104001, Oct 2006.